Facultad Ciencia

Departamento de Química Analítica y Análisis Instrumental

Nanostructured Direct Electron Transfer Based Biocathodes for Applications in Biofuel Cells

Chiara Di Bari

Madrid, 2017

Facultad Ciencia

Departamento de Quimica Analitica y Analisis Instrumental

Nanostructured Direct Electron Transfer Based Biocathodes for Applications in Biofuel Cells

Institute of Catalysis and Petrochemistry

Spanish Council for Scientific Research (CSIC)

Chiara Di Bari

Director: Dr. Antonio López de Lacey

Co-director: Dr. Marcos Pita Martinez

Tutora: Dra. Mª Encarnación Lorenzo Abad

Madrid, 2017

ANTONIO LÓPEZ DE LACEY Y MARCOS PITA MARTÍNEZ, DRS. EN CIENCIAS QUÍMICAS, INVESTIGADOR CIENTÍFICO Y CIENTIFICO TITULAR RESPECTIVAMENTE DEL C.S.I.C EN EL INSTITUTO DE CATÁLISIS Y PETROLEOQUÍMICA

CERTIFICAN: Que el presente trabajo "Nanostructured direct electron transfer based biocathodes for applications in biofuel cells", que constituye la Memoria que presenta la Licenciada en Química por la Universita degli Studi de Milán (Italia), Chiara Di Bari, ha sido realizado bajo su dirección en el Departamento de Biocatálisis del Instituto de Catálisis y Petroleoquímica del C.S.I.C., Campus de Excelencia Internacional UAM + CSIC, Madrid.

Para que conste, firman el presente certificado a 12 de Junio de 2017.

Dr. Antonio López de Lacey

Director de la Tesis Doctoral

Dr. Marcos Pita Martínez

Co-Director de la Tesis Doctoral

Acknowledgements

At the end of these years, I would like to express my gratitude to all the people who helped and supported me through this part of my life.

My first thanks go to my supervisors, Dr. Antonio Lopez de Lacey and Dr. Marcos Pita, for offering me the opportunity to work in their laboratories and discovering the world of bioelectrochemistry and also for their guidance and advices during my PhD.
Thanks to my tutor from UAM University, Dr. Mª Encarnacion Lorenzo Abad for her interest and for always be helpful every time I need.

To the European Commission for their financial support through BIOENERGY project, under the 7th framework ITN Marie Curie program and to all the partners involved in: Ruhr-Universität Bochum, Malmoe University, University of Limerick, National University of Ireland (Galway), Lund Universitet, Universität für Bodenkultur (Wien), University of Southampton**,** Centre National de le Recherche Scientifique (Bordeaux), University of Warsaw**,** Dropsens, Nanoflex Limited and Nanoinnova Technologies. I want to thank all the partners for the possibility to learn precious scientific and personal lessons.

My gratitude goes in particular to Prof. Dr. Alexander Khun and Dr. Nicolas Mano, from CNRS-Bordeaux University, Prof. Dr. Sergey Shleev from Malmoe University, Dr. Rafel Ferrito and Dr. Raquel Sainz, from Nannoinova Technologies for giving me the opportunity to work in their laboratory and learning new concepts and techniques. Thanks to everyone in Dr. M. Alcalde's group, from ICP-CSIC, for helping me producing and purifying my mutants. Finally, I will not forget all the PhD and PostDoc students part of this project: Asier, Ivan, Elena, Magdalena, Galina, Marta, Valentina, Francesca, Sabine, Su, Till, Xin-Xin, Ali, Kanso, Magnus, Nikola, Michal and Yulia. I am glad to have met you and thanks everyobody for the great moments shared together. In particular, my deepest gratitude goes to Asier for teaching, listening to and helping me, also during my toughest times and to Ivan and Elena for the beers and wine shared, for their advices and their friendship during these years. I hope this will continue in the future.

I would like to thank all the ICP members that helped me and shared these years with me. Thanks to all the special people I have met during these years: Cristina, Lara, Maria, Sonia, Carlos, Barbara, Sandro, Cesar, Diogo, Angela, Erik, Fernando, Cristina, Oscar, Ile, Alejandro, Janaina, Gabriel, Jose, Monica, and all the members of Alcalde's group. In particular, Cristina, my lab mate, thank you for helping me since my first days in Madrid and for all the time shared out the lab, and Lara, Maria and Sonia for all the travels and funny moments we shared.

Lara, in particular, deserves one of my deepest thanks. Thank you for helping and comforting me every time I need, for the laughs, for the shopping time, for the parties, for tasting different kind of restaurants with me, for never letting me feel alone even if my family and closest friends were far, thank you for your true friendship.

A huge thank to my closest friends in Italy: Deborah, Irene, Greta and Laura. I know that this time away from each other was as difficult for you as for me and I can only thank you for supporting me no matter what, for taking many flights to different European destinations only to meet me, for the endless skype calls and to have been my friends for so many years.

Dulcis in fundo, the biggest thanks go to my family. To my grandma and Raffaella that always call me to be sure that I eat enough and I am not alone, to zia Elisa for always being at my side, to Gussetti's family and in particular to Sarah to be more than a cousin, to Jose to be a special uncle and to Jaime.
My infinite gratitude goes to my parents and my brother for always believing in me and encouraging me in following my dreams even if this means going far from them. All of this is especially thanks to you.

"A scientist in his laboratory is not a mere technician:
he is also a child confronting natural phenomena that
impress him as though they were fairy tales"
Marie Curie

"Le donne che hanno cambiato il mondo non hanno mai avuto
bisogno di dimostrare nulla se non la loro intelligenza"
Rita Levi Montalcini

Summary

During the last years biofuel fuel cells (BFCs) have attracted great interest due to their possible applications, especially as electrical power sources for *in vivo* or *ex vivo* applications. In BFCs enzymes can be used as biocatalysts for fuel oxidation at the anode and oxidant reduction at the cathode. The majority of EFCs use oxygen-reducing enzymes at the cathode, and glucose-oxidizing enzymes at the anode, as they are very common substrates present in most human physiological fluids.

Two multi-copper oxidases, laccase and bilirubin oxidase, and cellobiose dehydrogenase have been studied as possible biocatalysts for the oxygen reduction reaction and glucose oxidation, respectively. Laccases usually exhibit higher activity at acid pH and they are more inhibited in the presence of chloride ions than bilirubin oxidase. Therefore, native laccases have been engineered by directed evolution for obtaining mutants that show activity also under physiological conditions, and cysteine residues have been introduced by site-directed mutagenesis for oriented immobilization on gold electrodes.

The major aim of the Thesis has been the development of biocathodes as they represent the rate-limiting part of the BFC due to the low O_2 availability in human body. The development of the bioelectrodes was carried out paying special attention to the different electrode materials and immobilization strategies used to manufacture the biodevices. Indeed, a good immobilization strategy enhances the long-term stability of the biodevice while achieving efficient wiring of the enzyme. Additionally, a larger surface area of the support material allows higher enzyme loading, therefore increasing the current density developed. Gold nanorods, macroporous gold, indium tin oxide and carbonaceous materials have been used for this purpose, obtaining current densities up to 1.5 mA/cm^2 for bioelectrocatalytic O_2 reduction.

Direct electron transfer (DET) based systems are preferred as some possible drawbacks of using mediators are overcome and allow making the miniaturization of the BFC easier. For these reason, all the immobilization strategies presented were developed in order to optimize DET between the enzyme and the electrode surface.

Combination of a conventional BFC with electrochemical capacitors is also presented in order to overcome the limitations of both systems, achieving a maximum power output of 0.6 μW at an operating voltage of 0.15 V. This hybrid biodevice was also tested in *ex vivo* conditions by connecting it directly to the dorsal venous of a human volunteer.

Resumen

En los últimos años las biopilas de combustible han suscitado un fuerte interés sobre todo por su posible utilizacion en condiciones *in vivo* y *ex vivo*. Las biopilas de combustible pueden utilizar catalizadores enzimáticos tanto en el ánodo como en el cátodo. La mayoría de las biopilas están basadas en oxidación de glucosa en el ánodo y reducción de oxígeno en el cátodo, siendo dos substratos muy comunes en los fluidos fisiológicos humanos.

Las dos oxidasas multicobre, lacasa y bilirrubina oxidasa, y celobiosa deshidrogenasa han sido estudiadas como posibles biocatalizadores, de la reducción de oxígeno y de la oxidación de glucosa, respectivamente. Las lacasas suelen presentar mayor actividad a pH acido y son más inhibidas por los iones cloruros que la bilirrubina oxidasa. Por lo tanto, se han diseñado lacasas mutadas por evolución dirigida, que sean activas también a pH fisiológico, y se han introducido cisteínas por mutagenesis dirigida para favorecer la orientación óptima de las enzimas sobre electrodos de oro.

El objetivo principal de esta Tesis doctoral ha sido enfocado en el desarrollo de biocatodos, porque representan la parte limitante del sistema debido a la baja disponibilidad de oxígeno en el cuerpo humano. El desarrollo de los bioelectrodos ha sido realizado estudiando distintos materiales como electrodos y la optimización de estrategias de inmovilización de enzimas. De hecho, la correcta estrategia permite de mejorar la estabilidad a largo plazo del bioelectrodo consiguiendo la óptima conexión del enzima con el soporte. Además, materiales nanoestructurados de gran área superficial permiten inmovilizar mayores cantidades de enzima y consecuentemente obtener mayor respuesta catalítica. Nanohilos de oro, oro macroporosos, ITO y materiales de carbón han sido utilizados para realizar este objetivo, obteniendose corrientes de 1.5 mA/cm^2 por la reducción de oxígeno.

Los sistemas basados en trasferencia electrónica directa se prefieren para el desarrollo de biopilas de combustible porque de esta manera se evitan las desventajas que pueden presentar el uso de mediadores y al mismo tiempo es más fácil el diseño de biopilas de combustibles miniaturizadas. Por estas razones todas las estrategias de inmovilización desarrolladas en esta Tesis han sido enfocadas en obtener trasferencia electrónica directa entre el biocatalizador y el electrodo.

Finalmente, se ha presentado la combinación de una biopila de combustible convencional con un capacitor electroquímico con el fin de superar las limitaciones de ambos sistemas, obteniendo una potencia máxima de 0.6 µW a un voltaje operacional de 0.15 V. Este sistema híbrido ha sido también utilizado in condiciones *ex vivo*, conectándolo directamente a la vena dorsal de un voluntario.

Index

Acronyms

- **ABTS:** 2,2'-azino-bis(3-ethylbenzothiazoline-6-sulphonic acid)
- **AP:** Aminophenyl
- **APTES:** (3-aminopropryl)triethoxysilane
- **AuNPs:** Gold nanoparticles
- **AuNRs:** Gold nanorods
- **BSA:** Bovine serum albumin
- **BFC:** Biofuel cell
- **BT:** 1,4–Benzenedithiol
- **CNTs:** Carbon nanotubes
- **CPs:** Conducting polymers
- **CTAB:** Hexadecyltrymethilammonium bromide
- **ctCDH:** *Corynascus thermophiles* cellobiose dehydrogenase
- **CV:** Cyclic voltammetry
- **DET:** Direct electron transfer
- **DTT:** Dithiothrethiol
- **ECD:** 1-Ethyl-3-(3-dimethylaminopropyl)carbodiimide
- **ED:** Electrodeposition
- **EDOT:** 3,4-ethylenedioxythiophene
- **EFC:** Enzymatic fuel cell
- **EIS:** Electrochemical impedance spectroscopy
- **erGO:** Electrochemical reduced graphene oxide
- **FeMeOH:** Ferrocene methanol
- **FTIR:** Fourier transform infrared spectroscopy
- **FPLC:** Fast protein liquid chromatography
- **GC:** Glassy carbon
- **GLYMO:** (3-glycidyloxypropyl) trimethoxysilane
- **GO:** Graphene oxide
- **GW:** Gold wire
- **HPLC:** High performance liquid chromatography
- **HRTEM:** High resolution transmission electron microscopy
- **ITO:** Indium tin oxide
- **K_m:** Michaelis-Menten constant
- **LDG:** Low density graphite

- **MCOs:** Multicopper oxidases
- **MES:** 2-(*N*-morpholino)-ethanesulfonic acid
- **MET:** Mediated electron transfer
- **mgBOx:** *Magnaporthe oryzae* bilirubin oxidase
- **MG:** Macroporous gold
- **MH:** Mercapto hexanol
- **MPA:** Mercaptopropionic acid
- **mtBOx:** *Myrothretium verrucaria* bilirubin oxidase
- **NA:** 6-amino-2-naphtoic acid
- **NPG:** Nanoporous gold
- **NTA:** nitrilotriacetic acid
- **NHE:** Normal hydrogen electrode
- **NHS:** N-hydroxysuccinimide
- **OCV:** Open circuit voltage
- **PEDOT:** Poly(3,4-ethylenedioxythiophene)
- **PEG:** polyethylene glycol
- **RT:** Room temperature
- **SAM:** Self-assembled monolayer
- **SCBSC:** Self charging biosupercapacitor
- **SEM:** Scanning electron microscopy
- **SHE:** Standard hydrogen electrode
- **TEMPO:** 2,2,6,6-Tetramethyl-1-piperidinyloxy
- **ThLc:** *Trametes hirsuta* laccase
- **THPC:** Tetrakis(hydroxymethyl) phosphonium chloride
- **TNC:** Trinuclear cluster
- **Uv-Vis:** Ultraviolet-visible spectroscopy
- **XPS:** X-ray photoelectron spectroscopy

1. Introduction

The demand for alternative energy sources to fossil fuels with low environmental impact is continuously increasing over the years. In consequence a great effort is been made in research on new catalytic processes with higher conversions and better selectivity for energy applications. Electrochemical energy production is considered a more sustainable and environmental friendly way to generate electrical power energy in than many traditional power generators. Electrochemical systems utilize the chemical energy stored in a fuel to produce electrical energy by direct conversion, such as batteries, fuel cells and electrochemical capacitors. Among them, fuel cells have attracted great interest due to their possible advantages over conventional batteries (Winter and Brodd 2004).

Simultaneously, the field of bioelectronics, which concerns the coupling of biomolecules with electronic or optoelectronic devices (Katz 2006), has been subject of increasing research studies. The electrical coupling of a bioelement with electronic devices can be indeed used to transduce the chemical signal generated by the biological components to electronic signals or to activate the bioelements by applying electronic signals. Bioelectronic devices open the way to exciting applications in sensing devices (health and environmental monitoring) and energy field. Their development has to focus on the achievement of an effective close contact and of an efficient electron transfer between the biological and electric parts. The recent success of nanotechnology in the development of new materials (such as carbon nanotubes, graphene, metallic nanoparticles, etc.), leads the way to new possibilities in interfacing biomaterials and electronic devices (Katz 2006, Cosnier, J. Gross et al. 2016).

Indeed, the combination of bioelectronics with fuel cells has led to the development of biofuel cells where the energy production derives from biologically renewables. This technology has paved the way to possible applications where conventional fuel cells present limitations, such as implantable fuel cells in the human body (*in vivo* or *ex vivo*) capable of monitoring physiological processes and data transmission (Falk, Narváez Villarrubia et al. 2013, Cosnier, J. Gross et al. 2016, Rasmussen, Abdellaoui et al. 2016). The main goal of recent research in this field is to increase the knowledge in the fabrication of three-dimensional nanoarchitectures for improving the activity and stability of the bioelectrocatalytic elements, as basis for obtaining efficient, stable and miniaturized biofuel cells (Heller 2004, Cosnier, J. Gross et al. 2016, Rasmussen, Abdellaoui et al. 2016).

1.1 Biofuel cells

In batteries and fuel cells the electrical energy is generated by conversion of chemical energy via redox reaction at the anode and the cathode. These systems consist of two electrodes in contact with an electrolyte solution. The anode is the negative electrode where the oxidation of the fuel takes place while the cathode is the positive electrode where occurs the reduction of the oxidant (Winter and Brodd 2004). The main difference between them is that batteries are closed systems meanwhile fuel cells are open systems: a fuel cell is an electrochemical conversion device that has a continuous supply of fuel and oxidant. Fuel cells present some interesting advantages compared to batteries as high theoretical efficiency, high energy density and possibility of miniaturization (Winter and Brodd 2004). Fuel cells, where at least one biologic catalyst (enzymes, microorganisms or mitochondria) is used, nevertheless the origin of the fuel and the oxidant, are defined as biofuel cells (BFCs) (Fig. 1.1.1) (Shleev, Bergel et al. 2015). BFCs can be classified according to the biocatalyst in: enzymatic fuel cells (EFCs), when enzymes are employed as catalyst, or in microbial fuel cells (MFC), when whole organisms, containing complete enzyme pathways, are used instead (Osman, Shah et al. 2011). A third intermediated group based on mitochondria has recently emerged (Arechederra, Boehm et al. 2009). Since only enzymes were used as biocatalysts in all the work presented in this Thesis, MFC will not be described here.

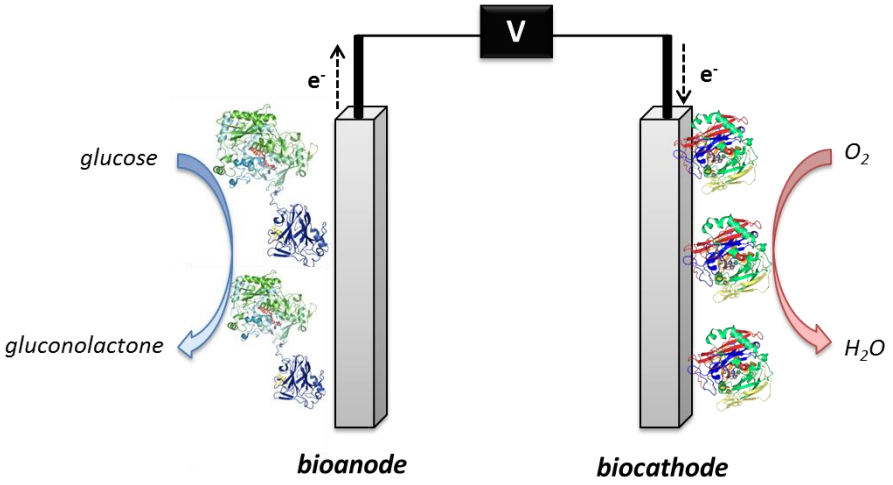

Figure 1.1.1 Single compartment BFC formed by a cellobiose dehydrogenase based anode and a bilirubin oxidase based cathode.

EFCs present several advantages that make them an attractive alternative to conventional fuel cells and batteries for different applications. Indeed, enzymes show high substrate specificity and selectivity towards the fuel or oxidant used, which eliminates possible problems of fuel crossover or poisoning, thus allowing the fabrication of membrane-less devices (Cosnier, J. Gross et al. 2016). Furthermore, enzymes are renewable and biocompatible materials that could offer significant cost advantages compared to traditional metal catalyst (Osman, Shah et al. 2011). Moreover, EFCs can operate under mild pH and temperature conditions (pH 5-8, 25-37 ºC), in contrast with the extreme pH and temperature conditions of traditional fuel cells (Meredith and Minteer 2012); and enzymes covert the

substrates in innocuous products that is very important for *in vivo* or *ex vivo* applications. EFCs also offer a clean energy alternative as they can employ renewable fuels such as glucose, fructose, lactose, ethanol, pyruvate and lactate to produce energy (Meredith and Minteer 2012).

The performance of EFCs is evaluated with the open circuit voltage (OCV), polarization curves and power curves (Fig. 1.1.2), as done for the conventional fuel cells. The OCV is the voltage value at which no current flows and therefore the highest voltage for the electrochemical cell. Theoretically, this voltage should be equal to the difference in the redox potentials of the fuels at each electrode (Fig. 1.1.2.a); however experimentally differences appear: the OCV value can be affected by different parameters such as the overpotential needed for the bioelectrocatalysis to start, or the use of mediators to shuttle electrons from the active site of enzymes and the electrode surface (Meredith and Minteer 2012). As conventional fuel cells, once the circuit is closed the voltage drops and the current starts flowing. As shown in Fig. 1.1.2.b, there are three major losses of the cell voltage: i) activation losses, ii) ohmic losses and iii) mass transport losses (Winter and Brodd 2004, Osman, Shah et al. 2011). At low currents activation losses, due to slow kinetics at the electrode surface, dominate; instead, mass transport losses result from diffusion limitations at high current densities. Ohmic losses are due to resistance to charge transport in the electrolyte, at the electrode surface and through the separating membrane, if it is present (Osman, Shah et al. 2011, Luz, Pereira et al. 2014). The electrical power density (P) of an EFC is defined as the product of the cell voltage and the generating current density; a typical profile for the power density as function of the current density is depicted in Fig. 1.1.2.b.

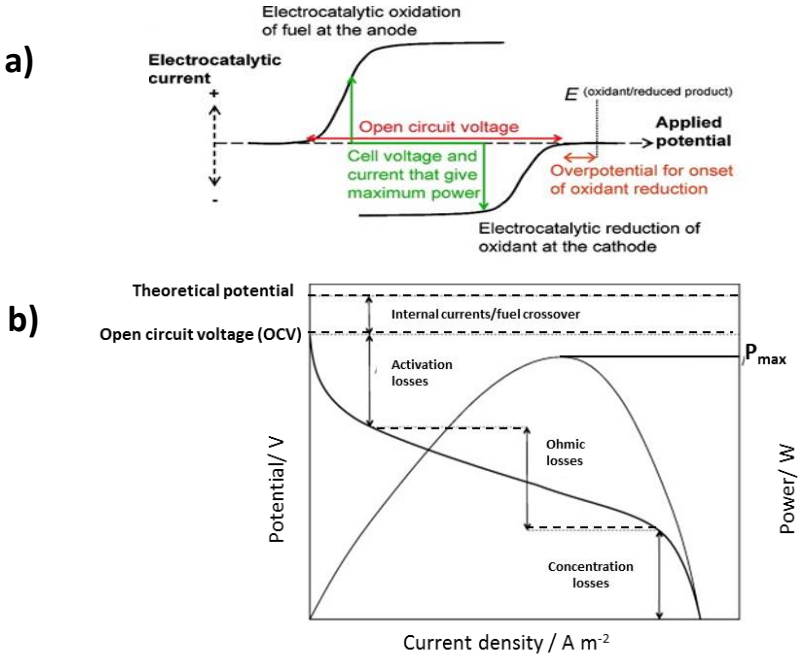

Figure 1.1.2 Voltage and current response and features that determining BFC performance when electrodes are tested separately a) and assembled into a complete BFC b). a) Adapted with permission from (Cracknell, Vincent et al. 2008), Copyright 2008 American Chemical Society and b) from (Osman, Shah et al. 2011), Copyright 2011 Biosensor and Bioelectronics.

The classical design of a BFC is based on two compartments containing the anode and the cathode separated by an ion-selective membrane. The employment of enzymes as electrocatalysts allows the development of membrane-less BFCs due to their high specificity and selectivity towards substrates, as mentioned above. One of the first examples of this idea was made by Katz and Willner in 1999 by immobilizing a selective enzyme at the anode and a separate selective enzyme at the cathode (Katz, Willner et al. 1999).

EFCs can be divided in two main groups depending on how the electronic connection between the enzyme and the electrode is realized: i) mediated electron transfer (MET) devices, in which redox species help to channel electrons between them, and ii) direct electron transfer (DET) based devices, where the enzyme is directly connected with the electrode surface (Falk, Blum et al. 2012). Employment of DET based systems allows significant simplification in the BFCs construction, making miniaturizing easier and overcomes some possible drawbacks (instability, toxicity and voltage loss) of using mediators. In this Thesis, the study is, for these reasons, focused in DET based systems.
The majority of EFCs have been based on glucose oxidation (1.1) and oxygen reduction (1.2), as the anodic and cathodic process respectively, as they are very common substrates present in most human physiological fluids:

$$glucose \rightarrow gluconolactone + 2H^+ + 2e^- \quad (1.1)$$

$$O_2 + 4H^+ + 4e^- \rightarrow 2H_2O \quad (1.2)$$

The redox potentials of their half reactions at pH 7, 25 ºC vs. SHE are -0.364 V and 0.815 V respectively. Therefore, they determine the thermodynamic maximum voltage of a glucose/oxygen EFC as 1.179 V; however the maximum open circuit voltage achieved so far is 0.95 V (Zebda, Gondran et al. 2011).

The field of applications of EFCs can be wide. The more realist application for EFC is the replacement of batteries in small electronic devices; indeed, the current densities produced by BFCs are generally in the range of microampers to ten millampers per square centimeter, which, if generated at high voltage, could be enough to power many portable electronic devices. This research has led to self-powered biosensors (Gellett, Kesmez et al. 2010), biobatteries (Stolarczyk, Łyp et al. 2012, Żelechowska, Stolarczyk et al. 2013) or paper-based biofuel cells (Narváez Villarrubia, Lau et al. 2014). However, the most exciting applications of BFCs, due to their biocompatible catalysts, is as implantable power sources *in vivo* or *ex vivo,* where *ex vivo* applications are attempted to operate in noninvasive contact situations. The first EFCs operating in a living organism was made by Mano and Heller in 2003, who implanted their biofuel cell in a grape producing 47 μW/cm^2 at 0.52 V (Mano, Mao et al. 2003). In 2010, Cosnier *et al*. implanted the first glucose biofuel cell in a rat with a maximum power of 24.4 μW/cm^2 at 0.13 V (Cinquin, Gondran et al. 2010). In 2011 Miyake et *al*. reported the first example of an implanted DET based EFC in grape, obtaining a maximum power 115

μW/cm^2 at 0.25 V (Miyake, Haneda et al. 2011). In 2012 BFCs were implanted in a cockroach (maximum power = 55 μW/cm^2 at 0.20 V) (Rasmussen, Ritzmann et al. 2012), in a snail (maximum power = 30 μW/cm^2 at 0.39 V) (Halámková, Halámek et al. 2012) and in a clam (Szczupak, Halamek et al. 2012). Katz et *al*. also implanted a glucose biofuel cell in a lobster (MacVittie, Halamek et al. 2013) in 2013 producing 640 μW/cm^2 at 0.28 V. Shleev and coworkers implanted a microscale EFC in the brain of living rat (maximum power = 2 μW/cm^2 at 0.54 V) (Andoralov, Falk et al. 2013). However, many difficulties have to be overcome to achieve implantable power systems. These include catalyst inhibition and achieving long-term stability, biocompatibility, and hemocompatibility. One of the major obstacles in developing efficient BFCs for implantable applications regards the oxygen biocathodes (Cosnier, J. Gross et al. 2016, Shleev 2017). This cathode limitation is caused by low O_2 concentrations in physiological fluids, coupled with high concentrations of low redox potential substances that may oxidize at the cathode. Indeed, the concentration of available O_2 in extracellular fluids is approx. two orders of magnitude lower than the concentration of fuels as glucose, so the power of a fuel cell located inside the human body will be limited by O_2 availability (Shleev 2017).

Taking into account these difficulties, *ex vivo* applications are a very promising field of EFCs applications to power biomedical devices in noninvasive contact situation, such us skin patches (Ogawa, Kato et al. 2015, Bandodkar and Wang 2016) or electronic contact lenses (Falk, Andoralov et al. 2012, Falk, Andoralov et al. 2013). *Ex vivo* devices operating in human tears (maximum power = 3.5 μW/cm^2 at 0.57 V) (Falk, Andoralov et al. 2012) or human saliva (maximum power = 2.1 μW/cm^2 at 0.63 V) have been developed (Falk, Blum et al. 2012). Wang and coworkers pioneered the field of tattoo-based biofuel cells by utilizing sweat lactate (Fig. 1.1.3.a) (Jia, Valdés-Ramírez et al. 2013), and

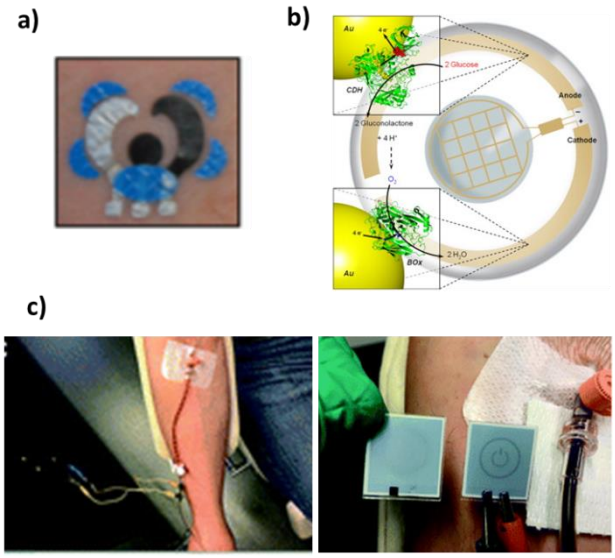

Figure 1.1.3 a) Temporary wearable BFC based tattoo (Windmiller, Bandodkar et al. 2012), Copyright 2012 Chemical Communications; b) principal scheme of a "smart" contact lens with an inserted BFC (adapted with permission from (Falk, Andoralov et al. 2012), Copyright 2012 Biosensor and Bioelectronics); and c) a completed artificial tubular system, including an enzymatic fuel cell connected to a potentiostat (left) and proof-of principle demonstration of electric power generation in human blood (right) (adapted with permission from (Pankratov, Ohlsson et al. 2016), Copyright 2016 Journal of Material Chemistry B).

Shleev et *al*. made many efforts on the development of BFCs to power glucose or lactate sensors in contact lens (Fig. 1.1.3.b) (Falk, Andoralov et al. 2013). Recently, an enzymatic fuel cell has also been reported that generates sustained electricity (maximum power = 0.74 μW/cm^2 at 0.16 V) in a vein replica, with authentic human blood stream, which is enough to power an e-ink display. (Fig. 1.1.3.c) (Pankratov, Ohlsson et al. 2016).

Nevertheless, significant progress has been done in the field of EFCs in the last years, the development of efficient EFCs has still to overcome issues such as lower stability and electrochemical performance (in terms of current densities, OCV and power output) than desirable for real applications. Researchers seek towards improving stability with the combination of enzyme engineering and new strategies for improving the chemical environment of enzymes at the electrode surfaces (Cosnier, J. Gross et al. 2016). Current densities and power output can be improved by the development of new nanostructured materials to load more enzyme molecules per geometric area of electrodes, and by new strategies for obtaining faster electron transfer (Rasmussen, Abdellaoui et al. 2016).

The work in this Thesis has followed these research directions: i) enhancement of the cathode performance by enzyme engineering and development of nanostructured electrodes with high surface area; ii) development of a BFC for potential *ex vivo* applications.

1.1.1 Self-charging bio supercapacitors

In order to increase the performance of a conventional BFC, different studies have emerged about the combination of capacitors/supercapacitors and biofuel cells. Indeed, in literature can be found examples of combing conventional fuel cell with supercapacitors (Papra, Büchi et al. 2010), or biofuel cell with capacitors (Miyake, Yoshino et al. 2011, Zebda, Cosnier et al. 2013) or supercapacitors (J. Keskinen 2010), which are always two different devices electrically connected. Very recently a one module showing dual features of an electrochemical capacitor (ECC) and an EFC has been reported (Pankratov, Blum et al. 2014), obtaining a power output of 1 mW/ cm^2 at 0.38 V. This result is 10-fold higher than the state-of the art for a glucose/oxygen EFC (0.01 mW/cm^2) (Falk, Blum et al. 2012). This new device was named as self-charging biosupercapacitor (SCBSC).

An electric double layer consits on two layers of charges: one electronic layer is in the surface lattice structure of the electrode, and the other, with opposite polarity, emerges from dissolved and solvated ions in the electrolyte. Electrochemical pseudocapacitance is achieved by reversible faradaic charge transfer process between electrode and electrolyte which is originated by fast sequence of reversible redox, intercalation or electrosorption process (Pletcher, Greff et al. 2010).

Electrochemical capacitors (ECCs), also called supercapacitors, are able to store large amount of electric energy. ECCs can be divided in: i) double-layer capacitors-based on nanostructured high surface area electrodes with high double layer capacitance (C_{dl}) but without electrochemical pseudocapacitance (C_ϕ); ii) pseudocapacitors-metal oxide or conducting organic polymer based electrodes with high C_ϕ values ($C_{dl} \geq 0$ and $C_\phi > 0$) and iii) hybrid capacitors-capacitors with asymmetric

electrodes, one of which exhibit electrostatic capacitance and the other primarily electrochemical capacitance.

However, these devices cannot produce electrical energy and therefore need to be charged externally. EFCs, on the other hand, convert chemical energy into electrical energy, as reported above. So, the combination of these two devices yields a hybrid biodevice that can operate in both steady state, in which the electrodes are charged by the enzymatic activity in presence of their substrates, and pulsed mode, in which the electrodes are discharged.

An electrode with high active surface area is an essential condition for double-layer SCBSCs, due to the direct dependence of C_{dl} on the electrochemically active surface area. Pseudocapacitive SCs are fabricated using metal oxides, conducting polymers (CPs) or combination of both (Yoon and Kim 2013, Lokhande, Lokhande et al. 2016). Pseudocapacitors normally have higher capacitance than simple double-layer SCs but have lower stability and lower maximal power density because of the slower process involved during charge storing. If a bioelement is immobilized on the electrode surface the double layer capacitance decreases due to the insulating properties of biomolecules on electrodes. However, in this case, if an electron transfer is established between the biocatalyst and the electrode, a significant increase in the pseudocapacitance contribution can be measured that leads to a general increase of the overall electrode capacitance (Pankratov, Blum et al. 2014). This effect has been reported for many proteins, living cells and enzymes (Lindgren, Gorton et al. 2001, Malvankar, Mester et al. 2012), demonstrating new possibilities in the fabrication of new renewable bioelectronics systems.

1.2 Design of enzyme-based biodevices

The key parameters for the fabrication of an efficient EFC will be detailed here.

1.2.1 Redox enzymes as biocatalysts

Enzymes, like all other catalysts, increase the rate of a chemical reaction without being consumed during the reaction by decreasing the activation energy needed for the reaction to take place (Lehninger 2000). One of the most important characteristics of enzymes is that they provide exceptional specificity towards their substrates; therefore, they allow to assembly membrane-less and noble metal-less fuel cells (Cosnier, J. Gross et al. 2016). Moreover, the ability of the enzymes to use as substrates biological fuels, such as carbohydrates (i.e. glucose, fructose, lactose), alcohols, ascorbate or amino acids, or oxidants, such as molecular oxygen or hydrogen peroxide, allows many possible applications of EFCs. Oxidoreductases (E.C.1) are the class of enzymes mostly employed for the fabrication of EFCs. In this Thesis two enzymes from the family of multicopper oxidase (MCOs), laccase and bilirubin oxidase, have been used as cathodic enzymes whereas cellobiose dehydrogenase was tested as anodic enzyme.

1.2.1.1 MCOs as cathodic enzymes

MCOs are a family of enzymes that oxidize a variety of substrates with the concomitant four electron reduction of dioxygen to water. The catalytic site of these proteins consists in at least four copper atoms that are classified, due to their spectroscopy features, into three types of sites (Table 1.2.1): type 1 (T1) or blue copper, type 2 (T2) and the type 3 (T3) binuclear copper centres. In the oxidized state Cu^{2+} the type 1 copper exhibits an intense absorption band at 600 nm, which is responsible for the deep blue colour due to a cysteine-sulphur to copper ligand to metal charge transfer transition. It also exhibits a very small Cu parallel hyperfine splitting in the EPR spectra due to the high covalency at the copper site. The T2 copper shows no significance absorbance features but exhibits EPR signals similar to those of tetragonal Cu (II) complexes. Binuclear Type 3 copper sites are EPR silent due to antiferromagnetic coupling resulting in a bridging hydroxo ligand between the two Cu^{2+} in the resting oxidized state. In addition, it displays a distinctive absorption band near 330 nm. Together with the T2 site, the T3 site forms the trinuclear copper cluster (TNC) (Quintanar, Yoon et al. 2005, Quintanar, Stoj et al. 2007).

	T1	T2	T3
Coordination	2 Hystidine and 1 cysteine in trigonal planar conformation + 1 variable ligand in axial position	Simple planar conformation	Two Cu coupled through a hydroxide bridge
Uv-vis spectroscopy	Absorbance at~ 600 nm	No	Absorbance at ~ 330 nm
EPR spectroscopy	EPR signal Paramagnetic Cu	EPR signal Paramagnetic Cu	EPR silent Diamagnetic Cu cluster

Table 1.2.1 Characteristics of each Cu of MCOs.

Based on the known crystal structures the ligation of the four copper centres is mostly conserved among MCOs (Shleev, Tkac et al. 2005, Jones and Solomon 2015). The T1 site is coordinated by a minimum of two His and one Cys residues. In MCOs, substrate oxidation occurs at the T1 site, which then transfers electrons through the Cys-His pathway to the TNC where finally the O_2 reduction takes place (Fig. 1.2.1). The first and second sphere residues surrounding the T1 control both the intermolecular ET to the T1 from the substrate and the intramolecular ET from the T1 to the TNC (Quintanar, Stoj et al. 2007, Solomon, Augustine et al. 2008).

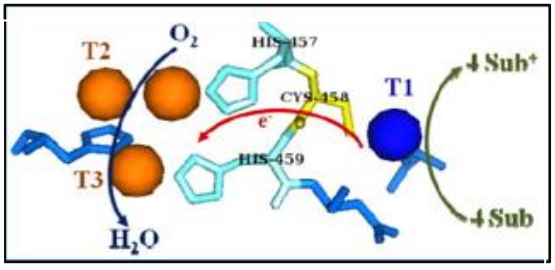

Figure 1.2.1 Representation of the active site of MCOs. The T1 site is represented in blue meanwhile the TNC site in orange. Reproduced by permission from (Mano and Edembe 2013), Copyright 2013 Biosensor and Bioelectronics.

Many studies have been carried out to understand the mechanism of O_2 reduction by MCOs (Solomon, Augustine et al. 2008, Heppner, Kjaergaard et al. 2014, Jones and Solomon 2015). In Fig. 1.2.2 is reported an overview of the reduction mechanism.

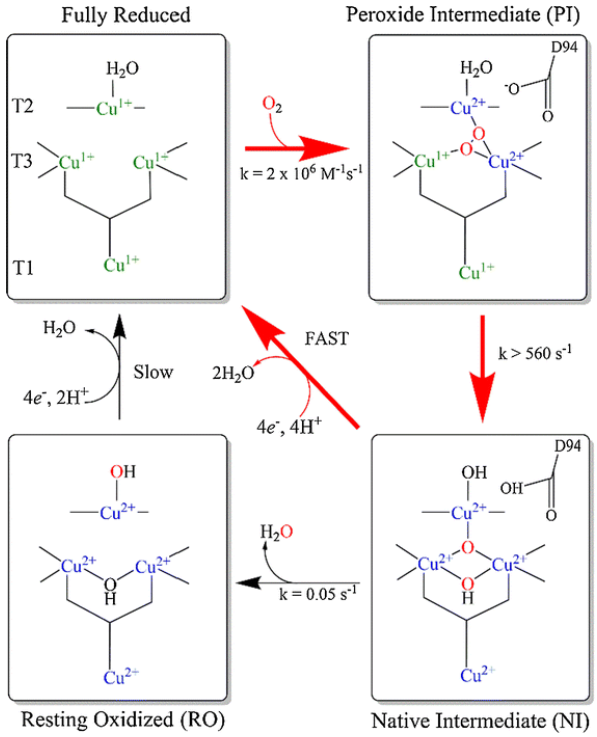

Figure 1.2.2 Mechanism of O_2 reduction by MCOs. Red arrows show the steps in the catalytic cycle. Black arrows show the reduction of resting enzyme to enter the catalytic cycle and decay of the native intermediate which ends catalysis. Reproduced by permission (Heppner, Kjaergaard et al. 2014), Copyright 2014 Journal of American Chemical Society.

The catalytic process starts with the fully reduced enzyme followed by two electron steps that reduce O_2 to H_2O with the formation of a peroxide intermediate (PI) in between. Finally, the fully oxidized intermediate (NI) formed after the oxygen reduction is then reduced again by the substrate faster than its decay to the resting oxidized (RO) enzyme. The RO oxidize form of the enzyme presents four oxidized Cu including a hydroxide-bridged T3 centre. The overall catalytic cycle consists in the donation of four electrons from the substrate that produce the complete reduction of O_2 with the formation of two molecules of H_2O (Solomon, Augustine et al. 2008, Heppner, Kjaergaard et al. 2014).

The group of MCOs more suitable for the construction of a biocathode are "blue" multicopper oxidases, such as laccase (Lc), bilirubin oxidase (BOx), ceruloplasmin (Cp) and ascorbate oxidase (AO). In this Thesis only the first two (Lc and BOx) have been used.

1.2.1.1.1 Laccase

Laccase (benzediol: oxygen reductases, EC 1.10.3.2) catalyses the oxidation of *ortho*- and *para*-diphenols, aminophenols, polyamines, lignins as well as some inorganic ions coupled to reduction of molecular oxygen to water (Yaropolov, Skorobogat'ko et al. 1994). Laccases (Lcs) are typically found in plants and fungi (Baldrian 2006); although there are some reports of laccase activity in bacteria

(Givaudan, Effosse et al. 1993, Martins, Soares et al. 2002) and insects (Barrett 1991). The X-ray structures of several Lcs have been reported (GenBank website), among them the structure of *Trametes hirsuta* Lc (Polyakov 2009), which was studied in this Thesis (Fig. 1.2.3). The fungal Lc is organized in three sequentially arranged domains. The electrostatic surface potential distribution reveals a predominance of negatively charges which is in agreement with the pI value (Table 1.2.2). The electron donor substrate binds in a small negatively charged cavity near the T1 site. As reported above, the T1 site is the primary electron acceptor that is connected to the TNC by a His-Cys-His chain. For all "blue" multicopper oxidase the distance between the T1 site and T2/T3 cluster is found to be around 12-14 Å (Shleev, Tkac et al. 2005).

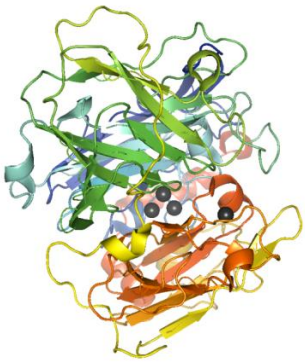

Figure 1.2.3 Tertiary structure of *T. hirsuta* laccase (PDB file: 3FPX). Copper ions are shown as dark grey spheres (Polyakov 2009).

	MW (kD)	pI	pH optimum	Carbohydrate content (%)	Inactivation half-life at 50ºC
***Trametes hirsuta* Lc**	70	4.2	3.5-4.5	12	65

Table 1.2.2 Principal physic-chemical characteristics of *T. hirsuta* laccase (Shleev, Morozova et al. 2004).

All laccases can be divided into three groups based on the redox potential of the T1 site: low, middle and high potential laccases. The low potential groups consist of Lcs from tree with a T1 site potential around 340-490 mV vs. NHE (Reinhammar 1972), whereas the middle potential laccases have a T1 site potential ranging from 470 to 710 mV vs. NHE (Xu, Shin et al. 1996, Koroleva, Stepanova et al. 2001). The high redox potential laccases, as *Trametes hirsuta*, have T1 site potentials of about 730-710 mV vs. NHE (Reinhammar 1972, Shleev, Tkac et al. 2005). It was suggested that the value of the redox potentials depends on the ligands of the T1 copper and on the amino acids that form the T1 pocket. Indeed, the axial ligand for laccases' T1 site is methionine for low redox potential laccases, leucine for the middle redox potential laccases and phenylalanine for the high redox potential laccases. However, successive studies on Lcs modified through site directed mutagenesis have shown only a small correlation between the type of the T1 ligand and its redox potential (Kojima, Tsukuda et al. 1990, Xu, Berka et al. 1998). Nevertheless, a different study suggested that the increase in the distance between the T1 copper and the His residue can influence the redox potential of the former as the

electron density at the metal and the ligand amino acid decreases (Piontek, Antorini et al. 2002). Although the redox potential of the T1 site is known for many Lcs, the redox potential of the T2 and T3 sites have not been determined so often. Nevertheless, for *T. hirsuta* Lc the redox potential of T1 and T2/T3 have been reported: it has a redox potential of 780 mV vs. NHE of the T1 site (Shleev, Morozova et al. 2004) and of 400 mV vs. NHE for the T2/T3 centre (Pita, Shleev et al. 2006).

Fungal laccases show their activity peak at acidic pH (Table 1.2.2) and they are strongly inhibited in the presence of chloride ions (Baldrian 2006). These features hinder their use for physiologically-friendly implantable devices, therefore native laccases have been engineered by directed evolution for obtaining mutants that show activity under physiological conditions (Mate, Gonzalez-Perez et al. 2013). An alternative strategy followed has been altering the local pH of the biocathode.

1.2.1.1.2 Bilirubin oxidase

Contrary to Lcs, BOxs (EC 1.3.3.5) display high activity and stability at neutral pH and are less sensitive to chloride ions, which makes them an ideal option for EFCs operating at physiological conditions (Mano and Edembe 2013, Falk, Pankratov et al. 2014). However, BOxs present lower T1 site redox potential compared to high redox potential fungal Lcs (Table 1.2.3), which results in a lower voltage of the developed biodevice. BOx specifically catalyses oxidation of bilirubin to biliverdin with the concomitant direct four-electron reduction of molecular oxygen to water (Solomon, Sundaram et al. 1996). They were discovered in 1981 by Tanaka and Murao (Murao and Tanaka 1981) and have been identified in various fungus and bacteria (Mano 2012). The determination of the crystal structure of *Myrothecium verrucaria* BOx (mtBOx) (Fig. 1.2.4) showed that its structure consists of three domains, as for others "blue" MCOs, and that the TNC and the T1 site lie close enough to the surface to achieve DET at biologically relevant rates (Cracknell, McNamara et al. 2011). Also, two well defined channels running from the TNC to the surface of the protein were observed: one channel terminates close to the T2 site, the other terminates at the two T3 Cu atoms. The "T2 channel" seems to be more hydrophilic and is therefore likely to be the main channel for water transport *in vivo* (Cracknell, McNamara et al. 2011). A narrow substrate-binding pocket can be identified within 5 Å of the T1 Cu site, formed by the interface between two of the protein domains. His-462, which coordinates the T1 Cu, is on the surface of the binding pocket, providing an easy path for electron transfer from the substrate. However, this cavity appears entirely internal, with no opening to the surface. The residues lining the substrate-binding pocket in mtBOx are predominantly hydrophilic although the surrounding protein surface shows hydrophobic character (Cracknell, McNamara et al. 2011).

In this Thesis two BOx enzymes have been used: *Myrothecium verrucaria* BOx (mtBOx) and *Magnaporthe oryzae* (mgBOx). Both show very similar characteristics (Table 1.2.3) but mgBOx was identified and produced very recently (Durand, Gounel et al. 2012) showing higher activity and stability than mtBOx.

	MW (kD)	pI	T1 redox potential vs. NHE (V)	T1 axial ligand	T2/T3 redox potential vs. NHE (V)
Myrothecium verrucaria	66	4.2	0.67	Met	~ 0.40
Magnaporthe oryzae	63.7	5.29	~ 0.69	Met	nd

Table 1.2.3 Comparison of the characteristics of *Myrothecium verrucaria* and *Magnaporthe oryzae* bilirubin oxidase (Mano and Edembe 2013).

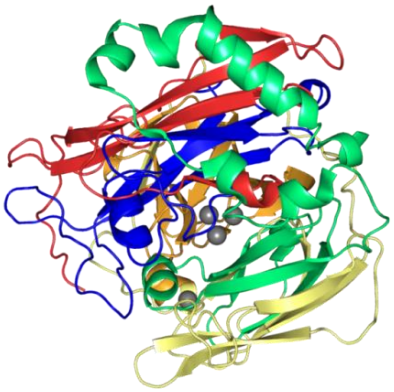

Figure 1.2.4 Tertiary structure of *M. verrucaria* bilirubin oxidase (PDB file: 2XLL) (Cracknell, McNamara et al. 2011). Copper ions are shown as grey spheres.

1.2.1.2 Anodic enzymes

Many oxidases and dehydrogenases originating from different bacteria and fungi are used to design highly efficient bioanodes of EFCs. Traditionally, the enzymes used for EFCs working under physiological conditions have been glucose oxidase (GOx) and glucose dehydrogenase (GDH) (Meredith and Minteer 2012). However, new enzymes have emerged which can overcome some of the GOx and GDH drawbacks such as the need to use mediators to achieve good electron transfer. Among them cellobiose dehydrogenase (CDH) has lately attracted more attention and has been used for DET based EFCs (Ludwig, Ortiz et al. 2013, Schulz, Kittl et al. 2016). In this Thesis only CDH was studied as anodic enzyme for the fabrication of mediator-less EFCs operating under physiological conditions.

1.2.1.2.1 Cellobiose dehydrogenase

Cellobiose dehydrogenase (CDH) is an extracellular fungal flavocytochrome (cellobiose: acceptor 1-oxidoreductase, EC 1.1.99.18) with MW ranging from 85 up to 101 kDa, depending on the degree of glycosylation. CDHs are subdivided in two classes based on sequences and catalytic proprieties. Class I CDHs have shorter amino acid sequences and an acidic optimum pH, while class II ones show good activity also at physiological pH. Some class II CDHs are able to oxidize other mono- and disaccharides (Kracher, Zahma et al. 2015). However, as glucose is not the target substrate of CDH even class II enzymes have low efficiency towards glucose oxidation (Ludwig, Harreither et al. 2010). CDH is a monomeric protein consisting of two domains connected by a flexible linker of about 20 amino acids. The larger flavodehydrogenase domain (DH_{CDH}) is catalytically active, while the smaller

cytochrome domain (CYT_{CDH}) contains haem b as cofactor and acts as an electron transfer protein between DH_{CDH} and a terminal macromolecular electron acceptor (Fig. 1.2.5) (Ludwig, Ortiz et al. 2013). The oxidation of carbohydrates is catalysed by the non-covalently bound FAD cofactor in DH_{CDH}, with the concomitant reduction of FAD to $FADH_2$. It can be reoxidized by various electron acceptors or by electron transfer to the cytochrome domain (Fig. 1.2.5.b). The haem cofactor is coordinated by Met 65 and His 163; this unusual ligation causes a relatively low redox potential, which is about 100-160 mV vs. NHE at pH 7 (Ludwig, Harreither et al. 2010). The N-terminal CYT_{CDH} is connected to DH_{CDH} via a flexible linker, which keeps the two domains in close contact and allows intramolecular electron transfer (IET) between them (Fig. 1.2.5.a). The isoelectric point of DH_{CDH} is low and varies for different enzymes, but is usually around 5. The CYT_{CDH} has an average molecular mass of around 22 kDa without glycosylation and the isoelectric point is very low (around 3).

The CDH used in this Thesis is from *Corynascus thermofilos* (ctCDH), which shows an optimal pH value in the range of human physiological fluids (pH 7.4) and one of the lowest K_m values for glucose among the CDHs investigated (Coman, Ludwig et al. 2009).

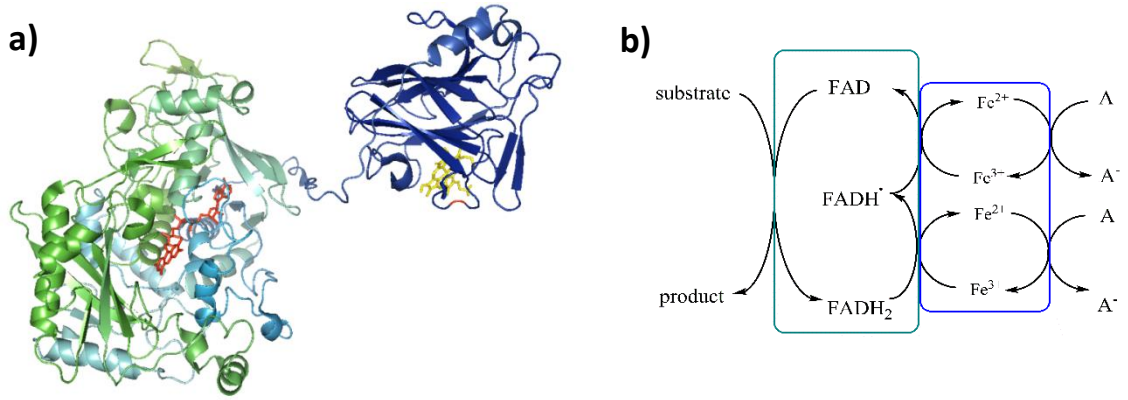

Figure 1.2.5 a) Tertiary structure of cellobiose dehydrogenase (PDB file: 4QI7) (Tan, Kracher et al. 2015). FAD: red sticks, haem: yellow sticks. b) Mechanism of the catalytic reaction.

1.2.2 Enzyme immobilization

The enzyme immobilization is defined as the physical confinement or localization of the enzymes in a certain defined region of space with retention of their catalytic activities and which can be used repeatedly and continuously (Wingard 1972). Many studies have focused on the immobilization of enzymes on both anodic and cathodic electrodes of different nature to increase long-term stability, resistance to extreme conditions and to chemical reagents. Moreover, a correct immobilization grants the access of substrates and mediators to the active site of the enzyme, improving electron transfer kinetics and in consequence increasing current densities (Arroyo 1998). Enzymes' immobilization also prevents the diffusion of the biocatalysts between anode and cathode, which allows fabricating miniaturized membrane-less biofuel cells.

The immobilization methods can be divided in two big categories, depending on the physical or chemical nature of the immobilization that takes place between the electrode and the enzyme molecules. Physical coupling methods include physical adsorption and the entrapment of the enzyme in three-dimensional matrixes or its encapsulation in an organic or inorganic polymer, whereas chemical coupling occurs by chemisorption or covalent binding between the support and the enzyme (Sheldon 2007, Fernández-Fernández, Sanromán et al. 2013).

Regardless of the method used, immobilization processes may affect the enzyme lifetime, alter the enzyme conformation or decrease the enzyme activity (Arroyo 1998).

1.2.2.1 Physical immobilization methods

1.2.2.1.1 Physical adsorption

Physical adsorption relies on the physical interactions between the enzyme and the support during the immobilization process, including Van der Waals forces, ionic interactions and/or hydrogen bonding (Arroyo 1998, Sheldon 2007). The major advantages of adsorption as immobilization method are that it is relatively simple and less expensive than other methodologies. However, because of the weak interactions involved, desorption of the protein takes place easily by *i.e.* pH, temperature or ionic strength changes. Besides, often the adsorption on bare metal electrodes results in the denaturation of the enzyme. Another drawback of this method is the further non-specific adsorption of other compounds on the support.

1.2.2.1.2 Entrapment

Entrapment is the physical retention of an enzyme in a porous solid/gel matrix formed generally by conducting polymers such as polyaniline (PANI) or poly(3,4-ethylenedioxythiophene) (PEDOT), polymers as polyacrylamide or collagen, among others (Fig. 1.2.6.a). Recently a liquid-crystalline lipid cubic phase, defined as a curved nonintersecting bilayer with unconnected water channels, has been proposed for this aim (Nazaruk, Sadowska et al. 2009). The enzyme is first suspended in the monomer solution and then the polymerization process (either electrochemical, photochemical or chemical) traps the enzyme molecules on the support surface. Entrapment is a very easy immobilization method and in most cases does not cause any structural alteration of the enzyme. Depending on the polymer, activity can be maintained and stability can be increased several-fold. However, a hard control of the polymerization parameters is needed, besides the limitations coming from mass transport and low enzyme loading are possible concerns.

1.2.2.1.3 Encapsulation

Encapsulation of enzyme protects it from the environment but the concomitant mass transport limitation restricts its use (Fig. 1.2.6.b). An alternative to this method is the microencapsulation, which confines the enzyme molecules in micro-sized spheres made from semipermeable material, such as polymers or inorganic materials (Fernández-Fernández, Sanromán et al. 2013). Micelles can also be

used for enzyme encapsulation increasing long-term stability, pH and thermal stability but decreasing mass transport through it (Minteer, Atanassov et al. 2012). The layer-by-layer (LbL) technique is another microencapsulation method used in the recent years (Deng, Shang et al. 2008, Szot, Lesniewski et al. 2008). The LbL approach is based on the electrostatic interaction between the components of the film. Encapsulation preserves the enzyme activity as it does not affect the enzyme´s degree of freedom needed for its catalytic activity.

Figure 1.2.6 Immobilization of enzyme by physical interactions: a) entrapment and b) encapsulation.

1.2.2.2 Chemical immobilization methods

1.2.2.2.1 Chemisorption

Adsorption can be also of chemical nature based on a strong affinity interaction between the modified electrodes and enzyme residue groups (Fig. 1.2.7.a). Many example of non-covalent binding via molecular tethering have been reported (Ramasamy, Luckarift et al. 2010, Lalaoui, Elouarzaki et al. 2013, Ulyanova, Babanova et al. 2014). Alternatively, Li and colleagues for example, proposed the chemisorption of laccases on gold electrodes, through the introduction of a cysteine at the N or C-terminus site of laccase peptide chain in order to facilitate the oriented immobilization of laccase (Li, Zhang et al. 2014).

1.2.2.2.2 Covalent binding

This methodology relies on the reaction between the functional groups present on the electrode surface and those pending on the enzyme surface (Arroyo 1998), as illustrated in Fig. 1.2.7.b. Among the 20 amino acids that are present in enzymes, lysine, cysteine, tyrosine, histidine, methionine, tryptophan, arginine, aspartic and glutamic acid are the main ones involved in the formation of covalent bonds. Indeed, the remaining amino acids, due to their hydrophobic character, are not exposed to the outer surface of the enzymes and thus cannot participate in the covalent binding.

Enzyme attachment on modified electrodes is improved when they contain short spacer arms for controlling the density of reactive groups, preventing physical adsorption directly on the electrode material and allowing optimal immobilization of the enzyme (Sosna, Chretien et al. 2010, Pita, Gutierrez-Sanchez et al. 2011). For example, gold electrodes have been modified with thiol self-assembled monolayers (SAMs) with carboxylic or amino terminal groups that can react with the enzyme's functional groups (Gooding, Mearns et al. 2003). Typical formation of amide bonds between

amino or carboxylic groups of the electrode surface and the carboxylic or amino residues of enzymes by ECD/NHS coupling have been reported by many groups (Vaz-Dominguez, Campuzano et al. 2008, Klis, Karbarz et al. 2009, Ardhaoui, Zheng et al. 2013).

The covalent immobilization of enzymes on the different supports permits easy manipulation, higher resistance to denaturing agents, and higher stability as the tertiary structure of the enzyme is stabilized (Arroyo 1998). Moreover, controlled orientation of the immobilized enzymes molecules can be obtained with this strategy, favouring direct electron transfer between the enzyme and electrode surface. However, the chemical binding can lead to a decrease of stability and activity due to three-dimensional structure alteration.

1.2.2.2.3 Cross-linking

Cross-linking immobilization is possible by the use of bifunctional cross-linkers such as dialdehydes, diisocyanates, diiminoesthers and diamine activated by carbodiimide (Fig. 1.2.7.c). The key factors for a successful crosslinking are pH, ionic strength, enzyme concentration and additives that can affect the enzymatic linkage (Arroyo 1998, Sheldon 2007). A cross-linker agent typically used for the immobilization of enzymes onto the electrode surface is glutaraldehyde (GA) (Pang, Liu et al. 2010, Luckarift, Ivnitski et al. 2012, Diaconu, Chira et al. 2014). Although GA is one of the most employed cross-linking agents, others have attracted attention for enzyme immobilization, such as poly(ethylene glycol) diglycidyl ether (PEGDGE) (Mano, Soukharev et al. 2006).

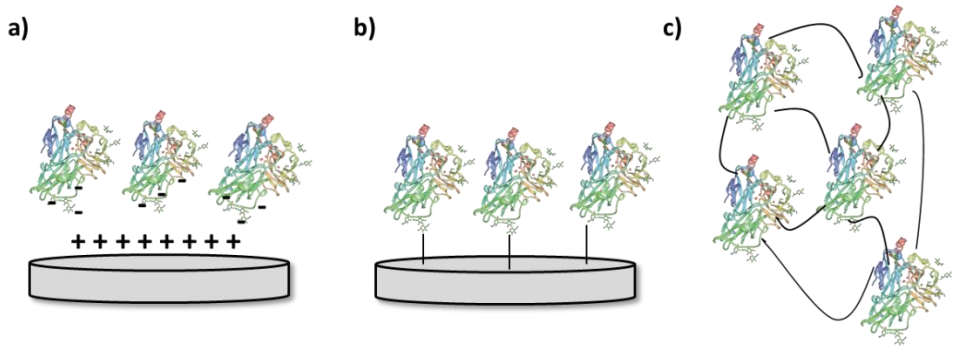

Figure 1.2.7 Chemical interactions for enzymes immobilization: a) electrostatic, b) covalent binding and c) cross-linking.

1.2.3 Nanostructured electrodes

Two factors are key to build up efficient enzymatic electrodes that fulfill the biofuel cell requirements. First, if current density values higher than 1 mA/cm^2 are desired several enzyme layers have to be immobilized on the electrode surface. The development of nanostructured electrodes, indeed, is a promising approach in order to have high useful surface area and high surface-to-volume ratio to load different layers of enzymes. Moreover, a larger surface area does not only increase the enzyme loading but may also enhance the stability of the immobilized enzyme (Falk, Blum et al. 2012, de Poulpiquet, Ciaccafava et al. 2014).

The second factor is the prompting of a fast electron transfer between the redox site of the immobilized enzyme and the electrode. Direct electron transfer (DET) is feasible *via* a correct orientation of the enzyme active site facing the electrode surface. Indeed, DET is obtained only when the distance between the active site and the electrode surface is inferior to tunneling distance (about 2 nm) (Page, Moser et al. 1999). DET can also be improved modifying the electrode surface with conductive nanomaterials, as these nanomaterials can improve direct enzyme wiring, without any deterioration of their activity, not only for their nano-scaled size similar to the proteins but also for their high surface area and high conductivity (Falk, Blum et al. 2012, Le Goff, Holzinger et al. 2015).

Different nanostructured materials have been used to design DET-based bioelectrodes. Two main groups of materials can be considered: carbon-based and metallic/oxide based materials.

1.2.3.1 Carbon materials

Carbon-based materials include spectrographic graphite (SPG), low density graphite (LDG), carbon nanotubes (CNTs), carbon black nanomaterials (CBNs) and graphene (Fig. 1.2.8).

Graphite-based electrodes had been widely used for the fabrication of bioelectrodes because graphite is a less expensive and well-characterized porous material. SPG material exhibits a porous dimension between 10-300 nm, whereas LDG presents an average pore diameter around 5 µm with some pores in 10-50 nm range. However, the electro-active area is higher for the LDG electrodes (Gutierrez-Sanchez et al 2012) (Dominguez 2009).

Carbon black (CB) is constituted by spherical particles whose size vary between 10 and 500 nm, providing a highly porous and high active surface area combined with remarkable conductivity (de Poulpiquet, Ciaccafava et al. 2014). Proteins adsorb onto CB surface principally via hydrophobic-hydrophobic interactions (Minteer, Atanassov et al. 2012).

Among the various nano-structured carbon materials, carbon nanotubes (CNTs) are the most frequently used ones. CNTs are cylindrical hollow fibers comprised of sheets of pure graphite. CNTs can consist of one (called single walled carbon nanotubes, SWCNTs) or more (called multi walled carbon nanotubes, MWCNTs) nanotubes. CNTs have diameters in the range of 0.4 to more than 3 nm for SWCNTs, and of 1.4 to more than 100 nm for MWCNTs (Baughman, Zakhidov et al. 2002). They show chemical inertness and electrochemical stability in a large potential window (de Poulpiquet, Ciaccafava et al. 2014). Because of their unique shape, size, and very high surface area they provide good electronic communication with the active site of enzymes without altering their activity; indeed CNTs show strong affinity with enzymes through hydrophobic interactions with the enzyme surface (Minteer, Atanassov et al. 2012). CNTs-based electrodes could be fabricated by drop casting, covalent binding of CNTs, co-deposition of CNT-doped polymers or direct-growth of CNT forests (Le Goff, Holzinger et al. 2015). CNTs can be easily functionalized through covalent binding at the edges and defect sites of the sidewalls or non-covalently at the sidewalls (Opallo and Bilewicz 2011). In this way

the CNTs conductivity can be improved, while providing additional reactive groups for enzyme immobilization and enhancing their DET (Falk, Pankratov et al. 2014). CNTs can be organized perpendicularly to the electrode surface, which allows a complete utilization of their large surface and takes advantages of the fast ET (Liu, Chou et al. 2005). CNTs are also used to fabricate buckypaper (BP), which is a new material with high surface area, chemical stability, flexibility, high mechanical strength and low toxicity both *in vitro* and *in vivo* (S Bellucci 2009).

Recently, graphene has been studied as a promising material for the fabrication of high surface area electrodes. Graphene consist on a one-atom thick layer of sp^2 hybridized carbon atoms in a crystalline hexagonal arrangement, and it shows high specific surface area, remarkable electronic proprieties and electron transport capabilities, strong mechanical strength and electrical conductivity (Chen, Feng et al. 2012). Graphene can be produced by mechanical exfoliation of highly oriented pyrolitic graphite; by thermal decomposition of SiC wafer under ultrahigh vacuum conditions; by chemical vapor deposition (CVD) growth on metal substrates and by chemical, thermal or electrochemical reduction of graphene oxide (GO) (Shao, Wang et al. 2010). Graphene exhibits a wide electrochemical potential window of ca. 2.5 V in 0.1 M PBS pH 7.0, which is comparable to that of graphite or glassy carbon, and has a much lower charge-transfer resistance than graphite or GC electrodes (Shao, Wang et al. 2010). Graphene based nanomaterials can be also further functionalized introducing on the surface functional groups that facilitate enzyme immobilization and a faster electron transfer to the protein (Pavlidis, Patila et al. 2014).

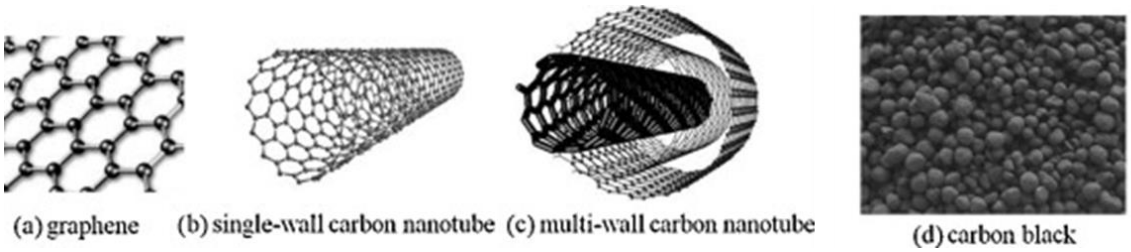

Figure 1.2.8 View of different carbon materials used. (Adapted with permission from (de Poulpiquet, Ciaccafava et al. 2014), Copyright 2014 Electrochemical Acta).

1.2.3.2 Metallic and oxide-based materials

Some other materials have been employed for the fabrication of nanostructured based electrodes. Among them, the most important examples are gold nanoparticles (AuNPs), nano-, meso-, macroporous gold electrodes or mesoporous metal oxide (i.e. ITO) (de Poulpiquet, Ciaccafava et al. 2014).

Gold has always been selected as material for bioelectrochemistry due to its high conductivity and biocompatibility. The conductivity of Au-based electrodes is obviously high, but bare Au electrodes have a very low roughness factor and so modification of gold with AuNPs or novel gold nanostructures has been carried out to fabricate electrodes with higher surface area (Fig. 1.2.9).

Gold nanoparticles (AuNPs) can provide many advantages for the fabrication of biosensors, such as a larger surface for the immobilization of biomolecules while retaining their biological activity. Moreover, AuNPs can facilitate DET between the immobilized enzymes and the electrode surface due to (I) their high surface to volume ratio, (II) shortening of the distance between enzymes and metal particles, (III) acting as an electron-conducting pathway between the enzymes and the surface (Yáñez-Sedeño and Pingarrón 2005). Another advantage for using AuNPs is controlling their size and morphology by adjusting the experimental parameters during the synthesis process. Gold NPs-enhanced electrodes can be prepared by direct deposition of NPs onto the electrode surface (Murata, Suzuki et al. 2009), by binding gold nanoparticles with functional groups of SAMs (Diaconu, Chira et al. 2014) or by mixing gold with the other components in the composite electrode matrix (Gutierrez-Sanchez, Pita et al. 2012, Luckarift, Ivnitski et al. 2012). Electroactive materials other than gold can be modified with gold NPs, such as ITO or graphite; in this way the properties of both materials may be combined (Gutierrez-Sanchez, Pita et al. 2012, Luckarift, Ivnitski et al. 2012). Recent reports show no dependence for nanomaterials larger than the size of the enzyme, and any increase in the current was attributed only to the increased electrochemically active surface area (Pankratov, Sundberg et al. 2014). Instead, when a nanomaterial presents a dimension comparable to or less than the diameter of the enzyme molecules, this could lead to an improvement of the bioelectrocatalytic performance by reducing the electron tunneling distance of the ET pathway (Gutierrez-Sanchez, Pita et al. 2012).

Macroporous gold (MG) electrodes can be obtained by electrodeposition of gold using colloidal crystal as templates. This method allows to control the pore diameter and the thickness of porous materials with high precision (Reculusa, Heim et al. 2011). This technique can be used using different supports, such as Pt or Au itself (Ben-Ali, Cook et al. 2005).

Nanoporous gold (NPG) is a highly porous and conductive material assembled in three-dimensional frameworks of bi-continuous pores and ligaments. NPG can be prepared by dealloying, hard template route, dynamic hydrogen bubble template method or anodization (Xiao, Si et al. 2016). A key feature of NPG is tuning its pore size from nanometer to micrometer range. A NPG requirement for a successful enzyme immobilization is that the tailored pore diameter is larger enough to accommodate the enzyme and allows its diffusion into the inner pores (Qiu, Xu et al. 2008, Xiao, Si et al. 2016).

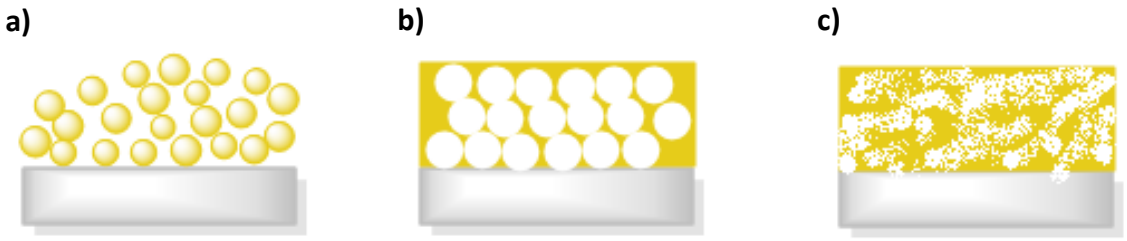

Figure 1.2.9 Example of gold nanostructured materials: a) AuNPs, b) macroporous and c) nanoporous gold.

ITO is a conductive oxide that consists of a solid solution of indium oxide (In_2O_3) and tin oxide (SnO_2). It presents the combination of numerous advantages, such as transparency, high electrical conductivity, homogeneous porosity and adjustable thickness (de Poulpiquet, Ciaccafava et al. 2014). It is highly hydrophobic but can also undergo thermal or chemical treatments to adjust its hydrophilicity (Choi, Jo et al. 2013). The synthesis method allows forming a nanosized columnar structure (Renault, Andrieux et al. 2012). ITO nanoparticles have been also used for enhancing the surface area of ITO electrodes (González-Arribas, Bobrowski et al. 2017).

1.2.3.3 Conductive polymers

Since their discovery, conductive polymers (CPs) have attracted great interest for many applications thanks to their remarkable proprieties. They merge the positive properties of metals and conventional polymers, as the ability to conduct charge, great electrical and optical properties, with the flexibility in processing and the ease of synthesis (Balint, Cassidy et al. 2014). They can also be made biocompatible, biodegradable and porous (Rivers and Takahashi 2002, Ghasemi-Mobarakeh, Prabhakaran et al. 2011).

CPs can conduct charge thanks to the facility with which electrons jump within and between the chains of the polymer. The conductivity in reality arises from a combination of different factors. The polymers possess a conjugated backbone formed by alternating single and doubled bounds. The p-orbitals in the series of π-bonds overlap each other, allowing the electrons to be more easily delocalized and move freely between the atoms (Balint, Cassidy et al. 2014). The other important factor that influences the conductivity of these polymers is the presence of a dopant. The dopant ions carry charge in the form of extra electrons to neutralize the unstable backbone of the polymer in its oxidized state by donating or accepting electrons (Balint, Cassidy et al. 2014, Kaur, Adhikari et al. 2015). The doping is reversible, as an electrical potential applied through the polymer will cause the dopant to leave or re-enter the polymer. Dopants can be divided in two groups based on their molecular size: small dopants (as Cl^-, Br^- or NO_3^-) and larger dopants (as peptides, hyaluronic acid or polymers) (Kaur, Adhikari et al. 2015). Both will affect the conductivity and structural properties of the polymer, but large dopants will modify more the material properties.

There are currently two main methods for synthetizing conductive polymers: chemical and electrochemical. During chemical synthesis the monomer solution is mixed with an oxidizing agent ($FeCl_3$, $(NH_4)_2S_2O_8$ among others) (Balint, Cassidy et al. 2014). Electrochemical polymerization, instead, occurs by applying an electrical current through electrodes placed into a solution containing the monomer of the polymer, the solvent and the doping agent (Balint, Cassidy et al. 2014). The main advantage of the latter method is the possibility to control the thickness and morphology of the polymer. The electrical current causes the monomer to deposit and oxidize on the positively charged working electrode, forming insoluble polymer chains (Guimard, Gomez et al. 2007).

Polypyrrole (PPy), polyaniline (PAni), and poly(3,4-ethylenedioxythiophene) (PEDOT) and their derivatives are the most commonly used CPs nowadays (Fig. 1.2.10). CPs can be used as matrix for the immobilization of enzymes (Shaolin and Jinqing 1995), in solar energy conversion (Ghosh, Kouamé et al. 2015), biomedical applications (Oh, Kwon et al. 2013), in microelectric devices (Beh 1999), in batteries or in supercapacitors (Ran Liu 2008, Pankratov, Falkman et al. 2014). PEDOT is a good candidate for the fabrication of a supercapacitor because of its high stability among other conductive polymers. The pseudocapacitance behavior of PEDOT is originated from diffusion of charged counter-ions during the redox process (Ran Liu 2008). PEDOT based supercapacitors required the diffusion of counter ions into/out of the polymer to balance the charges generated during the redox reaction. This doping/de-doping process involves not only charge (electrons and hole) transport but also ion transport.

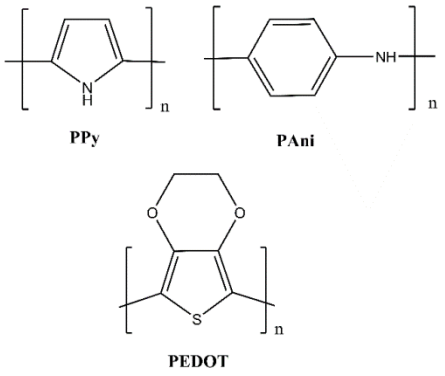

Figure 1.2.10 Structure of the most common CPs.

1.2.4 Electron transfer

Significant efforts have focused on optimizing the electric connection between electrodes and enzymes for developing efficient bioelectrodes in order to produce the highest current density of the device at low overpotentials. Wiring of enzymes to electrodes can be accomplished by two main strategies: i) direct wiring of the biomolecule to the electrode material (DET) or ii) by mediated electron transfer (MET) (Fig.1.2.11).

According to Marcus's theory the electronic transfer (ET) is governed by the driving force, the reorganization energy of the ET process and the distance between the donor and the acceptor (the two sites) as this distance influences the reorganization energy of the system (Marcus and Sutin 1985). This means that the active site of the biomolecules has to be not more distance than 14 Å from the electrode surface (Page, Moser et al. 1999) or connected to the electrode via a series of redox co-factors, such as iron-sulfur clusters or haeme groups (Cosnier, J. Gross et al. 2016).

In the MET approach redox mediators (organic or inorganic molecules) act as electron shuttles between the enzyme active site and the electrode surface. Their redox potentials have to be close to the redox potential of the active site (Le Goff, Holzinger et al. 2015). An important feature inherent to the

use of mediators is that its presence alters the electron transfer kinetics. The additional electron transfer step introduced may become the limiting step if not chosen carefully; on the other hand, it is desirable that the potential loss is as low as possible.

DET is harder to achieve and depends on the favourable orientation of the active site towards the electrode surface and how deep the active centre is buried into the protein matrix (Page, Moser et al. 1999). However, DET presents many advantages that make it the most suitable approach for the design of BFCs. Indeed, absence of redox mediators simplifies the fabrication process of the bioelectrodes and avoids the toxicity of many redox mediators, which is especially important in the case of implantable biofuel cell applications (Falk, Blum et al. 2012). Moreover, in DET regime the electrocatalysis is performed at the apparent redox potential of the enzymes at the anode and at the cathode, thus maximizing the biofuel cell voltage (Cracknell, Vincent et al. 2008). Therefore, the DET approach has become the more interesting for biodevices operating *in vivo* and *ex vivo* conditions. Efficient DET in the case of MCOs can be achieved if the T1 site is correctly oriented towards the electrode surface, while for CDH the CYT domain has to be oriented near the electrode surface.

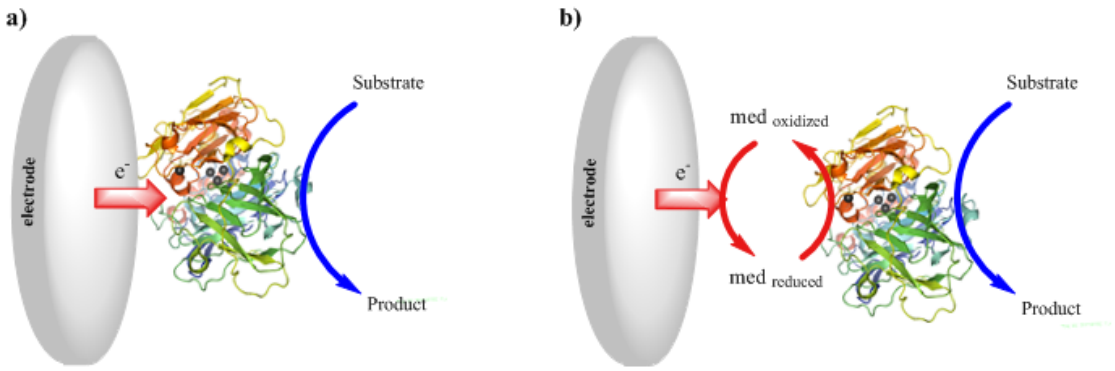

Figure 1.2.11 Schematic representation of a) DET and b) MET between an enzyme and the electrode surface.

2. Objectives

This Thesis project was carried out within the frame of an ITN (Initial Training Network) project of the European VII Framework Programme (BIOENERGY, FP7-PEOPLE-2013-607793). This European programme is based on the collaboration between the consortium members for the training of young researchers, combining the know-how of the different groups involved, ranging from enzyme engineering to bioelectrochemistry and from fabrication of different nanomaterials to the development of sensors, fuel cells and supercapacitors. Many chapters of this Thesis are indeed developed by the collaboration with several of the consortium members and three secondments (in total a duration of 4 months) were done in three other consortium laboratories.

The main goal of the European project BIOENERGY was to design nanostructured electrode materials and to improve the activity and stability of the redox enzymes used as immobilized electrocatalysts, and to fabricate BFCs with higher performance for possible *in vivo* and *ex vivo* applications.
Within this project, the main aim of this Thesis was focused in the development of DET based biocathodes, combing different nanostructured materials and different redox enzymes of the MCOs family. As final step of the project, a DET-based MCO biocathode was combined with an enzymatic anode for the study of a BFC for *ex vivo* applications. In order to reach the proposed global objective, different partial objectives were approached:

- To study the halides coordination to MCOs active centre and the inhibition mechanism derived, which is important for applications in physiological conditions, by spectroelectrochemistry using N_3^- as active infrared probe.
- To produce and purify new laccase mutants obtained by site directed mutagenesis with higher activity at neutral pH, and to develop new oriented immobilization strategies of laccase mutants on gold electrodes for the fabrication of DET based biocathodes.
- To develop new nanostructured materials as high surface area electrodes, in order to enhance direct electron transfer between enzyme and electrode.
- To study different electrode functionalization strategies of transparent electrodes for the development of mediator-less transparent biodevices.
- To develop a hybrid device combing a traditional BFC with an electrochemical supercapacitor and to test it in *ex vivo* conditions.
- To characterize all the enzymatic electrodes developed by electrochemical, microscopy and spectroscopy methods.

3. Materials and methods

3. 1 Materials

3.1.1 Chemicals

All chemicals used were of analytical grade and were used as purchased. 6-amino-2-naphtoic acid (NA) 90%, (3-aminopropyl)triethoxysilane (APTES) 99%, ammonium hydroxide, ammonium sulphate, L-ascorbic acid, 2,2'-azinobis-(3-ethylbenzothiazoline-6-sulfonic acid) diammonium salt (ABTS) 98%, 1-4 benzedithiol, quinhydrone, deutetared water (D_2O), 1-(3-dimethylamino-propyl)-3-ethylcarbodiimide (ECD) > 99%, dimethylformamide (DMF), 2,6-dimethoxyphenol (DMP), dimethylsulfoxide (DMSO), 3,4-Ethylenedioxythiophene (EDOT), ferrocene methanol (FeMeOH), gold (III) chloride trihydrate ($HAuCl_4$) (49% gold content), D-(+)-glucose 99%, glycerol, (3-glycidyloxypropyl) trimethoxysilane (GLYMO), Hexadecyltrymethilammonium bromide (CTAB), 2-Bis(2-hydroxyethyl)amino-2-(hydroxymethyl)-1,3-propanediol (BIS-TRIS), lithium perchlorate ($LiClO_4$), maleimide, 6-mercapto-1-hexanol (MH) 97%, mercaptoproprionic acid, methylene chloride, 2-(N-morpholino)ethanesulphonic acid (MES) 99.5%, 4-nitrobenzene diazonium perchlorate, piperazine, polyethylene glycol 2000 (PEG), potassium ferricyanide 99%, potassium ferrocyanide 99%, silver nitrate ($AgNO_3$), sodium acetate, sodium azide (NaN_3) >99.5%, sodium fluoride (NaF) 97%, sodium perchlorate ($NaClO_4$) 98%, sodium nitrite ($NaNO_2$) 99.99%, sodium L-lactate, sodium tetrahydroborate, tetrabutylammonium fluoride (BF_4Bu_4N) >99%, tetrakis(hydroxymethyl) phosphonium chloride (THPC) 80%, 2,2,6,6-Tetramethyl-1-piperidinyloxy (TEMPO), 1,4 dithiorethtiol (DTT), toluene, uric acid, xantham gum, were purchased from Sigma. Acetic acid 96%, acetonitrile (HPLC grade), absolute ethanol (EtOH), hydrochloride acid 37%, hydrogen peroxide (H_2O_2) 30% potassium chloride (KCl) 99% sodium chloride (NaCl) 98%, di-sodium hydrogen phosphate 99%, sodium carbonate, sodium di-hydrogen phosphate, sodium hydrogen carbonate, sodium hydroxide (NaOH), sodium periodate ($NaIO_4$) 99%, sulfuric acid 98% (H_2SO_4) were purchased from Panreac and N-hydroxysuccinimide (NHS) 97% was obtained from Fluka. Graphene oxide powder (GO) (Nanoinnova Technologies SL.) was used with no further purification. All aqueous solutions were prepared in deionized water (18.2 MΩ·cm Milli-Q grade, Millipore).

3.1.2 Enzymes

3.1.2.1 Laccase

Trametes hirsuta laccase (*Th*Lc) from basidiomycete (strain T. hirsuta 56), was provided by Prof. Dr. Sergey Shleev (Malmo University, Sweden). The enzyme received had been previously extracted and purified following the standard purification procedure (Shleev, Morozova et al. 2004). Samples of

*Th*Lc (5.8 mg/mL, Activity= 553 U/mg at pH 4.2 with 1 mM ABTS in acetate buffer) were stored in 0.1 M phosphate buffer, pH 6.5, at -20 °C.

Laccase mutants have been obtained by engineering of PM1 laccase by site directed mutagenesis (Alcalde 2010), in which two different serine residues near the T1 site were substituted with cysteine, in collaboration with Ivan Mateljak under the supervision of Dr. Miguel Alcalde (ICP-CSIC, Madrid). Two cysteine variants (S264C and S387C) and the parental type (7D3) have been produced and purified according to the following procedure:

Laccases were expressed in *Saccharomyces cerevisiae* yeast, incubated in minimal medium at 30 °C and 225 rpm until two growth phases were completed. After that, 450 mL of expression medium was inoculated with 50 mL of preculture and incubated for 48 h at 30 °C. Finally, the cells were separated by centrifugation for 15 min at 6000 rpm at 4°C and the obtained supernatant was filtered twice. The crude extract obtained was first purified by a fractional precipitation with ammonium sulphate at 55% (first cut) and the supernatant recovered was submitted to a 75% ammonium sulphate precipitation (second cut). The final pellet was recovered in 20 mM piperazine buffer pH 5.5, filtered and loaded onto a fast protein liquid chromatography (FPLC) coupled with a strong anionic exchange column. The proteins were eluted with piperazine buffer using a linear gradient from 0 to 1 M of NaCl in two phases (flow rate 1 mL/min): from 0 to 50% over 40 min and from 50 to 100% in 10 min. The fractions with laccase activity were collected, concentrated, dialyzed and purified again with high performance liquid chromatography (HPLC) coupled with a 10 μm high resolution anion exchange column. Again the proteins were eluted with piperazine buffer but this time using a linear gradient from 0 to 1 M NaCl from 0 to 8% in 60 min and from 8 to 100% in 10 min. The fractions with laccase activity were collected, dialyzed against 10 mM BIS-TRIS buffer pH 6.5, concentrated and stored at -20 °C. All through the purification procedure the fractions were analyzed by SDS-polyacrylamide gel electrophoresis (SDS-PAGE) (Maté, García-Burgos et al. 2010).

3.1.2.2 Bilirubin oxidase

Two bilirubin oxidase from different sources have been used in this Thesis. Purified samples of *Myrothecium verrucaria* Box (4 mg/mL, Activity= 121 U/mg at pH 7.4 with 1 mM ABTS in phosphate buffer), expressed recombinantly in *Aspergillus oryzae*, have been kindly provided by Dr. Miguel Toscano from Novozymes A/S (Denmark).

Magnaporthe oryzae bilirubin oxidase (mgBOx) samples (68.66 mg/mL, Activity= 758 U/mg at pH 4 with 4 mM ABTS in citrate-phosphate buffer) have been kindly provided by Dr. Nicolas Mano from Centre de Recherche Paul Pascal (CNRS, Bordeaux). The mgBOx sample was produced and purified as reported in literature (Durand, Gounel et al. 2012).

3.1.2.3 Cellobiose dehydrogenase

Cellobiose dehydrogenase from *Corynascus thermophiles* (ctCDH) (25 mg/mL, Activity =33.5 U/mg at pH 7.5 with cyctochrome c) expressed in *Pischia pastoris*, obtained as previously described (Coman, Ludwig et al. 2010), has been kindly provided by Dr. Roland Ludwig (BOKU University, Vienna).

3.1.3 Supports for enzyme immobilization

The following materials have been employed as electroactive support for their further modification and enzyme immobilization:

- glassy carbon (GC) with a diameter of 0.5 cm (PINE Instruments);
- low density graphite (LDG) with a diameter of 3 mm, grade of purity 99,999% supplied by Sigma-Aldrich;
- spectrographic graphite (type RW001, 3.05 mm in diameter) purchased from Ringsdorff Werke GmbH (Bonn, Germany);
- gold coated substrate (1 × 1 cm^2) from Metallhandler Schroer GMBH;
- gold wire (2-3 cm length, d= 250 µm) purchased from Goodfellow (United Kingdom);
- macroporous gold: provided by Prof. Dr. A. Khun (Bordeaux University, France);
- indium tin oxide (In_2O_3/SnO_2; ITO) conductive glasses (15-25 Ω/sq) purchased from Sigma-Aldrich.

3. 2 Methods

3. 2. 1 Enzyme characterization

The concentration of the enzymes was determined by the Bradford method (Bradford 1976), using BIO-RAD (Bio Rad Laboratories) and bovine serum albumin (BSA) for the calibration curve.

The specific activity of laccase mutants was measured spectrophotometrically at room temperature by following the oxidation of 1 mM ABTS at 414 nm ($\varepsilon_{414\ nm}$= 36.8 M^{-1} cm^{-1}) in 50 mM acetate buffer pH 4.2 with 100 mM $NaClO_4$ (Childs and Bardsley 1975), using a Shimadzu UV-2401 PC spectrophotometer. The measurement was carried out in aerobic conditions and started by the addition of 10 µL of enzyme (1:1000 diluted) to 990 µL of ABTS solution.

Enzyme kinetics studies of laccase mutants were performed by measuring their specific activities at different ABTS concentrations and fitting the data to the Michaelis-Menten model. The catalytic efficiency (k_{cat}/K_m) was obtained by plotting the initial turnover rates in s^{-1} (*f(x)*) *vs.* substrate concentration (*x*) and further fitting to a modified hyperbola:

$$f(x) = (ax)/[(1 + bx)] \quad (3.1)$$

where a is the catalytic efficiency and b is $1/K_m$ (Gonzalez-Perez, Mateljak et al. 2016).

3. 2. 2 FTIR spectroelectrochemistry measurements

Fourier transform infrared (FTIR) spectroscopy was performed with a Bruker Tensor 27 spectrometer equipped with a Globar IR source, a MCT detector cooled with liquid N_2 and a Whatman purge gas generator for removing CO_2 and H_2O. The FTIR spectroelectrochemical cell was designed by Moss et *al.* (Moss, Nabedryk et al. 1990). The cell comprises two CaF_2 windows (20 mm × 4 mm, Apollo Scientific Limited), a 6 μm thick gold mesh (200 gold mesh, Buckbee-Mears) serving as working electrode and Au foil as counter electrode, which is placed at the side of one CaF_2 window. For sealing the cell, two Viton rings (Epidor) surrounding the CaF_2 disks were used. Around the windows perimeter there is a space for injecting the electrolyte solution, allowing electric contact between the working and counter-electrodes and with a Ag/AgCl (3M KCl) reference electrode. The two CaF_2 windows are fitted into a Teflon body and pressed together between two steel plates (Fig 3.2.1).

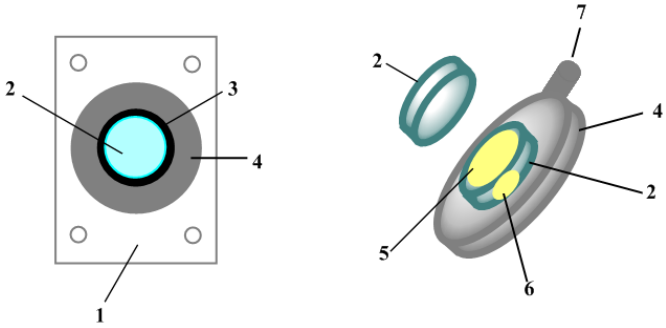

Figure 3.2.1 Schematic representation of the spectroelectrochemical cell: (1) steel plate; (2) CaF_2 window; (3) Viton ring; (4) Teflon body; (5) gold mesh working electrode; (6) Au counter electrode; (7) Ag/AgCl (3M KCl) reference electrode.

For each measurement 1024 scans were accumulated setting the resolution at 2 cm^{-1}. Background subtraction and baseline correction of the recorded spectra were performed using OPUS software from Bruker.

3.2.2.1 Multicopper oxidases FTIR characterization

For the FTIR characterization measurements an aliquot of purified ThLc enzyme (5.8 mg/mL, 96 μM) was concentrated 5 times by ultrafiltration in Centricon-30 (Amicon); whereas the mgBOx aliquot was used as received (concentration: 68.66 mg/mL, 1.14 mM). For the inhibition studies both enzymes were incubated in a 20 mM phosphate buffer solution pH 6.0 containing NaN_3 (1:2 enzyme:azide) overnight at 4 °C. 30 mM NaF or NaCl were included in the sample solution the day after incubation with azide and 15 min before the FTIR measurements. 10 μL of the sample solution plus 1 μL of a redox mediators' mixture (0.5 mM each) were placed in the spectroelectrochemical cell to record different FTIR spectra at different potentials in the 0-650 mV vs. Ag/AgCl (3 M Cl^-) range. The redox mediators employed were ABTS (E'_0= 690 mV vs. NHE), quinhydrone (E'_0= 345 mV vs. NHE at pH 6.0), DMP (E'_0= 640 mV vs. NHE at pH 6) and TEMPO (E'_0= 735 mV vs. NHE) (Jovanovic, Tosic et

al. 1991, Fabbrini, Galli et al. 2002, Kulys and Vidziunaite 2005). 0.2 mM KCl was used as electrolyte. The redox potential of the cell was controlled with a BAS CV-27 potentiostat and measured with a Fluke 77 serie II multimeter. Before recording a spectrum, the sample was poised to the selected potential for at least 15 min to be sure that redox equilibrium was achieved. The temperature of the cell was maintained at 25°C with a Julabo CC 230 thermostat. A spectrum of phosphate buffer sample was recorded as background. Peak fitting and deconvolution was carried out using OriginPro 8.0 software using a Gaussian fit in the range of 2100-2000 cm^{-1}.

3.2.2.2 Graphene oxide characterization

FTIR spectroelectrochemical measurements were carried out for a GO suspension (0.5 mg/mL) in D_2O after applying a reductive potential of -1.5 V vs. Ag/AgCl (3 M Cl^-) during 5, 30 and 60 minutes. 0.25 M NaCl in D_2O was used as electrolyte. A spectrum of D_2O sample was recorded as background.

3.2.3 Synthesis of nanostructured materials

3.2.3.1 Gold nanostructures

3.2.3.1.1 Gold nanorods (AuNRs)

A seedless growth technique was used for the synthesis of gold nanorods with low dimensions and aspect ratio (Ali, Snyder et al. 2012). The growth solution was prepared at 30 °C by the addition of 5 mL 1mM $HAuCl_4$ to 5 mL 0.2 M CTAB, followed by the introduction of 250 μL of 4 mM $AgNO_3$, 8 μL of HCl 37%, 70 μL of 78.8 mM ascorbic acid and 15 μL of 0.01 M ice-cold $NaBH_4$. Nanorods formed almost immediately, which was denoted by a color change to deep red, and confirmed by TEM images and UV-Vis characterization. However, in order to obtain a uniform morphology and an adequate yield, the samples were left to grow overnight. Afterward, the solution was centrifuged (at 6500 rpm during 30 minutes). The supernatant was removed and the nanorods were redispersed in deionized water and centrifuged at the same speed and time. The procedure was repeated for three times.

3.2.3.1.2 Gold nanoparticles (AuNPs)

AuNPs were synthetized in aqueous media by addition of 1mM $HAuCl_4$ to a solution containing 1 M NaOH and 1mM THPC under vigorous stirring (Duff, Baiker et al. 1993). The obtained nano-gold dispersion was filtered with a PTEF 0.4 μm pore size filter (Pall, Geldan Laboratory).

3.2.3.2 Graphene oxide

Graphene oxide (GO) was synthetized in Nanoinnova Technologies' laboratory during my secondment in the company. GO was produced by oxidation of graphite following the Hummers' method (Hummers and Offeman 1958). 10 g of graphite were mixed with 5 g of $NaNO_3$ in 230 mL of H_2SO_4 in an ice cooled bath, under stirring. Then, 30 g of $KMnO_4$ were added very slowly to the solution, paying attention that the temperature did not exceed 20°C. The ice bath was then removed

and the temperature of the suspension was brought at 30°C and kept under stirring for 1 hour and a half. Afterwards, 400 mL of H_2O were slowly added, causing an increase in the temperature. At this point the solution began to become brownish. The temperature of the solution was brought to 95°C and left under stirring for 15 min. Then the solution was diluted with more H_20 and treated with H_2O_2 in order to eliminate the residual permanganate and manganese dioxide. Finally, the suspension was filtered and dried under air atmosphere at 30°C. Two different batches of GO were synthetized: GO_01 and GO_02. The difference between them consisted only in a slight difference in one of the synthetic steps; GO_02 was prepared by a slower addition of the oxidant ($KMnO_4$) during 2h, whereas for the synthesis of GO_01 the oxidant was added slowly during 30 min. This difference in the synthesis method resulted in a different O/C ratio[1] for the two batches: GO_01 presented a C/O ratio of 0.65, whereas GO_02 had 0.45.

3.2.4 Fabrication of nanostructured electrodes

3.2.4.1 Nanostructured graphite-Au electrode

Low density graphite (LDG) electrodes were polished with sandpaper and sonicated in H_2O/EtOH 1:2 for 10 min. Then, the cleaned electrodes were modified with 4-aminophenyl groups by the following procedure: 2.5 mg of 4-nitrobenzene diazonium salt were dissolved in 5 ml of 0.1 M Bu_4NBF_4 prepared in anhydrous CH_3CN. The electrochemical reduction of the diazonium salt and the subsequent formation of a C-C bond between the LDG electrode and the formed nitrophenyl radical was performed by cycling the potential twice between 0.6 and −0.6 V (vs. Ag|AgCl|3 M KCl) at 200 mV/s.

The electrode was then transferred to a 1/9 EtOH/H_2O solution (containing 0.1 M KCl) previously deoxygenated and subjected to two cyclic voltammograms (CVs) between 0 and −1.4 V (vs. Ag|AgCl|3 M KCl) at 100 mV/s for reduction of the nitro groups of the attached phenyl rings (Vaz-Dominguez, Campuzano et al. 2008). Afterwards, the modified electrodes were immersed at RT in a 14.5 mM $NaNO_2$ and 0.5 M HCl solution for 2h in order to convert the aromatic amino groups of the electrode surface to diazonium groups, allowing in this way the attachment of AuNRs (Gutierrez-

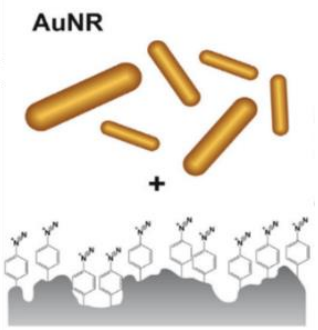

Figure 3.2.2 Functionalization of LDG electrodes and subsequent modification with AuNRs.

[1] O/C ration for the GO batches was determined by XPS analysis.

Sanchez, Pita et al. 2012). Following this, the electrodes were covered with 5 µL of AuNRs solution freshly prepared and then let to dry (Fig 3.2.2). Afterwards, these AuNRs-modified LDG electrodes were submitted to two CVs between 0.6 to -0.6 V at 200 mV/s, in 50 mM acetate buffer pH 4.2, $NaClO_4$ 100 mM at room temperature.

3.2.4.2 Graphene based electrodes

Graphene-based electrodes were fabricated by the simultaneous electrodeposition and electroreduction of GO. Electrodeposition (ED) was performed on glassy carbon (GC) and gold coated substrates. Previous to their use the electrodes were carefully cleaned. GC electrodes were polished with alumina slurry 0.05 µm in particle size, rinsed and then immersed into an EtOH/H_20 2:1 solution for ultrasound cleaning during 15 min. The gold coated substrates were firstly immersed in a freshly prepared piranha solution (H_2SO_4:H_2O_2 3:1) for 30 min, rinsed with water, polished with alumina slurry 0.05 µm and sonicated in EtOH/H_20 2:1 for 10 min. Finally, an electrochemical cleaning of the gold electrode was performed in 0.5 M NaOH first (25 CV scans from 0 to -1.5 V, scan rate 0.2 V/s) and then in 0.1 M H_2SO_4 (25 CV scans, from 0 to 1.5 V, scan rate 0.1 V/s). GO_01 and GO_02 dispersions (1 mg/mL) in 100 mM phosphate buffer pH 9 were prepared. Alternatively, an aqueous solution containing 150 mM NaCl and 0.5 mg/mL GO_02 was prepared and its pH neutralized with 0.5 M KOH solution. The GO dispersions prepared were sonicated for 30 min. The exfoliated GO dispersion was deoxygenated under N_2 atmosphere before starting the electrodeposition process.

Two different methods were studied for optimizing GO electrodeposition on GC electrodes:

- Cyclic voltammetry between 0.8 and -1.5 V vs. Ag/AgCl (3M KCl) using different scan rates (2-50 mV/s) and number of cycles (5-50).

- Pulsed electrodeposition by applying in sequence a reductive potential at -1.5 V and an oxidative potential at 0.6 V during fixed times and repeating these pulses a fixed number of times.

All electrodeposition experiments were carried out at room temperature, under deoxygenated conditions and magnetic stirring using a IKA RCT basic applying 400 rpm/min (Di Bari, Goñi-Urtiaga et al. 2016).

3.2.4.3 Macroporous gold electrodes

Macroporous gold (MG) electrodes with a cylindrical geometry have been prepared by the combination of Langmuir-Blodgett and electrodeposition techniques (Reculusa, Heim et al. 2011) in the laboratory of Prof. Dr. Alexander Khun (Bordeaux University, France). Gold wires were used as substrate and silica particles (diameter= 600 nm) as colloidal templates. It is possible to deposit through Langmuir-Blodgett technique a well-defined N numbers of monolayers of silica particles on a cylindrical gold wire (GW) repeating N time the transfer of a single layer (Fig 3.2.3.a) (Reculusa,

Heim et al. 2011). The modified wires were used as working electrode for electrodeposition of gold in the unfilled spaces of the silica particles network (Fig. 3.2.3.b). The counter electrode had a cylindrical shape and it was placed symmetrically around the working one in order to ensure a homogeneous deposition of gold. A gold plating bath was used and a constant potential of 0.66 V was applied during the electrodeposition. The electrochemical growth of gold, deposited onto the gold wire covered with N-monolayers of silica particles, can be easily controlled by the chronoamperometric curves obtained. Indeed, the current values oscillate more or less regularly and this oscillation can be attributed to the periodic variation of the outer surface of the growing gold deposit during the infiltration of the template voids. When the growth of the gold deposit was stopped before reaching the top surface of the template, the silica particles were removed by infiltration of a diluite hydrofluridric acid solution (Fig. 3.2.3.c). After the removal of the template the final macroporous material presents interconnected voids and top surface with a remarkable flatness. The macroporous electrodes used in this Thesis comprised either 7.5 layers or 15.5 layers of nanostructured Au. Previous to their use these electrodes were carefully cleaned following this procedure: first the electrodes were immersed in piranha solution (H_2SO_4:H_2O_2 3:1) for 20 min, and then in water for 10 min. Finally, an electrochemical cleaning was performed in 0.1 M H_2SO_4 by cycling the potential for 30 times, from 0.1 to 1.5 V at 0.1 V/s.

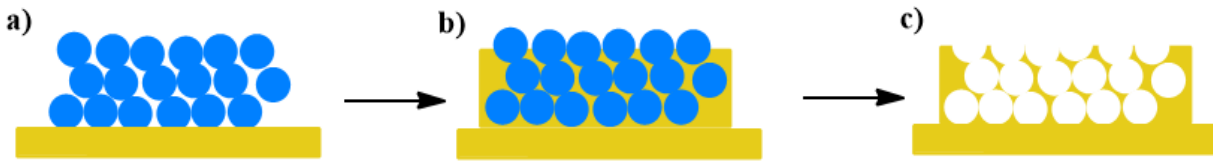

Figure 3.2.3 Scheme representing the fabrication of MG electrodes: a) deposition of SiO_2 beads on GW via Langmuir-Blodgett technique, b) electrodeposition of Au into the colloidal crystal structure and c) removal of the silica template by HF.

3.2.4.4 Tubular PEDOT-graphite electrodes

The outer part of spectrographic graphite rods was modified with PEDOT by electropolymerization of 20 mM EDOT dissolved in an aqueous solution also containing 1mM PEG, 0.1 M $LiClO_4$ and 0.1 M KCl. The electropolymerization was performed by immersion of the graphite rod in the solution during 1 min and a subsequent recording of 25 CVs between -0.2 to 1.3 V (vs. Ag/AgCl/ 3M KCl) at 50 mV/s scan rate (González-Arribas, Pankratov et al. 2016). The PEDOT modified graphite electrodes were cut in pieces of 10.0 ± 0.5 mm length. Each rod was drilled lengthwise in the center to fabricate tubular PEDOT-graphite electrodes with inner and outer diameters equal to 1.00 mm and 3.01 mm.

3.2.5 Enzyme immobilization

3.2.5.1 Trametes hirsuta laccase

3.2.5.1.1 Nanostructured graphite-Au electrodes

In order to allow a covalent immobilization of the enzyme on the electrode surface a previous functionalization of the surface is needed.

The AuNR-LDG electrodes were immersed in an acetonitrile solution containing 2 mM 4-nitrobenzene diazonium perchlorate and 100 mM Bu_4NBF_4 and subsequently one CV, from 0.6 to -0.6 V at 200 mV/s scan rate, was recorded. Then, the electrodes were taken into a 1:9 EtOH/H_2O 0.1 M KCl solution, and electrochemical reduction of the nitro groups on the AuNR-LDG surface was carried out running a CV from 0 to -1.4 V at 200 mV/s scan rate. The amino terminated AuNR-LDG electrodes were immersed overnight in an aqueous solution containing 1 mM MH, and then rinsed with water.

A 5 µL sample of *T. hirsuta* laccase (5.8 mg/mL) was placed into 55 µL of 47 mM $NaIO_4$ solution during 30 minutes to oxidize the laccase's saccharides by forming aldehyde groups. Afterwards 90 µL of 100 mM Na_2HPO_4 was added to the solution to obtain pH 7 for finishing the reaction. The modified AuNR-LDG electrodes were then incubated in the enzyme solution during 90 minutes for the formation of Schiff's bases between the amino groups of the electrode surface and the laccase´s aldehyde groups. The *Th*Lc-AuNR-LDG electrodes were rinsed with 10 mM MES buffer, pH 6.0. Finally, the electrode surface was covered with 10 µL of 10 mM MES pH 6.0 buffer solution, containing 36 mM EDC and 17 mM NHS. The electrode was put facing up and covered to avoid evaporation, letting the reaction take place for 2h. This reaction allowed forming amide bonds between electrode and the immobilized laccase by carbodiimide coupling (Fig 3.2.4) (Gutierrez-Sanchez, Pita et al. 2012).

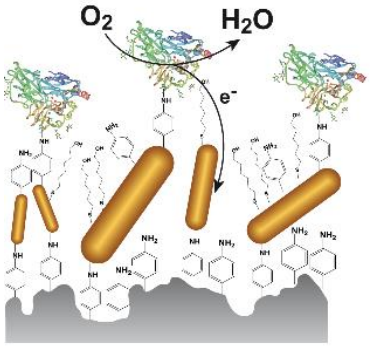

Figure 3.2.4 Laccase immobilization on AuNRs modified LDG electrodes.

3.2.5.1.2 Graphene-based electrodes

The electrochemically reduced graphene oxide-glassy carbons (erGO-GC) electrodes were functionalized with 4-aminoaryl diazonium salt following the same procedure reported before for nanostructured graphite-Au electrodes for *Th*Lc immobilization. The method yielded aminoaryl-functionalized electrodes (AP-erGO-GC). As before, the same protocol was used for the formation of covalent bonds between the amino groups of the electrode surface and the aldehydes groups of the enzyme (Fig. 3.2.5).

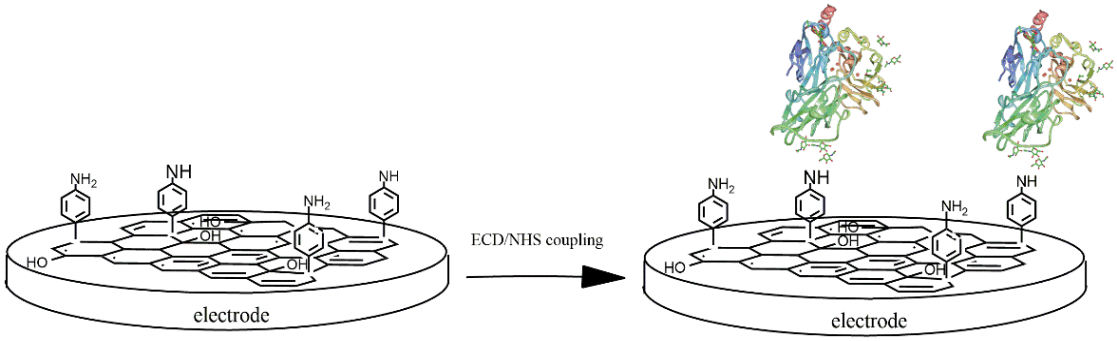

Figura 3.2.5 Scheme of laccase immobilization on graphene based electrodes.

3.2.5.2 Bilirubin oxidase

3.2.5.2.1 Graphene-based electrodes

BOx was covalently immobilized on the graphene-based electrodes *via* the formation of amide bonds between the lysine residues of the enzyme and the carboxylic groups of the electrode surface (Fig. 3.2.6).

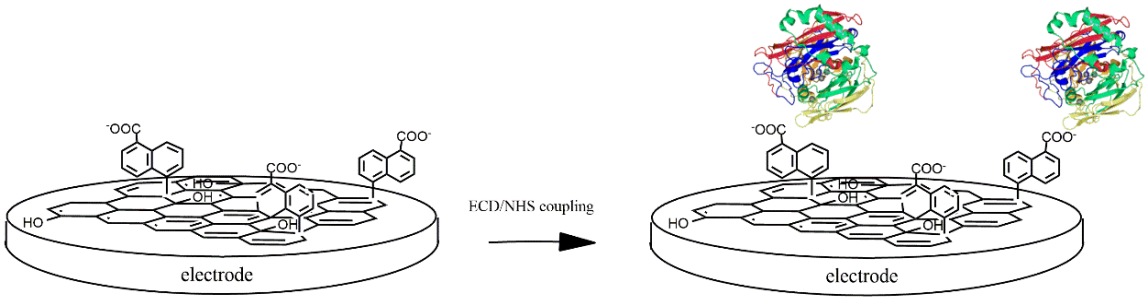

Figure 3.2.6 Scheme of BOx immobilization on graphene based electrodes.

This method was either done with the erGO-GC electrodes directly or after their functionalization with 2-carboxy-6-naphtoyl diazonium salt, which was synthesized *in situ* by mixing two ice-cooled aqueous solutions: 5 mL of 20 mM 6-amino-2-naftoic acid in acetronitrile and 5 mL of 2 mM $NaNO_2$ in 2 M HCl. Two reductive CVs from 0.6 V to -0.3 V vs. Ag/AgCl at 200 mV/s scan rate were recorded. This procedure yielded 6-carboxynaphtoyl functionalized electrodes (NA-erGO-GC). The enzyme immobilization on erGO-GC and NA-erGO-GC electrodes was done by incubation in 20 µL of 4 mg mL^{-1} mtBOx solution for 1h, followed by the deposition of 10 µL of 10 mM MES buffer solution (pH 6.0) containing 36 mM EDC and 17 mM NHS on the electrode surface for 2h.

3.2.5.2.2 Macroporous and gold wire electrodes

mgBOx was immobilized onto the gold surfaces by either physical adsorption or covalent immobilization. In the first case macroporous gold (MG) or gold wire (GW) electrodes were simply immersed in a 4 mg/mL enzyme solution for 3h and 1h, respectively. Instead, in the case of covalent immobilization MG or WG electrodes were previously functionalized with a naphtoic acid layer, following the same procedure reported above (Fig 3.2.7). The enzyme immobilization protocol was the same as in 3.2.5.2.1 but, the procedure was optimized as follows: when MG was used as support, the enzyme incubation time was increased to 3h and the ECD/NHS reaction was 4h.

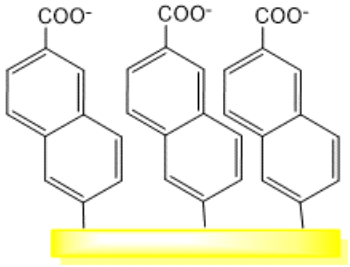

Figure 3.2.7 Functionalization of Au surfaces with a naphtoic acid monolayer studied for mgBOx immobilization.

3.2.5.2.3 ITO electrodes

The ITO conductive glass slices were cut in 25 mm × 10 mm pieces and cleaned by sonication, first in ethanol (15 min) and then in methylene chloride (15 min). The ITO glass was treated with a mixture of 30% NH_4OH, 33% H_2O_2 and H_2O 1:1:1 (v/v) during 1h at 60 °C, washed in water for 20 min, and then dried under a nitrogen flow. The freshly cleaned ITO glass was immersed in toluene with 0.1% (v/v) GLYMO for 20 min at 70 °C. The silanized ITO glass was rinsed with toluene and dried under nitrogen (Tam, Ornatska et al. 2008).

Initially, mtBOx was immobilized by simple adsorption, dropping 20 µL of 4 mg/mL mtBOx in 100 mM phosphate buffer pH 7.4 onto the ITO surface and let to react for 24h. Otherwise, the initial aliquot of mtBOx was diluted to 8 mg/mL by adding 50 mM bicarbonate-carbonate buffer, pH 9. 20 µL of mtBOx solution were dropped onto the silanized ITO surface and let to react during 24h at room temperature under moisturized conditions to avoid evaporation (Fig 3.2.8) (Abad, Vélez et al. 2002).

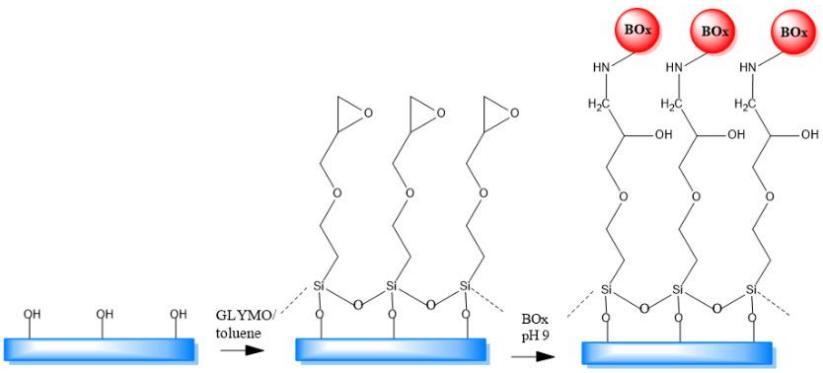

Figure 3.2.8 Chemical modification of ITO electrodes for BOx immobilization.

3.2.5.2.4 Tubular PEDOT-graphite electrodes

For the fabrication of a BOx-based biocathode using tubular PEDOT-graphite electrodes as support, 20 µL of mtBOx 3.9 mg/mL were physically adsorbed inside the tubular structure for 30 min at room temperature.

3.2.5.3 Laccase cysteine variants

3.2.5.3.1 Macroporous and wire gold electrodes

Three different strategies were tested for the immobilization of both S287C and S264C laccase variants and their corresponding parental type 7D3, on MG and WG electrodes.

In the first strategy 1,4-dithiothreitol (DTT) was co-adsorbed with the protein to yield a mixed self-assembled (SAM) thiol monolayer (Fig 3.2.9.a). The electrodes were immersed overnight in a solution containing an equimolar concentration of DTT in EtOH/H_2O 1:1 and enzyme (45 µM) at 4°C (Pia, Chi et al. 2011).

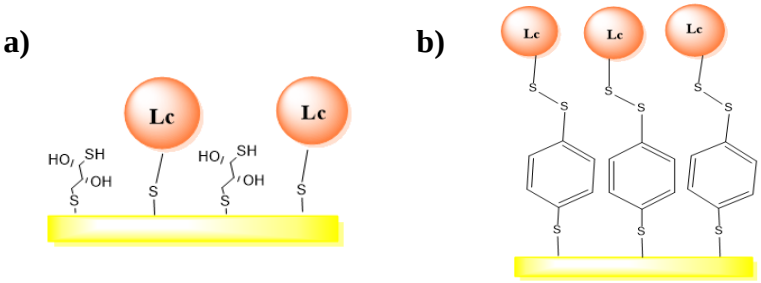

Figure 3.2.9 Two strategies for laccase mutants immobilization: a) mixed monolayer of DTT and enzyme and b) disulfide bond formation with 1,4-benzenedithiol monolayer.

In the second strategy, the gold electrodes were first incubated in an ethanol solution containing 5 mM 1,4-benzenedithiol at 4°C overnight (Xiao, Patolsky et al. 2003), afterwards they were incubated in the enzyme solution at 4°C overnight for formation of disulfide bonds (Fig 3.2.9.b).

The last strategy consisted in using maleimide as linker between the cysteine residues of the enzyme and the monolayer on the Au surface (Fig 3.2.10). First, gold electrodes were incubated overnight in a 5 mM solution of MPA and MH (1:9) in EtOH/H_20 (1:1) at RT. Afterwards, the carboxylic groups were activated by immersing the modified electrodes in a DMSO solution containing ECD 36 mM and NHS 17 mM for 2h (first step of the scheme shown in Figure 3.2.10), and then in a 30 mM maleimide solution in DMF media at pH 7.4 for 1h. This reaction yields the formation of a covalent bond between the ester groups of the electrode surface and hydroxylamino groups of maleimide (second step, Figure 3.2.10). Finally, the modified electrodes were incubated in enzyme solution at pH 7 for 2h as shown in the last step of Figure 3.2.9 (Sinz 2006).

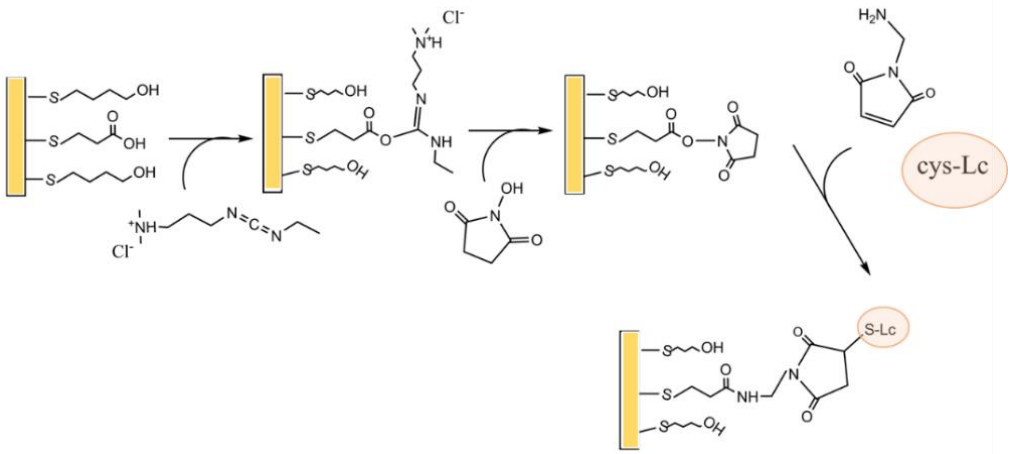

Figure 3.2.10 Immobilization strategy of mutant laccases using maleimide as linker.

3.2.5.4 Cellobiose dehydrogenase

3.2.5.4.1 ITO electrodes

Previous to their use, ITO conductive glass was cut in pieces (25 mm × 10 mm) and cleaned as reported in 3.2.5.2.3 section.

The freshly cleaned ITO glass was immersed in toluene with 1% (v/v) APTES for 20 min at 70 °C. The silanized ITO glass was rinsed with toluene and dried under nitrogen (Tam, Ornatska et al. 2008). Initially 20 µl of ctCDH 5 mg/mL were simply adsorbed on the modified electrode surface and let treact for 2h. Otherwise, 20 µL of ctCDH 5 mg/mL were dropped onto the silanized ITO surface for 2h and then, 30 µL of a solution of 36 mM EDC and 17 mM NHS in MES buffer were dropped over the enzyme layer and left to react for 2h at room temperature under controlled conditions to avoid evaporation (Fig 3.2.11). It was expected that the exposed negatively charged residues of CDH, such as aspartic or glutamic acids, would react with the amino groups of APTES forming amide bonds.

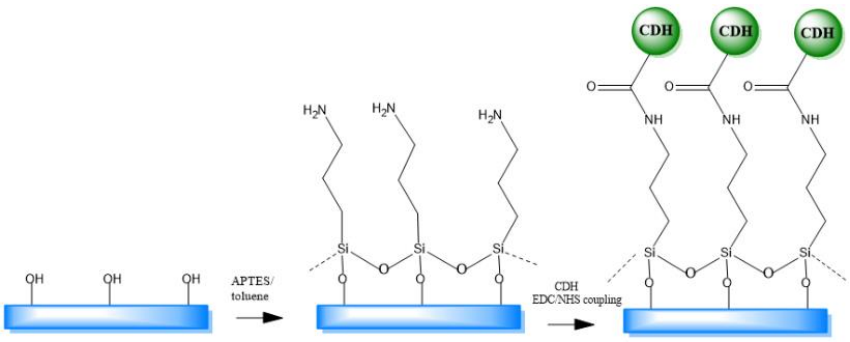

Figure 3.2.11 Chemical modification of ITO electrodes for CDH immobilization.

3.2.5.4.2 Tubular PEDOT-graphite electrodes

For the fabrication of a ctCDH based bioanode using tubular PEDOT-graphite electrodes as support, 20 µL of ctCDH 5 mg/mL were physically adsorbed inside the tubular structure for 30 min at room temperature.

3.2.6 Electrochemical measurements

In vitro electrochemical experiments were carried out in a standard three electrode cell, with a Pt wire from Goodfellow Cambridge Limited as counter electrode and Ag/AgCl/ 3M KCl from BAS as reference electrode. The measurements were controlled by a Autolab PGSTAT30/FRA2, µAutolab type II potentiostat/galvanostat, using GPES 4.9 or NOVA 1.9 software packages from Metrohm Autolab B.V. (Netherlands) or a 660C potentiostat (CH Instruments, Austin, TX, USA). All electrode potentials reported in this thesis are given vs. Ag/AgCl, 3 M KCl (+0.210 V vs SHE) unless otherwise stated.

Electrocatalytic O_2 reduction experiments were carried out at room temperature by cyclic voltammetry from 0.8 to 0 V, at 10 mV/s scan rate in 100 mM phosphate buffer pH 7.4, or in 50 mM acetate buffer pH 4.2 with 100 mM $NaClO_4$ for BOx-based or Lc-based biocathodes, respectively. Buffers were purged with N_2 prior to experiment for obtaining deoxygenated conditions as background control and with O_2 for oxygen catalytic reduction measurements. Mediated electron transfer (MET) measurements were carried out in presence of 0.1 mM ABTS.
The bioelectrocatalytic response of ctCDH-based bioanodes was tested under phosphate saline buffer (12 mM phosphate, 137 mM NaCl, 2.7 mM KCl), pH 7.4 with the addition of 0.5 mM glucose, by cyclic voltammetry from -0.6 to 0.2 V at 10 mV/s scan rate.

A blood mimicking buffer set at 37°C was used for the experiments mimicking physiological conditions. The blood mimicking buffer pH 7.2 comprised 0.1 M NaCl, 0.001 M KCl, 0.0178 M Na_2HPO_4, 0.005 M NaH_2PO_4, 0.045 mM ascorbic acid, 0.425 mM uric acid, 1.92 mM sodium L-lactate, 8.4 mM glucose, 0.05 mM O_2, 25.3 % (v/v) glycerol and 0.032 % (v/v) xantham gum. For *in vitro* measurements a tubular system, consisting of plastic tubes and tubular PEDOT-graphite electrodes, were connected to a 1 L closed buffer flask with the oxygen concentration appropriately adjusted to 0.05 mM by mixing argon and air saturated electrolytes. The flask was thermostated at 37°C using an Assistent WTE var 3185 thermostat from Glaswarenfabrik Karl Hecht GmbH (Sondheim v.d. Rhön, Germany). The electrolytes were pumped through the system using a peristaltic pump U1/4-8R from Alitea Instruments (Medina, WA, USA). A flow rate of 0.09 mL/s was used as it is the corresponding flow rate of blood in a dorsal venous (Pankratov, Ohlsson et al. 2016). For *ex vivo* measurements, the peripheral vein catheter (1.1 x 3.2 mm) was placed in the right hand dorsal venous of a human volunteer, according to standard medical practice and fixed with a medical tape IV3000 from Smith & Nephew Medical Ltd. (Hull, England). The fixed catheter was connected to a Luer Lock tube from Discofix®C, (Melsungen, Germany), with inner and outer diameters of 3 and 6 mm, respectively. The tube was connected to a freshly prepared enzymatic anode and cathode combination (1 cm length each), incorporated into plastic tubes from Becton-Dickinson Co. (Franklin Lakes, NJ, USA) inserted into a 250 mL graduated glass cylinder (Pankratov, Ohlsson et al. 2016).

Electrochemical characterization for studying the sequential surface modification steps of graphene based electrodes, ITO and gold modified electrodes was carried out by cyclic voltammetry at different scan rates in the presence of a redox probe. CVs from 0.6 to -0.2 V in 10 mM $K_3[Fe(CN)_6]$, 0.1 M KCl at 5-200 mV/s scan rate were carried out to study the modification of graphene-based electrodes. ITO surface modification was studied by cycling the potential from 0.8 to -0.6 V in 5 mM $K_3[Fe(CN)_6]$ / 5 mM $K_4[Fe(CN)_6]$ in 50 mM PBS with 0.1 M KCl, at 10-200 mV/s for 3 cycles. CVs from -0.1 to 0.5 V in 0.2 mM FeMeOH in 0.1 M KCl at 50 mV/s for 3 cycles were carried out for studying gold surface functionalization.

Electrochemical impedance spectroscopy (EIS) experiments were recorded by application of a 10 mV amplitude potential over a frequency range of 100 kHz to 0.1 Hz. 10 mM $K_3[Fe(CN)_6]$ in 0.1 M KCl or 5 mM $K_4[Fe(CN)_6]$ / 5 mM $K_3[Fe(CN)_6]$ in 50 mM PBS with 0.1 M KCl was used as electrochemical probe for graphene based electrodes or ITO modified electrodes, respectively. EIS experiments for tubular PEDOT-graphite electrodes were carried out in blood mimicking buffer or in blood applying as potential the open circuit voltage (OCV) value recorded for that electrode. All EIS measurements were controlled by an Autolab PGSTAT30 with the FRA2 module using NOVA 1.9 software. Impedance spectra were fitted using electrical equivalent circuits with ZView3.1c software (Scribner Associates Inc., USA), till a satisfactory approximation of χ^2 about 10^{-3}, where χ^2 represents how accurate the fitting is respect the experimental data, is achieved. In the equivalent circuit, R_s is the solution resistance, R_{ct} represents the charge-transfer resistance at the solid-liquid interface. CPE represents the constant phase element constituting the charge separation of the double layer or the polarization of the material. $CPE = [(Ci\omega)^{\alpha}]^{-1}$ is modelled as pure capacitor in the case of $\alpha=1$ or as non-ideal capacitor, due to porosity and non-homogeneity of the surface, for $0.5 < \alpha < 1$. The diffusional resistance (R_w) and the diffusional time constant (τ) are parameters of the Warburg element, resulting from the equation: $Z_w = R_w cth[(\tau i\omega)^{\alpha}] (\tau i\omega)^{-\alpha}$, where when $\alpha = 0.5$ an ideal 45º diffusion line is observed. During the modelling the α parameters are in general fixed.

Charge-discharge experiments of the biosupercapacitors were performed by chronopotentiometric and chronoamperometric measurements in blood-mimicking buffer or human blood. The biocathode was connected as working electrode and the bioanode as combined reference and counter electrode. The discharge was achieved by applying an external resistance, whereas self-charging was performed at open circuit until a constant OCV value was reached. The polarisation curves of the enzymatic fuel cell/bio-supercapacitor were obtained by applying sequential potential pulses in a range starting from the open circuit voltage (OCV) of the system to 0.01 V in 0.05 V intervals, and recording the steady-state current reached at every applied potential.

3.2.7 Materials characterization techniques

3.2.7.1 Scanning electron microscopy (SEM)

SEM images were obtained by using a TM-1000 Tabletop Hitachi microscope.

3.2.7.2 High resolution transmission electron microscopy (HRTEM)

A 200 KV JEOL 2100 transmission electron microscope equipped with an Oxford Instruments EDX analyzer was used for the analyses.

3.2.7.3 X-ray photoelectron spectroscopy (XPS)

XPS measurements were performed in a PECS GmbH with a PHOIBOS 150 9MCD analyser UHV system. Spectra with Mg (group 2) and Al (group 4) at 200 W and 12 kV were obtained. Peak fitting and deconvolution was carried out using CASAXPS 2.3.16Dev52 software using Shirley background, calibrating the spectra to 284.8 eV peak of C1s and using a Gaussian/Lorentzian fit of G/L=30.

3.2.7.4 Optical microscopy

Optical microscopy images were obtained using a NCL-2E long working distance zoom microscope (Union optical Co., Ltd) purchased with an optical magnification from 1.5 to 15x.

4. Results and discussion

4. 1 FTIR study of halides inhibition mechanism on multicopper oxidases

MCOs are inhibited in the presence of some inorganic anions such as cyanide, azide, halides or hydroxyls (Baldrian 2006, Mano and Edembe 2013). Many different studies have been lead in order to understand the different mechanisms behind the MCOs' inhibition processes. EPR studies have shown how azide binds to the T2/T3 site by blocking the catalytic process with a bridging bond between the type 2 and one type 3 copper cations. It was also suggested that a second azide, again, likely bridges the type 3 and type 2 coppers leading to a di-azide bound form (Cole, Clark et al. 1990, Peyratout, Severns et al. 1994). These EPR results have been validated also by other spectroscopy techniques, such as infrared spectroscopy among others, where Cu-N_3 stretching bands were observed around 2035 cm^{-1} and 2056 cm^{-1} for an azide adduct (Sakurai, Takahashi et al. 1996, Hirota, Matsumoto et al. 1998). The inhibition mechanism by halide anions has also been deeply studied, mainly due to the possible physiological applications of multicopper oxidase-based systems in biosensors/biomedical devices (Liu and Dong 2008, Enaud, Trovaslet et al. 2011, Falk, Alcalde et al. 2014, de Poulpiquet, Kjaergaard et al. 2017). EPR studies showed that fluoride interacts mainly with the TNC (Quintanar, Yoon et al. 2005). It is assumed that binding of the F^- to the TNC interrupts intramolecular electron transfer (IET) from the T1 site, abolishing completely the oxygen reduction ability of laccases (Naqui and Varfolomeev 1980) (Xu 1996, Champagne, Nesheim et al. 2013). More unclear is the inhibition mechanism by chloride. It was proposed that halides larger than fluoride cannot reach the TNC site due to the size of laccases' access channel for the substrate (Xu 1996). Furthermore, it has emerged from bioelectrocatalytic studies that in the presence of fluoride ions both direct and mediated electron transfer is fully inhibited, whereas chloride mainly interrupted the mediated one, hinting that fluoride and chloride caused different inhibition mechanisms (Vaz-Dominguez, Campuzano et al. 2008, Beyl, Guschin et al. 2011). Additional spectroscopy studies are indeed needed for clarifying the inhibition mechanism of MCOs by halides. FTIR spectroscopy is a powerful tool for studying structure-function relationship in metallo-enzyme (Wharton 1986), although a FTIR study for halides inhibition is not possible as the stretching modes of Cu-halide are not detectable.

The aim of this chapter of the Thesis is to verify the hypothesis of halides coordination to the MCOs active site by spectroelectrochemistry using azide as active FTIR probe. Two different multicopper oxidases were employed: *Magnaporthe oryzae* bilirubin oxidase (mgBOx) and *T. hirsuta* laccase (ThLc), aiming to evaluate the possible inhibition mechanisms when fluoride or chloride ions interact with the active site of laccase or bilirubin oxidase.

4.1.1 Study of enzyme-N_3 adduct formation

MCOs samples inhibited by azide (mgBOx-N_3 and ThLc-N_3) were prepared as reported in 3.2.2.1 section. In figure 4.1.1.a are shown the FTIR spectra of mgBOx-N_3 recorded from higher to lower redox potentials in a wavenumber range between 2100 and 2000 cm^{-1}, following the procedure reported in 3.2.2.1 section. The presence of at least two different peaks around 2056 and 2049 cm^{-1} is observed. In previous works reported in the literature, these two bands have been assigned to "high affinity azide" bound to MCOs (**b**_N_3) and free azide (**f**_N_3), respectively (Sakurai, Takahashi et al. 1996). When the enzyme is in its resting state, corresponding to the open circuit voltage (OCV) measurement (+300 mV), the presence of these two bands was detected. Upon reducing the potential to +100 mV the peak at 2056 cm^{-1} disappeared and the one at 2049 cm^{-1} was predominant. When oxidizing above +500 mV the peak of **b**_N_3 reappeared and the one of **f**_N_3 totally disappeared at +650 mV. At this redox potential (approximately +850 mV *vs.* NHE) all Cu atoms of the enzyme should be oxidized (Quintanar, Yoon et al. 2005, Quintanar, Stoj et al. 2007), thus these results indicate that azide only binds to the oxidized Cu^{2+} of the T2/T3 site, confirming the previous results reported in literature (Sorrell, O'Connor et al. 1985, Karlin, Cohen et al. 1987). Moreover, the process of binding/dissociation shows reversibility.

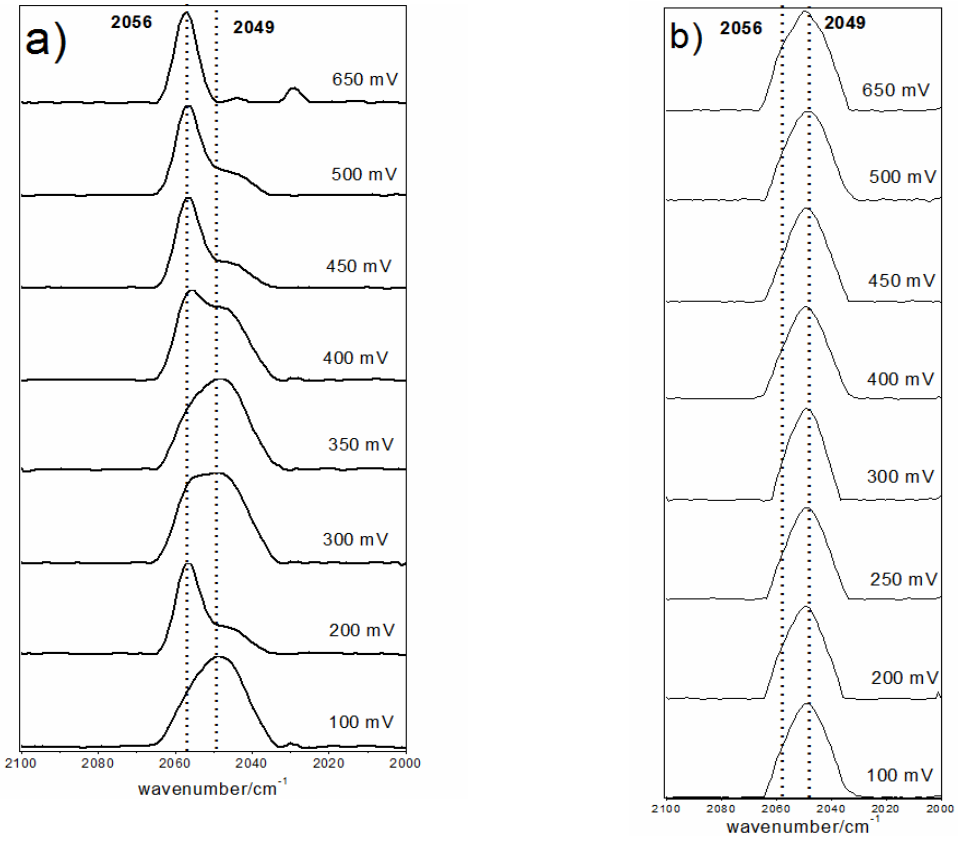

Figure 4.1.1 FTIR spectra of a) mgBOx-N_3 and b) ThLc-N_3 samples recorded at different redox potentials between 100 and 650 mV. The intensity of each spectrum has been normalized.

The same experiment has also been performed for the ThLc-N_3 sample, under the same conditions as reported in 3.2.2.1 section. In this case the two azide bands still appear but not as clear as in the case of mgBOx, due to bands broadening and overlapping (Fig. 4.1.1.b). However, it is still possible to observe that the **f**_N_3 band is predominant at reductive potentials and that **b**_N_3 is not detected, whereas the latter is observed at +500 mV potential or higher as a shoulder.

There are three possible N_3^- binding geometries to di-nuclear Cu complexes:

- terminally coordinated to one Cu;
- μ-1,3-azide bridge between the two Cu;
- μ-1-1-azide bridge between the two Cu.

The first two binding geometries are the most probable if the wavenumbers observed are < 2060 cm^{-1}, while if they are > 2060 cm^{-1} the third one is more likely (Sorrell, O'Connor et al. 1985, Karlin, Cohen et al. 1987, Hirota, Matsumoto et al. 1998). Our results agree with previously reported ones (Sakurai, Takahashi et al. 1996, Hirota, Matsumoto et al. 1998), indicating that the possible binding geometries are the first two. Moreover, Solomon et *al.* have proposed from EPR and UV-Vis spectral studies that azide ions bind in a bridging form between type 2 copper and one of the type 3 coppers (Cole, Clark et al. 1990, Cole, Avigliano et al. 1991). It was observed, in this experiment and all others performed, that the overall intensity of the azide infrared bands decreased upon time regardless of the applied potential. This effect could be due to lack of stability of the enzyme or the azide under the experimental conditions. As a control experiment, FTIR spectra at different potentials of 2.6 mM NaN_3, in 100 mM phosphate buffer pH 6.0, have been recorded in absence of enzyme (Fig. 4.1.2). The presence of only the **f**_N_3 peak is clear at every potential, noticing only a decrease of the peak intensity with time, due to the low stability of the NaN_3 sample. A small peak at approximately 2030 cm^{-1} was detected, which could correspond to degraded azide (Fig 4.1.2).

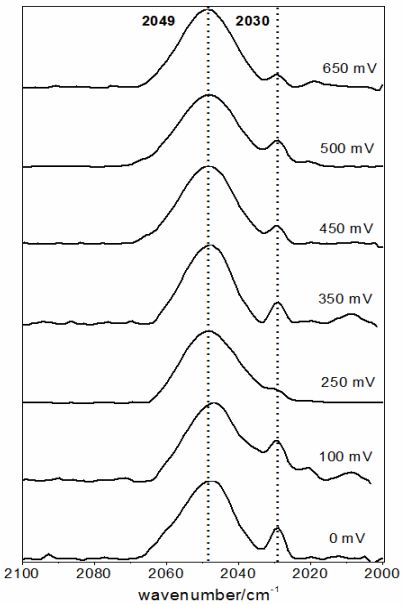

Figure 4.1.2 FTIR spectra of NaN_3 sample recorded at different redox potentials between 0 and 650 mV. The intensity of each spectrum has been normalized.

4.1.2 Effect of halide ions addition

In order to check if the addition of halide ions could affect the binding of N_3 to the active site, and consequently, how halides bind to the active site of multicopper oxidases and how inhibition takes place, NaF or NaCl were added to the enzyme-N_3 samples.

4.1.2.1 Bilirubin oxidase

Fig. 4.1.3.a shows the spectra recorded at different redox potentials for the mgBOx-N_3 sample after the addition of F^- ions. It can be observed that the predominant band is at 2049 cm^{-1}, attributed to **f**_N_3^-.

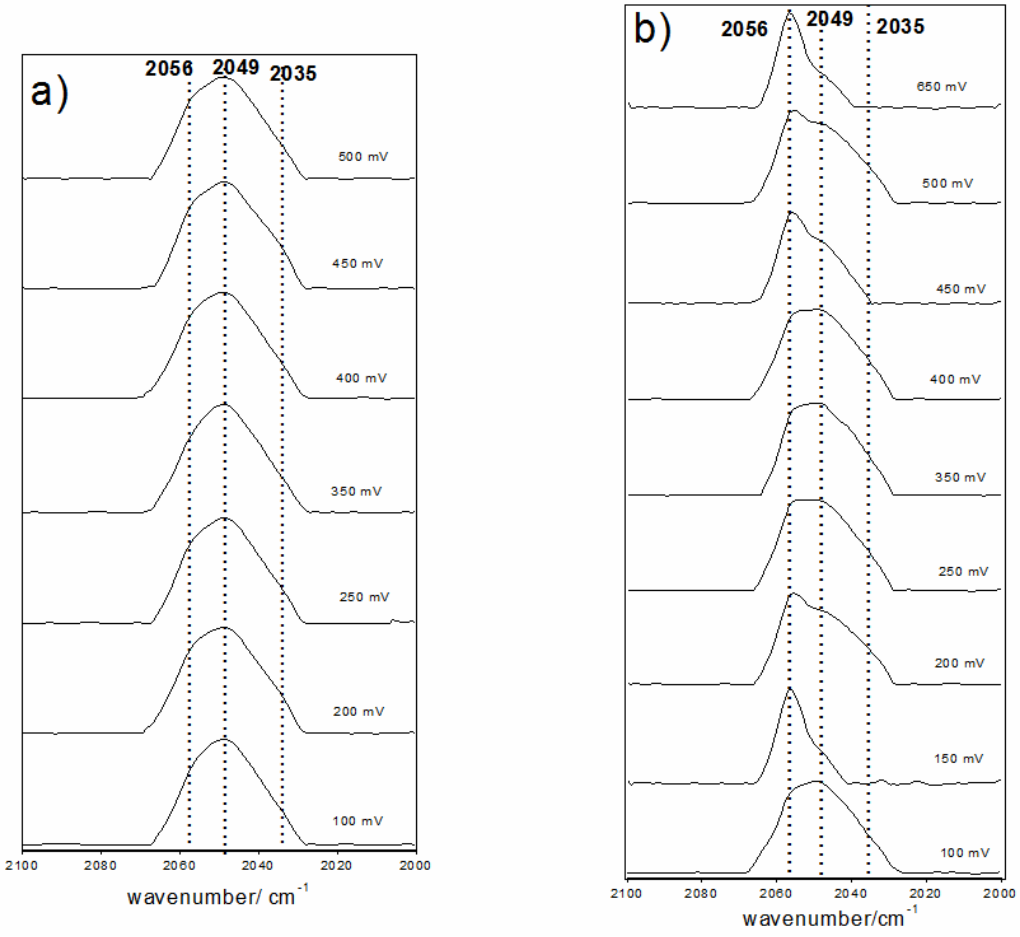

Figure 4.1.3 FTIR spectra for a) mgBOx-N_3-F and b) mgBOx-N_3-Cl sample recorded at different potential between 650-100 mV. The intensity of each spectrum has been normalized.

Changing the potential did not lead to big differences in the spectra and the **b**_N_3 barely appears at +500 mV as a shoulder. This result suggests that fluoride ions bind to the T2/T3 site or very near to it, displacing the binding azide; thus only free azide is observed in the spectra recorded. There are two possible explanations: either the F^- binds to one of the T2/T3 Cu to which azide binds or there is an electrostatic repulsion of azide due to the F^- bound near the T2/T3 site. However, the second explanation is unlikely because the spectroelectrochemical measurements were performed under high ionic strength, which should screen the electrostatic forces. Instead, when Cl^- ions were added to the mgBox-N_3 sample (Fig. 4.1.3.b), the situation changed from the previous case. In presence of Cl^- the **b**_N_3 peak clearly appeared after applying a potential of +500 mV. The band attributed to free azide (2049 cm^{-1}) almost completely disappeared at +650 mV, whereas it was predominant at reductive potentials, except for the spectrum at +150 mV. This discrepant result could be due to a decreased reversibility of the process over time, as it was the last spectrum recorded in this experiment. From these experiments it can be concluded that fluoride competes with azide for the same binding site of mgBOx during inhibition, while chloride does not.

To have a clearer picture of the results obtained with or without halide anions, in Fig.4.1.4 are shown at higher scale the superimposed spectra recorded at +500 mV (oxidizing conditions) for the mgBOx-N_3 sample. Clear differences are observed between the spectra depending on the presence or absence of halides and on which particular anions were added to the sample solution. Indeed, it can be observed the predominance of the **b**_N_3 peak when only N_3^- ions were present, and of the **f**_ N_3 peak when F^- ions were added, whereas an intermediate behavior is observed when Cl^- ions are included.

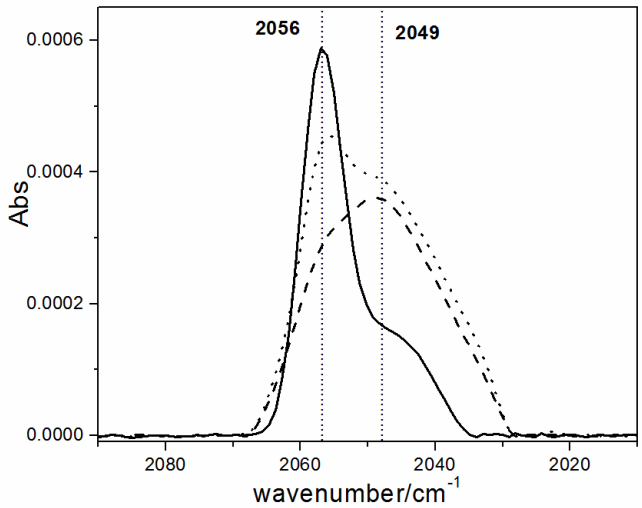

Figure 4.1.4. FTIR spectra recorded at 500 mV for the mgBOx sample when incubated with azide only (solid line), with azide-fluoride (dashed line) or with azide-chloride ions (dotted line).

4.1.2.2 Laccase

The same experiments have been performed for ThLc-N_3, using the same experimental set up described in the 3.2.2.1 section. For laccase could be also observed that F^- ions compete with N_3 for binding at the T2/T3 center, indeed the only peak detected is the one of free azide (**f**_N_3) (Fig. 4.1.5.a). The addition of Cl^- ions led to the presence of the **b**_N_3 band as a shoulder at potential above +500 mV, which is drastically reduced or even absent after applying reductive potentials (Fig. 4.1.5.b).

Nevertheless, it should be noted that the magnified spectra for ThLc-N_3 at 500 mV, with or without halides (Fig.4.1.6) hinder differentiating the two azide bands without any further data elaboration.

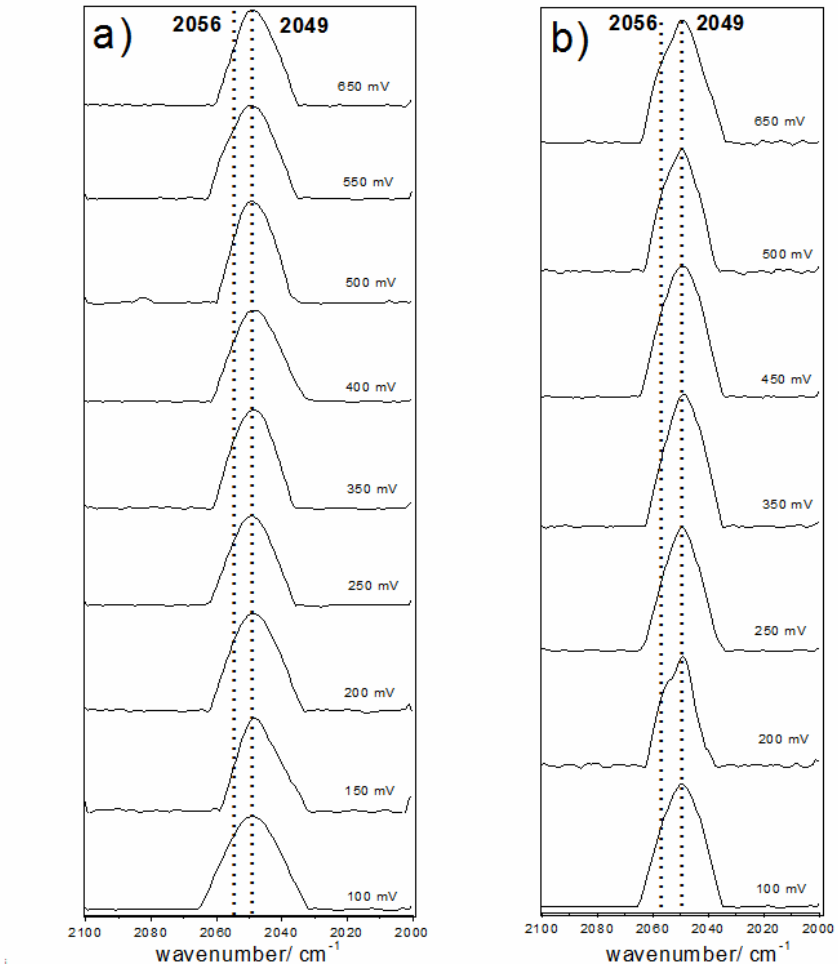

Figure 4.1.5 FTIR spectra for the a) ThLc-N_3-F and b) ThLc-N_3-Cl samples recorded at different redox potentials between 650-100 mV. The intensity of each spectrum has been normalized.

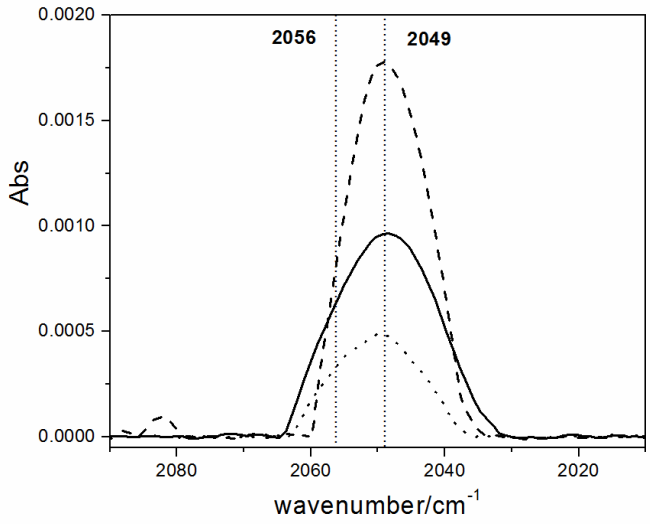

Figure 4.1.6. FTIR spectra recorded at 500 mV for the ThLc sample when incubated with only azide (solid line), with azide-fluoride anions (dashed line) or with azide-chloride anions (dotted line).

4.1.3 Data elaboration

In many of the FTIR spectra measured the two azide bands are not well resolved. Therefore, the bands were deconvoluted using a Gaussian fitting model, which was performed for each spectrum (Fig. 4.1.7, 4.1.8, 4.1.9, 4.2.10, 4.1.11, 4.1.12). The deconvolution allowed to confirm the presence of only two bands for the mgBOx-N_3 sample (Fig. 4.1.7) with the addition of a third weak band around 2035 cm^{-1} for the mgBOx-N_3-F and mgBox-N_3-Cl samples (Fig. 4.1.8 and 4.1.9). The deconvolution allows visualizing the peak of **b**_N_3 for the ThLc-N_3 sample (Fig. 4.1.10) and its absence when fluoride was added (Fig. 4.1.11). Moreover, additional peaks are observed for the ThLc-N_3-Cl sample (Fig. 4.1.12), including the one around 2035 cm^{-1} already observed for mgBOx samples.

The deconvolution process confirmed that the bilirubin oxidase/azide FTIR spectra are less affected by chloride anions than laccase, confirming previous works that indicate that mgBOx is less inhibited by chloride than laccases (Durand, Gounel et al. 2012). Indeed, for the mgBOx-N_3-Cl sample (Fig. 4.1.9) the contribution of the band attributed to free azide (2049 cm^{-1}) to the FTIR spectrum is lower if compared to that for the ThLc-N_3-Cl sample (Fig. 4.1.12), suggesting that chloride anions interact more with the T2/T3 site in ThLc than in mgBOx.

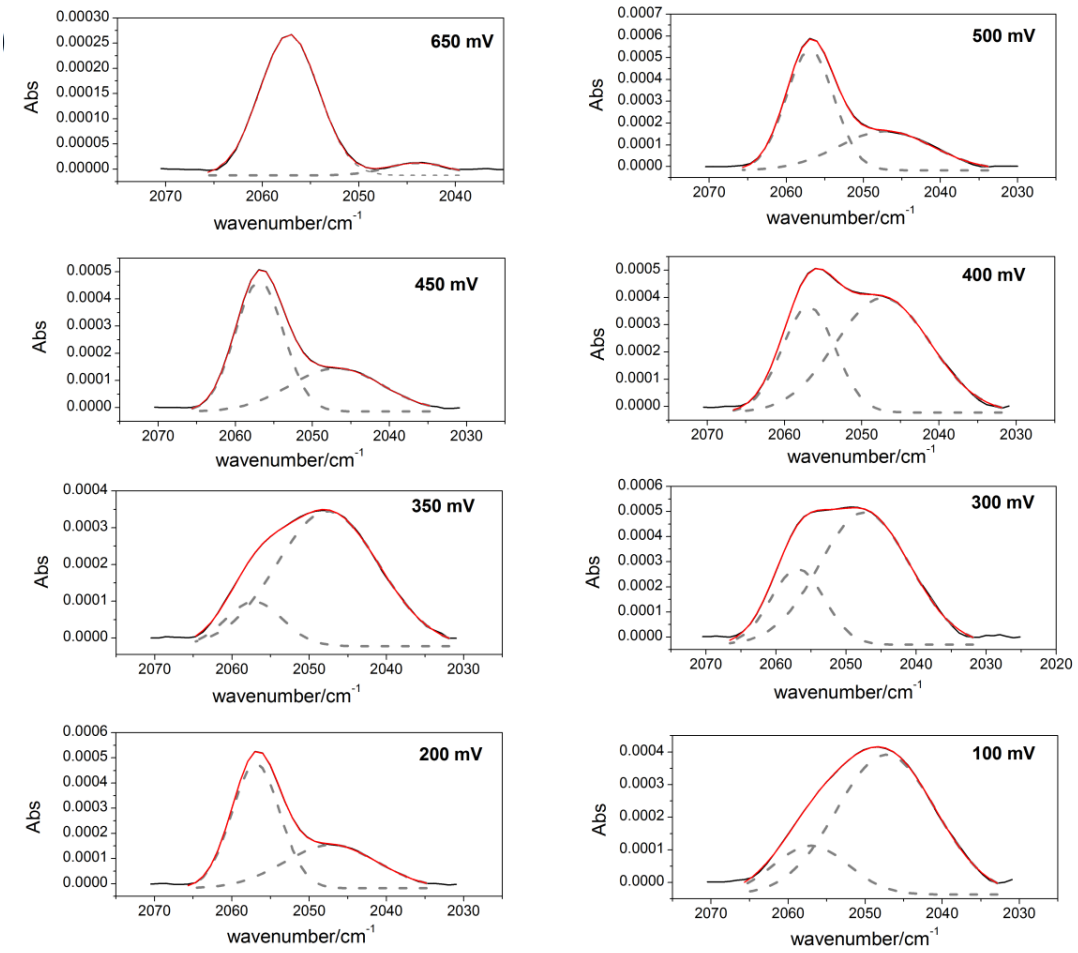

Figure 4.1.7 FTIR spectra for mgBOx-N_3 sample recorded at different redox potentials. In each spectrum the black line represents the experimental data, the hatched grey lines are the deconvoluted bands and the red ones are the total curves obtained by the sum of each component.

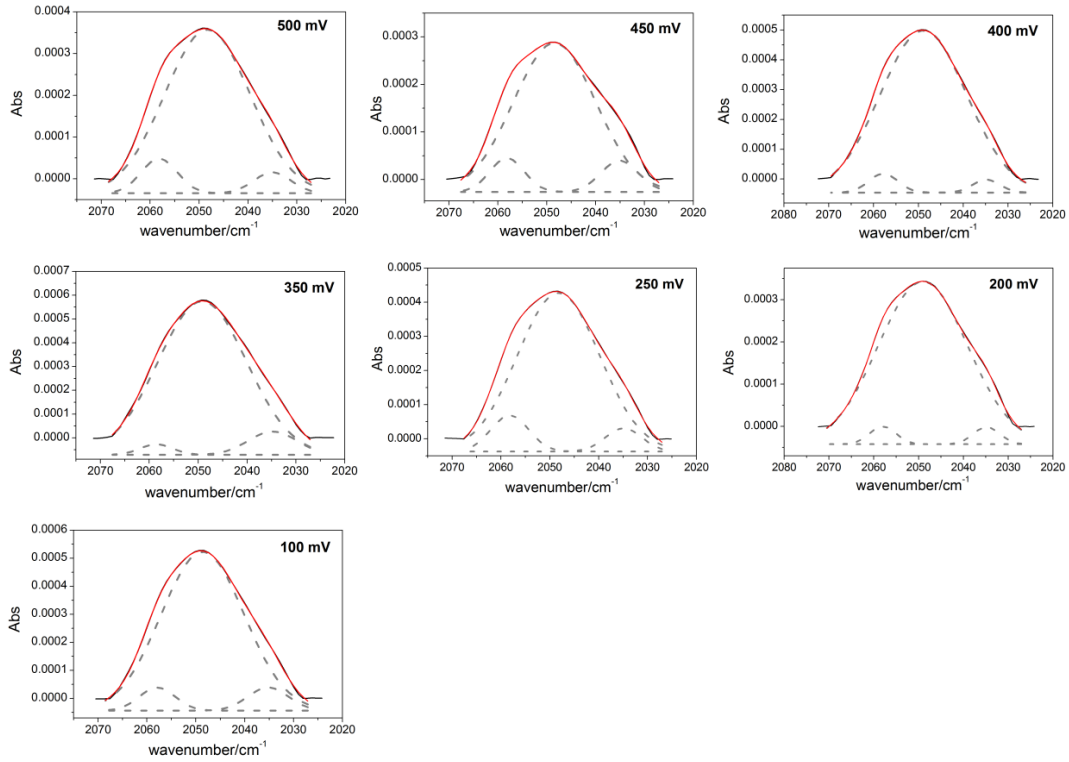

Figure 4.1.8 FTIR spectra for mgBOx-N_3-F sample recorded at different redox potentials. In each spectrum the black line represents the experimental data, the hatched grey lines are the deconvoluted bands and the red ones are the total curve obtained by the sum of each component.

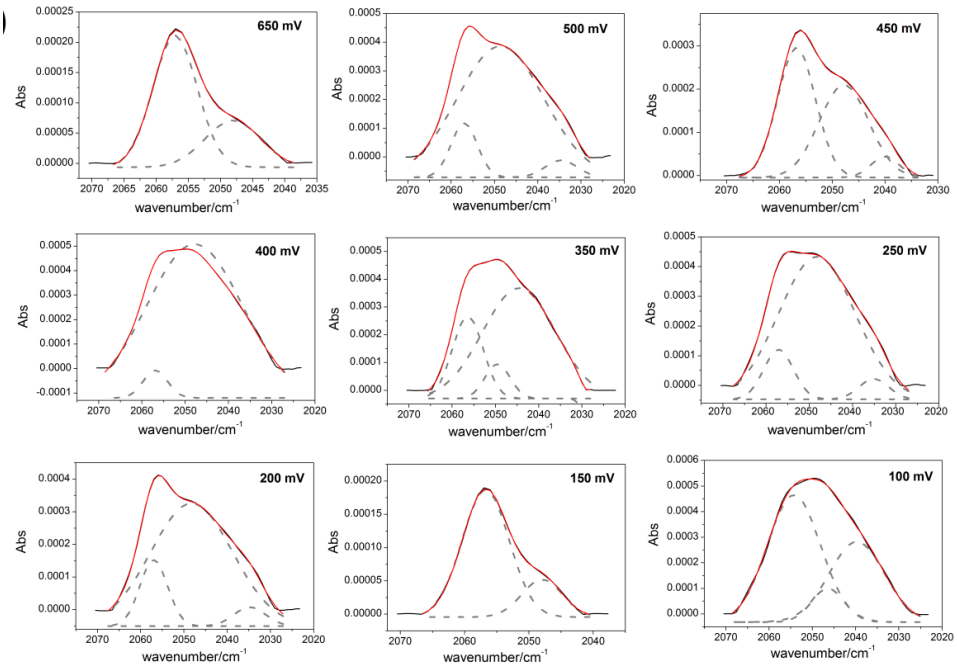

Figure 4.1.9 FTIR spectra for mgBOx-N_3-Cl sample recorded at different redox potentials. In each spectrum the black line represents the experimental data, the hatched grey lines are the deconvoluted bands and the red ones are the total curves obtained by the sum of each component.

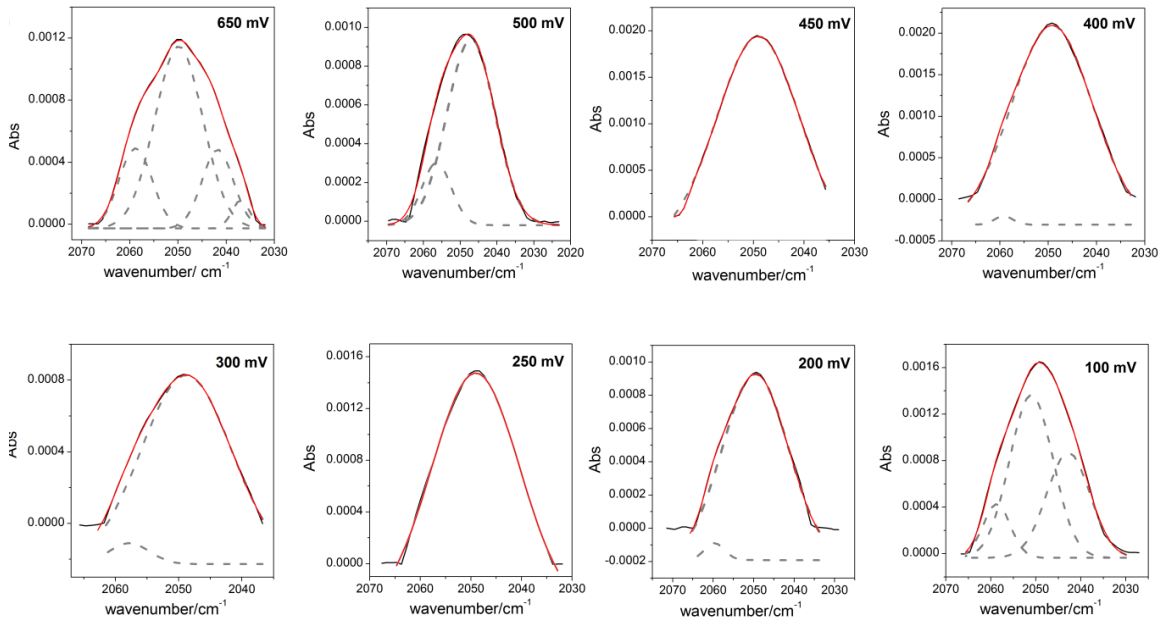

Figure 4.1.10 FTIR spectra for ThLc-N_3, sample recorded at different redox potentials. In each spectrum the black line represents the experimental data, the hatched grey lines are the deconvoluted bands and the red ones are the total curves obtained by the sum of each component.

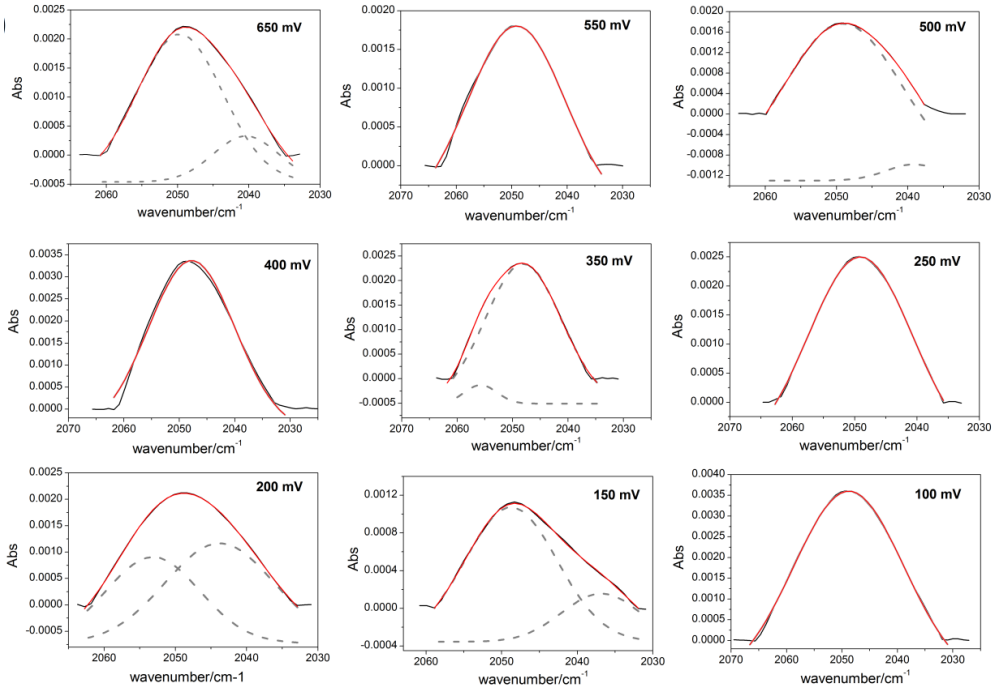

Figure 4.1.11 FTIR spectra for ThLc-N_3-F sample recorded at different redox potentials. In each spectrum the black line represents the experimental data, the hatched grey lines are the deconvoluted bands and the red ones are the total curves obtained by the sum of each component.

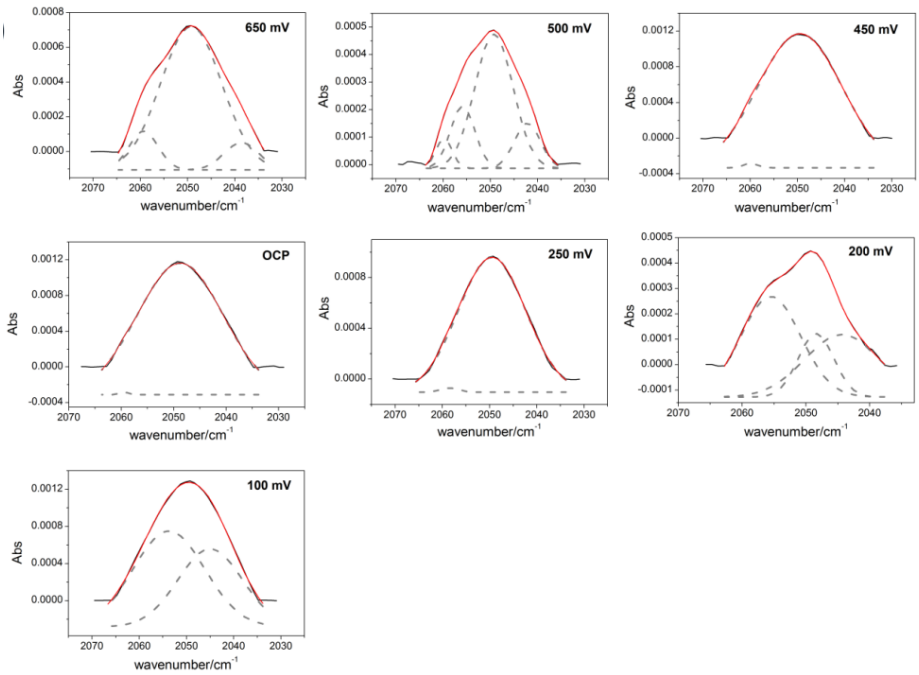

Figure 4.1.12 FTIR spectra for ThLc-N_3-Cl sample recorded at different redox potentials. In each spectrum the black line represents the experimental data, the hatched grey lines are the deconvoluted bands and the red ones are the total curves obtained by the sum of each component.

4.1.4 Conclusions

A FTIR spectroelectrochemical study about the possible coordination modes of azide to mgBOx and ThLc enzyme has been performed, confirming previous results present in literature (Sakurai, Takahashi et al. 1996, Hirota, Matsumoto et al. 1998). Furthermore, different behavior is observed upon addition of fluoride or chloride ions to the sample solution for both multicopper oxidases tested using azide as an infrared probe. Fluoride ions compete with azide for binding at one of the T2/T3 Cu atoms, whereas chloride ions do not or only do it partially. Indeed, it was reported that most likely F^- ions interact with T2/T3 center of multicopper oxidase blocking the intramolecular electronic transfer from the T1 site to the Cu cluster (Naqui and Varfolomeev 1980, Champagne, Nesheim et al. 2013). This could explain why for laccase or bilirubin oxidase based biocathodes both direct and mediated electron transfers were abolished after fluoride anions addition (Vaz-Dominguez, Campuzano et al. 2008, Salaj-Kosla, Poller et al. 2013). In those experiments reported in the literature the addition of chloride anions suppressed predominantly the mediated electron transfer but not the direct transfer, suggesting that chloride anions block the access of the e^- donor to the T1 site but cannot reach the T2/T3 site as fluoride anions do, due to steric impediment of the larger chloride ions than fluoride ones (Naqui and Varfolomeev 1980, Xu 1996, Vaz-Dominguez, Campuzano et al. 2008). However, in the case of laccases a double site binding process cannot be excluded (Champagne, Nesheim et al. 2013), in which may Cl^- may bind in some enzyme molecules to or near the TNC site in addition to the T1 pocket binding.

4. 2 Immobilization of new laccase mutants on macroporous gold for developing DET-based biocathodes

Gold has always been a preferred material for electrochemistry due to its high conductivity, its high resistance against corrosion and biocompatibility. Numerous studies have been performed using gold, nanoporous gold or nanostructured gold (as AuNPs, etc..) as support material for the fabrication of bioanodes and biocathodes (Pita, Gutierrez-Sanchez et al. 2011, Gutierrez-Sanchez, Pita et al. 2012, Luckarift, Ivnitski et al. 2012, Salaj-Kosla, Pöller et al. 2012, Salaj-Kosla, Poller et al. 2013, Siepenkoetter, Salaj-Kosla et al. 2017). Recently the fabrication of highly ordered macroporous materials has attracted great interest due to a large number of applications (Walcarius 2010, Reculusa, Heim et al. 2011); indeed, macroporous structures provide higher surface area than their flat homologues that make them good materials for biosensor or biofuel cell applications (Szamocki, Reculusa et al. 2006, Deng, Wang et al. 2008). These electrodes could be miniaturized and so be applicable also *in vivo* applications (Cadet 2015).

On the other hand, the development of direct electron transfer-based bioelectrocatalytic systems is challenging due to the structural complexity of the bio-element, the aim to achieve enough stability through protein immobilization, while maintaining the biological function under the operational conditions, and to the required control of the molecular orientation for optimizing direct electron transfer (Pia, Chi et al. 2011). Protein engineering allows palliating these challenges through rational changes in the amino acid sequence. Site directed mutagenesis is employed in this approach to replace an external aminoacid with easy-to-link residues, such as cysteine, on a specific position (Song, Clark et al. 1993, Alcalde 2010). In order to enable direct electron transfer between multicopper oxidases and the electrode the common approach is to favor that the T1 site of the protein faces the electrode surface (Shleev, Tkac et al. 2005).

The goal in this section of the Thesis has been to study the immobilization of laccase mutants, with cysteine substitutions near the access channel to the T1 site, on macroporous gold electrodes as DET-based biocathodes. The mutants have been prepared in collaboration with Ivan Mateljak from Dr. Miguel Alcalde´s group (ICP-CSIC, Madrid). The cysteine substitution was chosen in order to obtain oriented immobilization of the laccase mutants on the gold surfaces, either directly by Au-Cys chemisorption or by specific covalent bonds of the Cys residues with the chemically functionalized gold surface. In collaboration with Prof Dr. Alexander Khun and Dr. Nicolas Mano ((Bordeaux University-CNRS), macroporous gold (MG) electrodes have been fabricated, and tested as a high surface area support for the fabrication of DET-based laccase biocathodes. Three different modification strategies of the gold surfaces have been tested.

Part of the results shown in this section has been done during a 1-month secondment in the laboratory of Drs. Kuhn and Mano (Bordeaux University-CNRS).

4.2.1 Production and characterization of laccase mutants

Two different cysteine laccase variants have been prepared by site directed mutagenesis of the 7D3 parental type laccase. 7D3 laccase was obtained from ChU-B mutant with one stability mutation on the protein surface. ChU-B mutant is a blood tolerant laccase engineered after 2 mutations in the protein sequence of OB-1, another mutant obtained by directed evolution of PM1 laccase (wild type) in Dr. Alcalde´s group (Mate, Gonzalez-Perez et al. 2013). Indeed, an evolution of ChU-B mutant was chosen as starting point for the development of these laccase variants precisely due to its partial activity in physiological conditions. In these two cysteine laccase variants, named as S264C and S387C, a serine residue has been substituted with a cysteine in positions 264 and 387 of the protein sequence, respectively. These two positions have been selected as they are placed close to the T1 site, at 12.4 Å and 12.2 Å respectively (Fig. 4.2.1), in order to promote the correct orientation of these mutants for achieving direct electron transfer with the electrode.

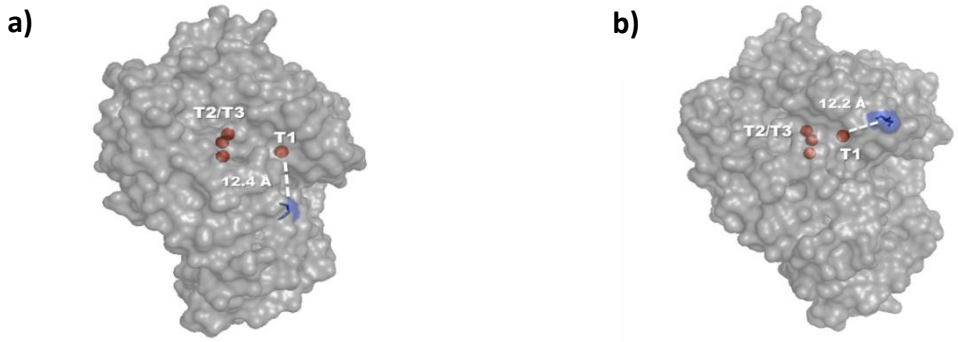

Figure 4.2.1 Schematic representation of a) S264C and b) S387C mutants. Copper ions are shown as red spheres and the mutation as blue stick.

The two variants S264C and S387C and the parental type 7D3 have been produced and purified as reported in 3.1.2.1 section. Figure 4.2.2 shows the SDS-polyacrylamide gels obtained at the end of the purification process (after the HPLC step, section 3.1.2.1).

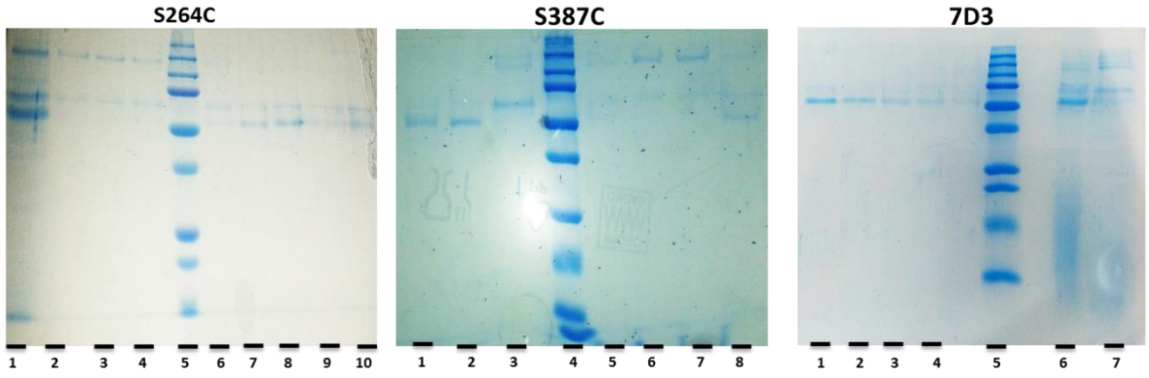

Figure 4.2.2 SDS-PAGE of the purified laccase mutants. S264C lines: 1 is FPLC fraction; 2 to 4 and 6 to 10 are HPLC fractions; 5 is protein ladder. S387C lines: 1 to 3 and 5 to 8 are HPLC fractions; 5 is protein ladder. 7D3 lines: 1 to 4 and 6 to 7 are HPLC fractions; 5 is protein ladder.

In the case of the S264C mutant the gel showed two close bands in the fractions from 7 to 10, which represent the pure protein. The appearance of two bands is due to the existence of two laccase glycoforms. These two glycoforms were not further separated to avoid further loss of enzyme as their properties are very similar. The presence of two glycoforms was detected also for the other two mutants. In the case of S387C mutant the fractions of pure protein are 1 and 2. The fractions from 1 to 4 are considered the pure ones in the case of 7D3-parental type laccase. The pure fractions were pooled and concentrated, as described in 3.1.2.1 section.

The concentration and the specific activity of the laccase mutants were determined following the procedure reported in 3.2.1 section. Table 4.2.1 shows that the concentration values were very similar for all the produced enzymes. However, the concentrations obtained were not so high due to the production in *S. cerevisae*, whose secretion levels are always low and also because basidiomycete laccases are expressed at a lower rate than others laccases (Mate, Gonzalez-Perez et al. 2013). Furthermore, there was not a considerable loss of activity after the mutation in comparison with the 7D3 parental type. Another contribution to the activity loss when compared to the wild type laccase (PM1), is that the directed evolution process may convey an activity decrease (Mate and Alcalde 2015). Although these mutants were obtained by mutating ChU-B mutant, a blood tolerant laccase, these variants were not so active at physiological conditions; the mutants retained ~10 % of their initial activity at physiological pH with ABTS as substrate.

	S264C	S387C	7D3
Concentration (mg/mL)	2.75	2.79	2.75
Activity (U_{ABTS}/mL)	151	97	134

Table 4.2.1 Concentration and activity values at pH 4.2 obtained for the laccase mutants.

Kinetic measurements were also performed, as described in 3.2.1 section. All the results were obtained at pH 4.0 using ABTS as substrate and are reported in Table 4.2.2. It can be concluded that upon the directed evolution process the turnover numbers (k_{cat}) decreased in comparison with the parental type, as also did the catalytic efficiency (k_{cat}/K_m). This decreasing trend had already been observed in earlier direct evolution stages when the kinetic parameters of PM1 wild type and OB-1 and ChU-B mutants were compared (Maté, García-Burgos et al. 2010, Mate, Gonzalez-Perez et al. 2013).

	S264C	S387C	7D3
K_m (mM)	0.076 ± 0.002	0.048 ± 0.002	0.057 ± 0.002
K_{cat} (s^{-1})	64.4 ± 0.4	47.9 ± 0.6	100.4 ± 0.8
k_{cat}/K_m (mM^{-1} s^{-1})	845	998	1761

Table 4.2.2 Comparison of the kinetic parameters of the laccase mutants produced.

4.2.2 Characterization of macroporous gold (MG) electrodes

The macroporous gold (MG) electrodes fabricated in Bordeaux University, as reported in section 3.2.4.3, were cut in order to observe the thickness and the morphology of the material by SEM technique. Figure 4.2.3 shows clearly the presence of a porous structure. Macroscopic pores organized in a highly ordered and compact arrangement are visible, and it can also be appreciated that pores of two consecutive layers are well-connected to each other (Fig. 4.2.3.b). The sample seems homogeneous over the large distance and the thickness of the electrodeposited layer can be measured easily as the original wire support is still visible (Fig. 4.2.3.b).

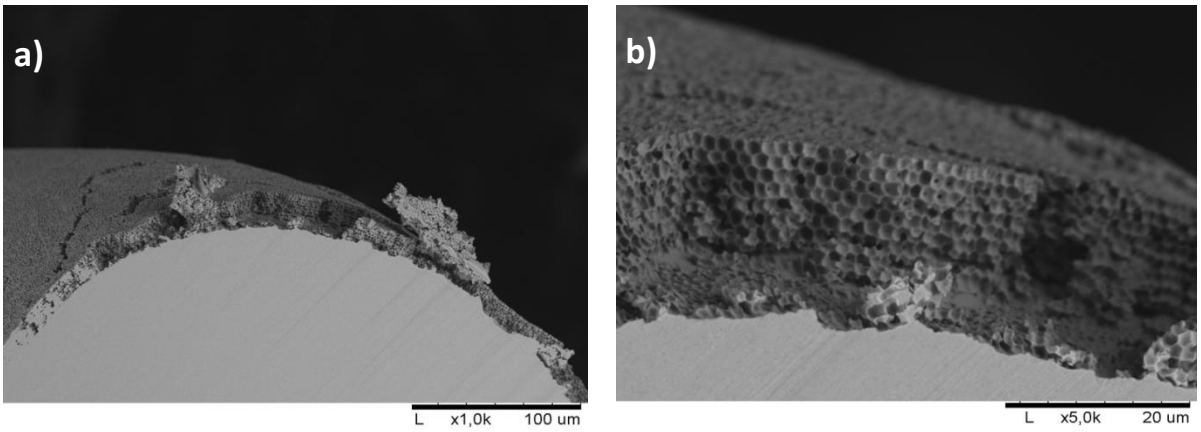

Figure 4.2.3 SEM images of a macroporous gold electrode cross-section at a) x1000 and b) x5000 magnification.

MG electrodes were characterized electrochemically by cyclic voltammetry in 0.1 M H_2SO_4 and compared with unmodified gold wire (GW) electrodes, as shown in Fig. 4.2.4. The CVs show two broad oxidation peaks at 1.2 and 1.4 V attributed to the formation of Au surface oxides (Trasatti and Petrii 1991), and a reductive peak centered at 0.85 V directly proportional to the active surface of the electrodes. Fig. 4.2.4 shows that the intensity of the oxidation and reduction processes increased greatly when a MG electrode is used (solid line) instead of a GW (dashed line). The active surface area was determined by integration of the gold oxide reduction peak, taking into account a charge density of 482 $\mu C/cm^2$ for the reduction of a gold oxide monolayer (Oesch and Janata 1983). The integrated charge yields active surface area values of 0.2 cm^2 and 1.6 cm^2 for GW and MG of 7.5 layers, respectively. These values are in good agreement with earlier reported ones for the same kind of electrodes (Reculusa, Heim et al. 2011).

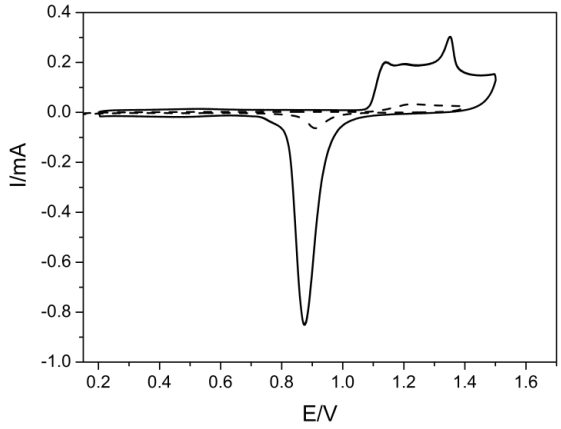

Figure 4.2.4 Cyclic voltammograms obtained for a macroporous gold electrode of 7.5 layers (solid curve) and bare gold wire electrode (dashed curve) recorded in 0.1 M H_2SO_4, at 100 mV/s. The 30^{th} scan is represented.

4.2.3 Functionalization of gold surfaces for Lc mutants immobilization

Three different functionalization strategies have been studied for the further covalent immobilization of laccase mutants, following the procedures described in 3.2.5.3.1 section:

- 1,4-dithiothreitol (DTT) was co-adsorbed with the protein to yield a mixed monolayer on the gold electrode (Pia, Chi et al. 2011);
- The gold electrodes were first functionalized with a 1,4-benzenedithiol (BT) monolayer and then incubated in the enzyme solution (Xiao, Patolsky et al. 2003);
- Maleimide was used as linker, which specifically reacts with the inserted cysteine residues of the Lc mutants(Sinz 2006). First the gold electrodes were modified with a mixed monolayer of mercaptopropionic acid (MPA) and 6-mercapto-1-hexanol (MH), then a covalent bond between the carboxylic groups of the electrode surface and the amino group of maleimide were formed by carbodiimide coupling; and finally the modified electrodes were incubated in the enzyme solution.

Gold wire (GW) and macroporous gold (MG) electrodes of 7.5 layers have been used, after their careful cleaning (section 3.2.4.3), as support for the chemical functionalization and further immobilization of the enzymes, and finally tested for O_2 electroreduction. This work was done in collaboration with Magdalena Murawska under the supervision of Dr. Mano and Prof. Dr. Kuhn from Bordeaux University-CNRS.

4.2.3.1 DTT strategy

DTT has been used as reducing agent to prevent the formation of protein dimers in solution via disulfide bonds and as surface diluent to generate isolated protein molecules on the electrode (Pia, Chi et al. 2011). DTT may be used together with laccase mutants to form a mixed thiol self-assembled monolayer (SAM) on the gold surface by the formation of Au-S bonds.

4.2.3.1.1 Study of the thiol self-assembled monolayer (SAM) formation

A study of the formation of the DTT SAM prior to enzyme immobilization was carried out. GW and MG electrodes were both incubated overnight at 4 ºC in a DTT solution (45 µM), afterwards the SAM formation was studied by: (i) CV in the presence of FeMeOH as redox probe, as described in 3.2.6 section; (ii) by CV in 0.5 M NaOH to monitor the thiol reductive desorption that takes place in the -0.8 and -1.2 V range. The CVs (Fig. 4.2.5.a and b) showed SAM formation on both gold surfaces as the capacitive current and intensity of the probe´s redox waves decreased compared with the bare electrode. However, the DTT coverage on the electrodes was probably not complete due to the molecule´s low size, which is not ideal for the formation of a compact SAM, and low concentration used (Troughton, Bain et al. 1988). When the reductive desorption was performed (Fig. 4.2.5.c and d), a reductive peak is barely observed around -0.8 V in the case of the GW electrode, whereas in the case of MG two reductive peaks are clearly observed at -0.9 and -1.09 V. Two peaks are observed probably because DTT is a dithiol and so can form two Au-S bonds with the gold surface. These peaks decreased and almost disappeared by increasing the number of reductive scans, but also phenomena of partial re-adsorption and re-desorption have been observed (data no shown) (Hager and Brolo 2003, Mezour, Perepichka et al. 2015). The reductive peak at -1.2 V observed for both GW and MG electrodes could be attributed to protons reduction at the bare gold zones. From the integration of the reductive peaks observed in the first scan it is possible to estimate the thiols coverage as the electroactive area of the electrodes is known (above section). A DTT coverage of $2.78 \cdot 10^{-10}$ mol cm^{-2} on MG was determined, which is quite small compared to other thiol SAMs on gold surfaces (see below), but expected for a small chain and polar thiol (Troughton, Bain et al. 1988). Nevertheless, it must be taken into account that the porous structure of MG electrode makes more difficult the diffusion and subsequent formation of SAM of thiols molecules inside all the structure. Being a concave structure it may also happen that bridging dithiols are more stable and can "jump" some gold atoms, blocking part of the surface.

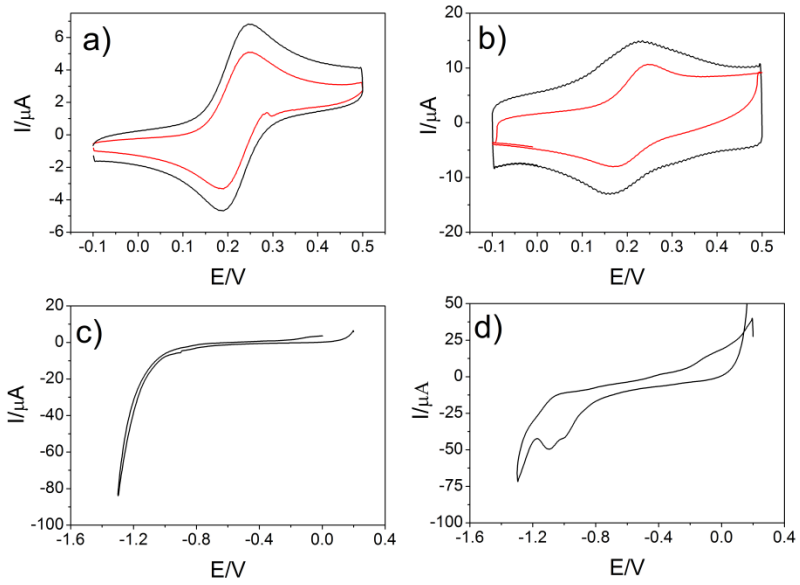

Figure 4.2.5 (a-b) CVs recorded at 50 mV/s in presence of 0.2 mM FeMeOH in 0.1 M KCl for a) GW and b) MG electrodes. The black curves represent bare electrodes and the red curves DTT-modified ones. (c-d) CVs recorded in 0.5 M NaOH at 100 mV/s under deoxygenated conditions for c) DTT-GW and d) DTT-MG electrodes. The 1st scan is represented.

4.2.3.1.2 Electrocatalytical response to O_2 reduction

MG and GW electrodes modified with a mixed monolayer of DTT and laccase cysteine variants have been tested as biocathode for O_2 reduction by cyclic voltammetry (Fig. 4.2.6) in acidic buffer. When the S264C mutant was immobilized (Fig. 4.2.6. a-b) no catalytic current was measured at the expected potential for a high-redox potential laccase, which should be around 0.6 V vs. Ag/AgCl (Shleev, Morozova et al. 2004, Shleev, Tkac et al. 2005). Moreover, when GW was used as support (Fig. 4.2.6.b) a reductive wave starting at around 0.3 V was measured, which may be attributed to direct O_2 reduction on Au, suggesting that the gold surface is not completely covered and acts as catalyst, or that only T2/T3 site is facing the electrode and H_2O_2 is produced, as already reported for laccases on bare gold electrodes (Pita, Shleev et al. 2006). The same behavior was observed also when S387C was used as biocatalyst (Fig. 4.2.6.d). However, when MG was used as support a very low catalytic current is observed with an onset at c.a. 0.6 V, in addition to a peak at ~0.19 V (Fig. 4.2.6.c), slightly shifted in comparison with the peak observed when GW is used as support. The same behavior than S387C was noticed when the parental type 7D3 was immobilized on the electrode surface (Fig. 4.2.7.a), suggesting that in both cases an unspecific binding of the enzymes on gold surface occurred. A clear catalytic current was not observed with this strategy whatever mutant was used. Addition of ABTS as redox mediator, also in very low concentration, did not lead to any improvement in the catalytic response, and only the redox signal of the mediator was detected (data no shown).

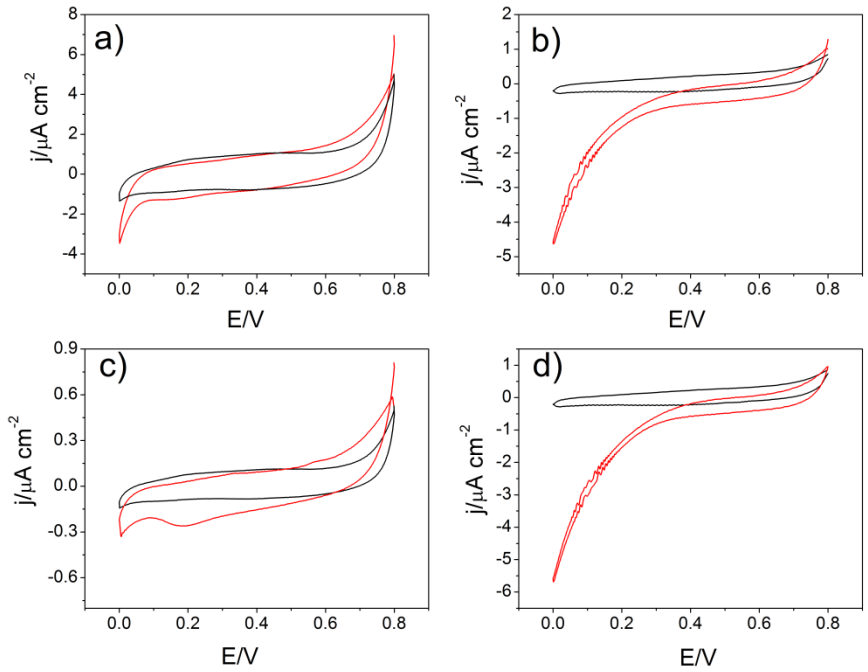

Figure 4.2.6 CVs recorded at 10 mV/s in 50 mM acetate buffer pH 4.2 containing 100 mM $NaClO_4$ at RT under N_2 (black curves) and O_2 (red curves) saturated conditions for a) S264C-DTT-MG, b) S264C-DTT-GW, c) S387C-DTT-MG and d) S387C-DTT-GW electrodes. The 2nd scan is represented.

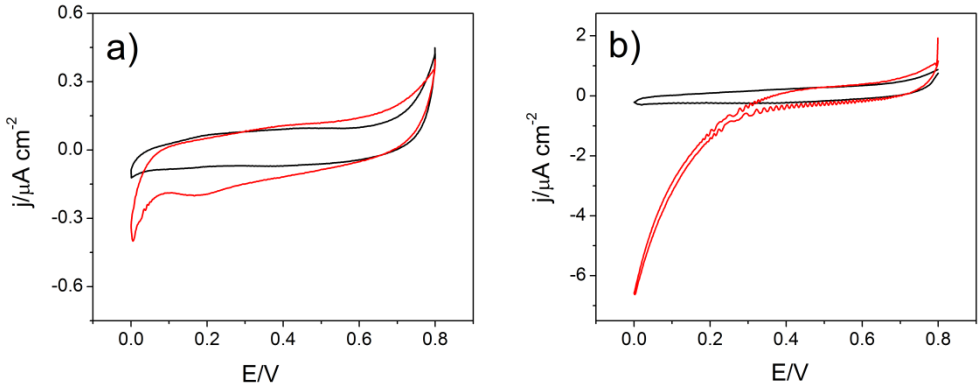

Figure 4.2.7 Cyclic voltammograms at 10 mV/s recorded in 50 mM acetate buffer pH 4.2 containing 100 mM $NaClO_4$ at RT under N_2 (black curves) and O_2 (red curves) saturated conditions for a) 7D3-DTT-MG and b) 7D3-DTT-GW electrodes. The 2nd scan is represented.

As very low catalytic currents were detected for O_2 reduction, one reason could be that the enzymes were not chemisorbed to the gold surface. To verify this hypothesis, the modified macroporous electrodes with DTT/laccase monolayer were submitted to a reductive desorption process by performing CVs in 0.5 M NaOH. In Fig. 4.2.8 are shown the first scans obtained. The reductive peak at -1.1 V previously attributed to the desorption of DTT (Fig. 4.2.8.d) appeared for all the electrodes. Furthermore, a second peak is present at -0.7 V that could be attributed to the desorption of amine groups, as the potential is too high for thiol desorption (Clarke, Jandik et al. 1999). This peak probably corresponds to enzyme molecules adsorbed on the gold surface by its lysine groups or other amino acids (such as histidines or asparagines). Indeed, this second peak is detected also when the parental

type was immobilized, supporting the hypothesis of amines desorption instead of thiols, as 7D3 parental type was not mutated with a cysteine near the T1 site.

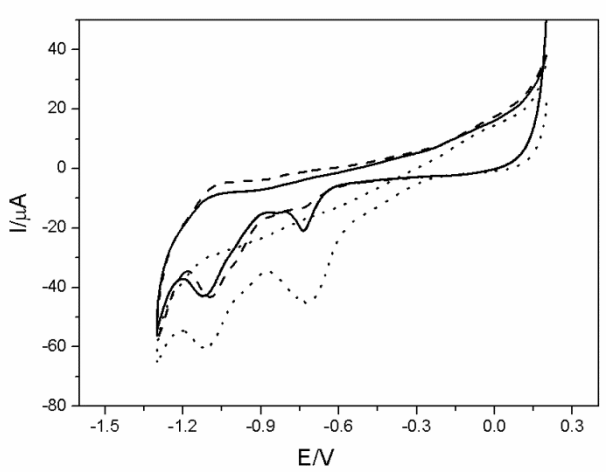

Figure 4.2.8 CVs recorded in 0.5 M NaOH at 100 mV/s under deoxygenated conditions for 7D3-DTT-MG (solid line), S264C- DTT-MG (dotted line) and S387C-DTT-MG (dashed line) electrodes. The 1st scan is represented.

4.2.3.2 1,4-Benzodithiol (BT) strategy

This strategy concerned the formation of a more compact monolayer, due to the π-π interactions between the aromatic rings. In this way the direct adsorption on the bare gold of the enzyme and its denaturation should be avoided. Moreover, BT was chosen as molecule for the formation of the self-assembled monolayer in order to facilitate the electron tunneling process from the enzyme to the electrode surface, thanks to the presence of an aromatic group (Xiao, Patolsky et al. 2003, Abad, Gass et al. 2009).

4.2.3.2.1 Study of thiol self- assembled monolayer formation

An initial study of the BT monolayer self-assembly was performed, as reported above. A clear decrease of the peak intensities of the redox probe CV signal was detected (Fig. 4.2.9.a-b, blue curves) compared to the bare surface one (black curves), which indicates a more compact monolayer than the DTT SAM described in the previous section. The decrease in capacitive current is also very evident and in agreement with a compact thiol SAM formation (Troughton, Bain et al. 1988). A clear reductive peak at ~-1.0 V is observed for the desorption process in basic medium with both GW and MG electrodes; MG yielded a higher peak current due to its larger active surface area. The thiols' coverage for the MG electrode was $1.19 \cdot 10^{-9}$ mol cm^{-2}, which corresponds approximately to a compact monolayer of aromatic thiols (Abad, Gass et al. 2009, Rüdiger, Gutiérrez-Sánchez et al. 2010) and is an increase of one order of magnitude when compared with the DTT SAM.

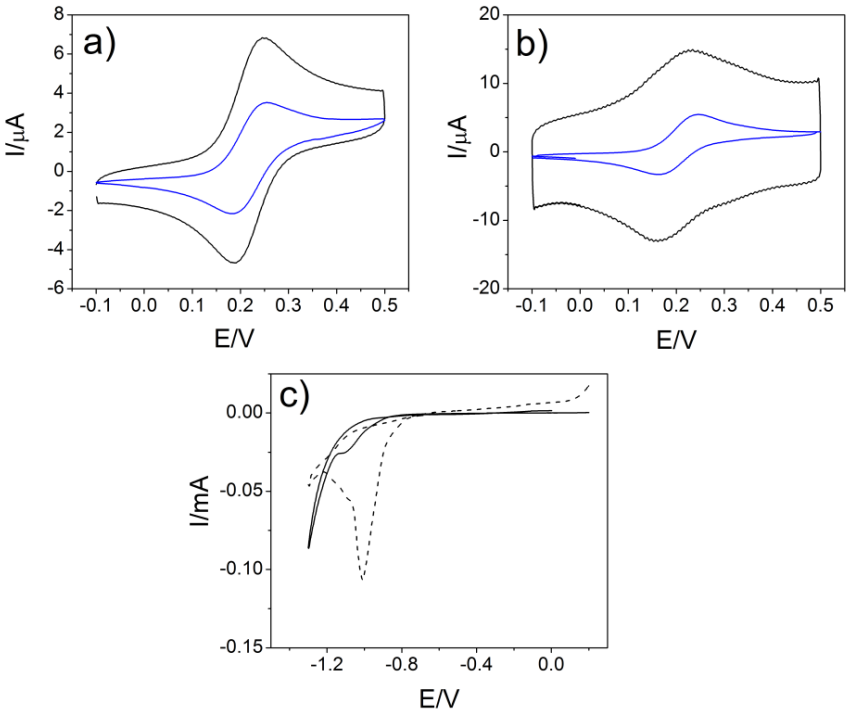

Figure 4.2.9 (a-b) CVs recorded in presence of 0.2 mM FeMeOH in 0.1 M KCl for a) GW and b) MG electrodes. Black curves represent bare electrodes and blue curves BT-modified ones. c) CVs recorded from in 0.5 M NaOH at 100 mV/s under deoxygenated conditions for BT-GW (solid line) and BT-MG (dashed line) electrodes. The 1st scan is represented.

4.2.3.2.2 Electrocatalytical response to O_2 reduction

Lc-BT-MG and Lc-BT-GW electrodes have been tested for the electrochemical reduction of O_2 by cyclic voltammetry in acetate buffer pH 4.2. Figure 4.2.10 shows the voltammograms obtained under O_2 saturated conditions for S264C-BT-MG (a), S387C-BT-MG (b) and 7D3-BT-MG (c) electrodes[2]. However, no catalytic current was registered for BT-modified MG modified with any of the laccase mutants (Fig. 4.2.10). Addition of ABTS as redox mediator, also in very low concentration, did not lead to any improvement in the catalytic response, and only the redox signal of the mediator was detected (data no shown).

Surface modification of gold electrodes with BT yielded worse results than with DTT for laccase mutants' immobilization. An explanation may be that very few enzyme molecules manage to form S-S bonds with the BT monolayer.

[2] The curves obtained with Lc-BT-GW electrodes are not reported since some technical problems have been come out during the experiments and not reliable signals have been obtained. Repetition of this experiment was not possible due to lack of purified enzymes.

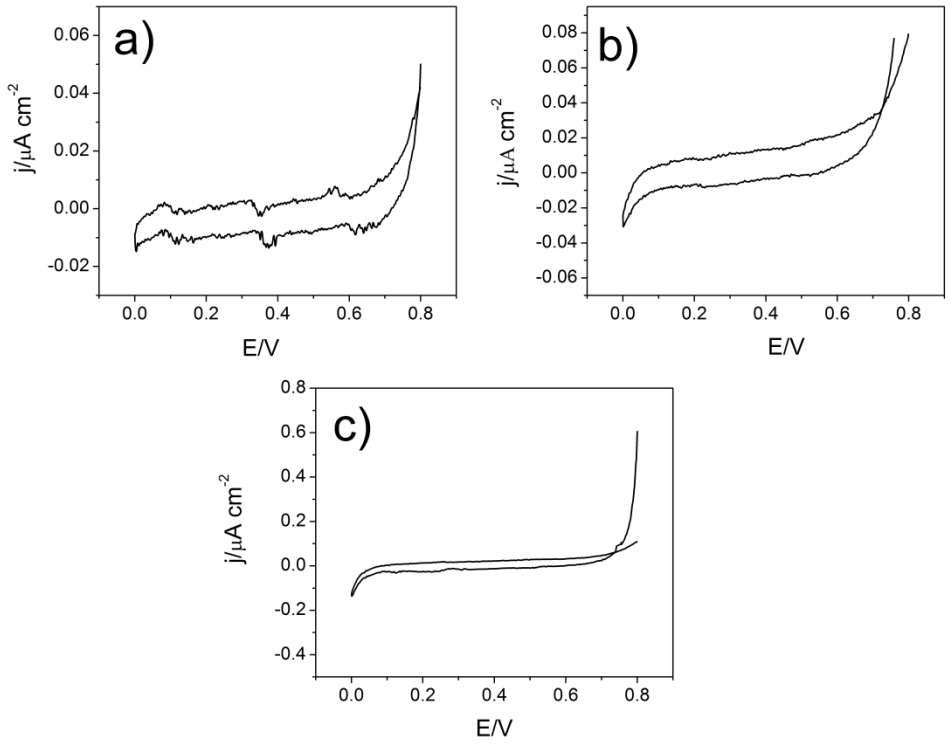

Figure 4.2.10 Cyclic voltammograms at 10 mV/s recorded in 50 mM acetate buffer pH 4.2 containing 100 mM $NaClO_4$ at RT under O_2 saturated conditions for a) S264C-BT-MG, b) S387C-BT-MG and c) 7D3-BT-MG electrodes. The 2nd scan is represented.

4.2.3.3 Maleimide cross-linking strategy

This strategy comprises several steps (section 3.2.5.3.1): first a mixed thiol SAM was formed (MPA/MH), afterwards amide bonds between the carboxylic groups on the electrode and maleimide (Mi) were formed by ECD/NHS strategy. Thereafter, cross-linking may take place between the maleimide groups present on the electrode surface and the thiols present on the Lc mutants. Indeed, maleimide is widely used as reactive agent in many heterobifunctional crosslinking reagents (Sinz 2006). Maleimide reactions are sulfhydryl specific in the pH range between 6.5 and 7.5; higher pH values favor its reaction with amines or hydrolysis of the maleimide group may occur to create an open maleamic form, which is not reactive towards sulphydryl groups (Sinz 2006).

4.2.3.3.1 Study of thiol self-assembled monolayer formation

Firstly, the formation of the mixed monolayer on GW and MG electrodes was studied. The formation of a monolayer is confirmed, indeed the CVs recorded with the presence of a redox probe (Fig. 4.2.11 a-b) show a decrease of the capacitive current and of the peak intensity of the probe´s redox peaks for the modified electrodes (green curves) if compared with the respective bare ones (black curves). The thiol desorption for the MG electrode showed (Fig. 4.2.11.c) three reductive peaks (dashed curve) at -0.88, -0.99 and -1.12 V in the first scan. The peaks at lower potentials are probably due to the presence of different facets of crystalline gold in MG, as peaks at the same positions have been detected in the previous thiol SAMs studied (Fig. 4.2.5.d and Fig. 4.2.9.c), while the peak at -0.88 V can be attributed

to the presence of a second thiol in the mixed SAM. This is confirmed when GW was used as support, as only broad two peaks were observed at -0.9 and -1.05 V, indicating the presence of two thiol species. The overall thiols coverage on the MG electrode in this case was estimated as $1 \cdot 10^{-9}$ mol cm^{-2}, a coverage expected for a compact thiol monolayer, which is very similar to that measured for the BT SAM.

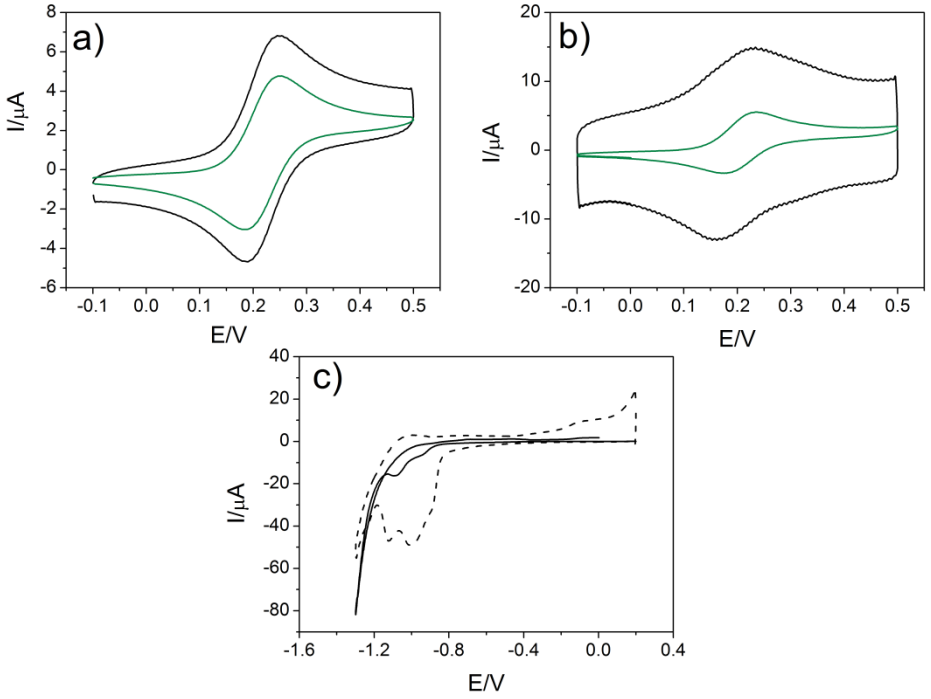

Figure 4.2.11 (a-b) CVs recorded at 50 mV/s in presence of 0.2 mM FeMeOH in KCl 0.1 M for a) GW and b) MG electrodes. Black curves represent bare electrodes and green curves MPA/MH-modified ones. c) CVs recorded in 0.5 M NaOH at 100 mV/s under deoxygenated conditions for MPA/MH-GW (solid line) and MPA/MH -MG (dashed line) electrodes. The 1st scan is represented.

4.2.3.3.2 Electrocatalytical response to O_2 reduction

Lc-Mi-MPA/MH-MG or Lc-Mi-MPA/MH-GW electrodes were tested for O_2 reduction in acidic conditions but no catalytic current was measured (Fig.4.2.12). MG electrodes showed (Fig. 4.2.12.a,c,e) higher capacitive area than GW electrodes, as expected (Fig. 4.2.12.b,d,f). A reversible redox process was detected at approximately 0.4 V when a S264C-Mi-MPA/MH-MG electrode was used under both N_2 and O_2 saturated conditions (Fig. 4.2.12.a). Performing more cycles did not lead to a decrease in the peak intensity, suggesting that probably these peaks belong to some impurities present on the electrode surface, as they do not appear on the other MG electrodes. When the parental type laccase 7D3 was used as catalyst, a high negative current starting at 0.1 V, which is attributed to O_2 reduction directly on gold was detected, suggesting that in this case a large region of gold surface was not covered with the thiols SAM. Also in this case, addition of ABTS as redox mediator, also in very low concentration, did not lead to any improvement in the catalytic response, and only the redox signal of the mediator was detected (data no shown).

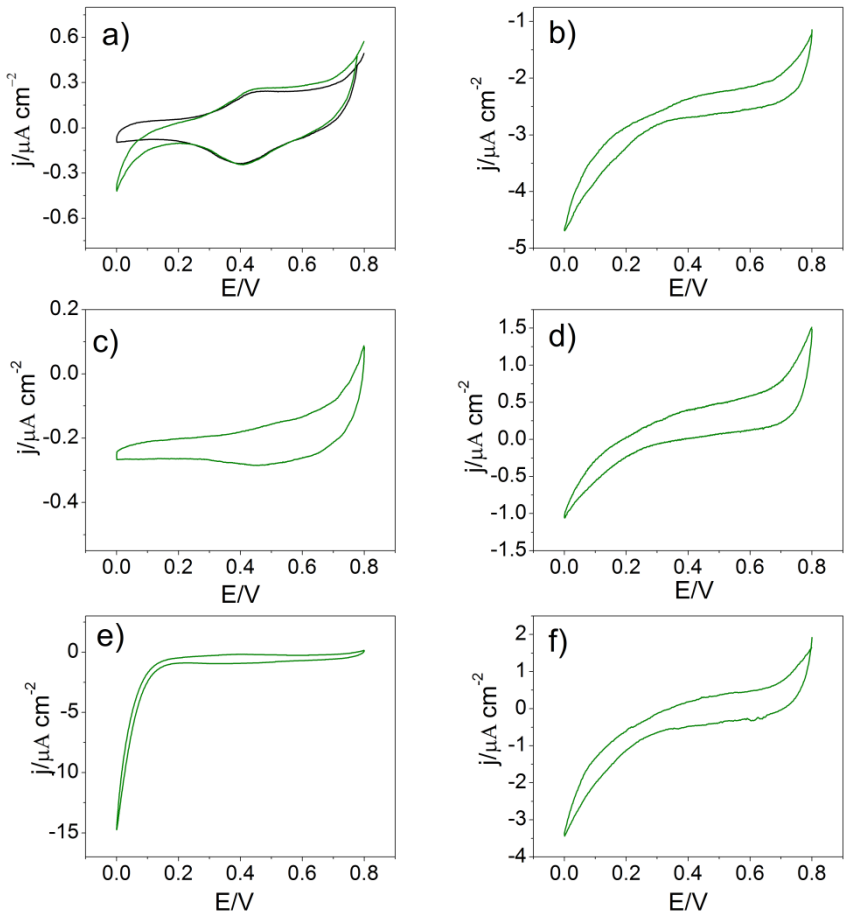

Figure 4.2.12 CVs recorded at 10 mV/s in 50 mM acetate buffer pH 4.2 containing 100 mM $NaClO_4$ at RT under N_2 (black curve) and O_2 (green curves) saturated conditions for a) S264C-Mi-MPA/MH-MG, b) S264C-Mi-MPA/MH-GW, c) S387C-Mi-MPA/MH-MG, d) S387C-Mi-MPA/MH-GW, e) 7D3-Mi-MPA/MH-MG and f) 7D3-Mi-MPA/MH-GW electrodes. The 2nd scan is represented.

4.2.4 Covalent immobilization of BOx on macroporous gold for DET-based electroenzymatic O_2 reduction

As no positive results were obtained with the laccase mutants for DET-based electroenzymatic O_2 reduction, an alternative enzyme was used for its covalent immobilization on the MG electrodes. The bilirubin oxidase mgBOx was tested because it is produced in the same laboratory as the MG electrodes (CNRS-Université de Bordeaux), and they had already studied its adsorption on MG modified with a thiol SAM but not its covalent immobilization, which should render a higher operational stability (Cadet 2015).

In order to immobilize mgBOx covalently on macroporous gold electrodes for the first time, the electrode surface was firstly cleaned and secondly functionalized with a naphtoic acid monolayer by electrochemical reduction of the respective diazo compound, as reported in 3.2.5.2.2 section. This immobilization strategy was used as it was already developed successfully for the immobilization of another BOx (*Myrothecium verrucaria* BOx) (Gutiérrez-Sánchez, Pita et al. 2013, Pita, Gutierrez-Sanchez et al. 2013). In Fig. 4.2.13 are reported the CV waves for the reduction of the diazo group

measured when MG of 7.5 layers (Fig. 4.2.13.a) or GW (Fig. 4.2.13.b) were used. Only two scans were performed in order to minimize the formation of multilayers. The voltammograms show an increase in the capacitive current when a MG electrode is measured (Fig. 4.2.13.a). Moreover, two reductive waves centered at ~0.44 and 0.07 V are observed (Fig. 4.2.13.), unlike the case of carbon-based electrodes where electrochemical reduction of the diazo group shows only one broad peak at around 0.4 V (as reported in Fig. 4.4.20, section 4.4.4.1). In the case of GW the reductive peak at 0.44 V is very low in intensity and cannot be well appreciated and the other peak at around 0 V is slightly shifted to lower potential compared to the macroporous gold case (Fig. 4.2.13.b). The presence of two reductive peaks could be due to the presence of different facets of crystalline gold.

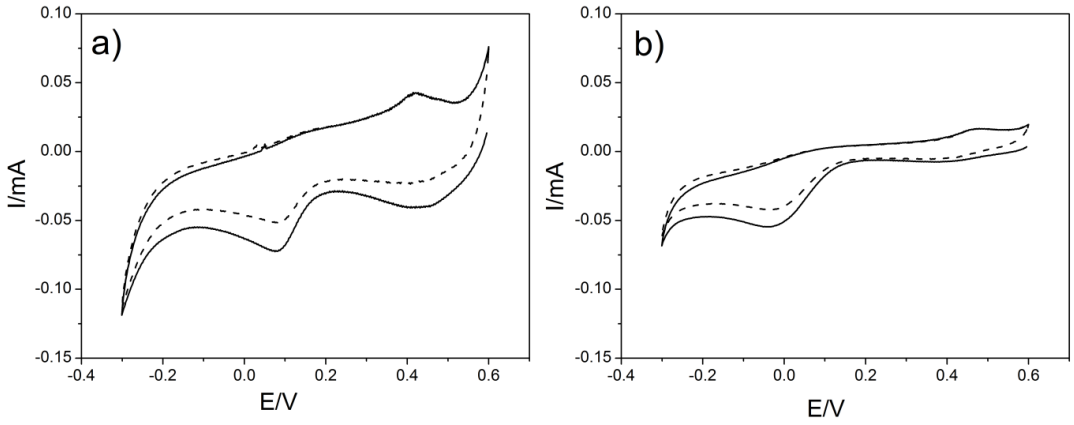

Figure 4.2.13 Electrochemical modification with 6-carboxy-2-naphtoyldiazonium cation prepared in situ of a) MG of 7.5 layers and of b) GW electrodes. The first scan is represented with a solid line, whereas the second scan with a dashed line.

The functionalization performed as reported above provided carboxylic groups on the electrode surface that allowed the covalent immobilization of mgBOx through amide bonds using the ECD/NHS strategy (section 3.2.5.2.1). The electrocatalytic response to O_2 reduction of mgBOx-gold based biocathodes was tested by cyclic voltammetry using as support MG of 7.5 layers (Fig. 4.2.14.a) or GW (Fig. 4.2.14.b). mgBOx-gold electrodes were prepared by covalent immobilization (Fig. 4.2.14.a-b, red curve), as described above, and also by adsorption of the biocatalyst (Fig. 4.2.14.a-b, green curve) as reported in section 3.2.5.2.2. Figure 4.2.14 a-b show a clear enhancement in the catalytic density current (relative to the determined electroactive area) when the enzyme is immobilized covalently on the electrode surface (red curves), in a DET-based regime. Reductive currents starting at 0.1 V are also observed, due to the O_2 reduction catalyzed by gold, indicating that part of the electrode surface is not covered by the naphtoic acid or the biocatalyst. Furthermore, the catalytic currents obtained for GW or MG were similar. Therefore, despite the considerable increase in the active surface area, there was not a clear increase in the catalytic current. These electrocatalytic results suggest that the amount of immobilized biocatalyst on MG has not been increased compared to the GW one.

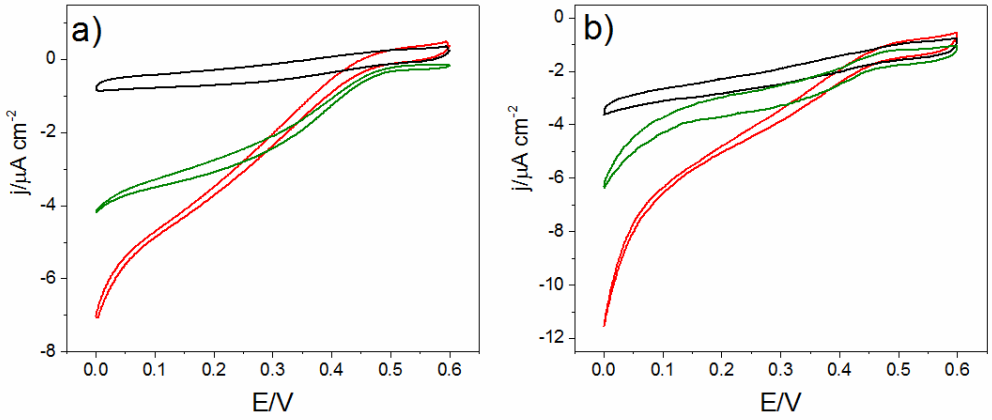

Figure 4.2.14 Electrocatalytic oxygen reduction at RT: a) mgBOx-MG electrode and b) mgBOx-GW electrode. CVs in N_2 (black curve) or O_2 (red, green curves) saturated atmosphere are represented. The enzyme was immobilized by adsorption (green curves) or covalently (red curves). CVs were performed at 10 mV/s in 100 mM phosphate buffer pH 7.4.

In consequence, the enzyme immobilization protocol was adapted to the higher active surface area generated on the macroporous gold electrodes by doubling the enzyme incubation time; thus favoring the amide bond formation catalyzed by ECD (as described in 3.2.5.2.2 section). During the immobilization process, the system was gently shaken to favor the enzyme diffusion inside all the porous structure of MG. Figure 4.2.15 shows the electrocatalytic response of O_2 reduction for mgBOx-based gold biocathodes prepared by simply adsorption (Fig. 4.2.15.a) and by covalent immobilization using the improved protocol as reported above (Fig. 4.2.15.b). This time GW (red curves), MG electrodes of 7.5 layers (black curves) or 15.5 layers (blue curves) were used as support.

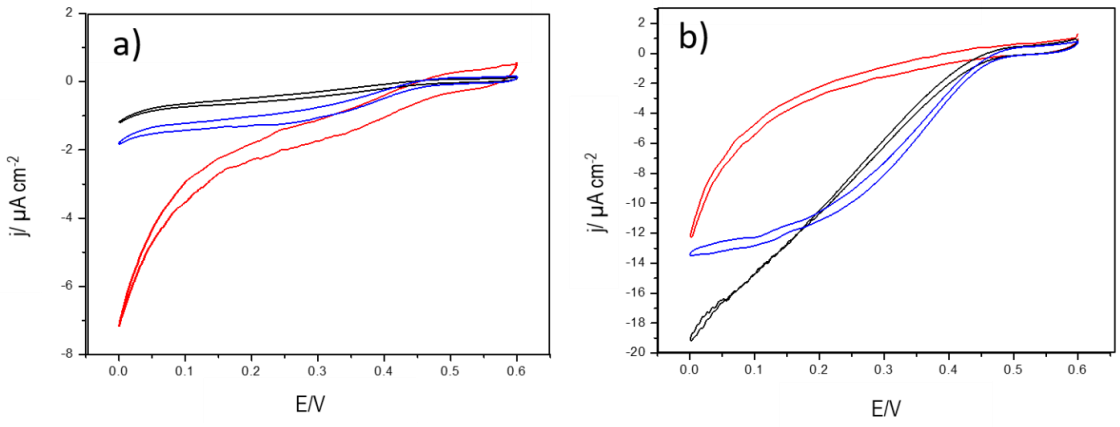

Figure 4.2.15 Electrocatalytic oxygen reduction at RT when mgBOx was immobilized a) by adsorption or b) by covalent immobilization using GW (red curves), MG of 7.5 layers (black curve) or of 15.5 layers (blue curve) as support. CVs were recorded in O_2 saturated atmosphere conditions, at 10 mV/s in 100 mM phosphate buffer pH 7.4.

When adsorption was used as immobilization method, the catalytic currents obtained for the mgBOx-GW electrode (Fig. 4.2.15.a, red curve) were higher than those for mgBOx-MG electrode (Fig. 4.2.15.a, blue and black curves). Therefore, the adsorption-immobilizing strategy does not take

advantage of the electrode nanostructure under these conditions. However, when covalent immobilization with the double-time protocol was carried out (Fig. 4.2.15.b), current densities up to 18 μA/cm^2 were obtained with the mgBOx-NA-MG electrodes. Furthermore, when a MG electrode of 15.5 layers was employed (Fig. 4.2.15.b, blue curve) mass transport limitation was more evident that in the case of electrodes of the 7.5 layers (Fig. 4.2.15.b, black curve), confirming the substrate hindrance to reach the bottom of the porous structure in the first case.

4.2.5 Conclusions

Two different laccase mutants enhanced with cysteine residues rationally added close to the T1 access channel have been successfully produced and purified. Three different functionalization strategies of gold surface have been tested. Modification of gold occurs with each strategy with a higher coverage for MG electrodes. Compact monolayers were obtained when BT or a mixed solution of MH and MPA was used. The mutant laccases did not lead to a significant catalytic response in any of the immobilization strategies. The less promising one seems be the strategy involved the formation of a BT monolayer, probably because very few enzyme molecules manage to form S-S bonds with the BT monolayer.

In the case of the DTT strategy, a possible cause of the negative results obtained could be that the enzymes were denatured on the bare gold surface regions, as the DTT SAM was the less compact one. Better results may be obtained by increasing the DTT concentration in order to cover the eventually bare regions of the electrode surface. The cross-linking strategy with maleimide could yield better results if some parameters of the immobilization protocol are improved, such as increasing the enzyme incubation time or a more efficient control of the pH during the cross-linking reaction. However, another potential cause for the failure of these experiments may come from the mutant biocatalysts; which may have suffered some structural/functional changes during the evolution process that hinder a good orientation of the enzymes for this application in spite of the introduced Cys. It was not possible to perform more experiments in order to verify all these hypotheses due to a lack of newly produced mutant laccases (the production process is very time-consuming and yields only a few mg of protein).

On the other hand, for the first time covalent immobilization of mgBOx on MG electrodes was carried out successfully. Few modifications in the standard immobilization protocol, as doubling the enzyme incubation time, led to current densities up to 18 μA/cm^2 using a mgBOx-NA-MG electrode, making possible in this way to take advantage from the higher active surface area of MG electrodes.

4. 3 Nanostructured graphite-Au nanorods laccase based-biocathodes

Low-density graphite (LDG) is known as a suitable electroactive material for interfacing multicopper oxidases (such as Laccase), showing more suitable properties than other candidates such as gold (Vaz-Dominguez, Campuzano et al. 2008). However, the synergy of both materials for optimizing fast direct electron transfer of redox metalloenzymes has barely been explored. The only successful report shows the immobilization of 5 ± 3 nm-diameter gold nanoparticles on LDG electrodes and their use as electronic bridges to improve the enzymes' wiring, achieving a Nernstian-like process at the potential of the Cu T1 site for the electrocatalytic reduction of O_2 (Gutierrez-Sanchez, Pita et al. 2012). In this section a different gold nanostructure, *i.e.* nanorods (AuNRs), was explored. This shape is particularly interesting due to the different crystalline facets shown in the nanorods, which may unveil some clues to optimize and control the direct electron transfer between laccase and a gold-enhanced graphite electrode.

4. 3. 1 AuNRs characterization

The gold nanorods were successfully synthetized by a seedless growth technique, as reported in the 3.2.3.1 section. TEM images of the AuNRs were obtained in order to verify the successful synthesis of the nanorods and to study their morphology. It is observed in Fig. 4.3.1.a that most Au^{3+} nucleated in rod shape. At higher magnification is clearly visible the formation of nanorods (Fig. 4.3.1.b).

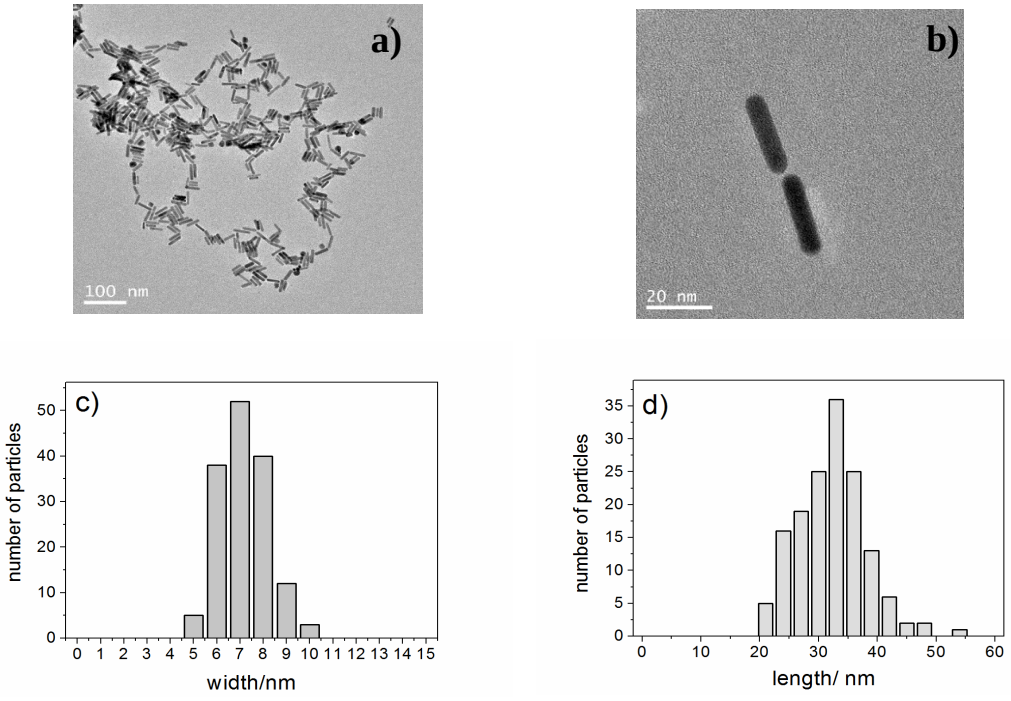

Figure 4.3.1 TEM images showing AuNRs freshly synthesized at a) lower and b) higher magnification. c) and d) show the measured width and length of the AuNRs shown in a).

The measurement of 150 rods, from Fig. 4.3.1.a, showed an average size of (7 ± 1) nm width (Fig. 4.3.1.c) and (31 ± 6) nm length (Fig. 4.3.1.d).

Moreover, UV-Vis spectra of an aqueous dispersion of the AuNRs were also measured. In Fig. 4.3.2 is reported the spectral response of gold nanoparticles (AuNPs) compared with that of gold nanorods. As expected, the spectrum of AuNPs (dashed curve) shows the characteristic single localized surface plasmon resonance absorption band, centered at λ= 520 nm; while the AuNRs spectrum (solid curve) shows two localized surface plasmon resonance bands: the same band at λ= 520 nm and another at λ= 780 nm, typical for gold nanorods (Grzelczak, Pérez-Juste et al. 2007). Furthermore, as silver was used in the synthetic process, it was also checked that no absorption band at 410 nm is present (Zaheer and Rafiuddin 2012), excluding the formation of silver nanoparticles as by-product.

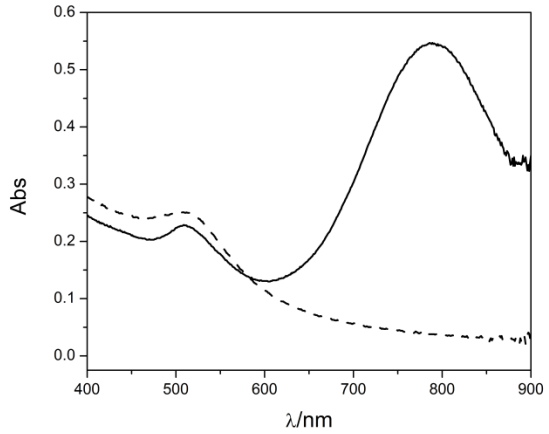

Figure 4.3.2 UV-Vis spectra obtained for AuNPs (dashed curve) and AuNRs (solid curve).

4. 3. 2 LDG functionalization and modification with AuNRs

The modification procedure of the LDG electrodes, as described in 3.2.4.1 section, accomplishes the formation of a layer of 4-aminophenyl groups (Vaz-Dominguez, Campuzano et al. 2008). In this modification method, carried out by cyclic voltammetry, the number of scans and scan rate were optimized in order to minimize multi-layers formation of diazonium reactants on the electrode surface. The CV for the reduction of the diazonium salt is shown in Fig. 4.3.3.a and the subsequent electrochemical reduction of Ar-NO_2 to Ar-NH_2 groups in Fig. 4.3.3.b. In the first scan (Fig 4.3.3.b, solid line) a reductive wave is observed at ~ -1.1 V, corresponding to the reduction of Ar-NO_2 groups; instead, in the second scan a reversible peak redox at ~ -0.3 V corresponding to the reversible redox equilibrium between Ar-NO/Ar-NHOH. This process appears only in the second scan because the reduction of nitro groups to amine takes place in two steps: first the reduction to hydroxylamine and then to amine, as shown in equation (4.1). The nitro groups are not totally reduced to amine, a portion of them remains as hydroxylamine due to a kinetic limitation of the process (Brooksby and Downard 2004).

$$-NO_2 \xrightarrow{4H^+/4e^-} -NHOH \underset{}{\overset{2H^+/2e^-}{\rightleftharpoons}} -NH_2 \qquad (4.1)$$

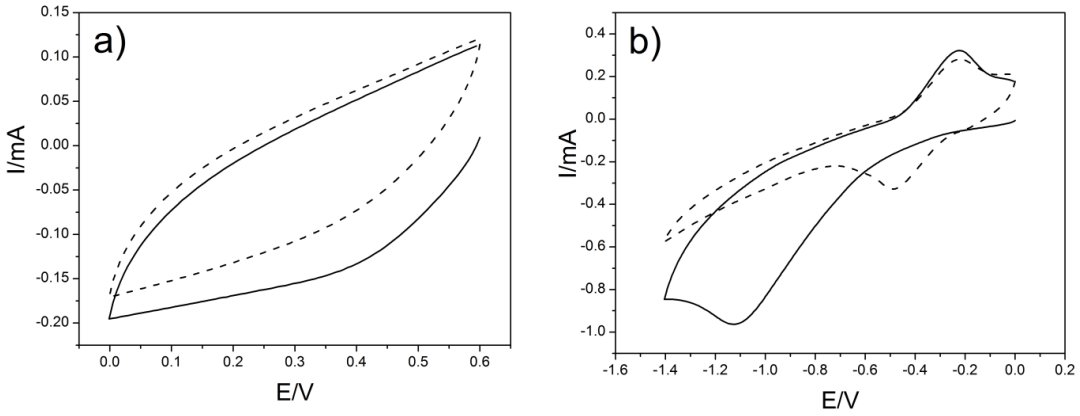

Figure 4.3.3 a) LDG modification with 4-nitrobenzene diazonium salt in CH_3CN, 0.1 M Bu_3NBF_4, performed at 200 mV/s. b) Electrochemical reduction of nitro groups to amino groups in EtOH/$H_2$0 1:9 0.1 M KCl, at 100 mV/s. The first scans are represented with a solid line while the second scans with a dashed line.

For the further attachment of AuNRs the anilinium groups attached to the electrode surface were chemically turned into diazonium groups by immersion of the modified LDG electrode in a solution of $NaNO_2$/HCl (Fig. 4.3.4) (Freeman, Whaley et al. 1986). Afterwards, the diazonium-modified electrodes were covered with a AuNRs dispersion and let to dry. In this way the negatively charged gold nanorods, were electrostatically attracted to the positively charged electrode surface. Spontaneous reaction of the diazo group with AuNRs takes place yielding aryl C-Au bonds formation (Laurentius, Stoyanov et al. 2011).

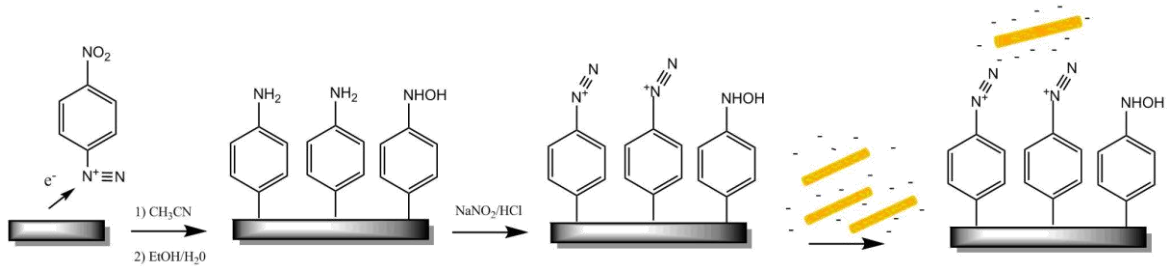

Figure 4.3.4 Schematic representation of the functionalization of LDG electrodes for the covalent attachment of AuNRs.

Hereafter, in order to reduce the remaining azo groups and to enhance the number of C-AuNR bonds, two CV cycles from 0.6 to -0.6 V in 50 mM acetate buffer pH 4.2 with 100 mM $NaClO_4$ were recorded for the AuNR-LDG electrodes (Fig. 4.3.5). In this case the reduction process started at lower potential (around -0.2 V) than in the previous case shown in Fig. 4.3.3.a. This difference is attributed

to a reduction process that involves a confined species bound, with the azo group not oriented towards the electrode surface, instead of an electroactive species in solution. Therefore, the electrochemical reduction takes place further from the electrode surface than in the previous case, and in consequence is kinetically limited, leading to a higher overpotential (Gutierrez-Sanchez, Pita et al. 2012).

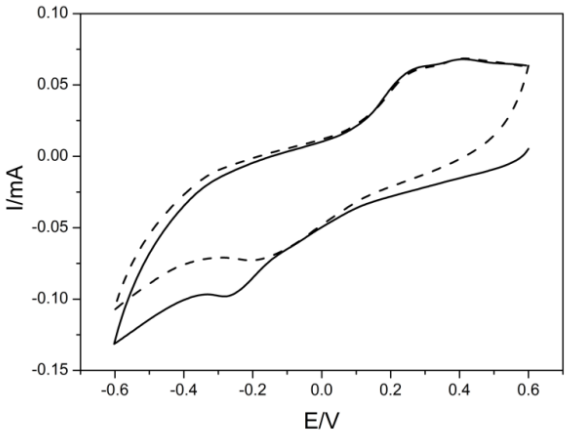

Figure 4.3.5 CVs of an AuNR-LDG electrode in 50 mM acetate buffer pH 4.2 with 100 mM $NaClO_4$, at 200 mV/s. The first scan is represented with a solid line and the second one with a dashed line.

4.3.2.1 LDG-AuNRs characterization

TEM characterization was done to verify the attachment of AuNRs to the electrode surface after their immobilization. However, the graphite bars cannot be directly measured by TEM, so an AuNRs-LDG electrode was scraped and the graphite powder produced was recovered and dispersed in EtOH. A 20-μL drop of EtOH containing graphite-AuNRs chips was placed on a TEM grid and let to dry. Fig. 4.3.6.a shows a large scale TEM image of a graphite chip with a high load of gold nanorods attached, as confirmed by EDX analysis. However, it is worth mentioning that the total amount of gold present onto the electrode surface probably had diminished due to the aggressive physical process for preparing the TEM sample. Also, as it could be observed by the images (Fig. 4.3.6 a-c), the nanorods show a deformed shaped after their immobilization on the electrode surface and the subsequent two CVs done for preparing AuNRs-LDG electrodes. It is already known that these electrochemical treatments affect the shape of gold nanoparticles (Murata, Kajiya et al. 2009). On the other hand, a massive aggregation of gold nanorods does not occur, which may be due to the presence of covalent bonds between the electrode surface and the gold nano-elements, which minimize the mobility of gold on the surface.

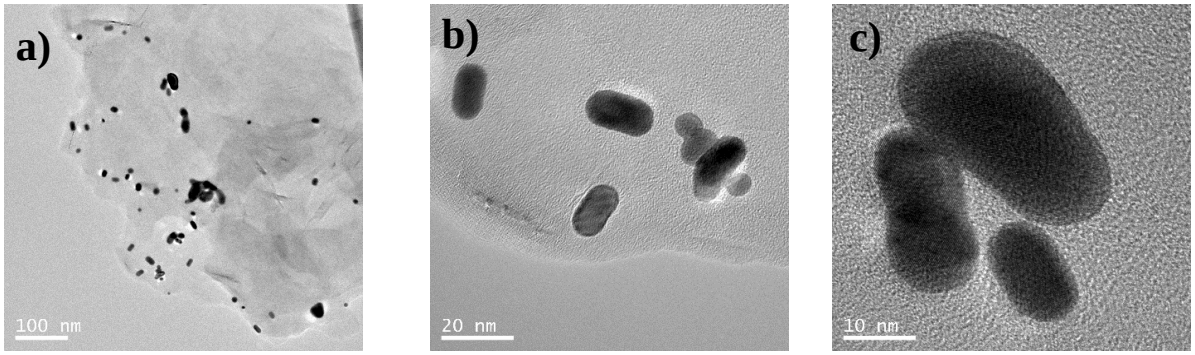

Figure 4.3.6 TEM images at different resolutions showing AuNRs after their immobilization on the surface of functionalized LDG (a,b,c).

The AuNR-LDG electrodes were also characterized electrochemically. Indeed, it is possible to observe the typical redox process of gold, also when it is immobilized as particles on the surface of graphite electrodes (Mirkhalaf and Schiffrin 2010, Gutierrez-Sanchez, Pita et al. 2012). In Fig. 4.3.7 is reported the CV in 0.1 M H_2SO_4 of a LDG electrode before (dashed curve) and after (solid curve) the covalent immobilization of AuNRs.

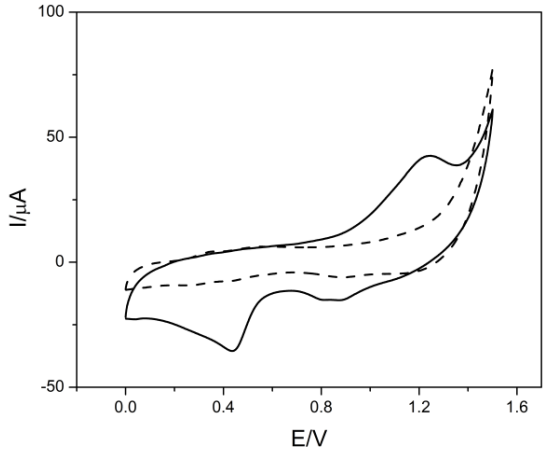

Figure 4.3.7 Cyclic voltammograms obtained for the aminophenyl-functionalized LDG electrode (black curve) and AuNR-LDG electrode (red curve) recorded in 0.1 M H_2SO_4 at 200 mV/s.

The oxidation of gold causes the anodic peak at +1.2 V and the three cathodic peaks are due to the gold oxide reduction: two similar in magnitude and centred at 0.8 V and 0.75 V, and a more intense one at 0.5 V. It is known that the different facets of crystalline gold present different redox potentials for the reduction of their oxides (Oesch and Janata 1983). The tops of the nanorods present a lower surface than the body of the cylinder. Consequently, the two cathodic processes at higher potential could be attributed to the tops of the cylinder, whereas the lower redox potential process, with a higher integrated peak area, probably corresponds to the surface of the cylinder body. The total surface of gold bound to the surface could be determined by integrating the obtained gold oxide reductive peaks

and considering a charge equivalent of -483 μC cm^{-2}, which is the charge density reported for the electrochemical reduction a gold oxide monolayer (Oesch and Janata 1983). Integration of the peaks in Fig. 4.3.7 indicated that the electrode has a bound gold surface area of (0.7 ± 0.2) cm^2, which is ca. 10-fold the geometrical surface of the graphite electrode.

4.3.3 Biocathode performance

4.3.3.1 Laccase immobilization

Once the AuNR-LDG electrodes were prepared, the next step was the subsequent functionalization of the modified surface for the correct immobilization of laccase, as explained in 3.2.5.1 section. A mixed 4-aminophenyl and MH monolayer was formed as previously reported for Au electrodes, showing that this strategy favoured oriented immobilization of ThLc for DET (Vaz-Domínguez, Pita et al. 2012, Pita, Gutierrez-Sanchez et al. 2013). Firstly, the AuNR-LDG electrode was electrochemically modified with 4-nitrobenzene diazonium salt (Fig. 4.3.8.a), followed by the electrochemical reduction of the nitro group to an amino group (Fig. 4.3.8.b). Then, the electrodes were immersed overnight in a solution of MH in order to self-assemble a monolayer on the bare gold regions or on those where are physically adsorbed molecules. In this way, direct adsorption and inactivation of the enzyme on the gold surface is prevented (Pita, Gutierrez-Sanchez et al. 2011) (Vaz-Domínguez, Pita et al. 2012).

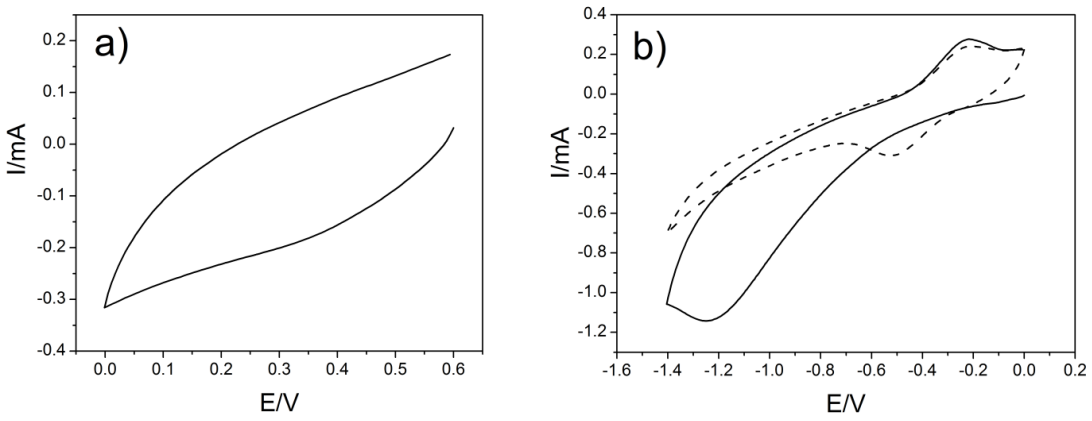

Figure 4.3.8 a) AuNR-LDG modification by electrochemical reduction of 4-nitrobenzene diazonium salt in CH_3CN, 0.1 M Bu_3NBF_4. b) Electrochemical reduction of nitro groups to amino groups in EtOH/$H_2$0 1:9, 0.1 M KCl, performed at 100 mV/s. The first scan is represented with a solid line and the second scan with a dashed line.

Prior to the immobilization process, ThLc was incubated in a solution containing $NaIO_4$ (as reported in 3.2.5.1 section), a mild oxidant able to convert the hydroxyl groups of the carbohydrates at the enzyme surface to aldehydes (Gupta, Rajendran et al. 2004). The functionalized AuNR-LDG electrodes were then incubated in the solution containing the aldehyde-modified ThLc for formation of imine bonds, yielding the oriented immobilization of the enzyme with its T1 site facing the electrode surface.

Further covalent attachment of the enzyme was performed by amide bonds formation between the electrode amine groups and the enzyme´s carboxylic groups. This strategy is well known to facilitate direct electron transfer (DET) between the biocatalyst and the electrode (Pita, Gutierrez-Sanchez et al. 2011, Gutiérrez-Sánchez, Jia et al. 2012).

4.3.3.2 Electroenzymatic reduction of O_2

The response of the enzymatic electrode to O_2 reduction was tested by cyclic voltammetry using 50 mM acetate buffer pH 4.2 with 100 mM $NaClO_4$ in oxygen saturated conditions. In each experimental set the reversible inhibitor NaF was added to record the background signal (Fig. 4.3.9 and Fig 4.3.10 a-b, black curve) (Naqui and Varfolomeev 1980). A strong catalytic effect was observed under oxygen saturated conditions, actually a quasi-plateau of reduction current density of ca. -0.5 mA cm^{-2} was reached (Fig. 4.3.9, red curve). This catalytic effect was due to laccase activity towards O_2 presence. Indeed, when NaF (typical inhibitor of laccase activity) was added to the buffer solution no catalytic response was observed (Fig. 4.3.9, black curve). Application of 500 rpm rotating speed to the electrode reduced the mass-transfer limitation of O_2 towards the electrode surface, therefore increasing the current density measured (Fig. 4.3.9, blue curve). However, further increase in the rotational speed barely improved the catalytic response, meaning that the oxygen transport to the electrode surface was not longer the limiting step of the O_2 bioelecatalytic reduction kinetics.

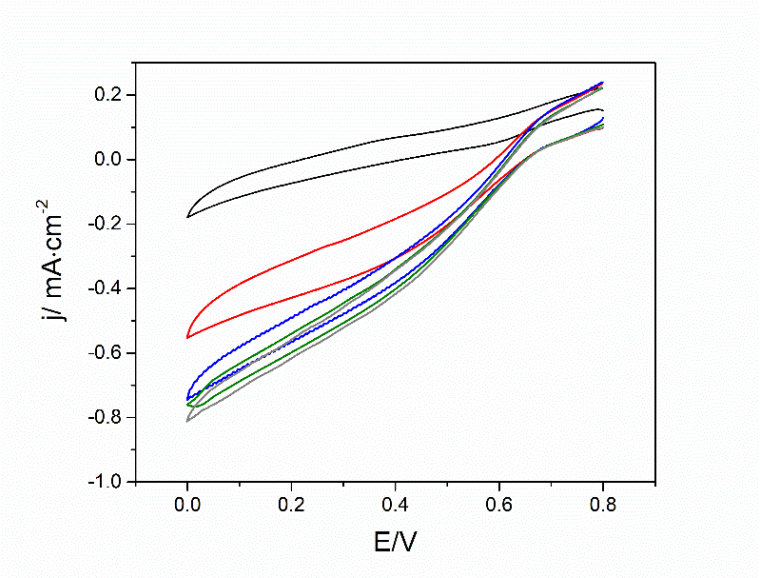

Figure 4.3.9 CVs recorded using a ThLc-AuNR-LDG electrode in 50 mM acetate buffer pH 4.2, 100 mM $NaClO_4$ in O_2 saturated atmosphere at 0 rpm (red curve), 500 rpm (blue curve), 1000 rpm (green), or 1500 rpm (grey curve) electrode rotation. The black curve corresponds to the background CV obtained after addition of 30 mM NaF. The scan rate was 10 mV/s.

Addition of the redox mediator (0.1 mM ABTS) to the solution increased the catalytic current density, which showed a quasi-plateau of ca. 0.7 mA cm^{-2} (Fig. 4.3.10.a, dashed line). The current increase measured when changing from DET to mediated electron transfer (MET) suggests that a portion of the enzyme molecules was not adequately oriented for a DET reaction regime. When the measurements were performed while rotating the electrode at 500 rpm, also in the presence of ABTS, a clear enhancement in the catalytic current was observed (Fig. 4.3.10.b, dashed line).

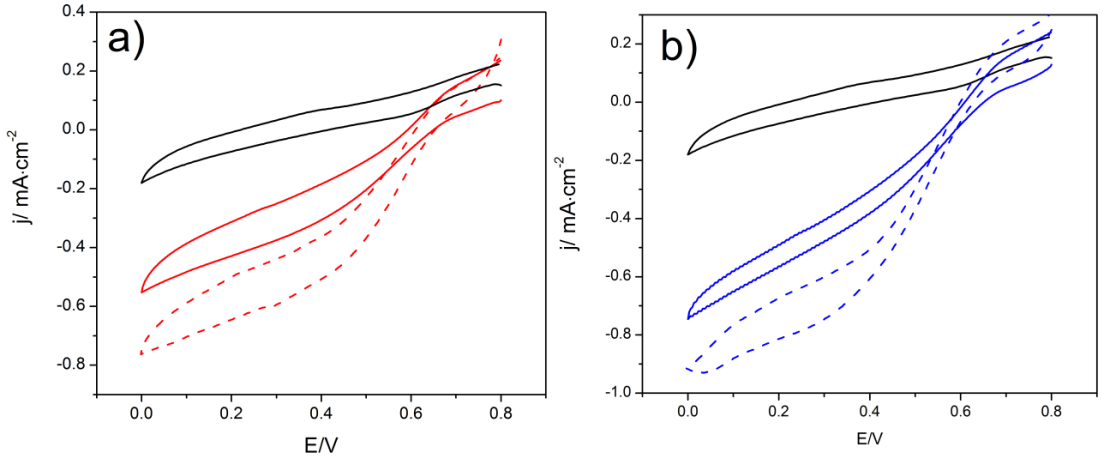

Figure 4.3.10 CVs recorded using a ThLc-AuNR-LDG electrode in 50 mM acetate buffer pH 4.2, 100 mM $NaClO_4$ at a) 0 rpm and b) 500 rpm electrode rotation in oxygen saturated conditions. The black curves are the CVs in presence of 30 mM NaF and the dashed curves are the CVs in presence of 0.1 mM ABTS. The scan rate was 10 mV/s.

The catalytic current densities obtained for ThLc-AuNR-LDG electrodes were compared to those obtained for planar gold electrodes modified with the same mixed aminoaryl-MH monolayer and bounded laccase reported in a previous work of our group (Pita, Gutierrez-Sanchez et al. 2011). The AuNRs-modified electrodes yielded a 12-fold higher current densities, although the Au surface area is 4-5 times lower. This much higher catalytic current density obtained can be explained because laccase may bind also to the LDG surface not covered by AuNRs. It must be taken into account that the surface roughness of LDG is much higher than that of planar gold electrodes, thus the electroactive area of the former is considerably larger (Pita, Gutierrez-Sanchez et al. 2011, Gutierrez-Sanchez, Pita et al. 2012).

The electrocatalytic response to O_2 reduction under increasing chloride concentration was studied by chronoamperometry at 0.2 V under O_2 saturated conditions and rotating the electrode at 500 rpm (Fig. 4.3.11). It could be observed that when the concentration of Cl^- reaches ~ 140 mM, the maximum concentration present in a human serum, the ThLc bioelectrocatalytic response decreased more than 30%. This result is in agreement with the previous one reported for AuNPs-modified LDG electrodes, where AuNPs of bigger dimension (d= 16 nm) were employed (Gutierrez-Sanchez, Pita et al. 2012).

Indeed, it is well known that the inhibition by chloride anions is higher on macroscopic gold than on carbon-based materials, probably because adsorption/desorption phenomena of the anions on the gold surface takes place (Vaz-Dominguez, Campuzano et al. 2008, Gutiérrez-Sánchez, Jia et al. 2012). Therefore, the use of nano-gold elements instead of macroscopic gold minimizes the gold surface exposed to the electrolyte solution, tempering the inhibition process by Cl^-. Moreover, when smaller AuNPs (d= 5 nm) were used this effect decreased, suggesting that the smaller AuNPs with similar size to ThLc (Piontek, Antorini et al. 2002) can be inserted in the smaller pores of LDG, and in this way much less gold surface is available for Cl^- adsorption (Gutierrez-Sanchez, Pita et al. 2012). In the case of AuNPs of higher diameter (16 nm) or the even larger AuNRs used in this Thesis, the gold surface area exposed to Cl^- adsorption is higher, leading to a higher decrease of the catalytic current.

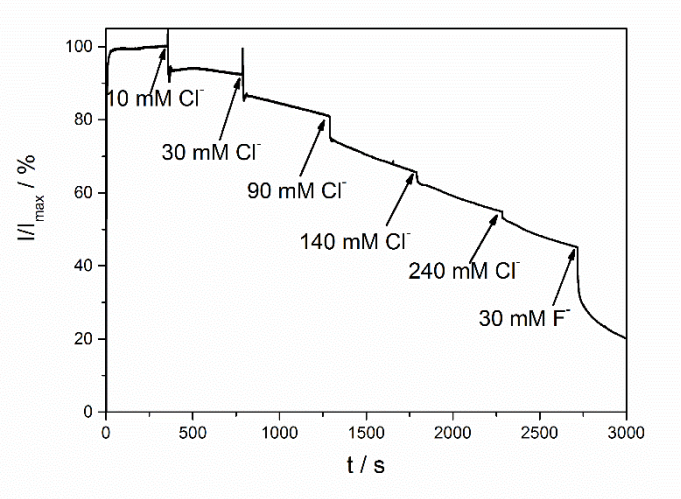

Figure 4.3.11 Chronoamperometry measured at 0.2 V with a ThLc-AuNR-LDG electrode rotated at 500 rpm in 50 mM acetate buffer pH 4.2, 100 mM $NaClO_4$ under bubbling with 1 atm oxygen and adding different amounts of laccase inhibitors.

The bioelectrocatalytic response given by the ThLc-AuNR-LDG electrode for O_2 reduction vs. the redox potential was further analyzed for studying the kinetics of the process (Fig. 4.3.12). The forward CV scan measured under 1 atm O_2 and 1500 rpm electrode rotation rate was taken and the scan measured in the presence of NaF inhibitor was subtracted to eliminate the non-catalytic current. In this way the capacitive current is eliminated and the dependence of the catalytic current on mass transport is negligible. The experimental curve shown in Fig. 4.3.12 does not follow the typical sigmoidal shape ending in a plateau limiting current for an electrocatalytic process limited by either mass-transfer or enzyme kinetics limitations (Léger and Bertrand 2008). Instead, the electrocatalytic response is comparable to a process rate limited by DET comprehending enzymes that are connected with different distances between the redox site and the electrode surface (Léger, Jones et al. 2002). Actually, the experimental curve for the ThLc-AuNR-LDG electrode at 1500 rpm (at this electrode rotation rate no mass transfer limitation of O_2 was observed) fits quite well in accordance to Leger's theoretical equation adapted to laccase electrocatalysis (4.2), express as follows:

$$i = \frac{i_{lim}}{1+e^{f(E-E_{T1})}}\left(1+\frac{1}{\beta d_0} ln \frac{1+ e^{f(E-E_{T1})} + \frac{k_{cat}}{k_0^{max}} e^{\frac{f}{2}(E-E_{T1})}}{1+ e^{f(E-E_{T1})} + \frac{k_{cat}}{k_0^{max}} e^{\frac{f}{2}(E-E_{T1})e^{\beta d_0}}}\right) \qquad (4.2)$$

Where:

- i is the catalytic current;
- i_{lim} is the limiting current controlled by laccase catalysis;
- f= F/RT where T, F and R are the temperature, Faraday and molar gas constants respectively;
- E is the redox potential and E_{T1} is the redox potential of the T1 site of laccase;
- βd_0 is a unit-less parameter accounting for the orientation dispersion of enzyme molecules taking part in the DET process (Léger, Jones et al. 2002);
- k_o^{max} is the rate constant for DET to the T1 site at the optimal laccase orientation;
- k_{cat} is the overall apparent rate constant for laccase catalysis (including intramolecular electron transfer from the T1 to T2/T3 sites, oxygen reduction to water at the T2/T3 site, and product and substrate transport within the laccase).

The data fitting gives a value of 0.79 V vs. NHE for the potential of the redox site of the laccase involved in DET. This potential is in agreement with the ones reported by spectroelectrochemical tritations (0.78 vs. NHE) for the Cu T1 site (Shleev, Morozova et al. 2004), confirming that DET of laccase with the electrode is via this metal ion. The following values were also determined from the model fitting: $k_{cat}/k_0^{max} = 0.003$ and $\beta d_0 = 16.6$, corresponding to the ratio between the enzymatic reaction rate constant and the heterogeneous electron transfer rate constant at the optimal enzyme orientation, and the parameter reflecting the orientations' dispersion of enzyme molecules involved in the DET process, respectively (Léger, Jones et al. 2002). In a previous work of our group, where AuNPs were used, approximately half of the immobilized laccase molecules were optimally wired to the electrode surface following a Nernstian-controlled electron transfer process, meanwhile the other half followed the non-optimal DET rate distribution (Gutierrez-Sanchez, Pita et al. 2012). In the case of the AuNRs modified electrode the Nernstian-controlled process has not been observed, where almost all the enzymes molecules followed the Leger's kinetic regime. This can be explained taking into account the larger size of AuNRs compared to AuNPs. Indeed, more efficient catalysis was achieved using 5 nm-diameter AuNPs than 16 nm-diameter AuNPs (Gutierrez-Sanchez, Pita et al. 2012). Recent studies have also reported that nanoparticles ranging between 20-80 nm in diameter do not influence the DET or the catalytic rates of the immobilized enzyme molecules, sustaining the hypothesis that when the Au nanoelements are bigger than the immobilized enzyme the improvement

effect in the electronic coupling does not occur (Pankratov, Sundberg et al. 2014). Therefore, a higher kinetic barrier for the electron transfer could be the reason of the lower efficiency of gold nanorods in wiring laccase for DET regime. In addition to this, the higher value of βd_0 (16.6) obtained for the AuNRs modified electrode compared to the one obtained for AuNPs modified one (11.0) also suggests a higher dispersion of laccase molecules orientations on the AuNRs due to the presence of different crystalline gold facets.

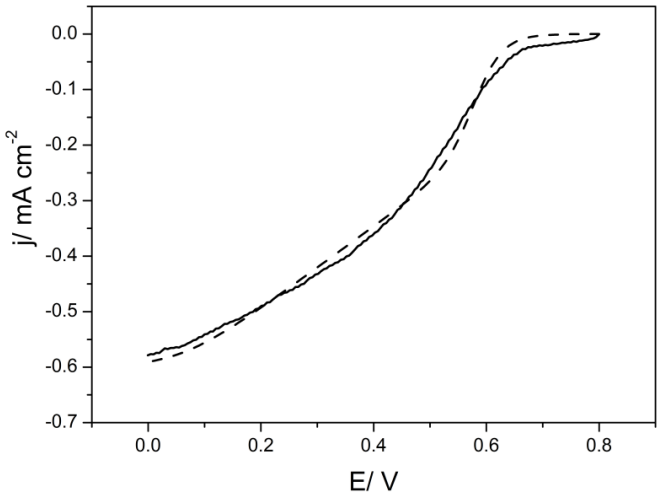

Figure 4.3.12 Blank-subtracted forward scan of the CV measured for a ThLc-AuNR-LDG electrode at 1500 rpm and 10 mV/s under O_2 saturated conditions (solid line) and fitted curve considering a DET rate-limited process with a distribution of non-optimally wired laccase molecules (dashed line).

4.3.4 Conclusion

LDG electrodes modified with covalently attached AuNRs (average length= 31±6 nm) have been successfully prepared and used as platform for the further covalent immobilization of laccase. High electrocatalytic currents for oxygen reduction up to -0.6 mA cm^{-2} have been obtained. Addition of ABTS as redox mediator increased by 28 % the catalytic response, suggesting that a part of the immobilized enzyme molecules is not properly oriented for DET process. Fitting of the experimental curve to Leger´s model for enzyme monolayer electrocatalysis points out that the process at high rotational speed for the ThLc-AuNR-LDG electrode is rate limited by DET from the T1 site of laccase to the electrode surface. Furthermore, a higher dispersion of enzyme molecules on gold nanorods is observed as there is a wider distribution of non-optimally wired laccase molecules than on AuNPs. For all these reasons, the results obtained with AuNRs-modified electrodes could be due to the larger size of the nanorods than the laccase molecules and to their different crystal facets.

4. 4 Graphene based electrodes

A crucial factor for the fabrication of efficient enzymatic electrodes able to provide high current densities is to maximize the biocatalyst's coverage on the electrode surface. For this reason, extensive research has always paid attention to different nanomaterials with high surface area and high conductivity. Among others, high surface area carbonaceous materials, in particular graphene, have attracted great interest in different applications due to their remarkable electrical and mechanical properties (Rao, Sood et al. 2009, De Volder, Tawfick et al. 2013, Filip and Tkac 2014). Graphene can be synthetized through different strategies; each of them provides graphene with different characteristics. The fabrication of graphene-based electrodes has to overcome the low reproducibility and low stability problems of the current manufacturing methods, such as drop-casting, spraying or brushing (Eda and Chhowalla 2010, Pumera, Ambrosi et al. 2010, Kashyap, Mishra et al. 2014). Lately, the electrodeposition (ED) of graphene oxide and its simultaneous electrochemical reduction has been proposed as reproducible method for the fabrication of stable and more uniform high surface area electrodes (Chen, Tang et al. 2011, Hilder, Winther-Jensen et al. 2011, Jiang, Lu et al. 2012).

The aim of this section was developing an efficient and reproducible fabrication method of graphene-based electrodes as support for enzyme immobilization and to study their bioelectrocatalytic performances. Firstly, the electrodeposition method was optimized: the electrochemical parameters involved, using either cyclic voltammetry or pulsed electrodeposition (*i.e.* scan rate, number of cycles, time of pulse, number of pulses, etc.), and the chemical composition of the used GO were studied. Two GO samples, with a different O/C ratio in their surface composition have been used to investigate how the chemical composition of GO can influence the ED process. The objective was to maximize the electroactive area of the graphene-based electrode while optimizing the electron transfer kinetics using potassium ferricyanide as redox probe. Once the process was optimized, the electrochemically reduced graphene oxide prepared was fully characterized from an electrochemical and a physico-chemical point of view. Finally, graphene-based electrodes were used for immobilizing MCOs and tested as direct electron transfer based biocathodes; performing also studies on the mechanism of enzymatic oxygen reduction by the calculation of Tafel slopes and transfer coefficients. This part of the work was done in collaboration with Dr. Asier Goñi Urtiaga from Nanoinnova Technologies (Madrid).

4. 4. 1 Optimization of the electrodeposition parameters

The preparation of GO by Hummer's method provides a material with high degree of oxygen functionalities, hydrophilicity and negative zeta potential over almost the whole pH range (Si and Samulski 2008, Chen, Feng et al. 2012, Kashyap, Mishra et al. 2014). Two GO samples, GO_01 and GO_02, prepared as reported in 3.2.3.2 section, with 0.65 and 0.45 O/C ratios respectively have been studied. The characteristics of GO allow the deposition of sheets of this material dispersed in aqueous

solution on the electrode surface induced both by the application of a positive electric field and by the electrochemical reduction to the more hydrophobic material (erGO). Two different electrochemical techniques have been tested to perform electrodeposition of graphene oxide solution: cyclic voltammetry and pulsed chronoamperometry, as reported in the 3.2.4.2 section.

4.4.1.1 GO_01 electrodeposition on GC electrodes

A GO_01 dispersion (1 mg/mL) in phosphate buffer 100 mM, pH 9 was prepared as reported in the 3.2.4.2 section. A basic pH for the dispersion solution was chosen as acid pH values enable side-reactions during the electrodeposition process that compete with GO reduction (Hilder, Winther-Jensen et al. 2011).

4.4.1.1.1 Effect of the solution stirring during the electrodeposition process

For this preliminary study, the electrodeposition (ED) process was performed under deoxygenated conditions by cyclic voltammetry from 0.8 to -1.5 V, at 10 mV/s scan rate, for 10 cycles with and without stirring the electrodeposition solution (Fig. 4.4.1.a-b). Magnetic stirring was performed at 400 rpm/min.

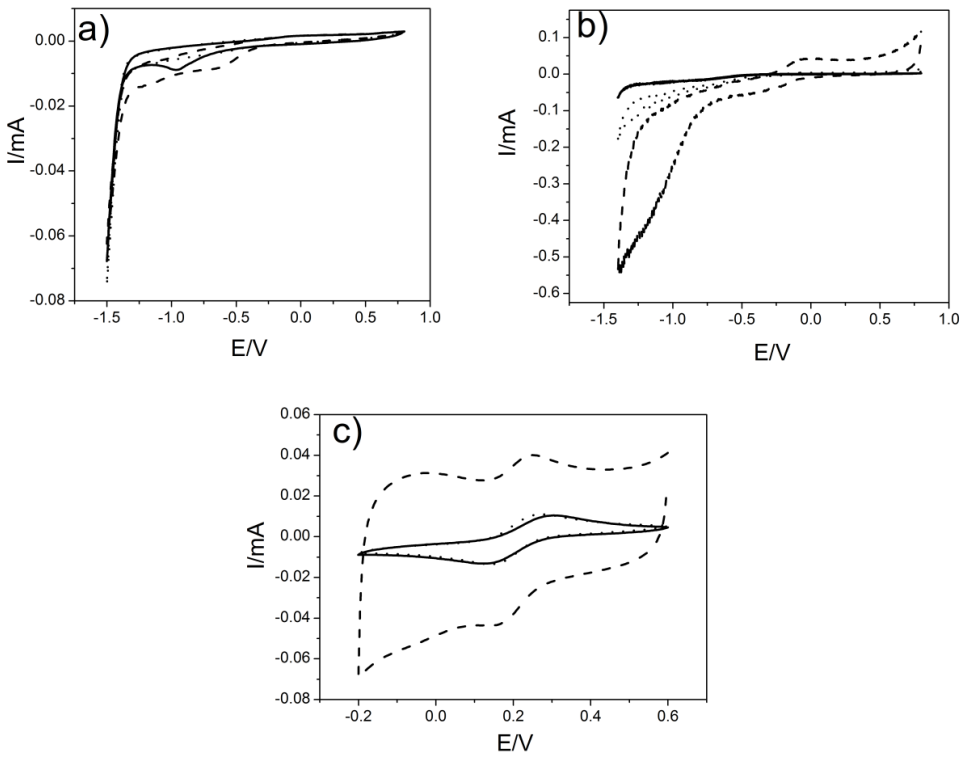

Figure 4.4.1. (a-b) Electrodeposition of GO_01 on GC electrodes in 100 mM PB pH 9 at 10 mV/s, without a) and with b) stirring. The 1st (solid line), 5th (dotted line) and 10th (dashed line) scans are shown. c) CVs of bare GC (solid line), erGO-01_GC without stirring (dotted line) and erGO-01_GC with stirring (dashed line) at a scan rate of 50 mV/s in the presence of 1 mM $[Fe(CN)_6]^{3+}$. The 3rd scan is represented in each case.

In Fig. 4.4.1.a it can be observed that a reduction wave centered at -1.0 V appears in the 1st scan, which is attributed to the irreversible electrochemical reduction of GO (Jiang, Lu et al. 2012).

However, after 10 CVs (dashed line) an increase in the anodic region of the voltammogram is not clearly appreciated, indicating that no deposition on the electrode has occurred with the quiescent solution. Nevertheless, when a continuous stirring is applied through the entire process (Fig. 4.4.1.b), higher cathodic and anodic currents are obtained as the number of scans increased, indicating that the deposition and concomitant reduction of GO_01 took place. Moreover, in the last scan (Fig. 4.4.1.b, dashed line) the cathodic wave starting at -1.0 V shows a 100-fold current increase and a cathodic and an anodic process at -0.4 and -0.1 V respectively appeared, which are attributed to the electrochemically active oxygen functionalities presents on the GO surface, as already reported in literature (Chen, Tang et al. 2011). As confirmation, CVs in the presence of a redox probe, 1 mM $K_3[Fe(CN)_6]$ in 0.1 M KCl, were recorded for bare and graphene modified GC electrodes (Fig. 4.4.1.c). The $Fe(CN)_6^{3-/4-}$ electrochemical signals given by the bare GC (solid line) and the unstirred GO_01 modified GC (dotted line) were almost the same, whereas a 6-fold increase in the capacitive current was measured when the electrodeposition was performed under stirring (dashed line). The latter result clearly indicates an increase of the electroactive area. Indeed, GO sheets diffused to the electrode surface at a higher rate during the electrodeposition process when a constant stirring was applied. Therefore, the GO_01 electrodeposition process was only effective when constant stirring was applied.

4.4.1.1.2 ED of GO-01 by cyclic voltammetry

Further optimization of the electrodeposition process required additional analysis of other parameters involved such as the scan rate and the number of cycles. GC electrodes were used as substrate for the electrodeposition of a GO_01 dispersion in 100 mM PB, pH 9, prepared as reported in section 3.4.4.2. In a preliminary study, 10 cyclic voltammograms were performed under deoxygenated conditions from 0.8 to -1.5 V using different scan rate: 2, 10, 25 and 50 mV/s (Fig. 4.4.2.a).

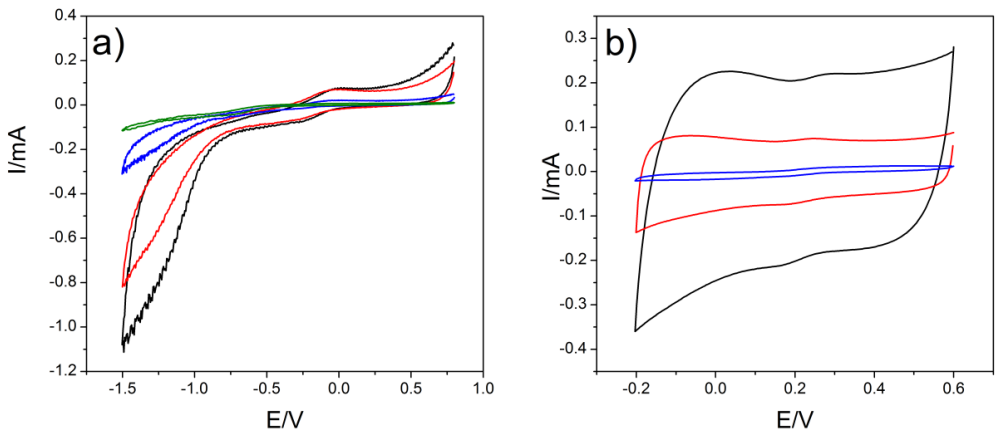

Figure 4.4.2 a) Electrodeposition of GO_01 in 100 mM PB pH 9 carried out by cyclic voltammetry, 10 cycles, at 2 (black curve), 10 (red curve), 25 (blue curve), and 50 mV/s (green curve), under constant stirring. The 10th scan is represented. b) CVs recorded in presence of 1mM $K_3[Fe(CN)_6]$, 0.1 M KCl at 50 mV/s, for the graphene-modified electrode prepared by ED of GO_01 by cyclic voltammetry at 2 (black curve), 10 (red curve) and 25 mV/s (blue curve). The 3rd scan is represented.

The results showed that a lower scan rate yielded higher anodic currents, meaning that more GO is deposited and reduced on the electrode surface. This is because a lower scan rate causes a longer exposition of GO to both the reductive potentials (deposition due to GO reduction) and oxidative potentials (GO deposition induced by the electric field). Indeed, Fig. 4.4.2.b clearly shows a higher capacitive current for the electrodes prepared at 2 mV/s (black curve) and 10 mV/s (red curve). Moreover, the electrodeposition of GO did not occur when a scan rate of 50 mV/s was used.

Both 10 mV/s (Fig. 4.4.3.b) and 25 mV/s (Fig 4.4.3.c) scan rates yielded a more homogenous deposition with smaller aggregates, as observed from optical microscopy images, than at 2 mV/s (Fig. 4.4.3.a). A homogeneous deposition of GO with smaller aggregates on the electrode surface leads to a more electrochemically reversible response of the redox probe, indicated by the smaller peak separation observed for the red CV (ED at 10 mV/s) compared to the black one (ED at 2 mV/s) in Fig. 4.4.2.b. However, ED at 25 mV/s yields a much lower electrode capacitive area. Considering all the results (Table 4.4.1), a cyclic voltammetry performed at 10 mV/s leads to optimized graphene-modified GC electrodes.

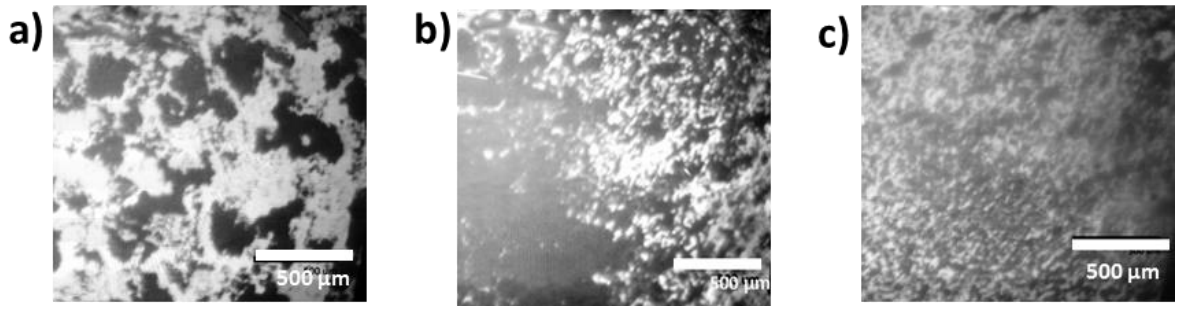

Figure 4.4.3 Optical microscopy images of graphene-modified electrodes prepared by cyclic voltammetry using as scan rate a) 2, b) 10 and c) 25 mV/s.

Method	Electro-deposition variables			C (F)	Agglomerate. size (µm)	Comments
	E_{ED} (mV) vs. As/AgCl	Scan rate (mV/s)	Nº cycles			
Cyclic	0.8 – (-1.5)	**2**	10	4.4×10^{-3}	200-400	Big and few agglomerates Long-time experiment
		10	10	1.4×10^{-3}	<100	Homogeneous deposition
		25	10	3.0×10^{-4}	<25	Lower capacitance Homogeneous deposition
		50	10	-	-	No deposition

Table 4.4.1 Parameters used during the electrodeposition process by cyclic voltammetry, capacitance values and morphological characteristics of the graphene-modified electrodes obtained.

After setting the optimal scan rate at 10 mV/s, the next parameter to optimize was the number of scans recorded. ED by applying 5, 10 or 20 cycles of voltammetry was studied (Fig. 4.4.4.a). As expected, increasing the number of scans lead to higher loads of reduced GO on the electrode surface and, thus, to a higher capacitance (Fig. 4.4.4.b and Table 4.4.2).

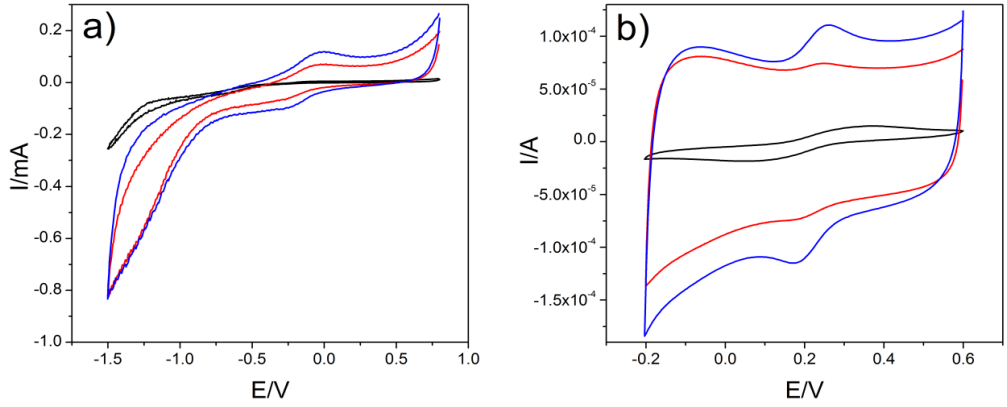

Figure 4.4.4 a) ED of GO_01 in 100 mM PB pH 9 carried out by cyclic voltammetry, 10 mV/s, for 5 (black curve), 10 (red curve) or 20 (blue curve) cycles, under constant stirring. The last scan is represented. b) CVs recorded in presence of 1mM $K_3[Fe(CN)_6]$, 0.1 M KCl at 50 mV/s, for the graphene-modified electrode prepared by ED of GO_01 by cyclic voltammetry for 5 (black curve), 10 (red curve) or 20 (blue curve) cycles. The 3rd scan is represented.

Method	Electro-deposition variables			C (F)	Agglomerate size (µm)	Comments
	E_{ED} (mV) vs. As/AgCl	Scan rate (mV/s)	Nº cycles			
Cyclic	0.8 – (-1.5)	10	5	1.07×10^{-4}	Few ~300 Rest <25	Very low deposition, very low capacitance
			10	1.4×10^{-3}	<100	Homogeneous deposition
			20	1.5×10^{-3}	10-150	Complete coverage but non-homogeneous aggregate size distribution

Table 4.4.2 Parameters used during the electrodeposition process by cyclic voltammetry, capacitance values and morphological characteristics of the graphene-modified electrodes obtained.

Application of 10 or 20 cycles granted an appropriate cover of ED graphene on the electrode surface, as shown in Fig. 4.4.5.b and 4.4.5.c, respectively.

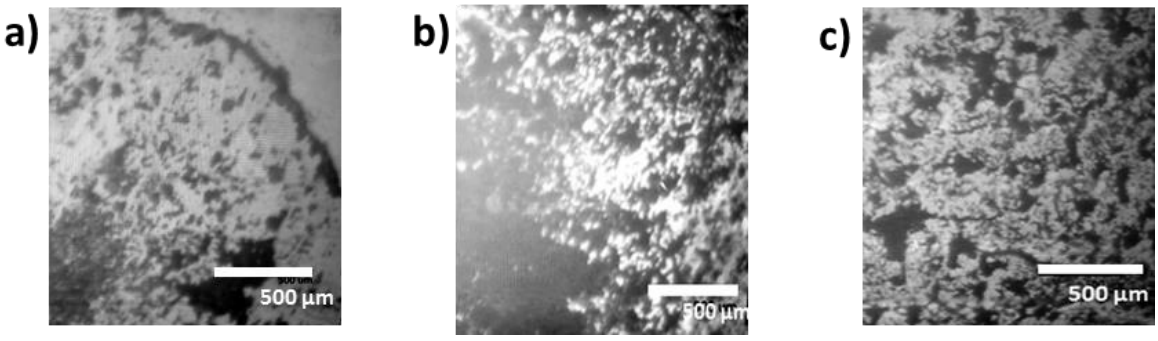

Figure 4.4.5 Optical microscopy images of graphene-modified electrode prepared by cyclic voltammetry cycling the potential for (a) 5, (b) 10 and (c) 20 times.

In conclusion, the optimal conditions to fabricate graphene-based electrodes by cyclic voltammetry are the application of 20 cycles at 10 mV/s scan rate.

4.4.1.1.3 ED of GO_01 by pulsed electrodeposition

A pulsed electrodeposition process of a GO dispersion was studied by applying successive steps of a reductive potential at -1.5 V and an oxidative potential at 0.6 V with fixed pulse times and repeating these pulses for a certain overall time. Pulses of 1s, 2s and 4s were tested, while the overall electrodeposition time was set to 2000 s. As a result, the 1s pulses yielded an electrode with lower capacitive area than those prepared under pulses of 2s or 4s electrodeposition (Fig. 4.4.6).

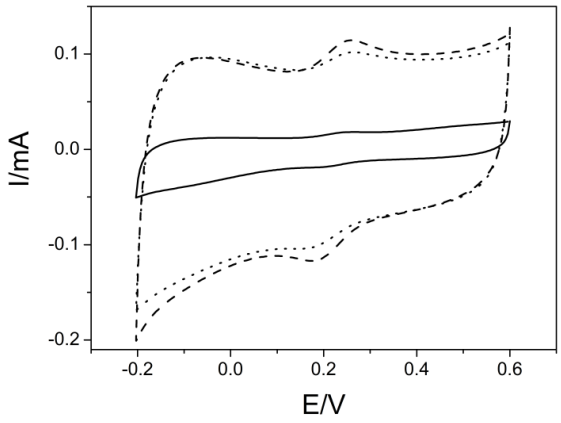

Figure 4.4.6 CVs recorded in presence of 1mM $K_3[Fe(CN)_6]$, 0.1 M KCl at 50 mV/s, for graphene-modified electrodes prepared by pulsed ED of GO_01 at 0.6 and -1.5 V. Each potential pulse was applied for 1s (solid line), 2s (dotted line) or 4s (dashed line) during a total period of 2000 s. The 3rd scan is represented.

As the results for 2s or 4s pulses were very similar, the study with different number of pulses was made in both cases. 250, 500 or 1000 cycles were applied for the 2s pulses measurements; whereas 125, 250 or 500 cycles were applied when 4s pulses were done. In this way the overall ED times were

comparable for the 2s and 4s pulses experiments. Electrodes with a higher capacitive area were obtained when pulses of 2s were applied during 1000 cycles (Fig. 4.4.7.a, blue curve) or when pulses of 4s were applied during 500 cycles (Fig. 4.4.7.b, blue curve). On the other hand, the aggregate size observed were very similar (around 100-200 μm), but in the case of electrode prepared with pulses of 4s a more uniform coverage was obtained than when pulses of 2s were applied (Fig.4.4.8 a-b). For this reason, a pulse time of 4s was selected for the future experiments.

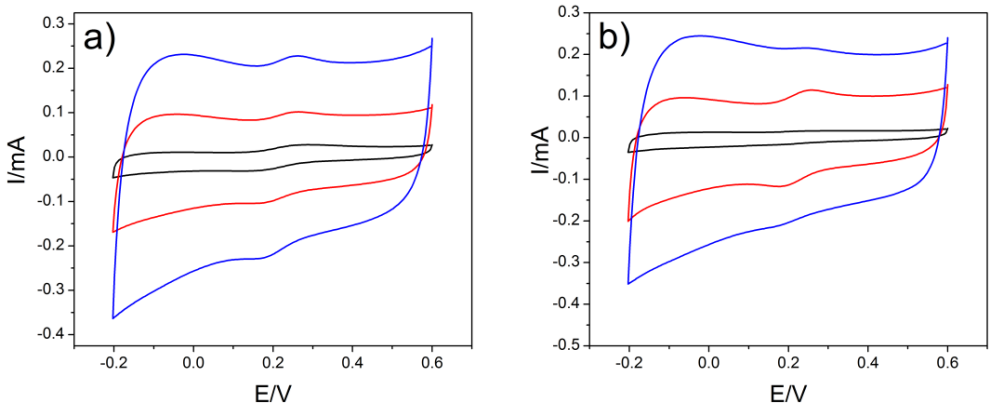

Figure 4.4.7 CVs recorded in presence of 1mM $K_3[Fe(CN)_6]$, 0.1 M KCl at 50 mV/s, for graphene-modified electrode prepared by pulsed ED of GO_01 applying pulses at 0.6 and -1.5 V for 2s a) or 4s b) for a total ED time of 1000 s (black curve), 2000s (red curve) or 4000s (blue curve). The 3rd scan is represented.

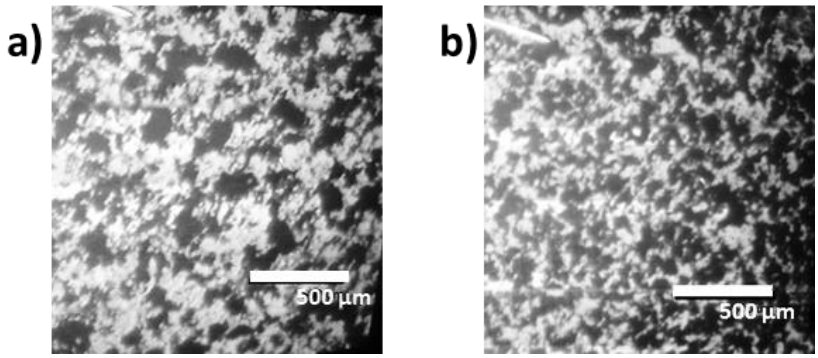

Figure 4.4.8 Optical microscopy images of graphene-modified electrode prepared by pulsed ED with pulses of 2s a) or 4s b) during 4000 s.

Despite the fact that 500 cycles of 4s pulses gave a higher capacitance of the electrodeposited graphene electrode, the electronic transfer with the redox probe is worse than for the electrode prepared with 250 cycles of 4s pulses, as in the former case a larger peak separation and lower peak resolution is observed in the CV recorded in presence of the redox probe (Fig. 4.4.7.b). The improved electron transfer kinetics for the case of the 4s pulses/250 cycles electrodes could be related to the smaller size of the ED aggregates (Table 4.4.3). Considering all these factors (Table 4.4.3), the optimal conditions for a pulsed electrodeposition are: a pulse time of 4s applied for 250 cycles.

Method	Electro-deposition variables				C (F)	Agglomerate size (μm)	Comments
	E_{ED} (mV) vs. As/AgCl	*Pulse time (s)*	*Nº cycles*	*Total time (s)*			
pulsed	0.6 – (-1.2)	1	1000	2000	4.0×10^{-5}	Few ~400 Rest <100	Non homogenous deposition
		2	250	1000	3.4×10^{-4}	20-100	Very low deposition
			500	2000	1.8×10^{-3}	100-150	Homogeneous dispersion of the aggregates
			1000	4000	4.6×10^{-3}	100-200	Homogeneous dispersion of the aggregate
		4	125	1000	3.0×10^{-5}	400	Low deposition, non-homogenous
			250	2000	2.0×10^{-3}	50	Homogenous aggregates size distribution
			500	4000	4.8×10^{-3}	150-200	Homogenous aggregates size distribution

Table 4.4.3 Parameters used during pulsed electrodeposition process, capacitance values and morphological characteristics of the graphene-modified electrodes obtained.

4.4.1.2 GO_02 electrodeposition on GC electrodes

GO_02 dispersion (1 mg/mL) in 100 mM PB pH 9 was prepared as reported in section 3.2.4.2. Electrodeposition of GO_02 dispersion was carried out by cyclic voltammetry and pulsed electrodeposition using the optimization protocols reported above, but the electrodeposition did not take place. The explanation may be that GO_02 was synthetized through a different protocol (as reported in section 3.2.3.2) that yielded a GO with a lower surface O/C ratio (0.45). This lower ratio may have caused that the dispersion pH dropped from 9 to 3, and it is known that acid pH values enable side-reactions during the electrodeposition process that compete with GO reduction (Hilder, Winther-Jensen et al. 2011). However, even after the pH was corrected the electrodeposition did not take place. Another possible problem may be the electrolyte concentration, so a new GO_02 dispersion in H_2O (0.5 mg/mL) containing 150 mM NaCl as electrolyte was prepared as reported in section 3.2.4.2. Indeed, a NaCl concentration ranging from 100 to 250 mM has been reported to provide enough ionic strength and conductivity to the electrolyte solution (Hilder, Winther-Jensen et al. 2011). As this new dispersion presented a pH around 3, in order to avoid possible side-reactions and ensure a successful electrodeposition, the pH of the solution was corrected to 7. With these new conditions the electrodeposition of GO_02 was carried out using cyclic voltammetry or pulsed technique, as shown in Fig. 4.4.9 a-b. Furthermore, the electrodeposition of GO_02 carried out by

cyclic voltammetry provided a graphene modified electrode with higher capacitive area (Fig. 4.4.9.c, solid line) than with the pulsed electrodeposition (Fig. 4.4.9.c, dashed line), unlike the case of GO_01, where the difference was not so pronounced. Higher anodic and cathodic currents are also obtained during the electrodeposition process when GO_02 was used compared to GO_01. GO_02 presents a higher dispersibility of the material in aqueous solution and a more successful ED process, probably due to the lower O/C ratio (0.45) than GO_01 (0.65) in the surface. For all these reasons, the next experiments were performed with electrodes modified with GO_02 following the latter methodology.

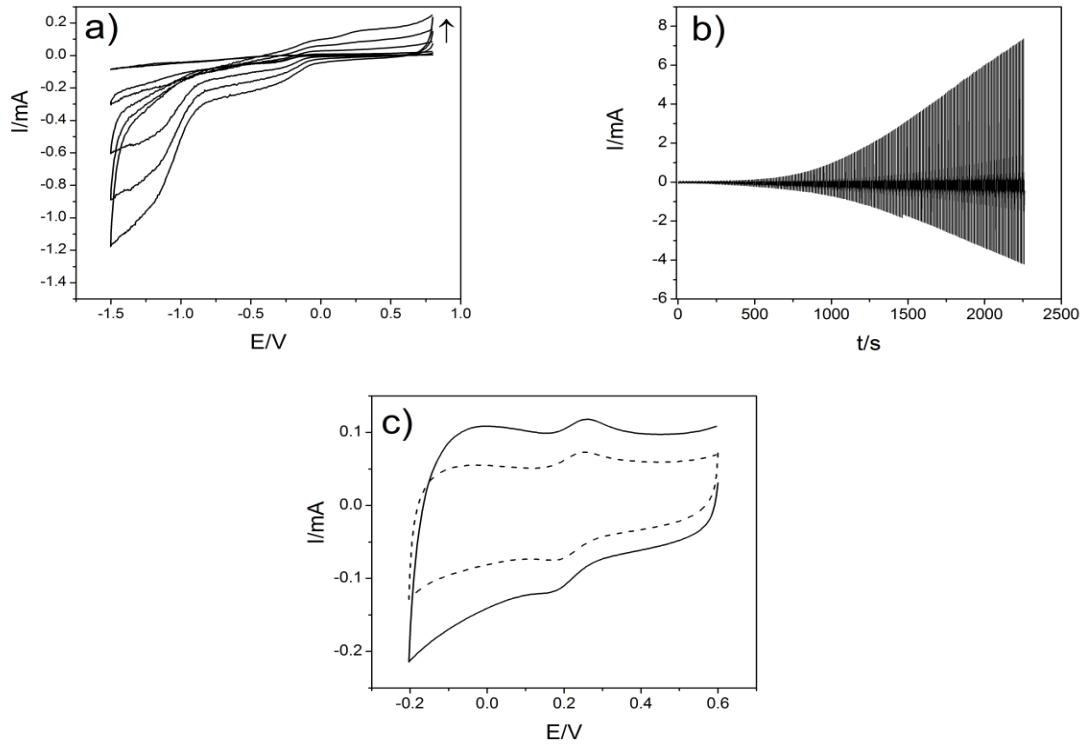

Figure 4.4.9 Electrodeposition of GO_02 in H_20, 150 mM NaCl on a GC electrode by a) cyclic voltammetry at 10 mV/s scan rate (1st, 5th,10th,25th,20th scans are shown), or by b) pulsed ED (4s, 250 cycles). c) CVs recorded in presence of 1mM $K_3[Fe(CN)_6]$, 0.1 M KCl at 50 mV/s, for a graphene-modified electrode prepared by CV (solid line) or pulsed technique (dashed line). The 3rd scan is represented.

Gold was tested as different electrode substrate for the fabrication of graphene-based electrodes in order to verify if the electrodeposition occurs despite of the substrate material employed. Fig. 4.4.10 shows the electrodeposition of GO on an Au-plated substrate. The ED occurred successfully also in this case. The capacitive current increased with the numbers of ED cycles, indicating that the material was deposited on the electrode surface. The capacitive area obtained on gold was very similar to the one obtained on GC electrodes.

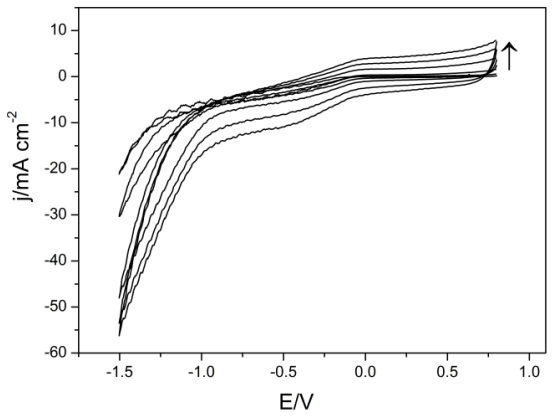

Figure 4.4.10 Electrodeposition of GO_02 on an Au-plated substrate at 10 mV/s scan rate (1st, 5th, 10th, 15th, 20th scans are shown).

4. 4. 2 Stability of the graphene-based electrodes prepared by electrodeposition

Fig.4.4.11 exhibits the CVs of the electrochemically reduced GO (erGO)-GC electrodes before (solid curve) and after (dashed curve) 30 min rotation at 1,500 rpm in presence of 5 mM $K_3[Fe(CN)_6]$ in 0.1 M KCl. The capacitive current, which is directly related to the surface area of the electrode, remains practically constant after the rotation, meaning that no material segregation occurs. Therefore, the electroreduction process created a stable graphene-based electrode due to the formation of strong bonds between the electrode and the erGO.

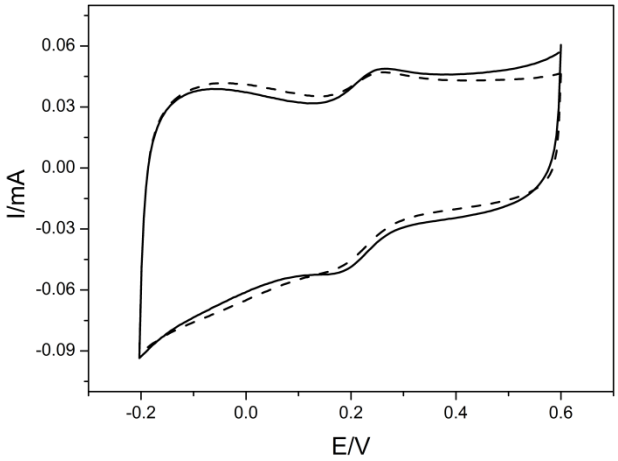

Figure 4.4.11 CVs of erGO-GC electrode at scan rate of 50 mV/s, in the presence of 5 mM $K_3[Fe(CN)_6]$ before (solid curve) and after (dashed curve) 30 min of rotation at 1500 rpm.

A further study of the stability of electrodeposited (ED) electrodes was carried out increasing the number of cycles. 20, 30, 40, 50 and 100 cycles were performed. As shown in Fig.4.4.12, it was possible to electrodeposit material up to 100 cycles, obtaining electrodes with high surface areas. However, in this later case the electrode was not stable for further applications as the excess of material fell down almost immediately. In fact, the electrode presented high stability up to 50 scans of ED, although the fabrication process was too long (as the scan rate used is 10 mV/s). To have a good compromise between capacitive area and fabrication time, the best option chosen was to perform cyclic voltammetry at 10 mV/s scan rate for 30 cycles. Therefore, in all the next experiments 30 scans were employed unless otherwise stated.

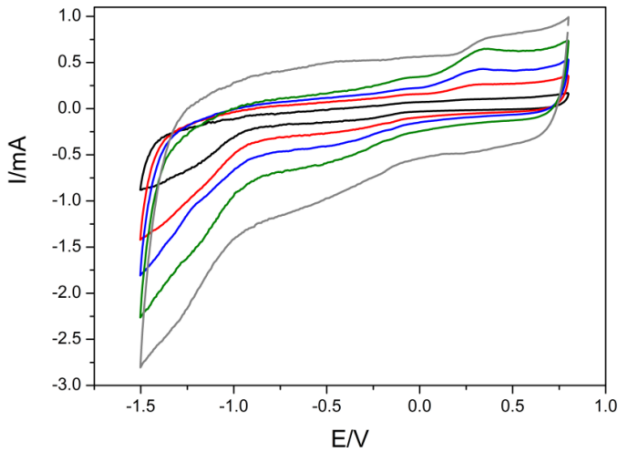

Figure 4.4.12 Electrodeposition of GO_02 on a GC electrode at 10 mV/s scan rate applying 20 (black curve), 30 (red curve), 40 (blue curve), 50 (green curve) and 100 (grey curve) cycles. The last scan of each ED process is shown.

4. 4. 3 Characterization of the optimized graphene-based electrodes

All the chemical and electrochemical characterizations were made using the graphene based electrodes prepared with the optimized conditions: cyclic voltammetry at 10 mV/s was performed for 30 cycles using a pH 7 aqueous GO_02 dispersion with 150 mM NaCl.

4.4.3.1 SEM analysis

The erGO sample was firstly characterized by SEM microscopy. This technique allows a more accurate characterization of the morphology of the sample than optical microscopy, which was used in a first place to visualize in a qualitative way how the different parameters involved in the ED process influenced the morphology of the electrodes prepared. Samples for SEM analysis were prepared on a Au plated substrate because it fits in the sample compartment of the SEM instrument. Fig 4.4.13 shows the morphology of graphene-modified gold substrate. In Fig. 4.4.13.a is observed a non-homogeneous deposition, suggesting that electrodeposition of GO followed a particle nucleation

mechanism and a subsequent growth of the electroreduced GO aggregates. During this process aggregates of ca. ~200 µm size were produced, generating also ca. 100 µm channels (Fig.4.4.13.a). Besides, the x1000 magnification image show pores of 10-20 µm in diameter within the aggregates (Fig. 4.4.13.b). The high dispersion and porosity of GO gives a concomitant high surface area and good diffusion proprieties of redox species to the electrodes.

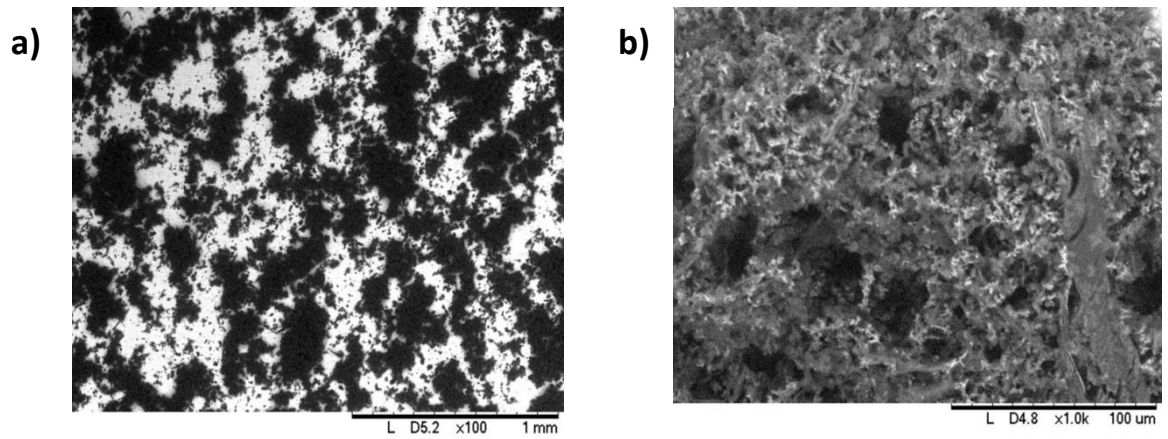

Figure 4.4.13 SEM micrographs at different magnification a) x100 and b) x1000 of electrodeposited GO_02 by cyclic voltammetry (30 cycles) on a Au electrode.

4.4.3.2 XPS results

XPS studies were performed on GO and erGO (Fig. 4.4.14 and 4.4.15). erGO sample was prepared by electrodeposition of GO on a Au-plated substrate for the XPS measurements to avoid interferences in the spectra coming from a carbon-based substrate; whereas a GO pellet sample was used for the analysis. The aim of the XPS characterization was to study whether during the electrodeposition process the GO is reduced to graphene (electrochemically reduced GO, erGO) through the reduction of different oxygen functionalities, which would allow recovering the aromatic structure of graphene and its electrical conductivity. The oxygen-carbon ratio quantification in the surface yielded 0.45 and 0.37 for GO and erGO, respectively. The whole XPS spectra are shown in Fig. 4.4.14.a-b.

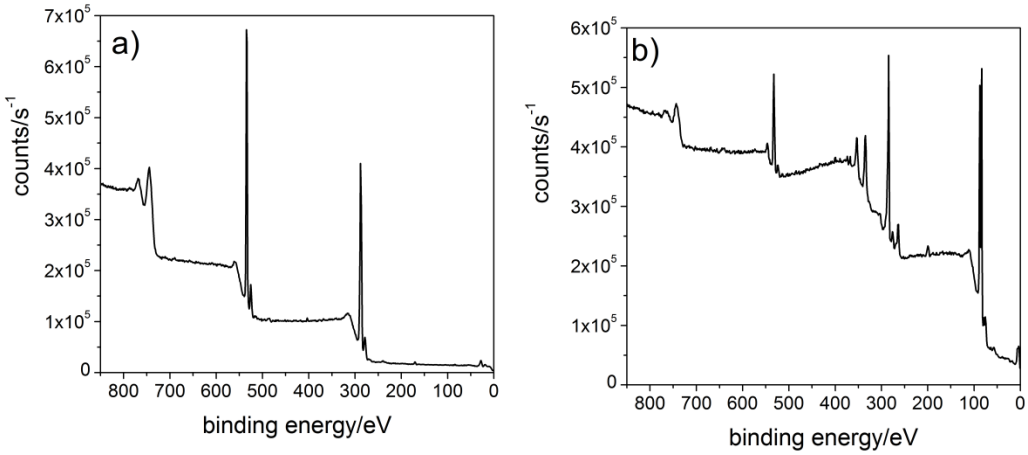

Figure 4.4.14 Whole XPS spectra for a) GO and b) erGO samples.

The analysis of the C1s binding energy region by peak deconvolution exhibited three different components in the case of GO (Fig. 4.4.15.a). These components are assigned to aromatic sp^2 structure at 248.3 eV (40.77%), single C-O bonds (in hydroxyl and epoxy groups) at 286.3 eV (48.54%) and carbon double bonded to oxygen at 287.6 eV (10.69%) (Pogacean, Socaci et al. 2015). In the O1s binding energy region (Fig. 4.4.15.b) again the deconvolution exhibits three different components attributed to double bonded oxygen (in carboxylic/carbonyl groups) at 530.6 eV (4.10%), single bonded oxygen (in hydroxyl, ether, epoxy and peroxy groups) at 532.4 eV (95.38%) and single bonded oxygen in peroxy-acid and peroxy-ester groups at 534.6 eV (0.52%) (Solís-Fernández, Rozada et al. 2012). Once the electrodeposition and electroreduction of GO was achieved, the XPS spectrum differs notably due to the elimination of some oxygen functionalities during the process. In the case of the C1s binding energy region of the erGO, the signal at 284.3 eV, corresponding to carbon-carbon double bonds (C=C, sp^2), increased (47.05 %) and a new component at 285.2 eV (3.86%) appeared, which is attributed to carbon-carbon single bonds (C-C, sp^3) (Fig. 4.4.15.c). This confirms the recovering of the graphitic structure of graphene after electrodeposition. Moreover, the signal at 286.3 eV corresponding to single bonded oxygen-carbon decreased (45.22%), suggesting a loss in hydroxyl and/or ether/epoxy groups. The component attributed to C=O groups at 287.6 eV disappeared, meaning the elimination of carbonyl groups. A small contribution of a new component at 290.4 eV (3.87%) is attributed to $\pi \rightarrow \pi^*$ shake up satellite of graphitic carbons (Bradshaw 1974). The O1s region of erGO (Fig. 4.4.15.d) showed a decrease in the signal at 532.4 eV (86.9%), in agreement with the data obtained in the C1s binding energy region, confirming the partial loss of hydroxyl and/or epoxy/ether groups. A new peak at 533.1 eV (13.1%) appeared which corresponds to single bonded

oxygen in acids, esters and hydroperoxides, indicating the formation of these groups from the reduction of other oxygenated groups, i.e. carboxylic acids.

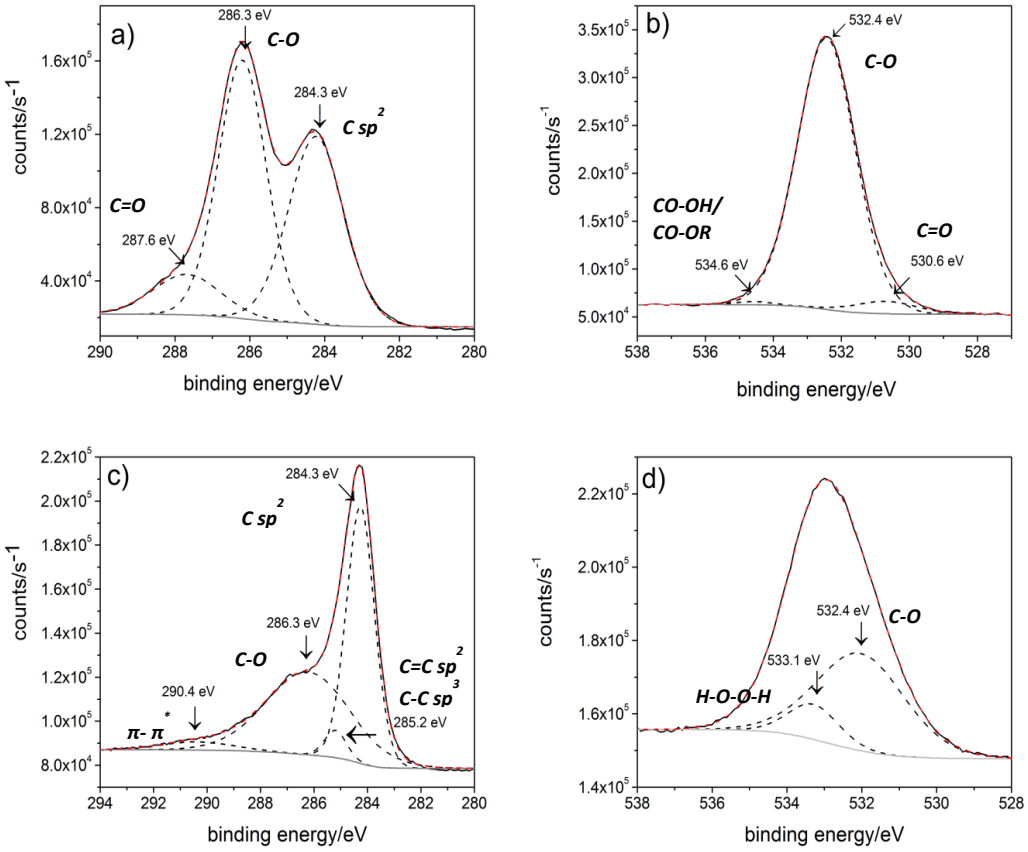

Figure 4.4.15 XPS spectra of C 1s (a, c) and O 1s (b, d) bands of GO (a, b) and erGO (c, d). In all spectra the continuous black and grey lines are the experimental curve and the baseline correction, respectively; the hatched black lines are the different components obtained by the deconvolution process and the red ones are the total curves obtained from the sum of each component, exhibiting an optimum fitting of the experimental data.

4.4.3.3 FTIR spectroelectrochemisty results

In order to obtain further chemical information of the changes imposed on GO upon electrodeposition, FTIR spectroelectrochemical measurements were carried out following the procedure reported in 3.2.2.2 section. As illustrated in Fig. 4.4.16 the spectrum of GO before applying any reduction potential is characterized by a broad and intense peak around 3500-3300 cm^{-1} assigned to O-H stretching, a peak at ~1720 cm^{-1} attributed to C=O stretching of carboxyl and /or carbonyl groups, peaks corresponding to aromatic rings, C=C and C-C in the region between 1620-1450 cm^{-1}, a peak around 1210 cm^{-1} assigned to aryl O-C stretching and a peak around 1100 cm^{-1} attributed to alkoxy or epoxy C-O stretching vibrations. The peaks immediately below 3000 cm^{-1} are generally imputed to symmetric stretching vibrations for $-CH_2$ groups (Simon , Acik, Lee et al. 2011, Toh, Loh et al. 2014). Upon applying a reductive potential, the relative intensity of the peaks assigned to oxygen functionalities, such as O-H at 3500-3330 and C=O at 1720 cm^{-1} decreased significantly. At the same

time the intensity of the bands typical of the aromatic region in general had increased, suggesting the restoration of the aromatic sp^2 structure. The intensity of the peak at~ 1100 cm^{-1} also increased, probably due to the formation of new C-O bonds from the reduction of the carboxylic groups.

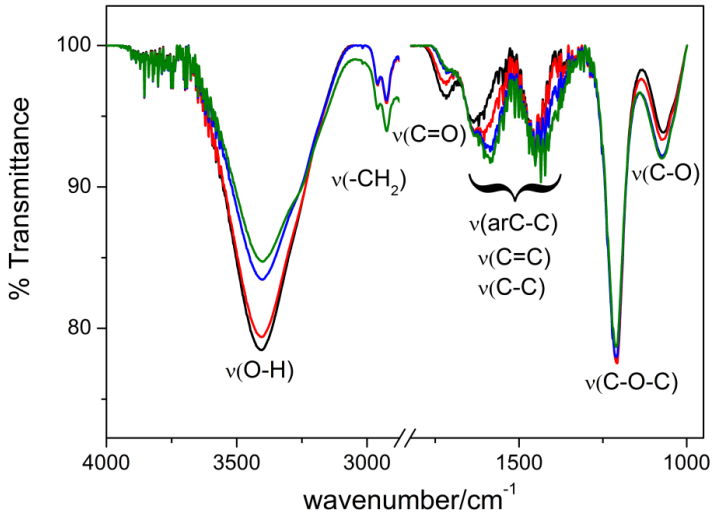

Figure 4.4.16 FTIR spectra of GO suspension in D_2O before (black curve) and after applying a potential of -1.5 V for 5 (red), 30 (blue) and 60 (green) minutes. Baseline correction and background subtraction (D_2O spectrum) were made for all spectra.

From the XPS and FTIR results it could be concluded that during the electrodeposition process the aromatic sp^2 graphitic structure was recovered and although oxygen functionalities were obviously eliminated, some still remained in the material after the process, mainly as hydroxyl and epoxy groups.

4.4.3.4 Electrochemical characterization

Electrochemical characterization of the modified electrodes was carried out by impedance spectroscopy (EIS) and cyclic voltammetry (CV) in presence of 10 mM $K_3[Fe(CN)_6]$ as redox probe, as described in 3.2.6 section. A good fitting of the EIS experimental data (Fig. 4.4.17.a) was obtained using the equivalent circuit reported in Fig 4.4.17.b. The equivalent circuits used for the elaboration of our system are in good agreement with others reported in the literature for similar systems (Navaee and Salimi 2015). In the circuit, R_s is the solution resistance, R_{ct} is the charge transfer resistance at the solid-liquid interface and Z_w is the Warburg impedance resulting from the diffusion of the redox couple towards the electrode surface. The Z_w element τ represent the diffusional time constant, meanwhile an ideal 45º diffusion line is observed when the Z_w exponent α is equal to 0.5. CPE_{dl} and CPE_{pol} are constant phase elements modeling a non-ideal capacitor, representing the charge separation of the double layer and the polarization of the erGO material, respectively. The CPE exponent α (Table 4.4.4) represents the roughness and non-uniformity of the electrode surface, with values between 1 and 0.5. In the case of the erGO-GC electrode, it was only possible to fit the spectra at the low frequency region without significant errors with the addition of an extra capacitance in series with

the Warburg element (Prathish, Barsan et al. 2013). The spectra (Fig. 4.4.17.a) exhibit a well-defined semicircle at high frequency region with a larger diameter for the bare GC, determining a R_{ct} value two orders of magnitude greater than that of erGO-GC (Table 4.4.4). Capacitive lines appear at the low frequency region of the erGO-GC spectrum that is typical for a restricted diffusion behavior within the graphene material (Pifferi, Barsan et al. 2013, Prathish, Barsan et al. 2013). The fact that erGO-GC showed smaller R_{ct} and Z_w values and higher CPE_{dl} values compared to the values obtained for bare glassy carbon electrodes, confirms improved electrode transfer at the electrode-electrolyte interface. The α_{dl} value is lower in the case of erGO-GC electrodes indicating higher porosity and non-uniformity of the graphene-electrode surface.

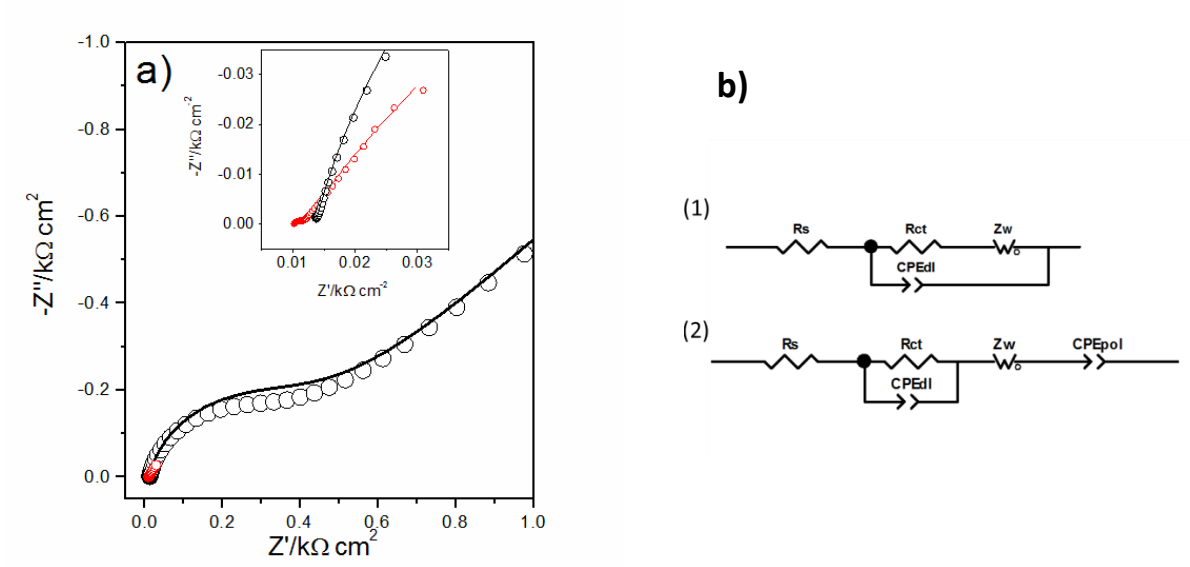

Figure 4.4.17 a) EIS experimental spectra for bare GC (black) and erGO-GC (red); the lines represent equivalent circuit fitting, whereas the dots represent the experimental data. Inset plot: magnification of the high frequency region of complex plane plot. b) Equivalent circuit of (1) bare GC and (2) erGO-GC electrode.

	Rs (Ω)	R_{ct} (Ω cm^2)	CPE_{dl} (F cm^{-2} s$^{\alpha-1}$)	α_{dl}	Z_w (Ω cm^{-2} s$^{\alpha-1}$)	τ	α	CPE_{pol} (F cm^{-2} s$^{\alpha-1}$)	α_{pol}
Bare GC	69.6 ± 0.9	151 ± 5	2.841E-05 ± 9E-08	0.88	19230 ± 57	0.8	0.22	-	-
erGO-GC	51.9 ±0.1	1.4 ± 0.2	1.81E-03 ± 1E-05	0.75	2335 ± 3	9	0.65	0.46 ± 0.08	0.55

Table 4.4.4 Values of the parameters obtained by fitting the impedance spectra with the equivalent circuits shown in Fig. 4.4.20 for bare GC and erGO-GC electrodes.

CVs of bare GC and erGO-GC electrodes were also recorded in the presence of a redox probe at different scan rates (Fig. 4.4.18). Well defined oxidation and reduction peaks are observed, as well as a significant increase in the capacitive area for the graphene-based electrodes (Fig. 4.4.18 a,b). For the erGO-GC electrode, the peak-to-peak separation ΔE_p was 65 mv at 10 mV/s. A low ΔE_p value close to the ideal one of 59 mV indicates a fast electron transfer for a single-electron electrochemical reaction (Shao, Wang et al. 2010). A slight peak potential shift with increasing the scan rate was observed indicating a level of quasi-reversibility in the system. Despite of this, the linear relationship of peak intensity *vs.* the square root of the scan rate, followed the Randles-Sevick equation (Bard and Faulkner 2000) indicating a predominantly diffusion controlled process (Fig.4.4.18 c,d). This diffusion limitation is also suggested by a modest three-fold increase in the peak currents of the erGO-GC electrode compared to the bare GC one, in spite of the ten-fold increase of the double layer capacitance of the modified electrode. This result is in agreement with the results of impedance spectroscopy, where the presence of a Warburg element confirms a diffusion-controlled behaviour.

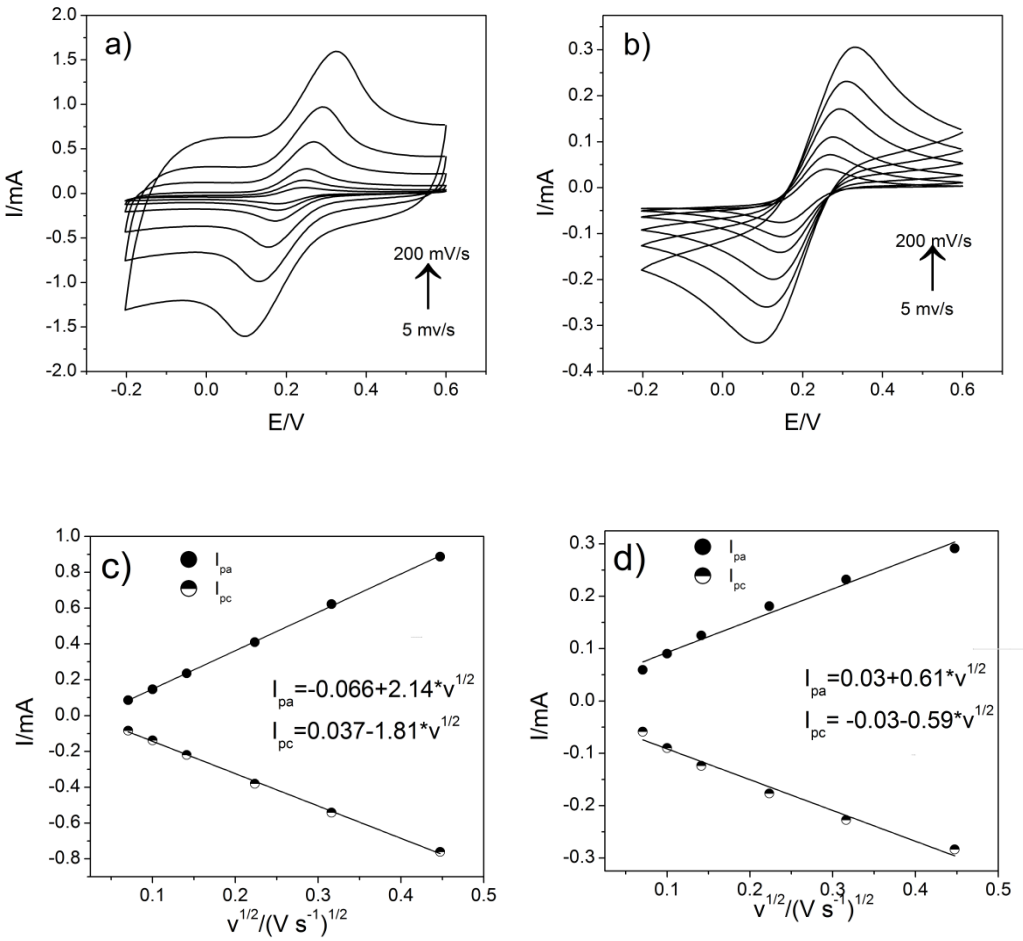

Figure 4.4.18 CVs recorded respectively for erGO-GC a) and bare GC b) electrodes at 5, 10, 20, 50, 100, 200 mV/s in presence of 10 mM $K_3[Fe(CN)_6]$. Peak intensity vs. the square root of the scan rate for erGO-GC c) and bare GC d) electrodes.

4.4.4 Electrocatalytic performance of enzymatic electrodes

The robust, stable and high surface area electrode prepared by ED of GO on GC may be used as support for different electrochemical applications, such as the immobilization of enzymes and tested as a biosensor or a biocathode/bioanode. In this section bilirubin oxidase and laccase have been used for the fabrication of graphene-based biocathodes and tested for the catalytic reduction of oxygen to water.

4.4.4.1 Bilirubin oxidase-modified biocathodes

The electrochemical reduction of GO yields a porous surface with oxygen-based functional groups, as demonstrated by XPS and FTIR analysis. The initial objective was to use these functional groups for the covalent immobilization of the enzyme without any further functionalization of the electrode surface. In this preliminary experiment an aliquot of mtBOx 4 mg/mL was immobilized on erGO-GC electrode prepared by ED of GO_02 by cyclic voltammetry at 10 mV/s for 20 cycles. Afterwards amide bonds were formed using ECD/NHS strategy between the functional groups still present on erGO surface and lysine groups on the enzyme surface, as reported in 3.2.5.2.1 section.
A small catalytic response to O_2 reduction is observed (Fig. 4.4.19) using this electrode.

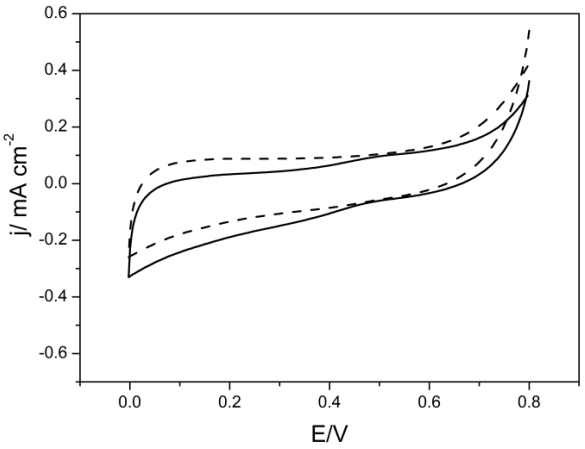

Figure 4.4.19 Electrocatalytic oxygen reduction at RT with a mtBOx-erGO-GC electrode without any further functionalization. CVs in N_2 (dashed curve) or O_2 (solid curve) saturated atmosphere at 0 rpm were shown. CVs were performed at 10 mV/s in 100 mM phosphate buffer pH 7.4.

In order to improve their electrocatalytic performance, the erGO-GC electrodes were electrochemically functionalized with a naphtoic acid monolayer (NA-erGO-GC) (Gutiérrez-Sánchez, Pita et al. 2013), as reported in 3.2.5.2.1 section. Such modification procedure increases the density of carboxylic groups for the further covalent immobilization of mtBOx. Fig. 4.4.20 shows the reductive curve for the reduction of diazo group; only two scans at 200 mV/s were performed in order to minimize the formation of multilayers on the electrode surface.

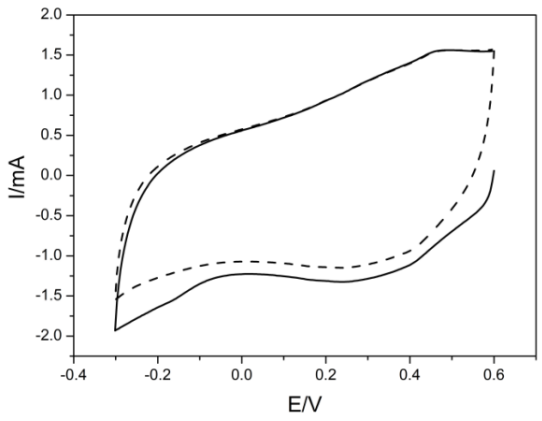

Figure 4.4.20 erGO-GC modification with 6-amino-2 napthoic diazonium salt prepared in situ. The first scan is represented with a solid line while the second scan is represented with a dashed line.

The covalent immobilization of mtBOx was carried out using the EDC/NHS strategy, in which the carbodiimide (EDC) activates the carboxylic groups of the electrode surface for the formation of amide bonds with the amino groups on the enzyme surface (3.2.5.2.1 section). NHS is added to stabilize the intermediate of the reaction against hydrolysis (Hermanson 2013). After the covalent immobilization of mtBOx on the NA-erGO-GC electrode surface, the catalytic response to O_2 reduction of this electrode was tested by cyclic voltammetry (Fig. 4.4.21). In this case, a strong electrocatalytic effect is detected (Fig. 4.4.21.a, red curve); moreover, mass transport limitation under stationary conditions (red curve) due to the thickness of the catalytic layer is observed, which is reduced when the electrode was rotated at 500 rpm (Fig. 4.4.21.a, blue curve).

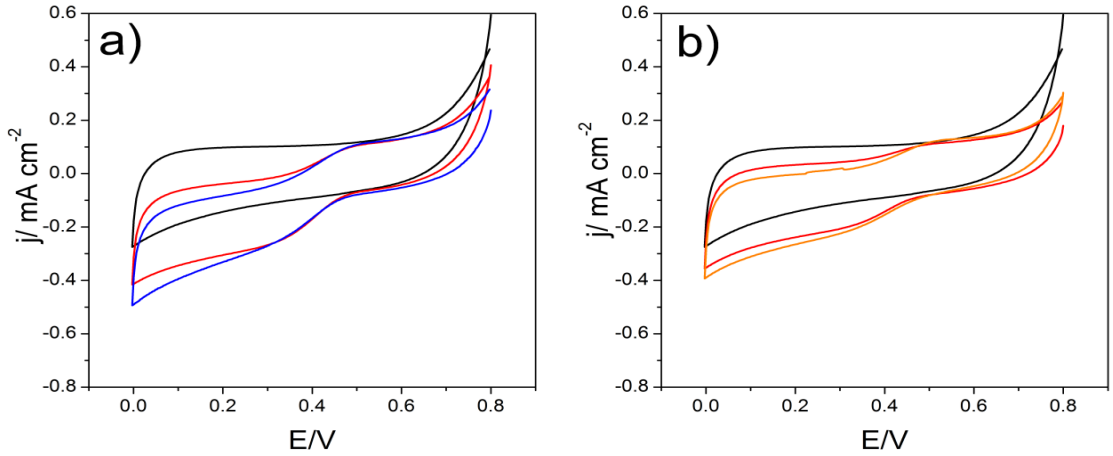

Figure 4.4.21 Electrocatalytic oxygen reduction at RT with mtBOx-NA-erGO-GC electrode: a) CVs in N_2 (black curve) or O_2 (red curve) saturated atmosphere at 0 rpm or 500 rpm (blue curve) are shown; b) CVs in N_2 (black curve) or O_2 (red curve) saturated atmosphere at 0 rpm or with the addition of 0.1 mM ABTS at 0 rpm (orange curve) are represented. CVs were performed at 10 mV/s in 100 mM phosphate buffer pH 7.4.

Addition of 0.1 mM ABTS, as redox mediator, increased the current density by ca. 24% under stationary conditions (Fig. 4.4.21.b), indicating that some enzyme molecules are not properly oriented for a DET regime. The current densities were measured at 100 mV from the onset potential, where a purely kinetic regime is expected.

The next test aimed to enhance the catalytic current by doubling the enzyme concentration to be immobilized up to 8 mg/mL. Fig. 4.4.22 shows a negligible catalytic current enhancement by changing the catalyst concentration. This result suggests that enzyme saturation of the catalytic layer is already achieved using a concentration of 4 mg/mL. For this reason, in the forthcoming experiments a concentration of 4 mg/mL of mtBOx was used always.

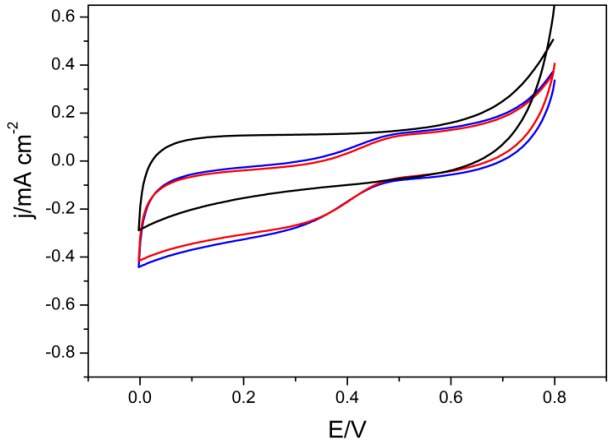

Figure 4.4.22 Electrocatalytic oxygen reduction at RT with a mtBOx-NA-erGO-GC electrode using 4 mg/mL (red curve) or 8 mg/mL (blue curve) of catalyst concentration. CVs in N_2 (black curve) or O_2 (red, blue curves) saturated atmosphere at 0 rpm are represented. CVs were performed at 10 mV/s in 100 mM phosphate buffer pH 7.4.

Another attempt to increase the enzyme density on the electrode consisted on using an electrode with higher surface area than the previous one. In this case an erGO-GC electrode prepared by ED of GO_02 by cyclic voltammetry at 10 mV/s for 30 cycles was used and further functionalized with naphtoic acid monolayer for the covalent immobilization of mtBOx, as previously reported in 3.2.5.2.1 section. The electrocatalytic performance of this electrode was tested by cyclic voltammetry (Fig. 4.4.23). Firstly, a clear enhancement of the capacitive current is observed in comparison to the previous cases; additionally, a strong catalytic effect is detected, reaching a current density plateau (after subtracting the capacitive current) of ca. 0.4 mA/cm^2 at 1500 rpm. Under stationary conditions (Fig. 4.4.23, red curve) a clear mass transport limitation is appreciated due to the thickness of the catalytic layer, limitation that is reduced upon rotating the electrode at 500 rpm (Fig. 4.4.23, blue curve). However, further increase in the rotating speed barely improved the electrocatalytic response (Fig. 4.4.23, green and grey curve), meaning that mass transport limitation of the substrate to the electrode surface has been overcome with the rotations. However, it is worth mentioning that the

electrode rotation does not eliminate the mass transport limitation of the substrate inside the porous structure of the electrode (Gara, Ward et al. 2013).

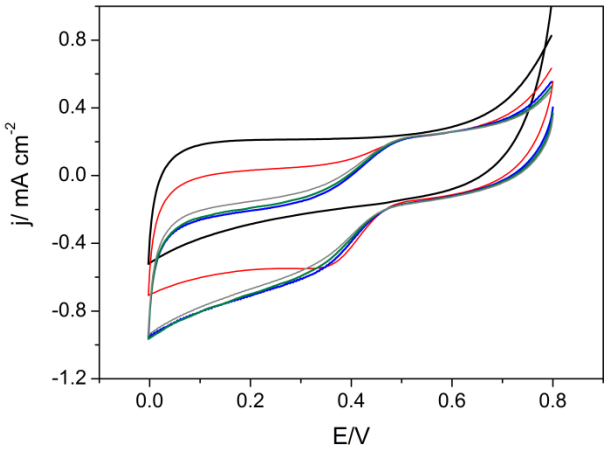

Figure 4.4.23 Electrocatalytic oxygen reduction at RT with a mtBOx-NA-erGO-GC electrode. CVs in N_2 (black curve) or O_2 (red curve) saturated atmosphere at 0 rpm are represented. Blue, green and grey curves were recorded at 500, 1000 and 1500 rpm, respectively in O_2 saturated conditions. CVs were performed at 10 mV/s in 100 mM phosphate buffer pH 7.4.

As illustrated in 4.4.2 section, it is possible fabricate stable erGO-GC electrodes by cyclic voltammetry performing up to 50 CVs. A deeper analysis of the catalytic response was performed using as support erGO-GC electrodes fabricated using 40 or 50 cycles during the ED process (Fig. 4.4.24). An enhancement of the capacitive area is observed, as expected. Similar increase of the catalytic current under rotational conditions (blue curve) compared to the stationary one (red curves) is recorded for both electrodes, indicating a good reproducibility of the functionalization and immobilization strategies.

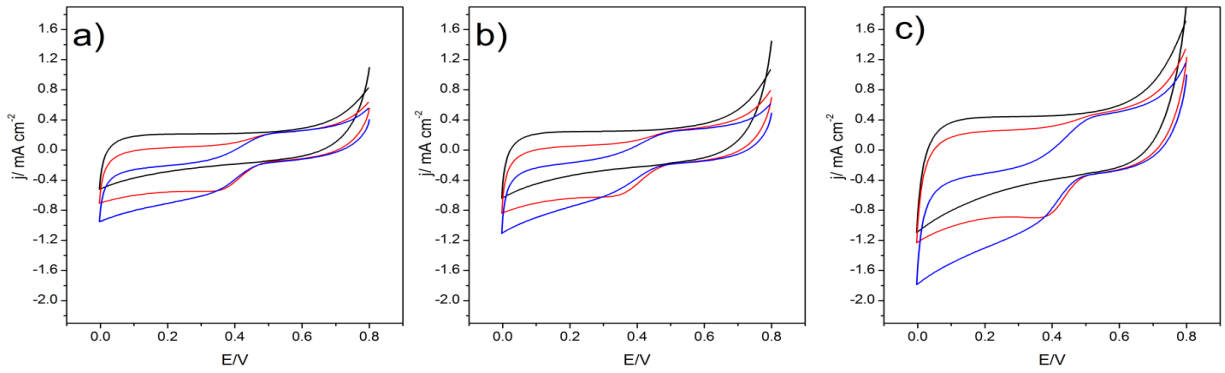

Figure 4.4.24 Electrocatalytic oxygen reduction at RT with a mtBOx-NA-erGO-GC electrode prepared by ED performing (a) 30, (b) 40 or (c) 50 cycles. CVs in N_2 (black curves) or O_2 (red curves) saturated atmosphere at 0 rpm or at 500 rpm (blue curves) are represented. CVs were performed at 10 mV/s in 100 mM phosphate buffer pH 7.4.

Table 4.4.5 shows that the general trend is that the catalytic current density (after subtracting the capacitive current) increases with the electroactive area of the erGO-GC electrode, as it allows a higher coverage of immobilized enzyme.

	j at 100 mV E_{onset} (mA cm^{-2})
20 scans	-0.09
30 scans	-0.28
40 scans	-0.26
50 scans	-0.36

Table 4.4.5 Current densities values (after subtracting the capacitive currents) for O_2 reduction at stationary conditions obtained using mtBOx-NA-erGO-GC electrodes prepared by ED performing different number of cycles. The current densities were measured at 100 mV from the onset potential, where a purely kinetic regime is expected.

4.4.4.2 Laccase-based biocathodes

Laccase-based biocathodes were prepared by direct functionalization of erGO-GC electrodes prepared by ED of GO_02 by cyclic voltammetry at 10 mV/s for 30 cycles. Such preparation grants an electrode with high surface area and good catalytic response. The erGO-GC electrodes were functionalized electrochemically with an aminoaryl monolayer (AP-erGO-GC), as explained in 3.2.5.1.2 section. Fig 4.4.25.a shows the CV for the reduction of diazo groups and in Fig. 4.4.25.b the subsequent reduction of the nitro groups to amino ones.

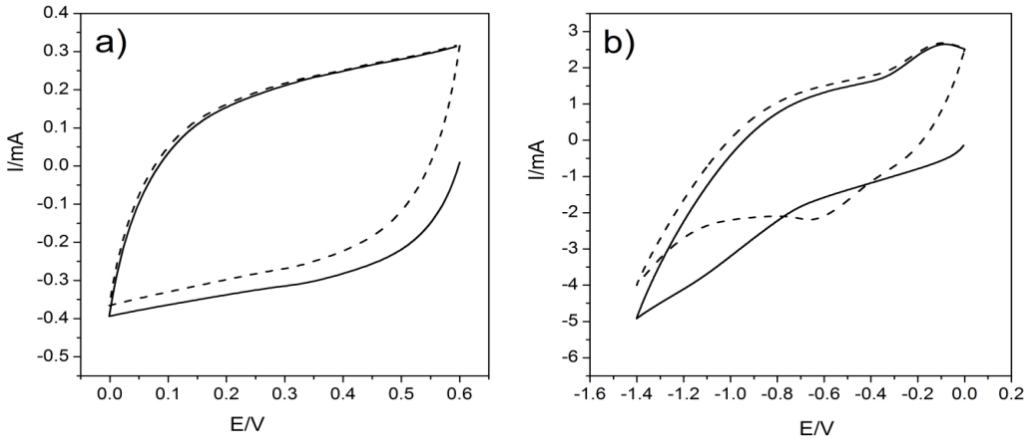

Figure 4.4.25 a) erGO-GC modification with 4-nitrobenzene diazonium salt in CH_3CN, 0.1 M Bu_3NBF_4. b) Electrochemical reduction of nitro groups to amino groups in $EtOH/H_2O$ 1:9, 0.1 M KCl. The first scan is represented with a solid line and the second scan is represented with a dashed line.

If the results obtained through this modification for graphene-based electrodes are compared with the ones obtained with a LDG electrode (described in the previous chapter, 4.3.2 section), a higher

capacitive area for the former ones is first noticed, but also a higher peak separation of the reversible redox equilibrium between ArNO/ArNHOH is observed (Fig. 4.4.25.b, dashed line).

This result suggests the existence of a kinetic limitation of the ArNO/ArNHOH redox process on the erGO-GC electrodes. The higher porosity of erGO-GC electrodes favours the formation of multilayers of aromatic rings and consequently a portion of Ar-NHOH groups would be more distant from the electrode surface, slowing down the electron transfer process with the electrode.

ThLc was then covalently immobilized following the procedure previously reported (3.2.5.1 section), which is the formation of imine and amide bonds between the enzyme and the electrode surface in two steps. The electrocatalytic response to O_2 reduction of the ThLc-AP-erGO-GC electrode was tested by cyclic voltammetry (Fig. 4.4.26). Fig. 4.4.26.a shows a clear catalytic effect under stationary conditions (red curve), reaching a current density plateau of ca. -0.9 mA/cm^2, higher that in the case of BOx-erGO-GC electrode. An explanation of this difference is that ThLc showed a higher specific activity in solution (using ABTS as electron donor) at the optimum pH than mtBOx at the same conditions. Again, the mass transport limitation was reduced by rotating the electrode at 500 rpm (Fig. 4.4.26.a, blue curve). Increasing the rotational speed rate barely improved the catalytic response. Addition of 0.1 mM ABTS as redox mediator (Fig. 4.4.26.b) increased the current density by 20% under stationary conditions, indicating that a significant portion of laccases were unable to connect with the electrode *via* DET regime. Furthermore, the increase in the rotational speed rate in a MET+DET regime yielded higher improvements of the catalytic response than in the case of only DET regime, indicating that transport of the redox mediator to the electrode is also rate-limiting the electrocatalytic process.

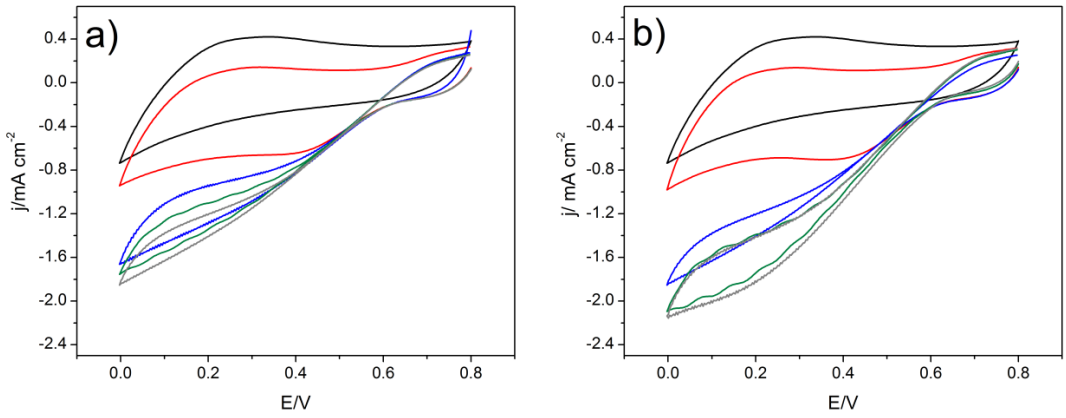

Figure 4.4.26 Electrocatalytic oxygen reduction at RT with a ThLc-AP-erGO-GC electrode in a) DET or b) MET regime. CVs in N_2 (black curve) or O_2 (red curve) saturated atmosphere at 0 rpm are represented. Blue, green and grey curves were recorded at 500, 1000 and 1500 rpm, respectively in O_2 saturated conditions. CVs were performed at 10 mV/s in 50 mM acetate buffer pH 4.2 containing 100 mM $NaClO_4$.

The electrocatalytic response obtained using ThLc-AP-erGO-GC electrodes with different graphene loading was studied. Fig 4.4.27 illustrates the results obtained in O_2 saturated conditions, under stationary conditions (red curves) or rotating the electrodes at 500 rpm (blue curves) for different

erGO-GC electrodes prepared by ED of GO_02. Increasing the number of voltammetry cycles during ED yielded the observed increase in the capacitive current of the erGO-GC electrode. The catalytic response is clearly enhanced when the 30 scans-erGO-GC electrode was tested, but the difference is not so pronounced when the 40 scans-erGO-GC electrode was used. Moreover, with the highest loading of graphene (Fig. 4.4.27.d) a strong catalytic effect is detected, improving the catalytic current density (after subtracting the capacitive area) (Table 4.4.6). Using different biocatalysts, BOx or laccase, the same trend is observed: increasing the loading of graphene increases the electrocatalytic response. However, lower reproducibility is expected with electrodes with such a high loading of graphene due to the fact that it is more difficult to control the surface functionalization for the further enzyme immobilization. This may explain some discrepancies observed in the bioelectrocatalytic response dependence on the increasing amount of the electrodeposited graphene. In conclusion, the optimum graphene loading in terms of time of fabrication and electrocatalytic response is the one obtained when 30 cycles are performed.

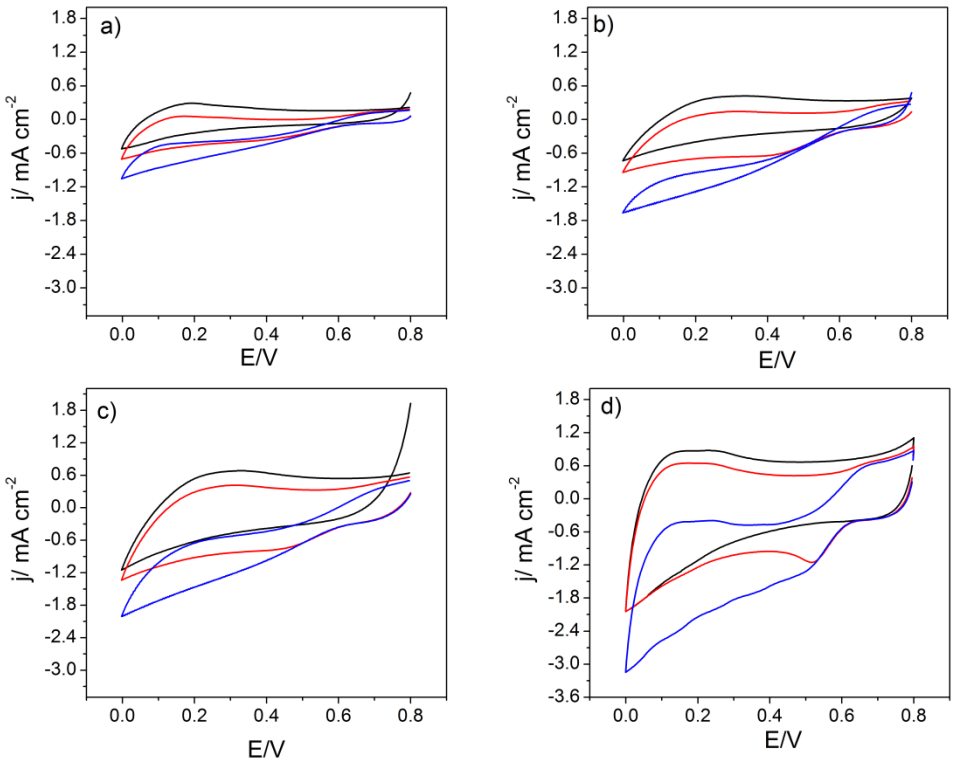

Figure 4.4.27 Electrocatalytic oxygen reduction at RT with a ThLc-AP-erGO-GC electrode prepared by ED performing a) 20, b) 30, c) 40 or d) 50 cycles. CVs in N_2 (black curves) or O_2 (red curves) saturated atmosphere at 0 rpm or at 500 rpm (blue curves) are represented. CVs were performed at 10 mV/s in 50 mM acetate buffer pH 4.2 containing 100 mM $NaClO_4$.

	j at 100 mV E_{onset} (mA cm^{-2})
20 scans	-0.68
30 scans	-1.09
40 scans	-1.38
50 scans	-0.88

Table 4.4.6 Current densities values (after subtracting the capacitive currents) for O_2 reduction at stationary conditions obtained using ThLc-AP-erGO-GC electrodes prepared by ED performing different number of cycles. The current densities were measured at 100 mV from the onset potential, where a purely kinetic regime is expected.

4.4.4.3 Tafel plots and reaction mechanism

A deeper study of the oxygen reduction reaction (ORR) kinetics with the enzymatic electrodes was performed. Polarization curves of the mtBOx-NA-erGO-GC and ThLc-AP-erGO-GC electrodes were obtained by subtracting the background cathodic scans measured under N_2 to the ones measured under O_2 at 500 rpm (Fig. 4.4.28.a). Tafel plots were obtained from the polarization curves after the correction of the ohmic drop caused by the resistance of the system, mainly the ionic resistance of the electrolyte, and of the mass transport limitations of the substrate from the solution to the electrode surface (Fig. 4.4.28.b) (Thorum, Anderson et al. 2010).

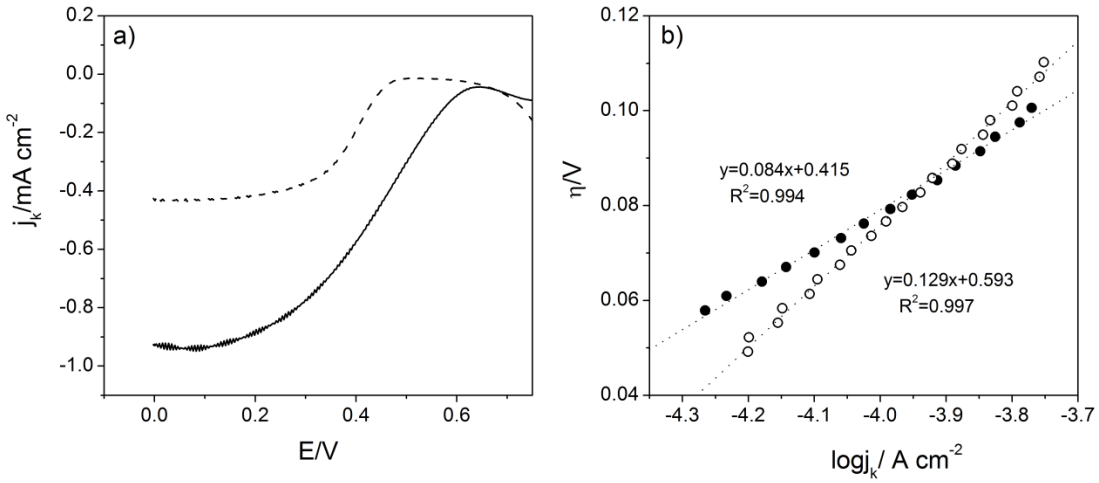

Figure 4.4.28 a) Background-corrected polarization curves for a mtBOx-NA-erGO-GC (dashed curve) and ThLc-AP-erGO-GC (solid curve) electrode at 500 rpm, room temperature and 10 mV/s scan rate and b) Tafel plots of mtBO-erGO-GC (black dots) and ThLc-erGO-GC (white dots) electrodes obtained after correcting the ohmic drop and the mass transport limitation.

The ohmic drop was corrected using the R_s value obtained by the intersection of the semicircle at the high frequency region of Nyquist plot. The mass transport corrected current density was calculated using eq. (4.3) (Thorum, Anderson et al. 2010), derived from the Koutecky-Levich equation for a first order reaction:

$$j_{k=} \frac{(j*j_L)}{(j_L-j)} \quad (4.3)$$

Where j_k is the calculated current density and j_L is the limiting current density under mass transport control. The j_L value at 500 rpm was theoretically calculated as -3.5 mA/cm^2 from the Levich eq. (4.4) (Bard and Faulkner 2000):

$$j_L = 0.62nFD_0^{2/3}v^{-1/6}C_0\omega^{1/2} \quad (4.4)$$

where:

- *n* is the number of electrons involved in the ORR process (4);
- F is the Faraday constant (96,486 C/mol);
- D_0 is the diffusion constant of O_2 ($2.4 \cdot 10^{-5}$ cm^2/s);
- υ is the kinetic viscosity ($9.2 \cdot 10^{-3}$ cm^2/s);
- C_o is the bulk concentration of O_2 in a saturated water solution ($1.1 \cdot 10^{-6}$ mol/cm^3) at the experimental conditions of 25 ºC, 705 mmHg and 0.1 M salt (Lide 1993);
- ω is the electrode rotation speed in rad/s.

An onset potential of 0.49 and 0.64 V was observed from the polarization curves for BOx-erGO-GC and ThLc-erGO-GC, respectively. The difference in the redox potential of the copper T1 site of each enzyme may explain the ca. 150 mV difference in the onset potential. However, it must be taken into account that the different pH values of the electrocatalytic measurements for each enzyme may also affect the onset potential (see below). In order to propose an oxygen reduction mechanism for the enzymatic electrodes, multistep and multi-electron reactions are considered with both an α transfer coefficient **(**4.5) and Tafel (4.6) expressions as follows (Thorum, Anderson et al. 2010):

$$\alpha = \left(\frac{\gamma}{v} + r\beta\right) \quad (4.5) \qquad \frac{dE}{dlogi} = \frac{2.3\ RT}{\alpha F} \quad (4.6)$$

Where:

- γ represents the number of electrons transferred in the step prior to the rate determining step;
- υ is the stoichiometric number (number of times the step occurs per cycle);
- r is the number of electrons transferred in the rate determining step;
- β stands for the symmetry factor;
- R, T and F are the ideal gas constant, the temperature and the Faraday constant respectively.

Tafel plots, represented as the log of the current density obtained after the correction of the ohmic drop and mass transport limitation *vs*. the overpotential, showed a linear region where slopes of 84 mV/dec and 129 mV/dec were obtained for BOx-NA-erGO-GC and ThLc-AP-erGO-GC, respectively (Fig. 4.4.28.b). From the slopes it is possible find out the α coefficient (Eq. 4.6) and then study the rate determining step of the reaction from Eq. 4.5. The difference in the Tafel slopes obtained, suggests that despite both enzymes carried out the same catalytic process, the rate determining step is different (Kear and Walsh 2005). Solomon et *al*. proposed a ping pong mechanism with four substrate molecules undergoing a single electron oxidation step at the T1 site for the four electron reduction of O_2 to H_2O at the trinuclear cluster (TNC) site (Solomon, Sarangi et al. 2007). This mechanism was applied for laccase-modified gold electrodes by Thorum et *al*. (Thorum, Anderson et al. 2010):

1. $Cu_{T1}^{2+} + e^- \rightarrow Cu_{T1}^{+}$
2. $Cu_{T1}^{+} + Cu_{T2/T3}^{2+} \rightarrow Cu_{T1}^{2+} + Cu_{T2/T3}^{+}$
3. $O_2 + Cu_{T3}^{+} \rightarrow$ *Peroxy intermediate (PI)*
4. *Peroxy intermediate (PI)* $\rightarrow$ *Native intermediate (NI)*
5. *Native intermediate (NI)* $+ 4H^+ \rightarrow 2H_2O + 4Cu^{2+}$

where PI and NI are the peroxy and native intermediates, respectively (Solomon, Sarangi et al. 2007).

Taking into account the expressions in equation (4.5) and (4.6), the rate determining step for each process can be suggested. For ThLc-erGO-GC electrode, an α transfer coefficient close to ½ is obtained from the Tafel slope value of 129 mV/dec, which is the expected value for an ideal one electron transfer process at room temperature (Agbo, Heath et al. 2013). A symmetry factor (β) of 0.5 is obtained if the first step of the reaction mechanism is considered the rate limiting step, where α = β (Thorum, Anderson et al. 2010). As a result, the Tafel plot indicates that DET to the T1 site of the immobilized laccase is the rate limiting step, accordingly with previous works on laccase electrodes reported by others authors (Blanford, Foster et al. 2009, Thorum, Anderson et al. 2010, Agbo, Heath et al. 2013). On the other hand, in the case of BOx-erGO-GC electrodes, a α value of ~ 2/3 is obtained from the Tafel slope of 84 mV/dec. If the same ORR mechanism is considered for this enzymatic electrode, α lays between the value expected for the first step being the rate limiting one (α = ½) and the one expected for the second step being rate limiting (α = 4/3). Therefore, this α value could be attributed to a mechanism where both the first (outer electron transfer from the electrode) and second (intramolecular electron transfer) are rate-limiting steps. However, it is not possible to rule out an effect of heterogeneous current density distribution due to the high surface area provided by graphene on the electrode surface (Newman and Tobias 1962).

Furthermore, polarization curves of the ThLc-AP-erGO-GC electrode were obtained as reported in the previous case aiming to study the pH effects on the reaction mechanism (Fig. 4.4.29.a). Tafel plots were obtained in the same manner (Fig. 4.4.29.b). Tafel plots showed a linear region where slopes of 130 mv/dec or 126 mV/dec were obtained for laccase-modified electrode at pH 4.2 or pH 5.5,

respectively. The slope values obtained are almost similar and a α transfer coefficient close to ½ could be extrapolated, indicating that the rate-determing step of the reaction mechanism is the first step in both cases, despite the change of 1.3 pH unit. However, from the polarization curve it could be observed a shift of the onset potential of almost -0.06 V/pH unit. A similar shift of the onset potential when the pH of the solution increased was observed by Dos Santos and co-workers for a mtBOx modified pyrolytic graphite electrode with naphthoyl-2-carboxylate groups (Dos Santos, Climent et al. 2010).

However, Shleev et *al*. report only a -0.02V/pH unit shift of the electrocatalytic onset in his study of Box-modified nanostructured gold electrodes. They argued that a significant shift of the onset potential is not expected when the pH of the solution changes as the redox transformation of the Cu T1 cluster should not involve H^+ transfer as in the case of the Cu-T23 cluster (Shleev, Andoralov et al. 2012).

Our results seem more in agreement with the work of Dos Santos et *al.*, which may be due to the similar immobilization strategy of BOx on the electrode, yielding an analogous interface, which is quite different from the physical absorption immobilization strategy used by Shleev et *al*. Nevertheless, in the case of Lc it is difficult to reconcile the electrocatalytic onset potential dependence on pH measured in Figure 4.4.29 with Cu T1 reduction being the rate determining step at both pH values. Deeper kinetic studies should be done in the future to clarify this apparent discrepeancy.

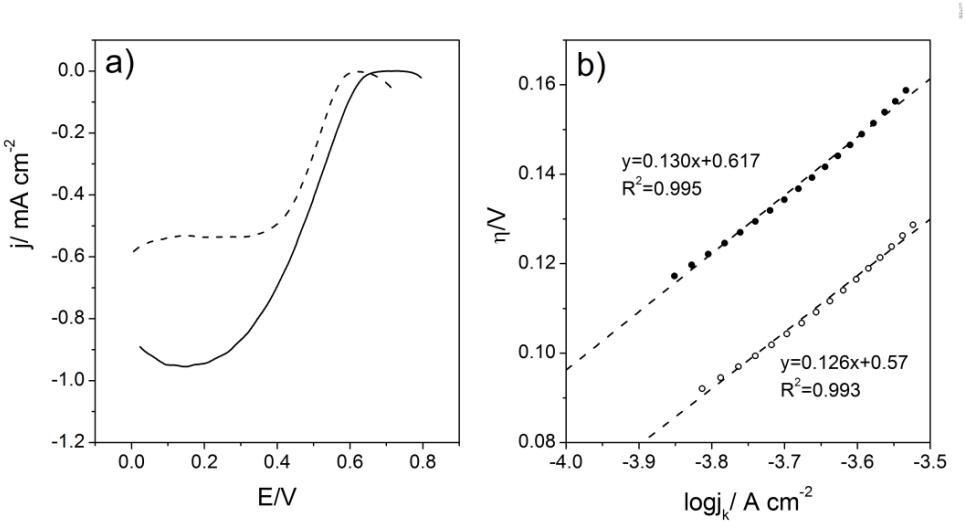

Figure 4.4.29 a) Background-corrected polarization curves for a ThLc-AP-erGO-GC electrode at 500 rpm, room temperature and 10 mV/s scan rate measured at pH 4.2 (solid line) or at pH 5.5 (dashed line) and b) Tafel plots of ThLc-AP-erGO-GC electrodes measured at pH 4.2 (black dots) or at pH 5.5 (white dots). The Tafel plots are obtained after correcting the ohmic drop and the mass transport limitation.

4.4.5 Conclusions

Graphene has been used to enhance the physicochemical and electrochemical properties of glassy carbon as support for the bioelectrocatalytic reduction of O_2. High surface area graphene electrodes have been prepared by simultaneous electrodeposition and electroreduction of GO. The electrodeposition process was optimized in terms of the electrochemical parameters and also in terms of the chemical composition of the GO employed. The electrodeposition of graphene oxide on glassy carbon electrodes results in a more uniform coverage than previously reported methods (Eda and Chhowalla 2010, Pumera, Ambrosi et al. 2010, Kashyap, Mishra et al. 2014), with extra advantages such as avoiding additional polymer layers. The electrochemical reduction of GO yielded a highly porous conductive surface that still has oxygen functionalities as was confirmed by XPS and FTIR analysis, which were used for the further functionalization of the surface and subsequent immobilization of two biocatalysits: mtBOx and ThLc. In both cases a high electroactive area and high catalytic current densities of ORR, up to -1.38 mA/cm^2, were obtained. From the studies performed it was found that the optimum graphene loading in terms of fabrication time, stability and electrocatalytic response resulted when 30 cycles have been used during the electrodeposition process by cyclic voltammetry. Mechanistic studies of both biocathodes showed that they exhibit different Tafel slopes, indicating different rate limiting steps during bioelectrocatalysis if the same ORR mechanism is used; whereas almost similar Tafel slope have been obtained at different pH values for the laccase-based biocathode.

All the results highlight that the fabrication of stable, robust and reproducible graphene-based electrodes was achieved by electrodeposition of GO, which could be used as biocathodes or other electrochemical applications.

4.5 ITO based electrodes

Indium-tin oxide (ITO) substrate is widely used for a variety of purposes due to its electrical conductivity and optical transparency. ITO consists in a combination of indium oxide (In_2O_3) and tin oxide (SnO_2), typically 5% to 10% SnO_2 by weight, in which tin acts as an impurity dopant. The relatively large amount of tin content in ITO causes a degenerate doping condition which gives rise to large conductivity ($\approx 10^4\ \Omega^{-1}cm^{-1}$) and metallic behavior (Dattoli and Lu 2011). Thanks to its properties the applications of ITO are numerous; it is used in electronics, electrical or optical devices, and in the bio-sensing field (Kim, Hong et al. 2004, Jeong, Lee et al. 2010, Baraton 2011). Moreover, ITO surfaces offer several other attractive physical properties such as its high stability under physiologic conditions (Yang and Li 2005). These properties make it a suitable material for potential *ex vivo* applications where also transparency is a key factor, *i.e.* smart contact lenses. Recently have appeared the first publications reporting biofuel cells (BFCs) powering electronic contact lenses using glucose/oxygen or ascorbate/oxygen as substrates (Falk, Andoralov et al. 2012, Falk, Andoralov et al. 2013), which are typical biofuels present in lachrymal fluids (Pankratov, Sundberg et al. 2015, Pankratov, González-Arribas et al. 2016), and have been tested in human lachrymal liquid. In this section, the chemical functionalization of ITO surface was investigated in order to optimize the immobilization of two different biocatalysts for the fabrication of a mediator-free BFC. ITO surface is generally modified with different organic compounds (Hillebrandt and Tanaka 2001, Kim, Hong et al. 2004, Arya, Prusty et al. 2007, Ganesh and Muthurasu 2012). Among them the modification of ITO surface through the formation of siloxane bonds via silane chemistry is very common. Here, ITO surface was chemically modified with GLYMO and APTES molecules for the covalent immobilization of a cathodic (*Myrothecium verrucaria* BOx) and an anodic (*Corynascus thermophiles* CDH) redox enzyme (schemes shown in Figures 3.2.8 and 3.2.11 respectively). These experiments were done in collaboration with Elena Gonzalez-Arribas from the group of Prof. Dr. Sergey Shleev (Malmö University).

4.5.1 Chemical functionalization of ITO electrodes

4.5.1.1 Bare ITO characterization

ITO conductive glasses were cut in pieces (10 mm x 25 mm x 1.1 mm) and cleaned prior their use following the procedure reported in section 3.2.5.2.3. An ITO electrodes' feature is their transparency (Fig. 4.5.1.a), indeed the average transmittance of bare ITO electrodes is higher than 80% in the whole visible light spectrum (Fig. 4.5.1.b)[3].

[3] SEM analysis was made by E. Gonzalez-Arribas from Malmö University.

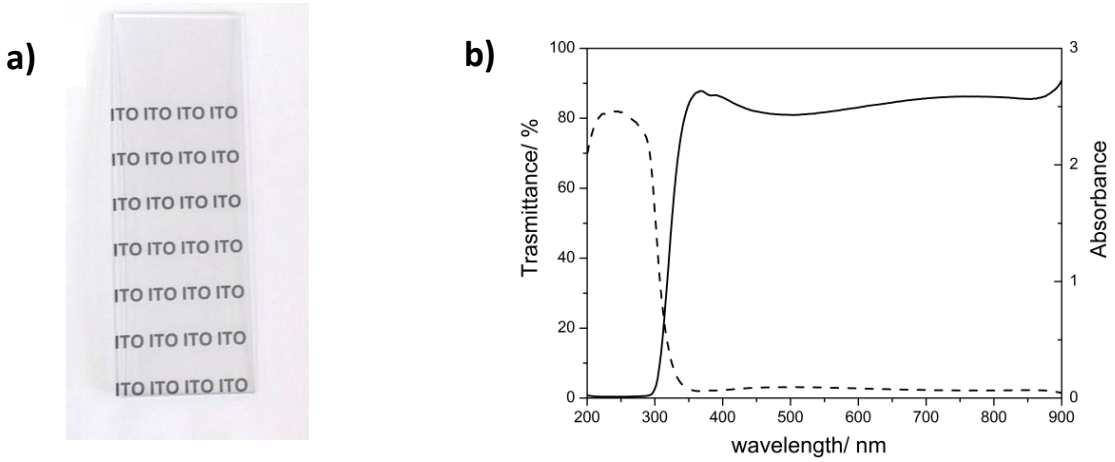

Figure 4.5.1 a) Photograph of an ITO electrode on top of a printed piece of paper and b) UV-Vis spectrum of ITO electrode. Transmitance (solid line) and absorbance (dashed line) vs. wavelength is represented.

The SEM image of the ITO electrode (Fig. 4.5.2) confirms a homogenous oxide coating of the glass support.

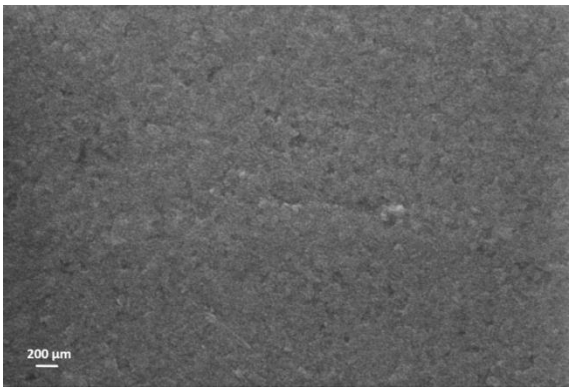

Figure 4.5.2 SEM image of an ITO electrode at 5000x magnification.

4.5.1.2 Silanization of ITO electrodes

The cleaning process of the ITO electrodes leaves hydroxyl groups on the ITO surface, which are essential for the subsequent reaction with silane molecules. ITO electrodes were chemically modified with either GLYMO or APTES silane-coupling agents following the procedure reported in section 3.2.5.2.3. The formation of the silane layer was characterized by cyclic voltammetry and EIS recorded in presence of 5 mM $K_4[Fe(CN)_6]$/ $K_3[Fe(CN)_6]$ in 50 mM PBS with 0.1 M KCl at pH 7, following the conditions reported in section 3.2.6. Figure 4.5.3 shows the ferrocyanide/ferricyanide CVs obtained for hydrolyzed ITO (black curve), GLYMO-ITO (red curve) and APTES-ITO (blue curve). In the case of GLYMO-ITO the CV peak currents are lower than for bare-ITO; this effect is attributed to the GLYMO chains hindering the access of the redox probe to the ITO for electron transfer, thus confirming their presence on the surface. However, the different shape of the CV observed for bare ITO is due to the presence of OH groups on its surface that are negatively polarized at neutral pH, thus repulsing the negatively charged molecules of the redox probe (Canbaz and Sezginturk 2014). In the case of the APTES-ITO electrodes, their aliphatic amines are protonated ($-NH_3^+$) at pH 7, resulting in

a positively charged surface that attracts electrostatically the negatively charged $FeCN_6^{3-/4-}$, thus improving the electron transfer between the redox probe and the APTES-ITO surface.

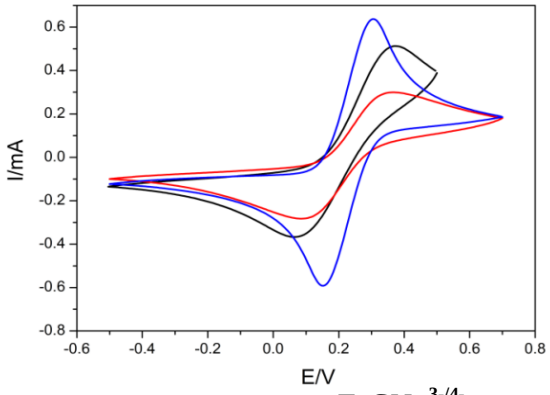

Figure 4.5.3 CVs recorded at 50 mV/s in the presence of 5 mM $FeCN_6^{3-/4-}$ in 50 mM PBS with 0.1 M KCl at pH 7 for bare ITO (black curve), GLYMO-ITO (red curve) and APTES-ITO (blue curve). The 3rd scan is represented.

Fig. 4.5.4.a shows the EIS spectra obtained for bare and modified-ITO electrodes. The experimental spectra are fitted using the model circuit shown in Fig. 4.5.4.b. The results obtained from EIS are quite in agreement with the CV results (Fig. 4.5.3). Indeed, smaller values of charge-transfer resistance (R_{ct}) have been obtained for the APTES-ITO electrode (blue curve) than for the bare-ITO (black curve), confirming a faster electron transfer due to the charge attraction between NH_3^+ groups on the ITO surface and $(FeCN_6)^{3-/4-}$ in the solution. The higher R_{ct} value obtained for bare ITO is expected because of the electrostatic repulsion between the negatively polarized oxygen atoms on the ITO surface and $(FeCN_6)^{3-/4-}$ in the solution, thus slowing the charge transfer. In the case of GLYMO-ITO electrode the Warburg impedance (Z_w) element, responsible for the diffusion of ions to the electrode interface from the bulk of the electrolyte, became more predominant and the R_{ct} is higher than that of APTES-ITO electrode. These results confirm that the presence of GLYMO molecules that partially block the access of the redox probe to the electron transfer (Table 4.5.1).

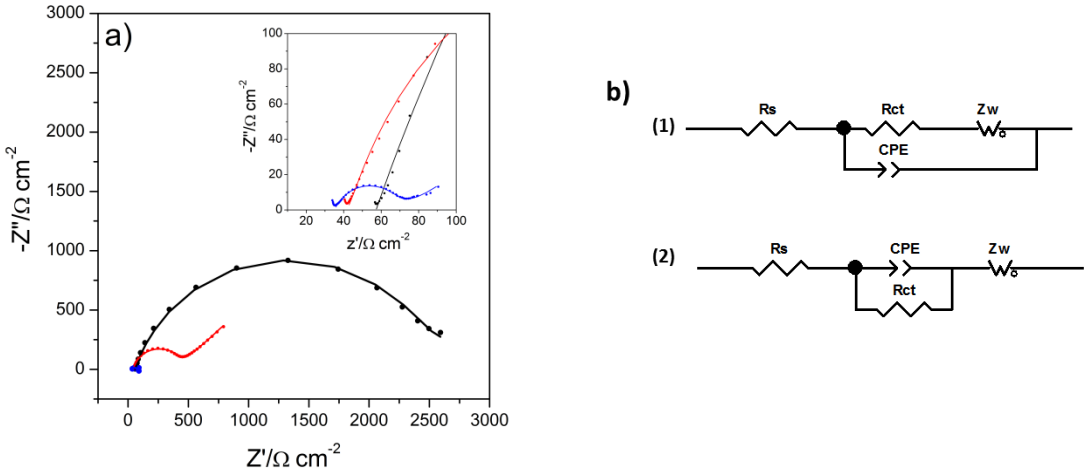

Figure 4.5.4 a) EIS experimental spectra for bare ITO (black), GLYMO-ITO (red) and APTES-ITO (blue) electrodes. The lines represent the equivalent circuit fitting, whereas the dots represent the experimental data. Inset plot: magnification of high frequency region of the complex plane plot. b) Equivalent circuit of (1) bare ITO and (2) GLYMO-ITO and APTES-ITO electrodes.

	Rs (Ω)	R_{ct} (Ω cm^2)	CPE_{dl} (F cm^{-2} $s^{\alpha-1}$)	α_{dl}	Z_w (Ω cm^{-2} $s^{\alpha-1}$)	τ	α
Bare ITO	57.2 ± 0.5	2506 ± 27	3.72E-05 ± 4E-07	0.8	1326 ± 80	73	0.55
GLYMO-ITO	41.2 ± 0.2	360 ± 2	2.18E-5 ± 1E-07	0.89	2636 ± 26	45	0.48
APTES-ITO	33.4 ± 0.3	28.3 ± 0.3	6.56E-5 ± 9E-07	0.87	54.8 ± 0.9	8.4	0.24

Table 4.5.1 Values of the parameters obtained by fitting the impedance spectra with the equivalent circuits shown in Fig. 4.6.4.b for bare and modified ITO electrodes.

CVs of GLYMO-ITO and APTES-ITO electrodes in the presence of the electroactive redox probes at different scan rates (10-200 mV/s) were also recorded (Fig. 4.5.5.a-b). Well-defined oxidation and reduction peaks and higher currents are detected for the APTES-ITO electrodes (Fig. 4.5.5.b) due to the faster ET earlier discussed. The slight peak potential shift observed as the scan rate was increased indicates electrochemical quasi-reversibility of the process. Furthermore, the linear relationship of peak intensity vs. the square root of the scan rate, following the Randles-Sevcik relationship (Bard and Faulkner 2000), indicates that the process is predominantly diffusion controlled (Fig. 4.5.5.c-d). This is in agreement with the EIS results where the presence of the Warburg element confirms diffusion control behavior.

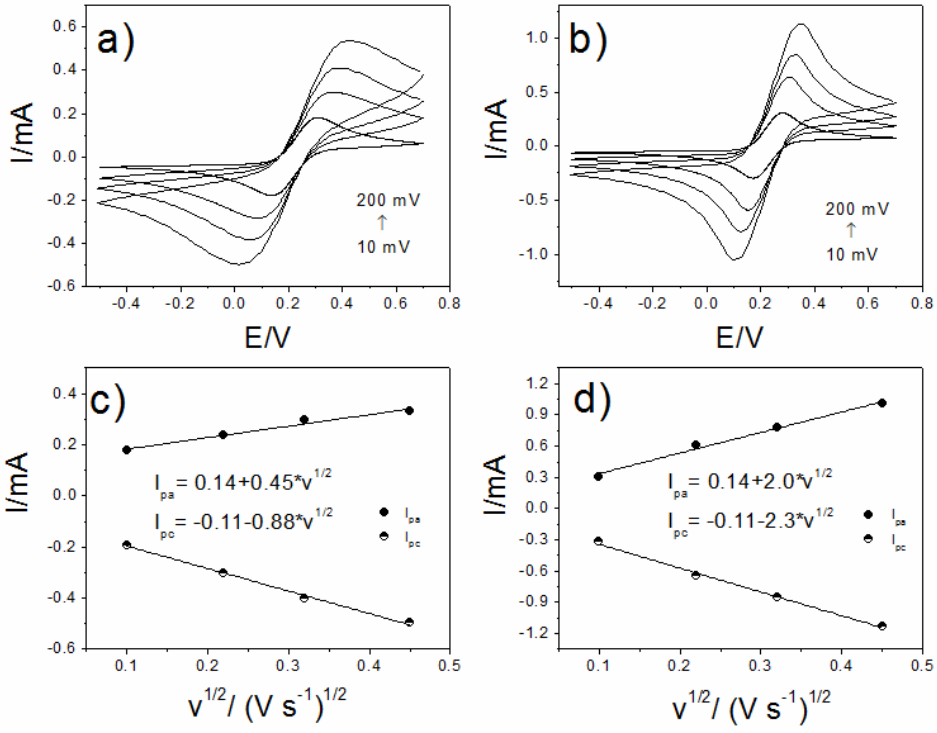

Figure 4.5.5 CVs recorded in the presence of 5 mM $K_4[Fe(CN)_6]$/ $K_3[Fe(CN)_6]$ in 50 mM PBS with 0.1 M KCl at pH 7 for a) GLYMO-ITO and b) APTES-ITO electrodes at 10, 50,100 and 200 mV/s. Peak intensity vs. the square root of the scan rate for c) GLYMO and d) APTES modified ITO electrodes.

4.5.2 Bio-electrochemical performance

4.5.2.1 Fabrication of ITO-based biocathode

GLYMO-ITO electrodes were modified with BOx (section 3.2.5.2.3) and tested for electroenzymatic O_2 reduction by CV. Initially 20 µl of 4 mg/mL BOx in 100 mM phosphate buffer at pH 7.4 were put on the GLYMO-ITO surface and let to react at RT for 24 h. Fig. 4.5.6 shows a very low catalytic performance even under O_2 saturated conditions. Alternatively, the pH of the enzyme solution was increased until 9 in 50 mM bicarbonate-carbonate buffer (section 3.2.5.2.3) and 20 µl of this new solution were dropped on the modified electrode and let to react for 24h at RT (Abad, Vélez et al. 2002). Increasing the pH of the enzyme solution promotes the deprotonation of enzyme amines that can more easily react with the GLYMO epoxy groups yielding the formation of secondary amine groups. At higher pH the hydrolysis of the epoxy groups to glycol groups, which do not react with the enzyme amines, can be predominant (Clayden, Greeves et al. 2012). In this way a correct oriented immobilization of BOx on the electrode surface allowing efficient DET is expected, as the Cu T1 site is surrounded by several lysine residues (Gutiérrez-Sánchez, Jia et al. 2012). Figure 4.5.7 shows the results obtained with the improved protocol. A clear catalytic current up to -1.2 µA/cm^2 was achieved with an onset potential at 0.49 V typical of BOx catalyst (Ramirez, Mano et al. 2008).

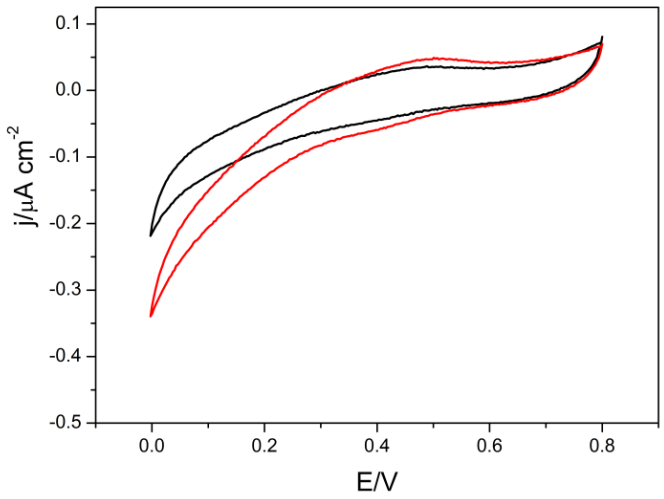

Figure 4.5.6 CVs recorded in 10 mM PBS pH 7.4 at 10 mv/s for a BOx-GLYMO-ITO electrode prepared by reaction with the enzyme at pH 7.4. CVs were recorded under deoxygenated (black curve) and O_2 saturated conditions (red curve). The 2nd scan is represented.

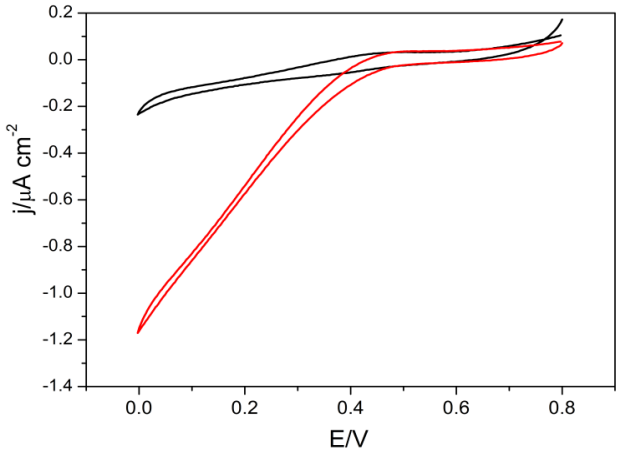

Figure 4.5.7 Electrocatalytic oxygen reduction with a BOx-GLYMO-ITO electrode prepared by reaction with the enzyme at pH 9. CVs were recorded under deoxygenated (black curve) and O_2 saturated conditions (red curve). CVs were performed at 10 mV/s in 10 mM PBS buffer pH 7.4; the 2nd scan is represented.

4.5.2.2 Fabrication of ITO-based bioanode

APTES-modified electrodes were used as support for the further immobilization of CDH for the fabrication of bioanodes. Previous works have shown how DET of CDH based electrodes can be improved using surface positively charged that can react with the negatively charged residues on the enzyme surface (Tasca, Harreither et al. 2011). Therefore, for ITO modification an alkyl silane with amino groups such as APTES was chosen for this purpose. The electrochemical response for glucose oxidation was tested by cyclic voltammetry in presence of 0.5 mM glucose. Initially 20 µl of enzyme solution were simply deposited on the modified electrode surface as reported in 3.2.5.4.1 section. Following this immobilization strategy, no catalytic current was observed after the addition of 0.5 mM glucose (Fig. 4.5.8, blue curve) into the PBS buffer solution. When a covalent immobilization strategy was used as reported in 3.2.5.4.1 section, a clear oxidative current was measured after glucose addition (Fig. 4.5.9, blue curve). Therefore, as expected in this protocol the negatively charged residues on the CDH surface (glutamic or aspartic acids) react with the NH_2 of APTES forming amides.

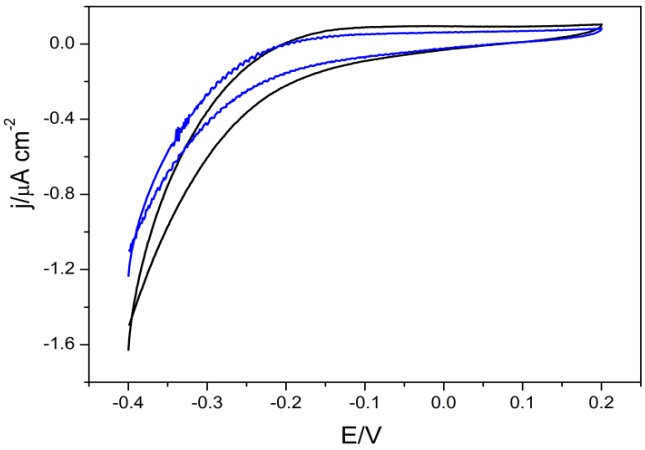

Figure 4.5.8 CVs recorded at 10 mV/s in 10 mM PBS buffer under deoxygenated conditions (black curve) and after 0.5 mM glucose addition (blue curve) using a CDH-APTES-ITO electrode prepared by adsorption of the enzyme. The 2nd scan is represented.

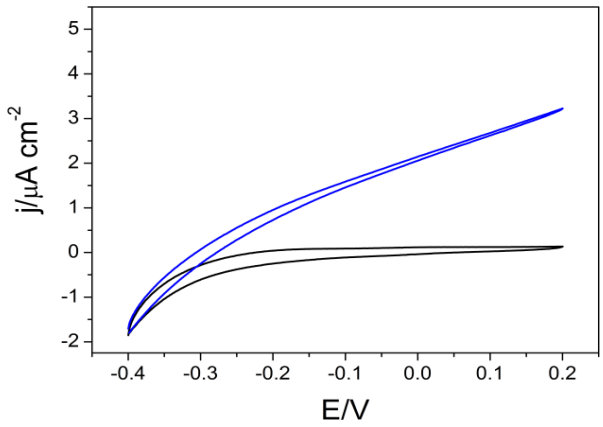

Figure 4.5.9 CVs recorded at 10 mV/s in 10 mM PBS buffer under deoxygenated conditions (black curve) and after 0.5 mM glucose addition (blue curve, 2nd scan) using a CDH-APTES-ITO electrode prepared by covalent immobilization of the enzyme.

4.5.3 Conclusions

ITO electrodes were chemically modified successfully with two different silane molecules: GLYMO and APTES. BOx and CDH have been adequately oriented and covalently immobilized on the GLYMO-ITO and APTES-ITO surface, respectively. Both electrodes showed catalytic current responses up to -1.2 μA/cm^2 and 3 μA/cm^2 in presence of O_2 saturated conditions or in PBS containing glucose without any extra addition of a redox mediator. These covalent immobilization strategies have further been applied to nanostructured electrodes with ITO nanoparticles for the fabrication of a BOx biocathode and a CDH bioanode, in an optically transparent BFC. The BFC had an OCV of 0.67 V and was able to generate a maximum power output of 1.4 μW/cm^2 at an operating voltage of 0.35 V (González-Arribas, Bobrowski et al. 2017).

4. 6 DET based biosupercapacitors for *ex vivo* applications

DET based electrodes have attracted much more interests in the last years as their use in BFCs can simplify their construction, facilitating miniaturization and overcoming the possible disadvantages of using redox mediators. Limitations of BFCs applications derive from lower performance and operational stability. In order to increase BFCs performances, a hybrid biodevice for simultaneous generation and storage of electric energy has been proposed very recently (Pankratov, Falkman et al. 2014). This hybrid biodevice could be described as a self-charging bio-supercapacitor (SCBSC), which combines the storage ability of a supercapacitor with the ability of charging, thanks to the direct transformation of chemical energy into electrical energy as occurs in biofuel cells (BFCs) (Pankratov, Blum et al. 2014b, Pankratov, Blum et al. 2014a). Here, biosupercapacitors based on tubular PEDOT modified graphite electrodes are presented. Such electrodes were used for the fabrication of DET-based enzymatic electrodes presenting good performance in physiological conditions. Based on previous knowledge and availability, the enzymes selected were *Myrothecium verrucaria* bilirubin oxidase (BOx) for the cathodic bioelectrode and *Corynascus thermophiles* cellobiose dehydrogenase (CDH) for the anodic bioelectrode. Tubular electrodes were chosen aiming to mimic a human blood vessel and to investigate the SCBSC performances *ex vivo* with a real human blood stream. *Ex vivo* applications represent a good alternative to *in vivo* ones, as some current problems regarding sterilization, biocompatibility and short lifetimes of implantable BFCs can be overcome. An enzymatic fuel cell in a vein replica able to generate sustained electricity fed with a human blood stream was very recently reported (Pankratov, Ohlsson et al. 2016). The present section aims an improvement of the reported EFC aiming to achieve higher potential values and consequently higher power output than the previous system. *In vitro* experiments mimicking all the experimental conditions of a real blood stream and *ex vivo* experiments were performed following the procedure reported in 3.2.6 section. These experiments were performed in collaboration with Elena Gonzalez-Arribas and Olga Aleksejeva from Prof. Dr. Sergey Shleev´s group (Malmö University, Sweden) during a 2 months secondment in his laboratory.

4.6.1 PEDOT-graphite electrodes

4.6.1.1 Fabrication of PEDOT-graphite electrodes

PEDOT modified graphite electrodes were prepared by electropolymerization of an EDOT solution as reported in 3.2.4.4 section. Spectrographic graphite rods of 4 cm length were immersed for 1 min in the EDOT solution under constant stirring, in this way the EDOT monomer can diffuse inside the graphite pores. When the electrodes were immersed for longer time it was found that a higher amount of EDOT monomer filled the pores, decreasing the active surface area of the electrode. After the immersion during one minute the electropolymerization was carried out following the cyclic voltammetry procedure reported in 3.2.4.4 section (González-Arribas, Pankratov et al. 2016). In the

first cycle a typical crossover of the reverse cathodic scan over the anodic one, known as electropolymerization loop, occurs (Fig. 4.6.1.a). It has been attributed to polymer nucleation effects (Downard and Pletcher 1986) or more recently to an homogeneous comproportionation reaction between an intermediate oligomer and the starting monomer (Heinze, Rasche et al. 2007). Upon increasing the number of cycles the capacitive current grew (Fig. 4.6.1.b), indicating that a progressive PEDOT layer was deposited on the electrode surface. Moreover, two oxidative peaks were observed: one at 0.8 V which was attributed to the adsorption of oxidized EDOT on the electrode surface and another starting at ~1 V caused by the oxidation of EDOT diffusing close to the electrode (Sakmeche, Aeiyach et al. 1999).

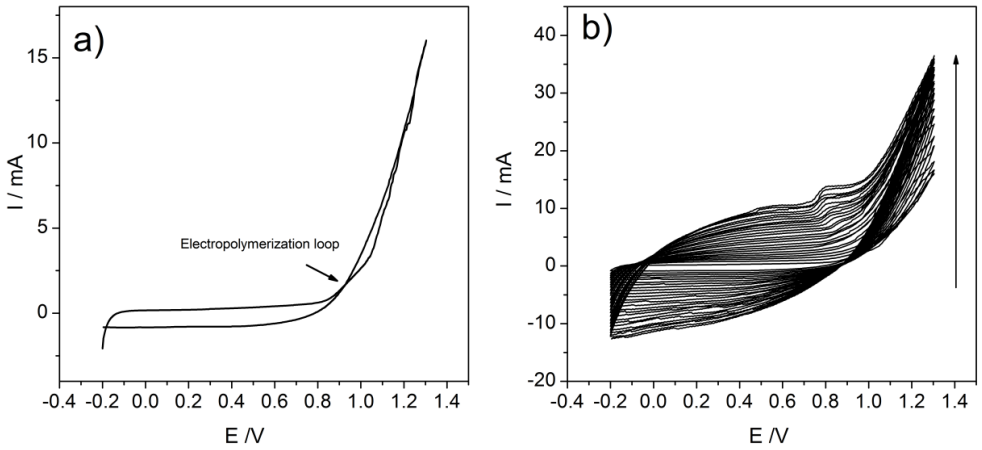

Figure 4.6.1 Electropolymerization of a 20 mM EDOT aqueous solution on graphite rods electrode performed at 50 mV/s. a) The first scan and b) the next 24 scans of the electropolymerization are reported.

The presence of PEDOT on the electrode surface is clearly observed in Fig. 4.6.2. Afterwards, the PEDOT-graphite (PEDOT_g) electrodes were cut in pieces of 1 cm length and drilled lengthwise to fabricate tubular capacitive electrodes as reported in 3.2.2.4 section.

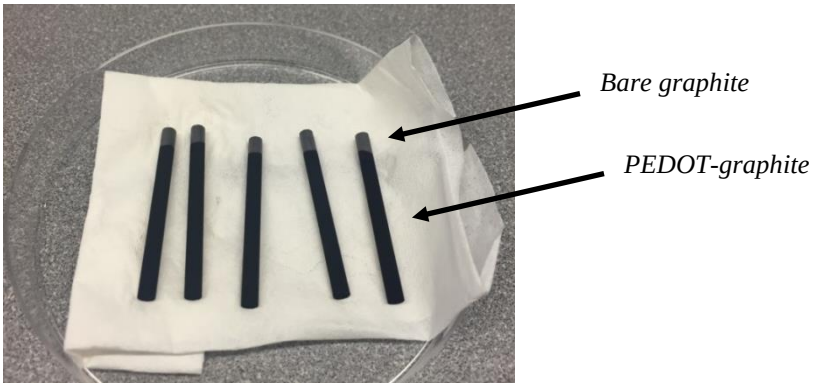

Figure 4.6.2 Photograph of PEDOT-graphite rods electrodes after the electropolymerization process. The darkest part is the PEDOT layer formed on the electrode surface.

4.6.1.2 Characterization of PEDOT-graphite electrodes

PEDOT modified and bare graphite electrodes were characterized by a morphological and electrochemical point of view through SEM analysis, and by CV and EIS measurements in blood mimicking buffer at pH 7.2, respectively.

The characterization was carried out for both planar (d= 3.05 mm) and tubular electrodes modified with or without PEDOT.

4.6.1.2.1 SEM analysis

The SEM image of planar PEDOT_g electrodes (Fig. 4.6.3) revealed that PEDOT forms aggregates with irregular shape and an average size around 400-500 nm.

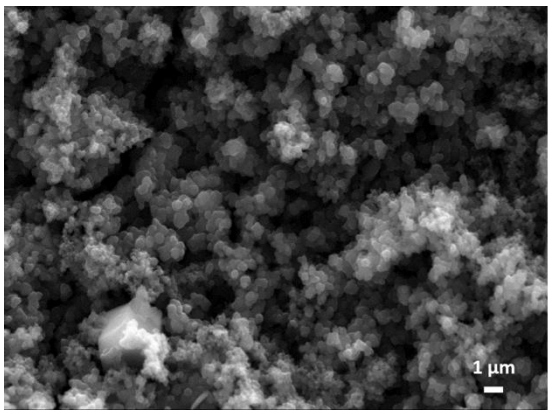

Figure 4.6.3 SEM image of the top of a planar PEDOT_g electrode at x10000 magnification.

When the SEM analysis was performed on the cross-section of tubular PEDOT_g electrode (Fig. 4.6.4), a 10 µm thickness of PEDOT layer on the outer part of the electrode was observed. However, with this technique, it was not possible investigate how deep PEDOT is penetrated in the porous structure of graphite electrode.

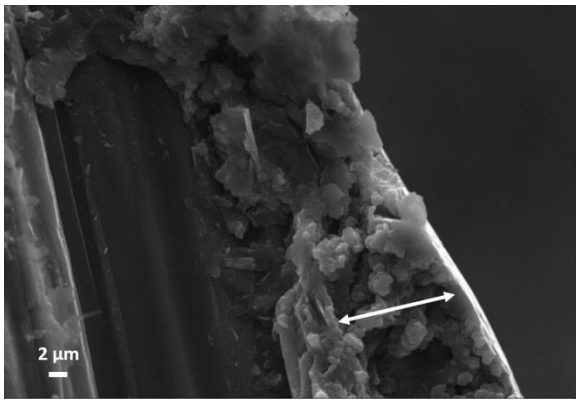

Figure 4.6.4 SEM image of a cross-section of a tubular PEDOT_g electrode at x5000 magnification.

4.6.1.2.2 Electrochemical characterization

The CV recorded shows a clear enhancement in the capacitive area for planar PEDOT_g (Fig. 4.6.5, solid line) compared to planar bare spectrographic graphite (Fig. 4.6.5, dashed line) electrodes. Indeed a 17-fold increase in the capacitance[4] is obtained (Table 4.6.1).

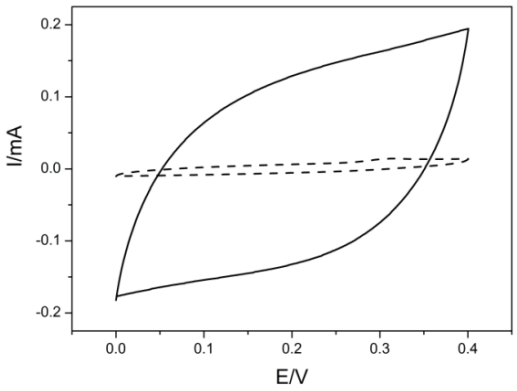

Figure 4.6.5 CVs recorded at 10 mV/s in blood mimicking buffer for bare (dashed line) or PEDOT_g (solid line) electrodes. The 3rd scan is represented.

	C (mF)
graphite	0.70
PEDOT-graphite	12

Table 4.6.1 Capacitance values obtained from the CVs reported in Fig. 4.6.2 for bare graphite and PEDOT-graphite electrodes.

EIS spectra were recorded under a 0.4 V bias potential, as at this potential PEDOT is in its oxidized state (Bisquert, Belmonte et al. 2000). The Nyquist plots obtained for bare spectrographic graphite (Fig. 4.6.6.a, black curve) and for planar PEDOT_g (Fig. 4.6.6.a, red curve) electrodes differ notably. The plot for PEDOT_g electrode (Fig. 4.6.6.a, red curve) is dominated by capacitive line which extents down to very low frequencies, whereas at high frequencies there is a deviation from the capacitive behavior, a sign of fast charge transfer at the electrode/polymer and polymer/solution interfaces, as well as a fast charge transfer in the polymer bulk (Bobacka, Lewenstam et al. 2000). The equivalent circuit (1) reported in Fig. 4.6.6.b is the one that fits best to the experimental data for PEDOT_g. A CPE element replaces the pure capacitor because the capacitive line, present at low frequencies, deviated from 90º. The experimental data fit better to the circuit where the finite-length Warburg diffusion element (Z_w) and CPE are connected in series instead of in parallel. The CPE exponent α (Table 4.6.2) represents the roughness and non-uniformity of the electrode surface, with values between 1 and 0.5. The Z_w element τ represent the diffusional time constant, while an ideal 45º diffusion line is observed when the Z_w exponent α is equal to 0.5. The diffusional pseudocapacitance (C_{pseudo}) can be determined if the Z_W and the diffusional time constant (τ) are known, applying the formula: $Z_w = \tau/C_{pseudo}$. The total capacitance value for a planar PEDOT_g electrode obtained by EIS (10 mF) was very similar to the one obtained previously by CV (12 mF). The bare graphite electrode presented instead a major Z_w diffusional component at low frequencies (Fig. 4.6.6.a and Table 4.6.2)

[4] The capacitance was calculated using the following equation: $C = \frac{Q}{2(E_2 - E_1)}$, where C is the capacitance, Q the charge and (E_2-E_1) is the applied potential window width.

and a total capacitance value lower than PEDOT_g electrode, confirming the same trend observed by CV.

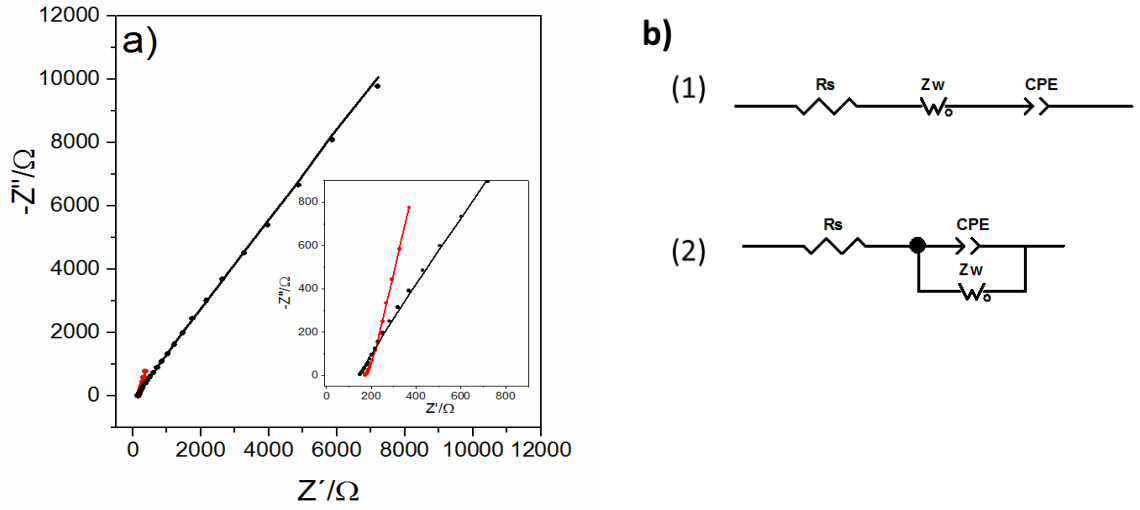

Figure 4.6.6 a) EIS experimental spectra for planar bare graphite (black) and planar PEDOT_g (red) electrodes; the lines represent the equivalent circuit fitting, whereas the dots represent the experimental data. Inset plot: magnification of high frequency region of the complex plane plot. b) Equivalent circuit of (1) PEDOT_g and (2) bare graphite electrodes.

	Rs (Ω)	CPE ($F\ s^{\alpha-1}$)	α	Z_w ($\Omega\ s^{\alpha-1}$)	τ	α	C_{pseudo} ($F\ s^{\alpha-1}$)	C_{tot} (F)
PEDOT-graphite	171.4 ± 0.4	1.199E-02 ± 8E-05	0.88	68 ± 2	7.6	0.35	0.14	0.010
graphite	151.3 ± 0.5	3.51E-05 ± 9E-07	0.89	52485	89.1±0.9	0.59	0.0017	1.72E-03

Table 4.6.2 Values of the parameters obtained by fitting the impedance spectra with the equivalent circuits shown in Fig. 4.7.3.b for bare and PEDOT-graphite electrodes.

However, when the CVs were performed for the tubular bare graphite (Fig. 4.6.7, dashed line) and the tubular PEDOT_g (Fig. 4.6.7, solid line) electrodes, the increase in the capacitive area was not as large as it was for planar electrodes; moreover, a more resistive behavior is observed. The explanation may be that the electropolymerization inside the tube should be slower than outside due to the monomer depletion, as it has to diffuse inside from the bulk solution. Also, it is worth mentioning that the electropolymerized area, in this case, was much larger than the simple planar electrode one.

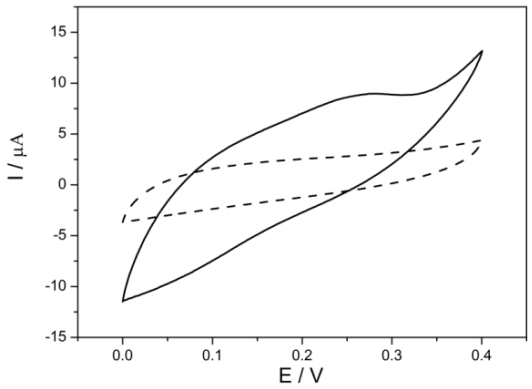

Figure 4.6.7 CVs recorded at 10 mV/s in blood mimicking buffer for bare (dashed line) or PEDOT_g (solid line) tubular electrodes. The 3rd scan is represented.

The EIS spectra recorded for the tubular electrodes (Fig. 4.6.8.a) also differ notably from those of the planar electrodes. The spectra of the tubular electrodes are typical of porous electrodes in presence of a concentration gradient (Lasia 1997). At high frequencies a line with a slope of 45º is observed followed by two well-defined semicircles. The low frequencies semi-circular loop is due to diffusion control associated with a concentration profile; whereas the high frequency loop is strongly dependent on parameters such as electrolyte resistivity, diffusion coefficient of the reacting species, pore depth and overall current flowing through the pore (Cachet and Wiart 1985). Numerous studies have been carried out to formulate a correct model that describes these porous systems (Raistrick 1990, Paasch, Micka et al. 1993, Lasia 1995, Lasia 1997). One model considers the cylindrical pore as a transmission line made of a large number of thin sections (Cachet and Wiart 1985). This model can be simplified with the equivalent circuit reported in Fig. 4.6.8.b to fit the experimental data, which facilitates extrapolating information about the system. The spectra (Fig. 4.6.8.a) and the data obtained (Table 4.6.3) show a clear decrease in the charge transfer resistance of the second RCPE circuit for the PEDOT_g electrode, indicating a better electron transfer achieved between the polymer/electrode surface and the solution. However, an optimal fitting of the experimental data obtained for PEDOT_g electrodes was not possible due to the lowest frequency point measured that indicates inductance behaviour, but the inclusion of an inductance element in the circuit did not improve in any way the final fitting. It is also noticed an increase in the capacitance value for the PEDOT_g electrode but not in the same extent than in the case of planar one. Moreover, in the case of tubular PEDOT_g electrodes it is not possible to discern between the double layer and pseudocapacitance contributions, as in the equivalent circuit only a CPE element is present that represents a non-ideal capacitor, but does not give any information about faradic processes.

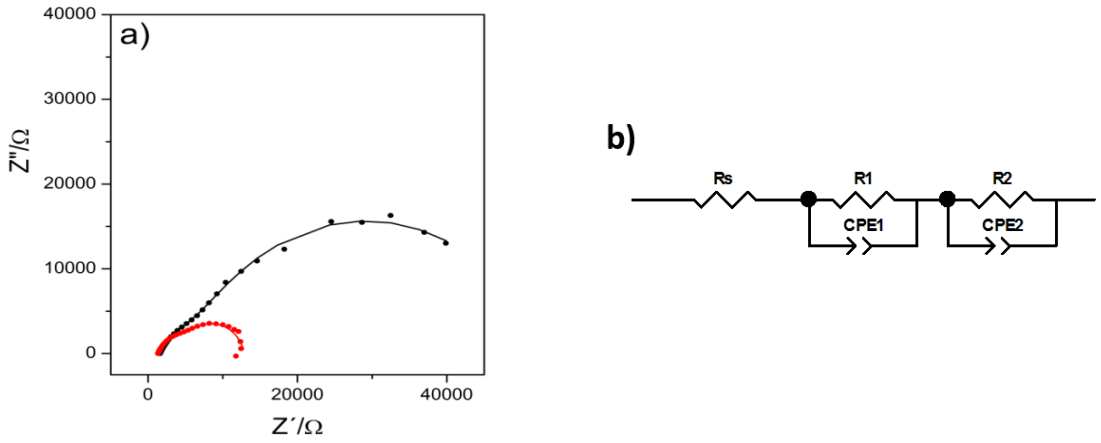

Figure 4.6.8 a) EIS experimental spectra recorded applying a potential of 0.4 V for bare graphite (black) and PEDOT_g (red) tubular electrodes; the lines represent the equivalent circuit fitting, whereas the dots represent the experimental data. b) Equivalent circuit for bare graphite and PEDOT_g tubular electrodes.

	Rs (Ω)	R1 (Ω)	CPE1 (F s $^{\alpha-1}$)	α	R2 (Ω)	CPE2 (F s $^{\alpha-1}$)	α
graphite	1592	4857	4.16E-05 ± 4E-07	0.7	46380	8.74E-05 ±4E-07	0.75
PEDOT-graphite	1348	4252	3.05E-05 ± 4E-07	0.78	7261	1.48E-04 ± 3E-06	0.89

Table 4.6.3 Values of the parameters obtained by fitting the impedance spectra with the equivalent circuits shown in Fig. 4.6.6.b for bare and PEDOT-graphite tubular electrodes.

4.6.2 *In vitro* measurements

The tubular PEDOT_g electrodes were used for the further immobilization of mtBOx and CDH enzyme, as reported in 3.2.5.2.4 and 3.2.5.4.2 sections, in order to fabricate a capacitive biocathode and bioanode and build up a SCBSC operating in physiological conditions. Fig. 4.6.9 shows the experimental set up: the blood mimicking buffer was termostated at 37 ºC and oxygenated in order to keep the O_2 concentration constant at 0.05 mM. The buffer flowed inside the tubular electrodes at a rate of 0.09 mL/s. For open circuit voltage measurements, the cathode was connected to the potentiostat through the working electrode cable and the anode through the reference and counter electrode cables (section 3.2.6).

Figure 4.6.9 Photograph of the experimental set-up used for performing the experiment.

4.6.2.1 Characterization of a SCBSC

4.6.2.1.1 Biosupercapacitor charge/discharge

The charge/discharge experiment was performed by chronopotentiometry at the OCV value in the blood mimicking buffer, as reported in 3.2.6 section. Self-charging was performed at open circuit until a more or less stable OCV value was reached, while discharging was performed by applying 1 kΩ external resistance. An initial OCV value of 0.25 V was achieved after 700 s (Fig. 4.6.10). This OCV value is lower than the 0.31 V measured for bare graphite electrodes reported in a previous work (Pankratov, Ohlsson et al. 2016). Moreover, also the corresponding OCV values of the capacitive biocathode and bioanode separately were lower than the typical ones of $OCV_{cathode} \approx 0.67$ vs. NHE and $OCV_{andone} \approx 0.1$-0.16 V vs. NHE at pH 7.

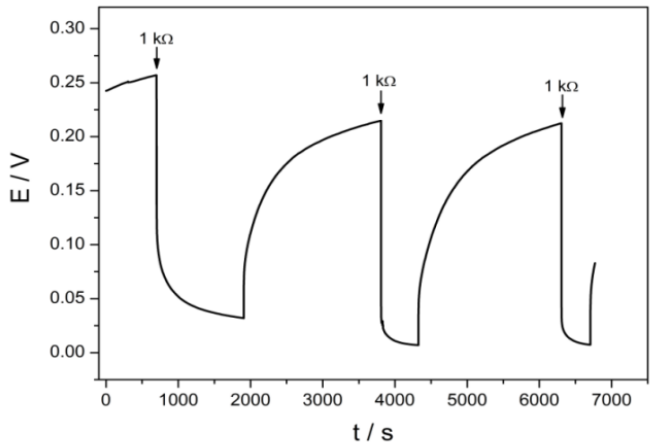

Figure 4.6.10 Charge/discharge cycles of one self-charching biosupercapacitor operating in blood mimicking buffer at 37 ºC.

This difference may be attributed to less enzyme coverage on the tubular PEDOT_g electrodes surface (the electroactive one) compared with bare graphite ones which affects the equilibrium potential. It is worth also mentioning that after the first cycle an OCV of 0.216 V is achieved, lower than the initial one. The following charge/discharge cycles reached the same OCV at equal charging time, denoting that the system is stable and reproducible. The integration of the discharging area yielded a charge

density[5] of 2.23 and 2.25 mC/cm^2 for the second and third cycles respectively, considering that the total geometric area of the electrode is 1.26 cm^2.

4.6.2.1.2 EIS measurement

In order to study the different contributions of the capacitive biocathode (mtBOx-PEDOT_g) and bioanode (CDH-PEDOT_g), EIS measurements were performed on them separately at 0.2 V and 0.01 V bias potential respectively, which corresponds to the OCV of the biocathode and the bioanode. Afterwards, the impedance of the full cell was recorded at 0.2 V, OCV of the whole cell. The EIS spectrum recorded for the CDH-PEDOT_g electrode (Fig. 4.6.11.a, red curve) differs from the one obtained for the mtBOx-PEDOT_g one (Fig. 4.6.11.a, blue curve). The EIS spectrum for the bioanode is characterized by a well-defined semicircle indicating a CPE element in parallel with a resistance (Lepage, Albernaz et al. 2012). Indeed using the equivalent circuit (1) reported in Fig. 4.6.11.b a good fitting is obtained. Instead, the biocathode shows a diffusion behavior in the low frequency region; so a Warburg element (Z_w) is necessary to fit the experimental data (equivalent circuit (2) Fig. 4.6.11.b). This result suggests that the major limitation of the system is the diffusion of O_2 to the cathodic electrode (Lepage, Albernaz et al. 2012), as only 0.05 mM O_2 concentration was used. When the whole cell was tested the spectrum shows differences with the individual ones. Indeed, two semicircles can be hinted. The experimental data fit well to the typical equivalent circuit described for a fuel cell: two CPE-R_{ct} elements in series and in series with the electrolyte resistance (Wagner 2002, Hosseini and Ahadzadeh 2013). In general, one CPE-R_{ct} element represents the anode and the other the cathode. The addition of a Z_w element to include the cathode diffusion limitation, as reported in others works (Lepage, Albernaz et al. 2012) did not yield a good fitting in our case.

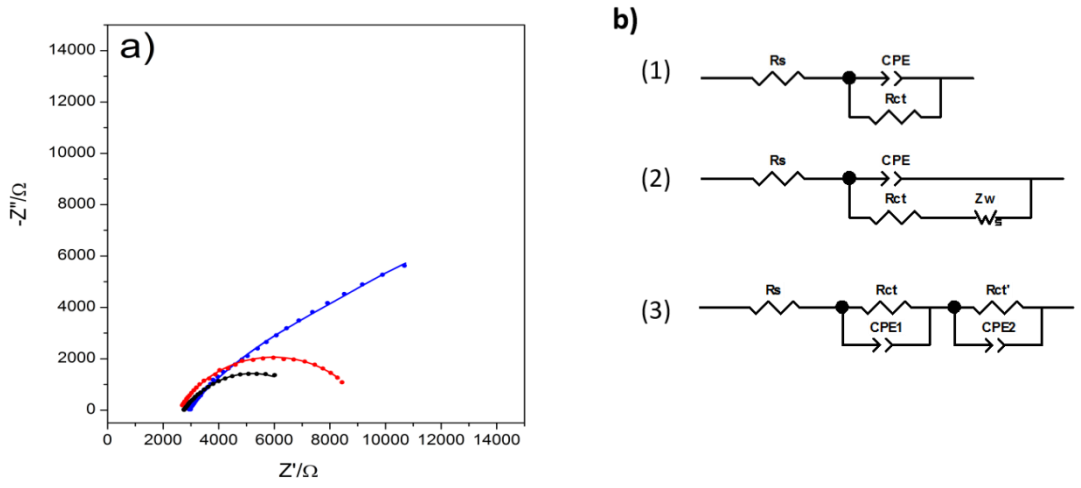

Figure 4.6.11 a) EIS experimental spectra for bare mtBOx-PEDOT_g (blue), CDH-PEDOT_g (red) tubular electrodes and a complete SCBSC (black); the lines represent the equivalent circuit fitting, whereas the dots represent the experimental data. b) Equivalent circuits for CDH-PEDOT_g (1), mtBOx-PEDOT_g (2) tubular electrodes and a complete SCBSC (3).

[5] The charge density value (Q) is obtained by the equation Q=I/t, where I is obtained from the recorded potential (E) values by application of the Ohm's relation: E=I x R.

	Rs (Ω)	Rct (Ω)	CPE1 (F s $^{\alpha-1}$)	α	Rct' (Ω)	CPE2 (F s $^{\alpha-1}$)	α	Z_w (Ω $s^{\alpha-1}$)	τ	α	C_{pseudo} (F s $^{\alpha-1}$)
anode	2594 ± 6	6730 ± 29	5.56E-05 ± 3E-07	0.7	-	-	-	-	-	-	-
cathode	2908	14559 ± 333	8.19E-05 ± 5E-07	0.6	-	-	-	11416 ± 552	4.94	0.5	4.33E-04
BFC	2749	197 ± 13	2.24E-04 ± 9E-06	0.79	4552 ± 21	1.82E-04 ± 2E-06	0.71	-	-	-	-

Table 4.6.4 Values of the parameters obtained by fitting the impedance spectra with the equivalent circuits shown in Fig. 4.6.10.b for mtBOx-PEDOT_g, CDH-PEDOT_g tubular electrodes and a complete SCBSC.

4.6.2.2 Connection of SCBSC in series

Connecting several self-charging biosupercapacitors simultaneously improved the setup described in 4.6.2.1 towards obtaining higher OCV and higher power output. Three couples of biocathode-bioanode electrodes were placed in series with respect the buffer flow, each at 1 cm distance from the next electrode. The biocathode and the bioanode at the extremes (external SCBSC) were connected to the potentiostat as illustrated in Fig. 4.6.12.b (1) and Fig. 4.6.13.a. A chronopotentiometry set at zero current (open circuit conditions), Fig. 4.6.12.a, showed that after 1000 s the OCV stabilized at 0.24 V. Afterwards the two inner SCBSCs were connected simultaneously (Fig. 4.6.12.b (2)), using a switcher as illustrated in Fig. 4.6.13.b, causing an instantaneous OCV increase up to 0.71 V (Fig. 4.6.12.a). However, the OCV slightly decreased with time until reaching a plateau at a higher OCV (0.33 V) than the initial one. Switching off the inner cells dropped the OCV to the initial value (Fig. 4.6.12.a). Switching on only one of the inner SCBSC (Fig. 4.6.12.b, (3)) increased the OCV less than in the previous case reaching an OCV value of 0.38 V (Fig. 4.6.12.a). The OCV decayed until reaching a plateau at 0.30 V, but the OCV only dropped to the initial value when the single inner cell was disconnected.

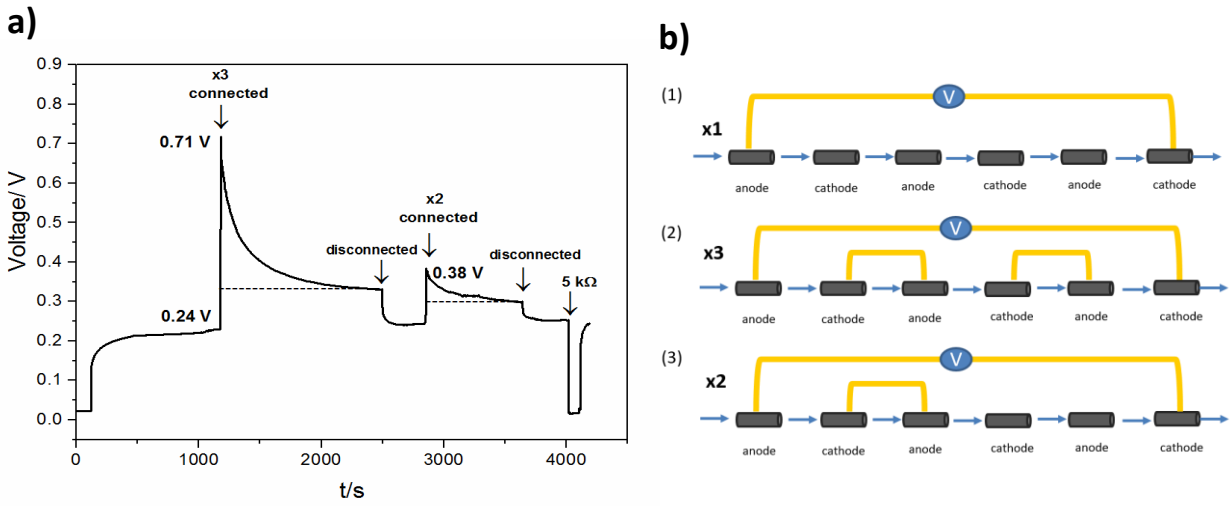

Figure 4.6.12 a) Chronopotentiometry at open circuit condition of the external SCBSC, while connecting and disconnecting the inner SCBSCs for six enzyme-PEDOT_g electrodes in series. b) Scheme of the experimental set-up when none (1), two (2) or one (3) inner SCBSCs were connected.

The voltage increase was attributed to the connection of three biosupercapacitors in series in the same electrolyte without any separation membrane. The potential decay after the inner cells were switched on may be attributed to the slow discharge of the pseudocapacitance contribution. The finally reached plateau might be due to the rate of the slow discharge process becoming equal to that of the BFC charge by the enzymatic reactions. This slow discharge observed could be caused by the low ionic strength of the blood mimicking buffer and the slow counter ions diffusion inside PEDOT structure.

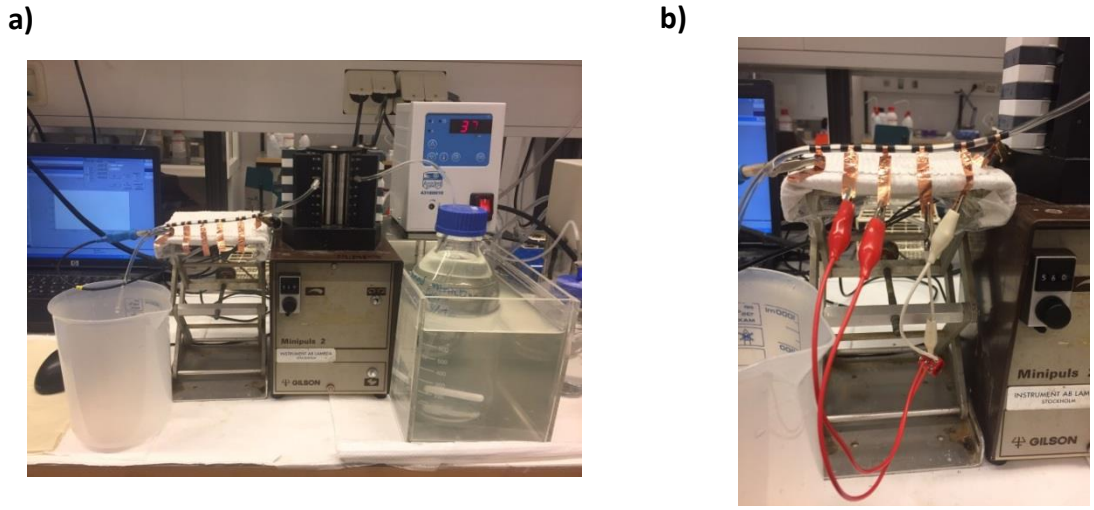

Figure 4.6.13 a) Photograph of the experimental set-up used for performing the experiments of the 6 bio-capacitive electrodes put in series. b) Photograph of the switch used to connect simultaneously the inner SCBSCs.

The experiment was repeated using tubular graphite electrodes without PEDOT (Fig. 4.6.14). In this case the initial OCV value recorded was higher than that of PEDOT_g electrodes (Fig.4.6.12.a), although the connection of the inner BFCs (all or only 2 of them) yielded a voltage decrease. In this case, the OCV reached faster a stable value, which was lower than the initial OCV. Switching off the inner cells restored the initial OCV.

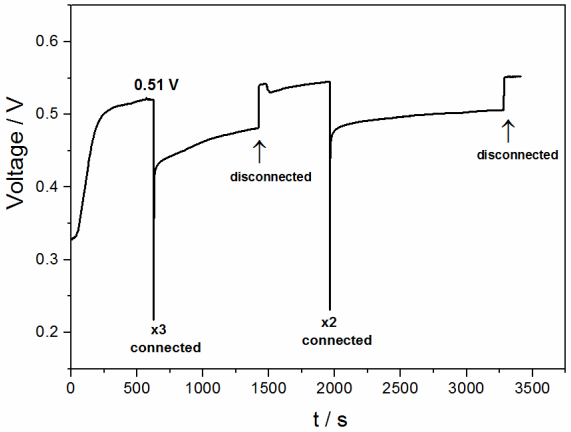

Figure 4.6.14 Chronopotentiometry at open circuit condition of an external BFC performed connecting and disconnecting inner BFCs with 6 enzyme-graphite electrodes in series as in Fig 4.6.12.b.

4.6.2.2.1 EIS characterization

EIS measurements were performed for the set-up of 6 capacitive bio-electrodes in series with and without connecting the inner cells. The first EIS was recorded with the two external bioelectrodes connected to the potentiostat (Fig. 4.6.15.a, black curve), applying as bias potential the OCV measured for the cell, while the inner bioelectrodes were not connected between them. Afterwards, EIS was performed connecting only one (x2) or both (x3) inner SCBSCs, setting as bias potential that corresponding to the plateau obtained when connected, 0.3 V and 0.35 V for x2 and x3 system respectively (Fig. 4.6.15.a, red and blue curves respectively). These potentials allowed performing the EIS measurements in steady-state conditions, avoiding the capacitor discharge that would disrupt the ~5 min-long EIS measurement. The signals obtained show a similar behavior to that obtained with one SCBSC (Fig. 4.6.11), so the same equivalent circuit could be applied for these experimental data (Fig. 4.6.15.b). The most interesting feature is the clear decrease of the R_s and the overall resistance (R)[6] values when the inner SCBSCs were connected (Fig. 4.6.15.a, Table 4.6.5). However, the R decrease was very similar when either one or both inner cells were connected (Table 4.6.5) and not as high as expected from the initial potential increase. This slight difference observed may be due to the EIS spectra recording at the plateau potential, which is very similar in both cases.

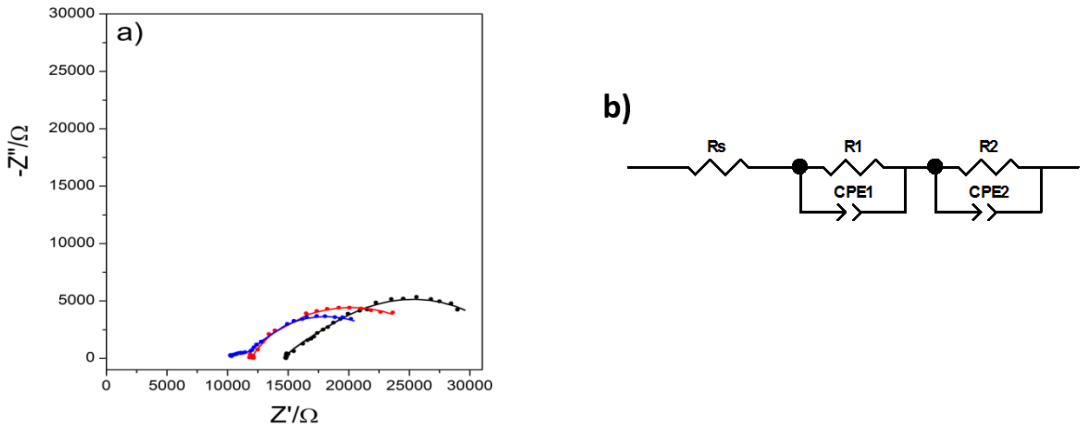

Figure 4.6.15 a) EIS experimental spectra for x1 at 0.24 V (black), x2 at 0.3 V (red) and x3 at 0.35 V(blue) SCBSCs; the lines represent the equivalent circuit fitting, whereas the dots represent the experimental data. b) Equivalent circuit used for the fitting of each system.

	Rs (Ω)	R1 (Ω)	CPE1 (F s $^{\alpha-1}$)	α	R2 (Ω)	CPE2 (F s $^{\alpha-1}$)	α	R overall (Ω)
X1_at OCV 240 mV	14622	3452 ± 331	3.1E-05 ± 1E-06	0.55	15966 ± 271	4.1E-05 ± 2E-06	0.69	34040 ± 602
X2_at 300 mV	11959 ± 24	6590	4.9E-05 ± 2E-06	0.68	9500 ± 295	1.01E-04 ± 4E-06	0.7	28049 ± 319
X3_at 350 mV	10146	1615 ± 39	5.4E-06 ± 2E-07	0.59	12718 ± 138	5.97E-05 ± 9E-07	0.66	24479 ± 177

Table 4.6.5 Values of the parameters obtained by fitting the impedance spectra with the equivalent circuits shown in Fig. 4.6.14.b with or without connecting the inner SCBSCs.

[6] The overall R values were obtained by the sum of each R element in series.

EIS spectra were recorded at 0.3 V and 0.35 V by connecting to the potentiostat the two electrodes at the edges and without the connection of the inner cells, in order to confirm that the resistance decrease was only due to the connection of the inner cells and not due to the different potentials applied during the measurement, which could influence PEDOT behaviour. As shown in Fig. 4.6.16 and Table 4.6.6 the values of R_s as well as the overall resistances are very similar, thus hardly dependent of the bias potential.

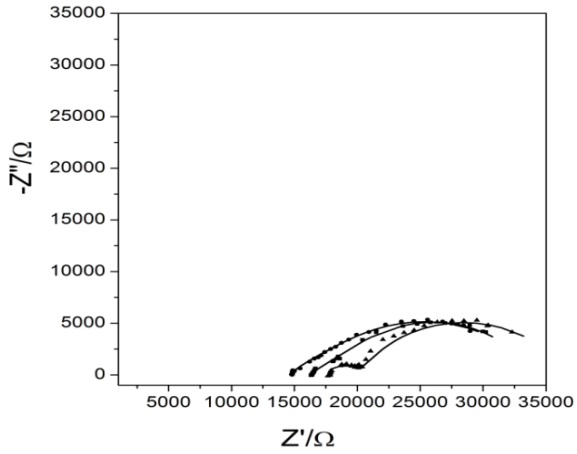

Figure 4.6.16 EIS experimental spectra for x1 bio-supercapacitor at 0.24 V (dots), at 0.3 V (triangles) and at 0.35 V (square) black); the lines represent the equivalent circuit fitting, whereas the dots, square and triangles represent the experimental data. The equivalent circuit reported in Fig. 4.7.14.b was used for the fitting.

	Rs (Ω)	R1 (Ω)	CPE1 (F s $^{\alpha-1}$)	α	R2 (Ω)	CPE2 (F s $^{\alpha-1}$)	α	R overall (Ω)
X1_at OCV 240 mV	14622	3452 ± 331	3.1E-05 ± 1E-06	0.55	15966 ± 271	4.1E-05 ± 2E-06	0.69	34040 ± 602
X1_at 300 mV	17508	2722 ±105	7.5E-07 ±7E-8	0.7	16483 ±367	3.196E-5 ±1E-8	0.7	36713 ±472
X1_at 350 mV	16300	3179 ±347	3.1E-5 ±2E-6	0.55	14330 ±292	3.8E-5 ±2E-6	0.75	33809 ±639

Table 4.6.6 Values of the parameters obtained by fitting the impedance spectra with the equivalent circuits shown in Fig. 4.6.14.b of the experimental spectra reported in Fig. 4.6.15.

4.6.2.2.2 Power output

The setup of six SCBSCs in series was tested by 2-electrode chronoamperometry, connecting the biocathode to the potentiostat as working electrode and the bioanode as combined reference/counter electrode. The system was studied with and without the connection of the inner SCBSCs. In the second case the polarization curve was obtained by applying different potential pulses starting from the system´s OCV (0.25 V) to 0.01 V in 0.05 V intervals, recording the steady state currents reached at each potential applied. The polarization curve for the system including the inner SCBSCs was obtained by starting at the potential where the OCV stabilizes after the connection (0.4 V). The corresponding power output curves were obtained for each case (Fig. 4.6.17). A maximum power output of 0.34 µW at an operating voltage of 0.15 V was determined when the inner SCBSCs were not

connected (Fig. 4.6.17.a). A maximum power output of 0.6 µW at operating voltage of 0.2 V was obtained when the inner SCBSCs were connected (Fig. 4.6.17.b).

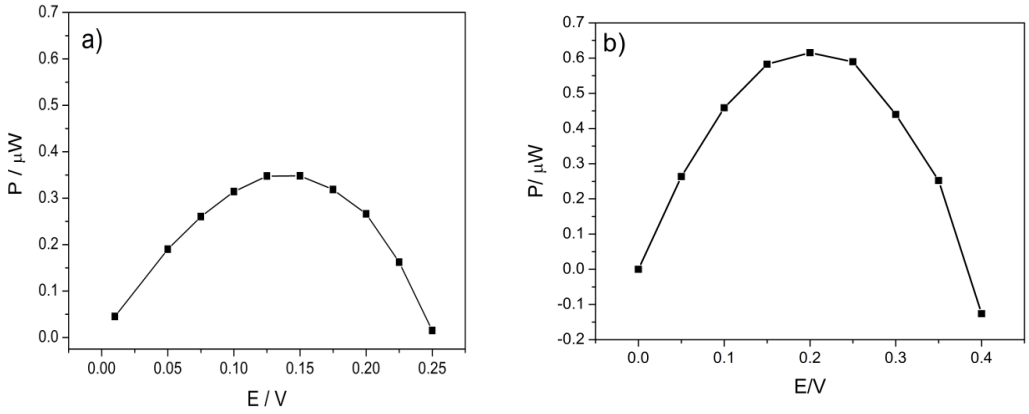

Figure 4.6.17 Power output curves obtained without (a) or with (b) the connection of the inner SCBSCs.

4.6.3 *Ex vivo* measurements

The same set of experiments performed *in vitro* conditions were repeated in *ex vivo* conditions. The electrodes were prepared and modified with the enzymes as reported in 3.2.6 section.

4.6.3.1 Experimental set up

Figure 4.6.17 illustrates how the enzymatic PEDOT_g electrodes were connected in series and connected directly to the dorsal venous of a human volunteer. Figure 4.6.18.a shows how the external electrodes were connected to the potentiostat, whereas Fig. 4.6.18.b shows the switching on of the inner cells.

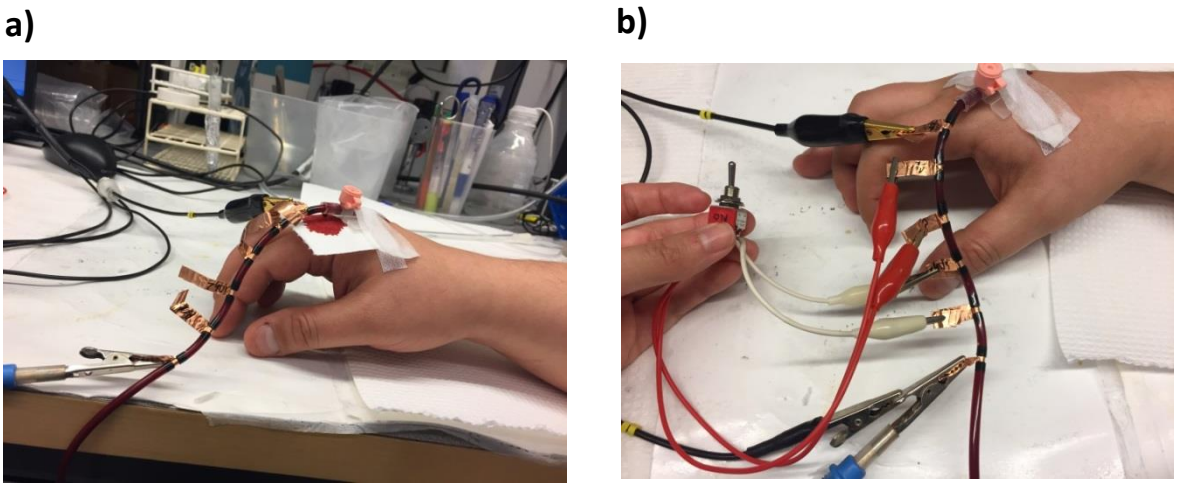

Figure 4.6.18 a) Photograph of the experimental set-up used for performing the experiments ex vivo connecting the 6 capacitive bio-electrodes in series directly to a dorsal venous of a hand. b) Photograph of the switch used to connect simultaneously the inner cells.

4.6.3.2 Measurements in blood

4.6.2.3.1 Charge and connection of the SCBSCs in blood stream

The *ex vivo* experiments were performed twice. Figure 4.6.19.a-b reports the two experiments performed. Initially the electrodes were fully discharged and then let to charge until a stable value of OCV (0.234 V) was reached. The initial OCV obtained for both experiments was comparable (0.234 V vs. 0.247 V), which also matched with the initial OCV values obtained in blood mimicking buffer. Connecting one inner SCBSC (Fig. 4.6.19.a) yielded a 0.44 V OCV value, which is the same behavior observed for *in vitro* conditions after connecting the inner cells in the *ex vivo* experiments. Connection of the two inner cells yielded an OCV of 0.58 V (Fig. 4.6.19.b), which is lower than expected from the *in vitro* results. When they were re-connected again a lower value was measured but that was quite reproducible in the third cycle. This decrease in the OCV value observed might have been caused by not letting the capacitors charging for enough time.

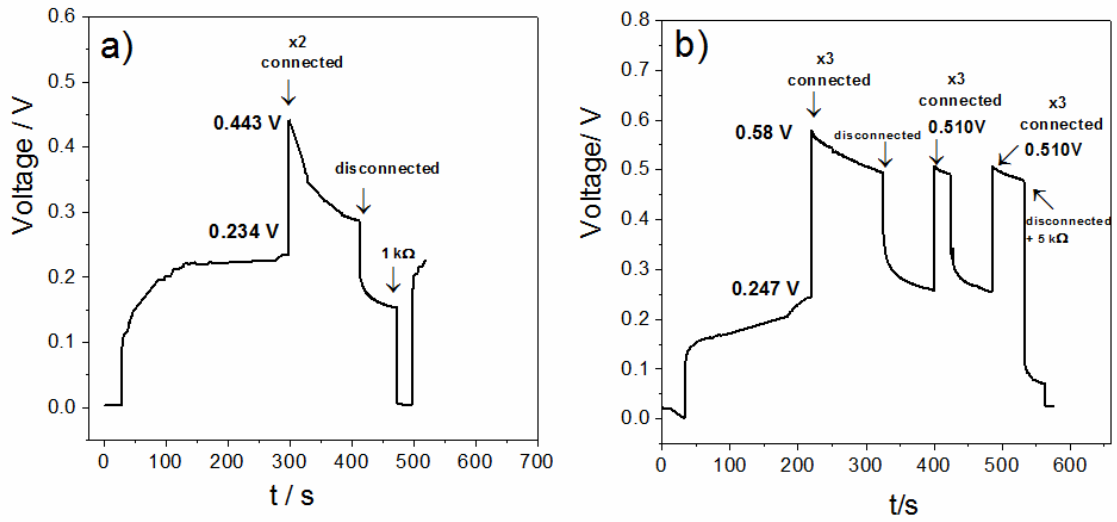

Figure 4.6.19 Chronopotentiometry at open circuit condition of the external SCBSC performed *ex vivo* connecting and disconnecting internal SCBSCs with enzyme-PEDOT_g electrodes in series. a) and b) represent two different *ex vivo* experiments using the same set up showed in Fig.4.6.18.

4.7.2.3.2 EIS measurements

EIS spectra were also recorded for *ex vivo* experiments at the OCV value (Fig. 4.6.20.a, red curves). The analyses were performed by connecting the external electrodes to the potentiostat (x1_edges) or connecting two sequential electrodes (x1_near) as illustrated in Fig. 4.6.19.b. All spectra fitted to the equivalent circuit reported in Fig. 4.6.20.c. As expected the resistance decreased (5-fold) as the distance between the electrodes was shortened (Table 4.6.8). The same behavior was observed when the experiment was performed in blood mimicking buffer (Fig. 4.6.20.a, black curves). A notorious difference is observed when comparing the electrolyte resistances (Fig. 4.6.20.a) and the overall R of

real blood and blood mimicking buffer (Table 4.6.8), real blood offers much higher resistance because blood could coagulate after certain time.

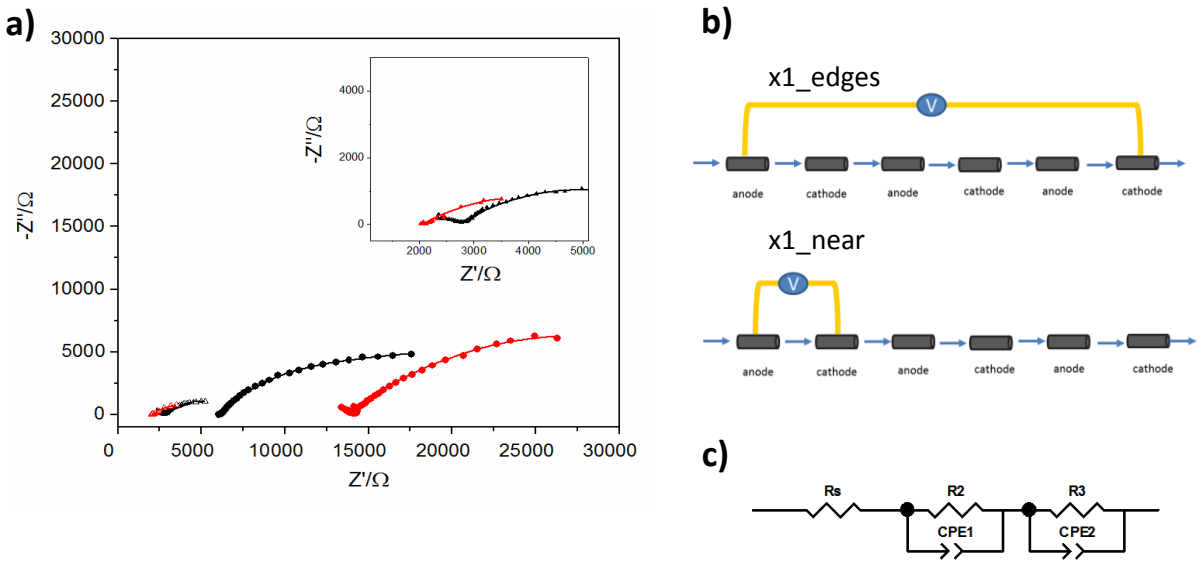

Figure 4.6.20 a) EIS experimental spectra for x1_edges (dots) and x1_near (triangles) SCBSC *in vitro* (black) *or ex vivo* (red) conditions; the lines represent the equivalent circuit fitting, whereas the dots represent the experimental data. B) Representation of how the cells are connected to the instrument. c) Equivalent circuit used for the fitting of each system.

		R overall (Ω)
in vitro exp	x1_near	7090
	x1_edges	34294
ex vivo exp	x1_near	5237
	x1_edges	39908

Table 4.6.8 Values of the overall resistance obtained by fitting the impedance spectra reported in Fig. 4.6.18 with the equivalent circuits shown in Fig. 4.6.18.c.

4.6.4 Conclusions

Tubular PEDOT modified graphite electrodes were successful manufactured. SEM images confirmed the presence of an approximately 10 µm thickness PEDOT layer. Electrochemical characterization showed that the PEDOT conductive polymer increased the capacitance and improved the charge transfer at the electrode/electrolyte interface compared to bare graphite electrodes. Characterization of a complete SCBSC demonstrated that the cathodic part is the limiting one due to O_2 diffusion limitations, confirming the previous results in literature (Lepage, Albernaz et al. 2012). An initial OCV value of around 0.24 V was measured that was very stable and reproducible in all the *in vitro* and *ex vivo* experiments. This value is slightly lower than one previously reported for the same set up

but using bare tubular graphite (Pankratov, Ohlsson et al. 2016) indicating that PEDOT presence might decrease the overall initial OCV because it is more difficult to cover the whole surface area with the biocatalyst. A maximum power output of 0.34 μW at an operating voltage of 0.15 V was determined when the inner SCBSCs were not connected, which is a lower than 0.74 μW at a cell voltage of 0.16 V obtained when bare tubular graphite electrodes were used (Pankratov, Ohlsson et al. 2016). This difference may be understood if the slightly lower initial OCV and the different design of the system (the electrodes connected to the potentiostant were placed at higher distance between them) are taken into account. When more than one SCBSC were connected in series in a membrane-less set-up and in the same electrolyte, a notable increase in the OCV value was measured (≈ 0.7 V) that decreased with time until reaching a plateau value, which was higher than the initial one. This effect is attributed to the slow discharge of the electrodes pseudocapacitance due to the slower diffusion of counter ions inside PEDOT structure, until a plateau potential is reached once the discharge process equilibrates with the charging process of the BFC. EIS measurements also denoted a clear decrease in the R_s and so in the overall R when more cells were connected. Very reproducible results have been obtained even for the *ex vivo* experiments: the same initial OCV was obtained indicating that the blood mimicking buffer used takes into account all the parameters of real blood, which sometimes can be underestimated or neglected. Furthermore, in *ex vivo* conditions the same behaviour was observed when the inner SCBSCs were connected, but even if the results were very reproducible not the same high voltage was obtained as *in vitro*. This difference may be a result of a not correct functioning of each of the six electrodes. In particular, the cathode components are rate-limiting the BFC due to the low O_2 availability in the system. This design represents a good starting point for the fabrication of a system operating in *ex vivo* conditions, achieving a high OCV and enough power to use it for personal electronics applications.

An increase in the maximum power output (0.6 μW) was also achieved when the inner SCBSCs are connected. However, the power output obtained was not higher than the state of art achieved for a similar system (Pankratov, Ohlsson et al. 2016). Anyway, it is worth mentioning that this represents a first attempt to connect in series several membrane-less SCBSCs in the same electrolyte and further optimization of the system can be achieved. Further development has to be turned to reach a higher constant OCV for the enough time to power an electronic device, to improve bio-modification of the electrodes or to test more efficient biocatalysts for example.

5. Global discussion

The aim of this chapter is to make a general discussion of the all results presented in the previous chapters.

The development of DET based biocathodes with high activity towards O_2 reduction at physiological conditions was one of the principal goals of this Thesis. Indeed, due to the possible physiological application of MCOs based systems, the inhibition mechanism by halide anions (F^- and Cl^-) was firstly studied, by infrared spectroelectrochemistry using N_3^- as active FTIR probe. Two different MCOs were used: mgBOx and ThLc. As reported in chapter 4.1, two different behaviours are observed upon the addition of fluoride or chloride ions. Fluoride ions compete with azide for binding at one of the T2/T3 copper atoms, whereas chloride ions do not or only do it partially. These results confirm previous reported results that showed that F^- probably interacts with the T2/T3 site of MCOs blocking the intramolecular electronic transfer between the T1 site to the TNC centre (Naqui and Varfolomeev 1980, Xu 1996). The results of section 4.1 are also in agreement with the electrocatalytic behaviour of MCOs based biocathodes, in which both DET and MET are abolished after fluoride addition, whereas only MET is suppressed after chloride addition (Vaz-Dominguez, Campuzano et al. 2008, Beyl, Guschin et al. 2011). Moreover, comparison of the results obtained for the two MCOs indicates that the chloride interaction is more pronounced with the TNC of Lc than with the TNC of BOxs, in agreement with previous characterization results of different BOx (Durand, Gounel et al. 2012, Durand, Kjaergaard et al. 2012, Cadet 2015). Mostly for this reason and for its higher activity at neutral pH, BOx is usually the preferred cathodic enzyme for the design of BFCs (Falk, Pankratov et al. 2014), despite its lower onset potential compared to high redox potential Lcs. Indeed, a BOx was used as cathodic catalyst of the BFC developed in section 4.6.

In order to try to overcome the possible drawbacks of using Lcs at physiological conditions (negligible activity at neutral pH and halide inhibition), two different cysteine mutants produced from a blood tolerant laccase obtained by directed evolution (ChU-B) (Mate, Gonzalez-Perez et al. 2013) were presented in section 4.2. The cysteine mutations were placed near the T1 site (as depicted in Fig. 4.2.1) in order to favour their correct immobilization on gold electrodes for DET regime. The development of laccase mutants by site directed mutagenesis is a well-known strategy to try to achieve, through a correct immobilization, DET. Several examples have been reported in literature for Lcs in which the modifications were performed near the T1 centre, inserting for example an unnatural aminoacid (Guan, Kurra et al. 2015) or pyrene (Lalaoui, Rousselot-Pailley et al. 2016), achieving in this last case an electrocatalytic current density of O_2 reduction of almost -3 mA/cm^2. Other modifications were inserted at the end of the N-terminus. In this way histidine-tagged laccase was immobilized on a GC electrode modified with nitrilotriacetic acid (NTA) achieving current densities of -0.7 $\mu A/cm^2$ (Sosna,

Boer et al. 2013). However, when a gold surface was modified with a NTA-terminated alkanethiol no DET was achieved using another histidine tagged laccase. Only MET could be measured, probably because the alkanethiol linker was too long in this case for achieving a fast DET (Balland, Hureau et al. 2008). In this Thesis, different functionalization strategies have been tested but none gave positive results, whatever mutant was used. As commented in the discussion of that section, different causes can lead to the failure of these experiments. Maybe, a better strategy would be to substitute the non-targeted free surface cysteines with other amino acid residues to ensure single point attachment. It is also possible that the thiol-based linkers used were not adequate for achieving DET, as in the case reported above. However, the most likely reason is related to the mutants, which during the evolution process may have suffered some structural/functional changes that preclude an adequate orientation for DET with the functionalization strategies used. Surely, it is always difficult to reach the adequate compromise between activity and stability during the evolutional process (Romero and Arnold 2009, Mate 2013), which might have not been obtained in the case of the mutants used in section 4.2. Nevertheless, the very limited amounts of mutant laccases available have impeded further research in this direction.

The successive sections of this Thesis are focused in the development of high surface area nanostructured electrodes. Indeed, the development of nanostructured electrodes is a promising approach in order to immobilize several enzyme layers and in this way achieve higher current densities (Falk, Blum et al. 2012, de Poulpiquet, Ciaccafava et al. 2014).

The macroporous gold electrodes studied present an active surface area value of ≈ 1.6 cm^2, 8-fold higher than a gold wire. However, untill now only MET based approaches have been used for immobilizing the biocatalyst on macroporous gold electrodes (Cadet 2015, Karajic 2015), due to the difficulties to immobilize in a oriented way the enzyme molecules and, at the same time, take advantage from the huge active surface area. In section 4.2, for the first time a covalent immobilization of mgBOx on macroporous gold electrodes was presented, achieving a current density of -0.35 mA/cm^2 (vs. geometric area). This value is 10-fold higher than that measured when a non-nanostructured support, such as gold wire, was used (-0.031 mA/cm^2) and almost 30-fold higher than when adsorption is used as immobilization strategy (-0.012 mA/cm^2). The current density achieved is still lower than the current density of -0.8 mA/cm^2 achieved when mtBOx was immobilized on nanoporous gold electrodes (Salaj-Kosla, Pöller et al. 2012, Siepenkoetter, Salaj-Kosla et al. 2017). However, the immobilization strategy could be improved, for example, by optimizing the macroporous gold surface functionalization with a mixed thiol/naphtoic acid monolayer in order to cover the bare gold surface that was not eventually covered during the diazonium reduction process.

In sections 4.3 and 4.4, high surface area electrodes based on different nano-structured materials, such as AuNRs and graphene have been presented. AuNRs, prepared by a seedless growth method, were attached covalently to LDG electrodes and used as support for the covalent immobilization of ThLc,

achieving current densities up to -0.6 mA/cm^2 under stationary conditions, very similar to the currents obtained when LDG were modified with AuNPs (Gutierrez-Sanchez, Pita et al. 2012). However, the electrocatalytic response (Fig. 4.3.12) seems to be completely rate limited by DET when the electrode is rotated, concluding that the enzyme molecules are not as well wired than with AuNPs and that there is a distribution of different distances between the active site and the electrode surface (Léger, Jones et al. 2002). This can be explained considering the larger size of AuNRs compared to AuNPs. Indeed, a valid hypothesis is that when the Au nanolements are bigger than the enzyme molecules the improvement effect in the electronic coupling does not occur (Pankratov, Sundberg et al. 2014).

The fabrication of stable, robust and reproducible graphene based electrodes was achieved by electrodeposition of GO on GC electrodes. The process was optimized in terms of pH and conductivity, and by fixing the electrochemical parameters involved. This technique leads to a more uniform coverage and controlled thickness than previous reported methods, while avoiding the use of extra binders (Eda and Chhowalla 2010, Pumera, Ambrosi et al. 2010, Kashyap, Mishra et al. 2014). Electrochemical characterization by EIS (Fig. 4.4.17) and CV (Fig. 4.4.18), confirmed an improved electron transfer at the electrode-electrolyte interface for the graphene based electrodes, which presented a predominantly diffusion-controlled behaviour. XPS (Fig. 4.4.15) and FTIR (Fig. 4.4.16) spectroscopic measurements confirmed that during the electrodeposition process the aromatic sp^2 carbon structure is restored and some oxygen funtionalities remain in the material after the process, mainly as hydroxyl and epoxy groups. These remaing oxygen functionalities of erGO provide reactive groups, where further functionalizations can be performed in order to carry out covalent immobilization of mtBOx and ThLc and to fabricate DET based biocathodes. In both cases the capacitive area of the cathode is clearly enhanced and a strong electrocatalytic effect is detected, up to -1 mA/cm^{-2} for ThLc, almost double than the current obtained for AuNRs modified electrodes with the same enzyme. Tominaga et *al*., however, reported current density of -1.6 mA/cm^2 when Lc is immobilized on graphene-nanoplatelet film electrodes prepared in the presence of 0.01 g NaH_2PO_4 additive (Tominaga, Noda et al. 2015). This good result was achieved because, thanks to this preparation method, a material with surface area of 0.70 x10^3 m^2 g^{-1} was obtained, which is much higher than the surface area of GO used for the electrodeposition process (≈ 0.10 x10^3 m^2 g^{-1}). However, in this work the Lc was just physically adsorbed on the electrode instead of covalently bound, and no data were given about the reproducibility or the stability of the catalytic current density reported (Tominaga, Noda et al. 2015).

The current density obtained in this Thesis using the graphene based electrodes for BOx immobilization is 2-fold higher than the values achieved with the macroporous glod electrodes reported above, and higher than the current density obtained in the work of Filip et *al*. that achieved -280 µA/cm^2 by deposition of BOx and GO on GC, followed by electrochemical reduction of GO (Filip and Tkac 2014). It is worth mentioning that, when highly nanostructured surfaces are used, such as graphene or macroporous gold), the mass transport limitation of the substrate (in this case O_2) inside

the porous structure due to the thickness of the catalytic layer has to be considered (Gara, Ward et al. 2013). It is also important to remark that increasing the loading of graphene on the electrode will increase the electrocatalytic response, although the reproducibility of the results in this case will be lower due to the difficulty in controlling the surface functionalization.
Among all the nanostructured electrodes tested in this Thesis, the graphene based electrodes prepared by ED of GO showed the best results in terms of catalytic currents, capacitance and stability. Indeed, the higher current densities are obtained with these electrodes, the fabrication method is easier than for macrocoporous gold electrodes and the results are more reproducible than with the AuNRs modified electrodes.

In section 4.5 for the first time the fabrication of mediator-less transparent bioelectrodes have been presented, opening the possibility to use this modification approach for *ex vivo* applications, such as smart contact lenses. Electrochemical characterizations confirmed the successful functionalization of the ITO surface and covalent immobilization of the enzymes. However, the DET catalytic currents obtained were not so high (-1.2 $\mu A/cm^2$ and 3 $\mu A/cm^2$ for the cathode and anode, respectively). The cause is that only an enzyme monolayer can be covalently immobilized on a flat electrode, confirming the necessity of developing nanostructured devices for obtaining higher enzyme coverage, and thus a higher electrocatalytic performance. Indeed, application of this immobilization strategy with nanostructured ITO electrodes has recently been reported for the fabrication of a mediator-less transparent BFC with higher performances (González-Arribas, Bobrowski et al. 2017).

In the last section, a combination between a conventional BFC and a supercapacitor for possible *ex vivo* applications has been reported using as biocathode a DET-based MCO electrode. The presence of a conducting polymer, such as PEDOT, improved the electronic transfer between the electrode/electrolyte surface, as demonstrated by EIS measurements (Fig. 4.6.8). Moreover, the EIS characterization of the bioanode and the biocathode by separate (Fig. 4.6.11) confirmed that the major limitation in the system is represented by the cathode element. A first attempt to connect in series in the same electrolyte several SCBSCs showed a clear increase in the voltage and in the power output of the device when compared to the performance of only one SCBSC (Fig. 4.6.12 and Fig. 4.6.17). This system was also used for *ex vivo* measurements obtaining a high reproducibility of the *in vitro* experiment. These results confirm that all the parameters considered during *in vitro* measurements reflect with high accuracy the real parameters of the human body, which often are underestimated. Future work is envisaged for optimizing the immobilization of the bioelectrocatalysts on the electrodes, especially for enhancing operational stability, a crucial issue in bioelectrochemical devices for energy conversion/storage (Falk, Narváez Villarrubia et al. 2013, Shleev 2017).

The results presented in this Thesis show how DET based systems can be developed with different functionalization strategies and how the use of nanostructured electrodes can enhance the

electrocatalytic performance. Especially, graphene based electrodes prepared by electrodeposition represent a valid alternative to the fabrication of stable, robust and reproducible electrodes for many applications.

DET based BFC systems presenting good performance in physiological conditions have been also showed. These results open the possibility for *ex vivo* applications, where the typical drawbacks presented for *in vivo* applications can be avoided (Cosnier, J. Gross et al. 2016, Shleev 2017).

6. Conclusions

- FTIR spectroelectrochemistry studies confirm that fluoride ions compete with azide for binding at one of the T2/T3 Cu ions of MCOs, blocking the intramolecular electronic transfer from the T1 site to the Cu cluster, whereas chloride ions barely do it. Moreover, chloride inhibition is less accentuated for BOx than for Lc.
- Two Lc mutants, with Cys substitution near the T1 site, were produced and purified successfully. However, these mutants did not show high catalytic performance towards O_2 reduction when they are used as catalysts for DET based gold modified biocathodes, probably because of low operational stability of the mutants or a not fully optimized immobilization protocol due to lack of newly produced mutants.
- Nanostructured high surface area electrodes modified with different materials have been developed for MCOs immobilization aiming to efficient DET:
    a) LDG electrodes were covalently modified with AuNRs and used as a nanostructured plataform for Lc immobilization achieving catalytic currents of oxygen reduction in a DET regime up to -0.6 mA/cm^2 and reflecting a wired distribution of non-optimally wired Lc molecules that might be resulting from the larger size of AuNRs than enzyme molecules.
    b) High surface area graphene based electrodes were prepared by electrodeposition of GO on GC electrodes. The electrodeposition process yield to a highly porous conductive surface that still presents some oxygen based functional groups (as hydroxyl or epoxy) as confirmed by XPS and FTIR measurements. The covalent immobilization of ThLc or BOx on these electrodes lead to the fabrication of high capacitive and stable DET based biocathodes achieving current densities up to -1 mA/cm^2 for O_2 reduction.
    c) Macroporous gold electrodes, with higher active surface area, were employed successfully for the first time as support for the covalent immobilization of mgBOx. Current densities up to -18 $\mu A/cm^2$ in a DET based regime have been obtained, which is almost nine times higher than the current densities obtained so far by simply adsorption ($\approx$ -2 $\mu A/cm^2$).
- ITO electrodes were chemically modified successfully with GLYMO and APTES silane for the covalent immobilization of mtBOx and ctCDH, respectively. Thanks to this modification approach, mediator-less transparent bioelectrodes that show catalytic response have been fabricated.
- DET based SCBSC have been fabricated for possible *ex vivo* applications. For the first time several SCBSCs were connected in series in the same electrolyte in a membrane-less and mediator-less set up, achieving higher voltage ($\approx$ 0.7 V) and power output (0.6 μW) compared to only one SCBSC. The experimental results showed a good reproducibility of the *ex vivo* results compared to the *in vitro* ones.

6. Conclusiones

- Las medidas espectroelectroquìmicas de FTIR confirmaron que los iones fluoruros compiten con la azida para unirse a uno de los cobres del centro T2/T3 de las oxidasas multicobre, bloqueando la transferencia electrónica intermolecular desde el centro T1 hasta el T2/T3, contrariamente a los iones cloruros que apenas bloquean este tipo de transferencia. Además, la inhibición por parte de cloruros es menor para BOx que para Lc.
- La producción y purificación de dos mutantes de Lc, los cuales presentan una Cys cerca del centro T1, ha sido llevada al cabo con éxito. Sin embargo, ninguna respuesta catalítica ha sido obtenida con ninguno de los mutantes cuando han sido utilizados como biocatalizadores sobre soporte de oro, debido probablemente a la baja estabilidad operacional de los mutantes o a la imposibilidad de optimizar el protocolo de inmovilización por la falta de más enzimas purificadas.
- Distintos materiales nanoestructurados de gran área superficial han sido desarrollados para la inmovilización de oxidasas de multicobre con el fin de obtener trasferencia electrónica directa:
    a) Electrodos de grafito de baja densidad se modificaron covalentemente con nanohilos de oro para inmovilizar de forma orientada y covalente ThLc, obteniendo corrientes catalíticas de -0.6 mA/cm^2. La respuesta bioelectrocatalitica obtenida refleja una distribucion de moléculas de enzima no adecuadamente orientadas, debido a las mayores dimensiones de los nanohilos respecto a las moléculas de enzima.
    b) Electrodos de grafeno se prepararon a través de la electrodeposición de óxido de grafeno (GO) sobre electrodos de carbón vidrio. El proceso de electrodeposicion permite obtener una superficie altamente porosa y conductora, caracterizada por la presencia de grupos funcionales como hidroxilos o epòxidos, como se ha podido demostrar con medidas de XPS y FTIR. La inmovilización covalente de ThLc o BOx sobre estos electrodos nanostructurados ha permitido el diseño de biocatodos estables y de gran área superficial, obteniendo corrientes cataliticas de -1 mA/cm^2.
    c) Por primera vez se llevó a cabo la inmovilización covalente de mgBOx sobre electrodos macroporosos de oro. Se obtuvo una corriente de -18 $\mu A/cm^2$, casi diez veces mayor que las corrientes obtenidas por simple adsorción ($\approx$ -2 $\mu A/cm^2$).
- Se modificaron con éxito electrodos de ITO con los silanos GLYMO y APTES para la inmovilización covalente de mtBOx y ctCDH, respectivamente. Se han desarrollado de esta manera bioelectrodos transparentes capaces de proporcionar transferencia electrónica directa.
- Por primera vez distintos SCBSC han sido conectados en serie, en el mismo electrolito, sin membranas de separación, obteniendo valores de voltaje ($\approx$ 0.7 V) y potencia máxima (0.6 μW), mayores que un solo SCBSC, demostrando también posibles aplicaciones *ex vivo*.

7. References

Abad, J. M., M. Gass, A. Bleloch and D. J. Schiffrin (2009). *"Direct electron transfer to a metalloenzyme redox center coordinated to a monolayer-protected cluster."* Journal of the American Chemical Society 131(29): 10229-10236.

Abad, J. M., M. Vélez, C. Santamaría, J. M. Guisán, P. R. Matheus, L. Vázquez, I. Gazaryan, L. Gorton, T. Gibson and V. M. Fernández (2002). *"Immobilization of peroxidase glycoprotein on gold electrodes modified with mixed epoxy-boronic acid monolayers."* Journal of the American Chemical Society 124(43): 12845-12853.

Acik, M., G. Lee, C. Mattevi, A. Pirkle, R. M. Wallace, M. Chhowalla, K. Cho and Y. Chabal (2011). *"The role of oxygen during thermal reduction of graphene oxide studied by infrared absorption spectroscopy."* The Journal of Physical Chemistry C 115(40): 19761-19781.

Agbo, P., J. R. Heath and H. B. Gray (2013). *"Catalysis of dioxygen reduction by thermus thermophilus Strain HB27 laccase on ketjen black electrodes."* The Journal of Physical Chemistry B 117(2): 527-534.

Alcalde, M. (2010). *Mutagenesis protocols in saccharomyces cerevisiae by in vivo overlap extension.* In Vitro Mutagenesis Protocols: Third Edition. J. Braman. Totowa, NJ, Humana Press: 3-14.

Ali, M. R., B. Snyder and M. A. El-Sayed (2012). *"Synthesis and optical properties of small Au nanorods using a seedless growth technique."* Langmuir 28(25): 9807-9815.

Andoralov, V., M. Falk, D. B. Suyatin, M. Granmo, J. Sotres, R. Ludwig, V. O. Popov, J. Schouenborg, Z. Blum and S. Shleev (2013). *"Biofuel cell based on microscale nanostructured electrodes with inductive coupling to rat brain neurons."* Scientific Reports 3: 3270.

Ardhaoui, M., M. Zheng, J. Pulpytel, D. Dowling, C. Jolivalt and F. A. Khonsari (2013). *"Plasma functionalized carbon electrode for laccase-catalyzed oxygen reduction by direct electron transfer."* Bioelectrochemistry 91: 52-61.

Arechederra, R. L., K. Boehm and S. D. Minteer (2009). *"Mitochondrial bioelectrocatalysis for biofuel cell applications."* Electrochimica Acta 54(28): 7268-7273.

Arroyo, M. (1998). *"Inmobilized enzymes: Theory, methods of study and applications."* Ars Pharmaceutica 39: 23-39.

Arya, S. K., A. K. Prusty, S. P. Singh, P. R. Solanki, M. K. Pandey, M. Datta and B. D. Malhotra (2007). *"Cholesterol biosensor based on N-(2-aminoethyl)-3-aminopropyl-trimethoxysilane self-assembled monolayer."* Anal Biochem 363(2): 210-218.

Baldrian, P. (2006). "*Fungal laccases - occurrence and properties."* FEMS Microbiol Rev 30(2): 215-242.

Balint, R., N. J. Cassidy and S. H. Cartmell (2014). *"Conductive polymers: Towards a smart biomaterial for tissue engineering."* Acta Biomaterialia 10(6): 2341-2353.

Balland, V., C. Hureau, A. M. Cusano, Y. Liu, T. Tron and B. Limoges (2008). *"Oriented immobilization of a fully active monolayer of histidine-tagged recombinant laccase on modified gold electrodes."* Chemistry – A European Journal 14(24): 7186-7192.

Bandodkar, A. J. and J. Wang (2016). "*Wearable biofuel cells: a review*." Electroanalysis 28(6): 1188-1200.

Baraton, M.-I. (2011). *"The future of tco materials: stakes and challenges."* MRS Proceedings 1209.

Bard, A. J. and L. R. Faulkner (2000). *Electrochemical methods: fundamentals and applications*, Wiley.

Barrett, F. M. (1991). "*Phenoloxidase and the integument."* K. Binnintgon & R. retnakaran (Eds), Physiology of the insect epidermis Australia: CSIRO Publications: 195-212.

Baughman, R. H., A. A. Zakhidov and W. A. de Heer (2002). *"Carbon nanotubes--the route toward applications."* Science 297(5582): 787-792.

Beh, W. S., Kim, I. T., Qin, D., Xia, Y. and Whitesides, G. M. (1999). "*Formation of patterned microstructures of conducting polymers by soft lithography, and applications in microelectronic device fabrication."* Adv. Mater 11: 1038–1041.

Ben-Ali, S., D. A. Cook, P. N. Bartlett and A. Kuhn (2005). "*Bioelectrocatalysis with modified highly ordered macroporous electrodes.*" Journal of Electroanalytical Chemistry 579(2): 181-187.

Beyl, Y., D. A. Guschin, S. Shleev and W. Schuhmann (2011). "*A chloride resistant high potential oxygen reducing biocathode based on a fungal laccase incorporated into an optimized Os-complex modified redox hydrogel."* Electrochemistry Communications 13(5): 474-476.

Bisquert, J., G. G. Belmonte, F. F. Santiago, N. S. Ferriols, M. Yamashita and E. C. Pereira (2000). *"Application of a distributed impedance model in the analysis of conducting polymer films."* Electrochemistry Communications 2(8): 601-605.

Blanford, C. F., C. E. Foster, R. S. Heath and F. A. Armstrong (2009). *"Efficient electrocatalytic oxygen reduction by the 'blue' copper oxidase, laccase, directly attached to chemically modified carbons."* Faraday Discussions 140(0): 319-335.

Bobacka, J., A. Lewenstam and A. Ivaska (2000). "*Electrochemical impedance spectroscopy of oxidized poly(3,4-ethylenedioxythiophene) film electrodes in aqueous solutions.*" Journal of Electroanalytical Chemistry 489(1–2): 17-27.

Bradford, M. M. (1976). "*A rapid and sensitive method for the quantitation of microgram quantities of protein utilizing the principle of protein-dye binding."* Analytical Biochemistry 72(1): 248-254.

Bradshaw, A. M. C., S. L.; Domcke, W.; Krause, U. (1974). *"Plasmon coupling to core hole excitations in carbon."* Journal of Physics C: Solid State Physics, Volume 7, Issue 24, pp. 4503-4512 (1974). Volume 7(Issue 24): pp. 4503-4512.

Brooksby, P. A. and A. J. Downard (2004). *"Electrochemical and atomic force microscopy study of carbon surface modification via diazonium reduction in aqueous and acetonitrile solutions."* Langmuir 20(12): 5038-5045.

Cachet, C. and R. Wiart (1985). "*Couple axial gradients of potential and concentration in a cylindrical pore electrode: an impedance model."* Journal of Electroanalytical Chemistry and Interfacial Electrochemistry 195(1): 21-37.

Cadet, M. (2015). "*Vers la conception d'une biopile enzymatique a glucose/oxygene efficace en milieu biologique*." PhD Thesis.

Canbaz, M. C. and M. K. Sezginturk (2014). "*Fabrication of a highly sensitive disposable immunosensor based on indium tin oxide substrates for cancer biomarker detection."* Anal Biochem 446: 9-18.

Cinquin, P., C. Gondran, F. Giroud, S. Mazabrard, A. Pellissier, F. Boucher, J.-P. Alcaraz, K. Gorgy, F. Lenouvel, S. Mathé, P. Porcu and S. Cosnier (2010). "*A glucose biofuel cell implanted in rats.*" PLOS ONE 5(5): e10476.

Clarke, A. P., P. Jandik, R. D. Rocklin, Y. Liu and N. Avdalovic (1999). "*An integrated amperometry waveform for the direct, sensitive detection of amino acids and amino sugars following anion-exchange chromatography."* Analytical Chemistry 71(14): 2774-2781.

Clayden, J., N. Greeves and S. G. Warren (2012). *Organic chemistry*. Oxford; New YorK, Oxford University Press.

Cole, J. L., L. Avigliano, L. Morpurgo and E. I. Solomon (1991). *"Spectroscopic and chemical studies of the ascorbate oxidase trinuclear copper active site: comparison to laccase."* Journal of the American Chemical Society 113(24): 9080-9089.

Cole, J. L., P. A. Clark and E. I. Solomon (1990). *"Spectroscopic and chemical studies of the laccase trinuclear copper active site: geometric and electronic structure."* Journal of the American Chemical Society 112(26): 9534-9548.

Coman, V., R. Ludwig, W. Harreither, D. Haltrich, L. Gorton, T. Ruzgas and S. Shleev (2010). *"A direct electron transfer-based glucose/oxygen biofuel cell operating in human serum."* Fuel Cells 10(1): 9-16.

Cosnier, S., A. J. Gross, A. Le Goff and M. Holzinger (2016). *"Recent advances on enzymatic glucose/oxygen and hydrogen/oxygen biofuel cells: Achievements and limitations."* Journal of Power Sources 325: 252-263.

Cracknell, J. A., T. P. McNamara, E. D. Lowe and C. F. Blanford (2011). *"Bilirubin oxidase from Myrothecium verrucaria: X-ray determination of the complete crystal structure and a rational surface modification for enhanced electrocatalytic O_2 reduction."* Dalton Transactions 40(25): 6668-6675.

Cracknell, J. A., K. A. Vincent and F. A. Armstrong (2008). "*Enzymes as working or inspirational electrocatalysts for fuel cells and electrolysis."* Chemical Reviews 108(7): 2439-2461.

Champagne, P.-P., M. E. Nesheim and J. A. Ramsay (2013). "*A mechanism for NaCl inhibition of Reactive Blue 19 decolorization and ABTS oxidation by laccase.*" Applied Microbiology and Biotechnology 97(14): 6263-6269.

Chen, D., H. Feng and J. Li (2012). *"Graphene oxide: preparation, functionalization, and electrochemical applications."* Chem Rev 112(11): 6027-6053.

Chen, L., Y. Tang, K. Wang, C. Liu and S. Luo (2011). "*Direct electrodeposition of reduced graphene oxide on glassy carbon electrode and its electrochemical application."* Electrochemistry Communications 13(2): 133-137.

Childs, R. E. and W. G. Bardsley (1975). "*The steady-state kinetics of peroxidase with 2,2'-azino-di-(3-ethyl-benzthiazoline-6-sulphonic acid) as chromogen.*" Biochemical Journal 145(1): 93-103.

Choi, M., K. Jo and H. Yang (2013). *"Effect of different pretreatments on indium-tin oxide electrodes."* Bulletin of the Korean Chemical Society 34(2): 421-425.

Dattoli, E. N. and W. Lu (2011). "*ITO nanowires and nanoparticles for transparent films."* MRS Bulletin 36(10): 782-788.

de Poulpiquet, A., A. Ciaccafava and E. Lojou (2014). "*New trends in enzyme immobilization at nanostructured interfaces for efficient electrocatalysis in biofuel cells."* Electrochimica Acta 126: 104-114.

de Poulpiquet, A., C. H. Kjaergaard, J. Rouhana, I. Mazurenko, P. Infossi, S. Gounel, R. Gadiou, M. T. Giudici-Orticoni, E. I. Solomon, N. Mano and E. Lojou (2017). *"Mechanism of chloride inhibition of bilirubin oxidases and its dependence on potential and pH."* ACS Catalysis 7(6): 3916-3923.

De Volder, M. F. L., S. H. Tawfick, R. H. Baughman and A. J. Hart (2013). "*Carbon nanotubes: present and future commercial applications."* Science 339(6119): 535-539.

Deng, L., L. Shang, Y. Wang, T. Wang, H. Chen and S. Dong (2008). "*Multilayer structured carbon nanotubes/poly-l-lysine/laccase composite cathode for glucose/O_2 biofuel cell."* Electrochemistry Communications 10(7): 1012-1015.

Deng, L., F. Wang, H. Chen, L. Shang, L. Wang, T. Wang and S. Dong (2008). "*A biofuel cell with enhanced performance by multilayer biocatalyst immobilized on highly ordered macroporous electrode."* Biosensors and Bioelectronics 24(2): 329-333.

Di Bari, C., A. Goñi-Urtiaga, M. Pita, S. Shleev, M. D. Toscano, R. Sainz and A. L. De Lacey (2016). *"Fabrication of high surface area graphene electrodes with high performance towards enzymatic oxygen reduction."* Electrochimica Acta 191: 500-509.

Diaconu, M., A. Chira and L. Radu (2014). "*Modulating indium doped tin oxide electrode properties for laccase electron transfer enhancement."* Thin Solid Films 565: 84-88.

Dominguez, C. V. (2009). *"Inmovilizacion covalente y orientada de enzima lacasa para su uso como catodo en pilas des combustible."* Tesis Doctoral.

Dos Santos, L., V. Climent, C. F. Blanford and F. A. Armstrong (2010). *"Mechanistic studies of the 'blue' Cu enzyme, bilirubin oxidase, as a highly efficient electrocatalyst for the oxygen reduction reaction."* Phys Chem Chem Phys 12(42): 13962-13974.

Downard, A. J. and D. Pletcher (1986). *"A study of the conditions for the electrodeposition of polythiophen in acetonitrile."* Journal of Electroanalytical Chemistry and Interfacial Electrochemistry 206(1): 147-152.

Duff, D. G., A. Baiker and P. P. Edwards (1993). *"A new hydrosol of gold clusters. 1. Formation and particle size variation."* Langmuir 9(9): 2301-2309.

Durand, F., S. Gounel, C. H. Kjaergaard, E. I. Solomon and N. Mano (2012). "*Bilirubin oxidase from Magnaporthe oryzae: an attractive new enzyme for biotechnological applications."* Applied microbiology and biotechnology 96(6): 1489-1498.

Durand, F., C. H. Kjaergaard, E. Suraniti, S. Gounel, R. G. Hadt, E. I. Solomon and N. Mano (2012). *"Bilirubin oxidase from Bacillus pumilus: A promising enzyme for the elaboration of efficient cathodes in biofuel cells."* Biosensors and Bioelectronics 35(1): 140-146.

Eda, G. and M. Chhowalla (2010). *"Chemically Derived Graphene Oxide: Towards Large-Area Thin-Film Electronics and Optoelectronics."* Advanced Materials 22(22): 2392-2415.

Enaud, E., M. Trovaslet, F. Naveau, A. Decristoforo, S. Bizet, S. Vanhulle and C. Jolivalt (2011). *"Laccase chloride inhibition reduction by an anthraquinonic substrate."* Enzyme and Microbial Technology 49(6–7): 517-525.

Fabbrini, M., C. Galli and P. Gentili (2002). "*Comparing the catalytic efficiency of some mediators of laccase."* Journal of Molecular Catalysis B: Enzymatic 16(5–6): 231-240.

Falk, M., M. Alcalde, P. N. Bartlett, A. L. De Lacey, L. Gorton, C. Gutierrez-Sanchez, R. Haddad, J. Kilburn, D. Leech, R. Ludwig, E. Magner, D. M. Mate, P. Ó. Conghaile, R. Ortiz, M. Pita, S. Pöller, T. Ruzgas, U. Salaj-Kosla, W. Schuhmann, F. Sebelius, M. Shao, L. Stoica, C. Sygmund, J. Tilly, M. D. Toscano, J. Vivekananthan, E. Wright and S. Shleev (2014). *"Self-powered wireless carbohydrate/oxygen sensitive biodevice based on radio signal transmission."* PLoS ONE 9(10): e109104.

Falk, M., V. Andoralov, Z. Blum, J. Sotres, D. B. Suyatin, T. Ruzgas, T. Arnebrant and S. Shleev (2012). *"Biofuel cell as a power source for electronic contact lenses."* Biosens Bioelectron 37(1): 38-45.

Falk, M., V. Andoralov, M. Silow, M. D. Toscano and S. Shleev (2013). *"Miniature biofuel cell as a potential power source for glucose-sensing contact lenses."* Analytical Chemistry 85(13): 6342-6348.

Falk, M., Z. Blum and S. Shleev (2012). *"Direct electron transfer based enzymatic fuel cells."* Electrochimica Acta 82: 191-202.

Falk, M., C. W. Narváez Villarrubia, S. Babanova, P. Atanassov and S. Shleev (2013). *"Biofuel cells for biomedical applications: colonizing the animal kingdom."* ChemPhysChem 14(10): 2045-2058.

Falk, M., D. Pankratov, Z. Blum and S. Shleev (2014). *Direct-electron-transfer-based enzymatic fuel cells in vitro, ex vivo, and in vivo.* Implantable Bioelectronics, Wiley-VCH Verlag GmbH & Co. KGaA: 315-346.

Fernández-Fernández, M., M. Á. Sanromán and D. Moldes (2013). *"Recent developments and applications of immobilized laccase."* Biotechnology Advances 31(8): 1808-1825.

Filip, J. and J. Tkac (2014). *"Effective bioelectrocatalysis of bilirubin oxidase on electrochemically reduced graphene oxide."* Electrochemistry Communications 49: 70-74.

Filip, J. and J. Tkac (2014). *"Is graphene worth using in biofuel cells?"* Electrochimica Acta 136: 340-354.

Freeman, H. S., W. M. Whaley, M. K. Esancy and J. F. Esancy (1986). *"Anomalous behavior of aminohydroxynaphthalenesulfonic acids during diazo coupling."* Dyes and Pigments 7(3): 215-230.

Ganesh, V. and A. Muthurasu (2012). *"Strategies for an enzyme immobilization on electrodes: structural and electrochemical characterizations."* Journal of Physics: Conference Series 358: 012003.

Gara, M., K. R. Ward and R. G. Compton (2013). *"Nanomaterial modified electrodes: evaluating oxygen reduction catalysts."* Nanoscale 5(16): 7304-7311.

Gellett, W., M. Kesmez, J. Schumacher, N. Akers and S. D. Minteer (2010). *"Biofuel cells for portable power."* Electroanalysis 22(7-8): 727-731.

Ghasemi-Mobarakeh, L., M. P. Prabhakaran, M. Morshed, M. H. Nasr-Esfahani, H. Baharvand, S. Kiani, S. S. Al-Deyab and S. Ramakrishna (2011). *"Application of conductive polymers, scaffolds and electrical stimulation for nerve tissue engineering."* Journal of Tissue Engineering and Regenerative Medicine 5(4): e17-e35.

Ghosh, S., N. A. Kouamé, L. Ramos, S. Remita, A. Dazzi, A. Deniset-Besseau, P. Beaunier, F. Goubard, P.-H. Aubert and H. Remita (2015). *"Conducting polymer nanostructures for photocatalysis under visible light."* Nat Mater 14(5): 505-511.

Givaudan, A., A. Effosse, D. Faure, P. Potier, M.-L. Bouillant and R. Bally (1993). *"Polyphenol oxidase in Azospirillum lipoferum isolated from rice rhizosphere: Evidence for laccase activity in non-motile strains of Azospirillum lipoferum."* FEMS Microbiology Letters 108(2): 205-210.

González-Arribas, E., T. Bobrowski, C. Di Bari, K. Sliozberg, R. Ludwig, M. D. Toscano, A. L. De Lacey, M. Pita, W. Schuhmann and S. Shleev (2017). *"Transparent, mediator- and membrane-free enzymatic fuel cell based on nanostructured chemically modified indium tin oxide electrodes."* Biosensors and Bioelectronics 97: 46-52.

González-Arribas, E., D. Pankratov, S. Gounel, N. Mano, Z. Blum and S. Shleev (2016). *"Transparent and capacitive bioanode based on specifically engineered glucose oxidase."* Electroanalysis 28(6): 1290-1297.

Gonzalez-Perez, D., I. Mateljak, E. Garcia-Ruiz, F. J. Ruiz-Duenas, A. T. Martinez and M. Alcalde (2016). *"Alkaline versatile peroxidase by directed evolution."* Catalysis Science & Technology 6(17): 6625-6636.

Gooding, J. J., F. Mearns, W. Yang and J. Liu (2003). *"Self-Assembled monolayers into the 21st century: recent advances and applications."* Electroanalysis 15(2): 81-96.

Grzelczak, M., J. Pérez-Juste, F. J. García de Abajo and L. M. Liz-Marzán (2007). *"Optical properties of platinum-coated gold nanorods."* The Journal of Physical Chemistry C 111(17): 6183-6188.

Guan, D., Y. Kurra, W. Liu and Z. Chen (2015). *"A click chemistry approach to site-specific immobilization of a small laccase enables efficient direct electron transfer in a biocathode."* Chemical Communications 51(13): 2522-2525.

Guimard, N. K., N. Gomez and C. E. Schmidt (2007). *"Conducting polymers in biomedical engineering."* Progress in Polymer Science 32(8–9): 876-921.

Gupta, G., V. Rajendran and P. Atanassov (2004). *"Bioelectrocatalysis of oxygen reduction reaction by laccase on gold electrodes."* Electroanalysis 16(13-14): 1182-1185.

Gutiérrez-Sánchez, C., W. Jia, Y. Beyl, M. Pita, W. Schuhmann, A. L. De Lacey and L. Stoica (2012). *"Enhanced direct electron transfer between laccase and hierarchical carbon microfibers/carbon nanotubes composite electrodes. Comparison of three enzyme immobilization methods."* Electrochimica Acta 82: 218-223.

Gutiérrez-Sánchez, C., M. Pita, M. D. Toscano and A. L. De Lacey (2013). "*Bilirubin oxidase-based nanobiocathode working in serum-mimic buffer for implantable biofuel cell."* Electroanalysis 25(6): 1359-1362.

Gutierrez-Sanchez, C., M. Pita, C. Vaz-Dominguez, S. Shleev and A. L. De Lacey (2012). *"Gold nanoparticles as electronic bridges for laccase-based biocathodes."* J Am Chem Soc 134(41): 17212-17220.

Hager, G. and A. G. Brolo (2003). *"Adsorption/desorption behaviour of cysteine and cystine in neutral and basic media: electrochemical evidence for differing thiol and disulfide adsorption to a Au(1 1 1) single crystal electrode."* Journal of Electroanalytical Chemistry 550–551: 291-301.

Halámková, L., J. Halámek, V. Bocharova, A. Szczupak, L. Alfonta and E. Katz (2012). *"Implanted biofuel cell operating in a living snail."* Journal of the American Chemical Society 134(11): 5040-5043.

Heinze, J., A. Rasche, M. Pagels and B. Geschke (2007). *"On the origin of the so-called nucleation loop during electropolymerization of conducting polymers."* The Journal of Physical Chemistry B 111(5): 989-997.

Heller, A. (2004). "*Miniature biofuel cells.*" Physical Chemistry Chemical Physics 6(2): 209-216.

Heppner, D. E., C. H. Kjaergaard and E. I. Solomon (2014). *"Mechanism of the reduction of the native intermediate in the multicopper oxidases: insights into rapid intramolecular electron transfer in turnover."* J Am Chem Soc 136(51): 17788-17801.

Hermanson, G. T. (2013). Chapter 4 - *Zero-Length Crosslinkers.* Bioconjugate Techniques (Third edition). Boston, Academic Press: 259-273.

Hilder, M., B. Winther-Jensen, D. Li, M. Forsyth and D. R. MacFarlane (2011). "*Direct electro-deposition of graphene from aqueous suspensions."* Phys Chem Chem Phys 13(20): 9187-9193.

Hillebrandt, H. and M. Tanaka (2001). "*Electrochemical characterization of self-assembled alkylsiloxane monolayers on indium−tin oxide (ITO) semiconductor electrodes."* The Journal of Physical Chemistry B 105(19): 4270-4276.

Hirota, S., H. Matsumoto, H.-W. Huang, T. Sakurai, T. Kitagawa and O. Yamauchi (1998). *"Observation of Cu–N_3 stretching and N_3 asymmetric stretching bands formono-azide adduct of Rhus vernicifera laccase."* Biochemical and Biophysical Research Communications 243(2): 435-437.

Hosseini, M. G. and I. Ahadzadeh (2013). *"Electrochemical impedance study on methyl orange and methyl red as power enhancing electron mediators in glucose fed microbial fuel cell."* Journal of the Taiwan Institute of Chemical Engineers 44(4): 617-621.

Hummers, W. S. and R. E. Offeman (1958). *"Preparation of graphitic oxide."* Journal of the American Chemical Society 80(6): 1339-1339.

J. Keskinen, E. S., M. Bergelin, J. E. Eriksson, P. Sjöberg-Eerola, M. Valkiainen, M. Smolander, A. Vaari, J. Uotila, H. Boer, S. Tuurala (2010). *"Printed supercapacitor as hybrid device with an enzymatic power source."* Advances in Science and Technology 72: 331-336.

Jeong, J.-A., J. Lee, H. Kim, H.-K. Kim and S.-I. Na (2010). *"Ink-jet printed transparent electrode using nano-size indium tin oxide particles for organic photovoltaics."* Solar Energy Materials and Solar Cells 94(10): 1840-1844.

Jia, W., G. Valdés-Ramírez, A. J. Bandodkar, J. R. Windmiller and J. Wang (2013). *"Epidermal biofuel cells: energy harvesting from human perspiration."* Angewandte Chemie International Edition 52(28): 7233-7236.

Jiang, Y., Y. Lu, F. Li, T. Wu, L. Niu and W. Chen (2012). *"Facile electrochemical codeposition of "clean" graphene–Pd nanocomposite as an anode catalyst for formic acid electrooxidation."* Electrochemistry Communications 19: 21-24.

Jones, S. M. and E. I. Solomon (2015). *"Electron transfer and reaction mechanism of laccases."* Cellular and Molecular Life Sciences 72(5): 869-883.

Jovanovic, S. V., M. Tosic and M. G. Simic (1991). "*Use of the Hammett correlation and .delta.+ for calculation of one-electron redox potentials of antioxidants."* The Journal of Physical Chemistry 95(26): 10824-10827.

Karajic, A. (2015). *"Development of electrode architectures for miniaturized biofuel cells."* PhD Thesis.

Karlin, K. D., B. I. Cohen, J. C. Hayes, A. Farooq and J. Zubieta (1987). "*Models for methemocyanin derivatives: structural and spectroscopic comparisons of related azido-coordinated (N_3^-) mono- and dinuclear copper(II) complexes.*" Inorganic Chemistry 26(1): 147-153.

Kashyap, S., S. Mishra and S. K. Behera (2014). *"Aqueous colloidal stability of graphene oxide and chemically converted graphene."* Journal of Nanoparticles 2014: 1-6.

Katz, E. (2006). "*Bioelectronics*." Electroanalysis 18(19-20): 1855-1857.

Katz, E., I. Willner and A. B. Kotlyar (1999). *"A non-compartmentalized glucose / O_2 biofuel cell by bioengineered electrode surfaces."* Journal of Electroanalytical Chemistry 479(1): 64-68.

Kaur, G., R. Adhikari, P. Cass, M. Bown and P. Gunatillake (2015). "*Electrically conductive polymers and composites for biomedical applications."* RSC Advances 5(47): 37553-37567.

Kear, G. and F. C. Walsh (2005). "*The characteristics of a true Tafel slope."* Corrosion and Materials 6: 51-55.

Kim, C. O., S. Y. Hong, M. Kim, S. M. Park and J. W. Park (2004). "*Modification of indium-tin oxide (ITO) glass with aziridine provides a surface of high amine density."* J Colloid Interface Sci 277(2): 499-504.

Klis, M., M. Karbarz, Z. Stojek, J. Rogalski and R. Bilewicz (2009). "*Thermoresponsive Poly(N-isopropylacrylamide) Gel for Immobilization of Laccase on Indium Tin Oxide Electrodes.*" The Journal of Physical Chemistry B 113(17): 6062-6067.

Kojima, Y., Y. Tsukuda, Y. Kawai, A. Tsukamoto, J. Sugiura, M. Sakaino and Y. Kita (1990). *"Cloning, sequence analysis, and expression of ligninolytic phenoloxidase genes of the white-rot basidiomycete Coriolus hirsutus."* Journal of Biological Chemistry 265(25): 15224-15230.

Koroleva, O. V., E. V. Stepanova, V. I. Binukov, V. P. Timofeev and W. Pfeil (2001). "*Temperature-induced changes in copper centers and protein conformation of two fungal laccases from Coriolus hirsutus and Coriolus zonatus."* Biochimica et Biophysica Acta (BBA) - Protein Structure and Molecular Enzymology 1547(2): 397-407.

Kracher, D., K. Zahma, C. Schulz, C. Sygmund, L. Gorton and R. Ludwig (2015). "I*nter-domain electron transfer in cellobiose dehydrogenase: modulation by pH and divalent cations.*" FEBS J 282(16): 3136-3148.

Kulys, J. and R. Vidziunaite (2005). "*Kinetics of laccase-catalysed TEMPO oxidation."* Journal of Molecular Catalysis B: Enzymatic 37(1–6): 79-83.

Lalaoui, N., K. Elouarzaki, A. L. Goff, M. Holzinger and S. Cosnier (2013). "*Efficient direct oxygen reduction by laccases attached and oriented on pyrene-functionalized polypyrrole/carbon nanotube electrodes."* Chemical Communications 49(81): 9281-9283.

Lalaoui, N., P. Rousselot-Pailley, V. Robert, Y. Mekmouche, R. Villalonga, M. Holzinger, S. Cosnier, T. Tron and A. Le Goff (2016). *"direct electron transfer between a site-specific pyrene-modified laccase and carbon nanotube/gold nanoparticle supramolecular assemblies for bioelectrocatalytic dioxygen reduction.*" ACS Catalysis 6(3): 1894-1900.

Lasia, A. (1995). "*Impedance of porous electrodes."* Journal of Electroanalytical Chemistry 397(1): 27-33.

Lasia, A. (1997). "*Porous electrodes in the presence of a concentration gradient."* Journal of Electroanalytical Chemistry 428(1): 155-164.

Laurentius, L., S. R. Stoyanov, S. Gusarov, A. Kovalenko, R. Du, G. P. Lopinski and M. T. McDermott (2011). "*Diazonium-derived aryl films on gold nanoparticles: evidence for a carbon–gold covalent bond."* ACS Nano 5(5): 4219-4227.

Le Goff, A., M. Holzinger and S. Cosnier (2015). *"Recent progress in oxygen-reducing laccase biocathodes for enzymatic biofuel cells."* Cellular and Molecular Life Sciences 72(5): 941-952.

Léger, C. and P. Bertrand (2008). *"Direct electrochemistry of redox enzymes as a tool for mechanistic studies."* Chemical Reviews 108(7): 2379-2438.

Léger, C., A. K. Jones, S. P. J. Albracht and F. A. Armstrong (2002). "*Effect of a dispersion of interfacial electron transfer rates on steady state catalytic electron transport in [nife]-hydrogenase and other enzymes."* The Journal of Physical Chemistry B 106(50): 13058-13063.

Lehninger, A. L., David L. Nelson, and Michael M. Cox. (2000). "*Lehninger Principles of Biochemistry."* New York: Worth Publishers 6th edition.

Lepage, G., F. O. Albernaz, G. Perrier and G. Merlin (2012). *"Characterization of a microbial fuel cell with reticulated carbon foam electrodes."* Bioresource Technology 124: 199-207.

Li, Y., J. Zhang, X. Huang and T. Wang (2014). "*Construction and direct electrochemistry of orientation controlled laccase electrode."* Biochem Biophys Res Commun 446(1): 201-205.

Lide, D. R. (1993). *Handbook of chemistry and physics*. Boca Raton,FL, CRC Press.

Lindgren, A., L. Gorton, T. Ruzgas, U. Baminger, D. Haltrich and M. Schülein (2001). "*Direct electron transfer of cellobiose dehydrogenase from various biological origins at gold and graphite electrodes.*" Journal of Electroanalytical Chemistry 496(1–2): 76-81.

Liu, J., A. Chou, W. Rahmat, M. N. Paddon-Row and J. J. Gooding (2005). "*Achieving direct electrical connection to glucose oxidase using aligned single walled carbon nanotube arrays."* Electroanalysis 17(1): 38-46.

Liu, Y. and S. Dong (2008). *"Electrochemical Characteristics of Mediated Laccase-Catalysis and Electrochemical Detection of Environmental Pollutants."* Electroanalysis 20(8): 827-832.

Lokhande, V. C., A. C. Lokhande, C. D. Lokhande, J. H. Kim and T. Ji (2016). "*Supercapacitive composite metal oxide electrodes formed with carbon, metal oxides and conducting polymers."* Journal of Alloys and Compounds 682: 381-403.

Luckarift, H. R., D. M. Ivnitski, C. Lau, C. Khripin, P. Atanassov and G. R. Johnson (2012). "*Gold-decorated carbon composite electrodes for enzymatic oxygen reduction."* Electroanalysis 24(4): 931-937.

Ludwig, R., W. Harreither, F. Tasca and L. Gorton (2010). *"Cellobiose dehydrogenase: a versatile catalyst for electrochemical applications."* ChemPhysChem 11(13): 2674-2697.

Ludwig, R., R. Ortiz, C. Schulz, W. Harreither, C. Sygmund and L. Gorton (2013). "*Cellobiose dehydrogenase modified electrodes: advances by materials science and biochemical engineering."* Anal Bioanal Chem 405(11): 3637-3658.

Luz, R. A. S., A. R. Pereira, J. C. P. de Souza, F. C. P. F. Sales and F. N. Crespilho (2014). *"Enzyme biofuel cells: thermodynamics, kinetics and challenges in applicability."* ChemElectroChem 1(11): 1751-1777.

MacVittie, K., J. Halamek, L. Halamkova, M. Southcott, W. D. Jemison, R. Lobel and E. Katz (2013). *"From "cyborg" lobsters to a pacemaker powered by implantable biofuel cells."* Energy & Environmental Science 6(1): 81-86.

Malvankar, N. S., T. Mester, M. T. Tuominen and D. R. Lovley (2012). "*Supercapacitors based on c-type cytochromes using conductive nanostructured networks of living bacteria."* ChemPhysChem 13(2): 463-468.

Mano, N. (2012). "*Features and applications of bilirubin oxidases."* Applied Microbiology and Biotechnology 96(2): 301-307.

Mano, N. and L. Edembe (2013). "*Bilirubin oxidases in bioelectrochemistry: features and recent findings."* Biosens Bioelectron 50: 478-485.

Mano, N., F. Mao and A. Heller (2003). *"Characteristics of a miniature compartment-less glucose–O_2 biofuel cell and its operation in a living plant."* Journal of the American Chemical Society 125(21): 6588-6594.

Mano, N., V. Soukharev and A. Heller (2006). *"A Laccase-Wiring Redox Hydrogel for Efficient Catalysis of O_2 Electroreduction."* The Journal of Physical Chemistry B 110(23): 11180-11187.

Marcus, R. A. and N. Sutin (1985). "*Electron transfers in chemistry and biology."* Biochimica et Biophysica Acta (BBA) - Reviews on Bioenergetics 811(3): 265-322.

Martins, L. g. O., C. M. Soares, M. M. Pereira, M. Teixeira, T. Costa, G. H. Jones and A. O. Henriques (2002). "*Molecular and biochemical characterization of a highly stable bacterial laccase that occurs as a structural component of the bacillus subtilis Endospore Coat."* Journal of Biological Chemistry 277(21): 18849-18859.

Maté, D., C. García-Burgos, E. García-Ruiz, A. O. Ballesteros, S. Camarero and M. Alcalde (2010). "*Laboratory Evolution of High-Redox Potential Laccases."* Chemistry & Biology 17(9): 1030-1041.

Mate, D. M. (2013). "*Diseño de lacasas fungicas activas en sangre mediante evolucion dirigida.*" PhD Thesis.

Mate, D. M. and M. Alcalde (2015). "*Laccase engineering: from rational design to directed evolution."* Biotechnol Adv 33(1): 25-40.

Mate, Diana M., D. Gonzalez-Perez, M. Falk, R. Kittl, M. Pita, Antonio L. De Lacey, R. Ludwig, S. Shleev and M. Alcalde (2013). "*Blood Tolerant Laccase by Directed Evolution.*" Chemistry & Biology 20(2): 223-231.

Mate, D. M., D. Gonzalez-Perez, R. Kittl, R. Ludwig and M. Alcalde (2013). "*Functional expression of a blood tolerant laccase in Pichia pastoris.*" BMC Biotechnology 13(1): 38.

Meredith, M. T. and S. D. Minteer (2012). *"Biofuel Cells: Enhanced Enzymatic Bioelectrocatalysis."* Annual Review of Analytical Chemistry 5(1): 157-179.

Mezour, M. A., I. I. Perepichka, O. Ivasenko, R. B. Lennox and D. F. Perepichka (2015). "*Tridentate benzylthiols on Au(111): control of self-assembly geometry."* Nanoscale 7(11): 5014-5022.

Minteer, S. D., P. Atanassov, H. R. Luckarift and G. R. Johnson (2012). "*New materials for biological fuel cells."* Materials Today 15(4): 166-173.

Mirkhalaf, F. and D. J. Schiffrin (2010). "*Electrocatalytic Oxygen Reduction on Functionalized Gold Nanoparticles Incorporated in a Hydrophobic Environment."* Langmuir 26(18): 14995-15001.

Miyake, T., K. Haneda, N. Nagai, Y. Yatagawa, H. Onami, S. Yoshino, T. Abe and M. Nishizawa (2011). "*Enzymatic biofuel cells designed for direct power generation from biofluids in living organisms."* Energy & Environmental Science 4(12): 5008-5012.

Miyake, T., S. Yoshino, T. Yamada, K. Hata and M. Nishizawa (2011). "*Self-regulating enzyme−nanotube ensemble films and their application as flexible electrodes for biofuel cells."* Journal of the American Chemical Society 133(13): 5129-5134.

Moss, D., E. Nabedryk, J. Breton and W. MÄNtele (1990). *"Redox-linked conformational changes in proteins detected by a combination of infrared spectroscopy and protein electrochemistry."* European Journal of Biochemistry 187(3): 565-572.

Murao, S. and N. Tanaka (1981). "*A new enzyme "Bilirubin Oxidase" produced by Myrothecium verrucaria MT-1."* Agricultural and Biological Chemistry 45(10): 2383-2384.

Murata, K., K. Kajiya, N. Nakamura and H. Ohno (2009). "*Direct electrochemistry of bilirubin oxidase on three-dimensional gold nanoparticle electrodes and its application in a biofuel cell."* Energy & Environmental Science 2(12): 1280-1285.

Murata, K., M. Suzuki, K. Kajiya, N. Nakamura and H. Ohno (2009). "*High performance bioanode based on direct electron transfer of fructose dehydrogenase at gold nanoparticle-modified electrodes.*" Electrochemistry Communications 11(3): 668-671.

Naqui, A. and S. D. Varfolomeev (1980). "*Inhibition mechanism of Polyporus laccase by fluoride ion.*" FEBS Letters 113(2): 157-160.

Narváez Villarrubia, C. W., C. Lau, G. P. M. K. Ciniciato, S. O. Garcia, S. S. Sibbett, D. N. Petsev, S. Babanova, G. Gupta and P. Atanassov (2014). "*Practical electricity generation from a paper based biofuel cell powered by glucose in ubiquitous liquids.*" Electrochemistry Communications 45: 44-47.

Navaee, A. and A. Salimi (2015). "*Graphene-supported pyrene-functionalized amino-carbon nanotube: a novel hybrid architecture of laccase immobilization as effective bioelectrocatalyst for oxygen reduction reaction*." J. Mater. Chem. A 3(14): 7623-7630.

Nazaruk, E., K. Sadowska, K. Madrak, J. F. Biernat, J. Rogalski and R. Bilewicz (2009). *"Composite bioelectrodes based on lipidic cubic phase with carbon nanotube network."* Electroanalysis 21(3-5): 507-511.

Newman, J. S. and C. W. Tobias (1962). "*Theoretical analysis of current distribution in porous electrodes."* Journal of The Electrochemical Society 109(12): 1183-1191.

Oesch, U. and J. Janata (1983). "*Electrochemical study of gold electrodes with anodic oxide films—I. Formation and reduction behaviour of anodic oxides on gold."* Electrochimica Acta 28(9): 1237-1246.

Ogawa, Y., K. Kato, T. Miyake, K. Nagamine, T. Ofuji, S. Yoshino and M. Nishizawa (2015). *"Organic transdermal iontophoresis patch with built-in biofuel cell."* Advanced Healthcare Materials 4(4): 506-510.

Oh, W.-K., O. S. Kwon and J. Jang (2013). "*Conducting polymer nanomaterials for biomedical applications: cellular interfacing and biosensing."* Polymer Reviews 53(3): 407-442.

Opallo, M. and R. Bilewicz (2011). "*Recent developments of nanostructured electrodes for bioelectrocatalysis of dioxygen reduction.*" Advances in Physical Chemistry 2011: 21.

Osman, M. H., A. A. Shah and F. C. Walsh (2011). "*Recent progress and continuing challenges in bio-fuel cells. Part I: Enzymatic cells."* Biosensors and Bioelectronics 26(7): 3087-3102.

Paasch, G., K. Micka and P. Gersdorf (1993). "*Theory of the electrochemical impedance of macrohomogeneous porous electrodes."* Electrochimica Acta 38(18): 2653-2662.

Page, C. C., C. C. Moser, X. Chen and P. L. Dutton (1999). *"Natural engineering principles of electron tunnelling in biological oxidation-reduction.*" Nature 402(6757): 47-52.

Pang, H. L., J. Liu, D. Hu, X. H. Zhang and J. H. Chen (2010). "*Immobilization of laccase onto 1-aminopyrene functionalized carbon nanotubes and their electrocatalytic activity for oxygen reduction*." Electrochimica Acta 55(22): 6611-6616.

Pankratov, D., Z. Blum and S. Shleev (2014). "*Hybrid electric power biodevices*." ChemElectroChem 1(11): 1798-1807.

Pankratov, D., Z. Blum, D. B. Suyatin, V. O. Popov and S. Shleev (2014). "*Self-charging electrochemical biocapacitor*." ChemElectroChem 1(2): 343-346.

Pankratov, D., P. Falkman, Z. Blum and S. Shleev (2014). "*A hybrid electric power device for simultaneous generation and storage of electric energy."* Energy & Environmental Science 7(3): 989.

Pankratov, D., E. González-Arribas, Z. Blum and S. Shleev (2016). "*Tear based bioelectronics*." Electroanalysis 28(6): 1250-1266.

Pankratov, D., L. Ohlsson, P. Gudmundsson, S. Halak, L. Ljunggren, Z. Blum and S. Shleev (2016). "*Ex vivo electric power generation in human blood using an enzymatic fuel cell in a vein replica*." RSC Advances 6(74): 70215-70220.

Pankratov, D., R. Sundberg, J. Sotres, I. Maximov, M. Graczyk, D. B. Suyatin, E. González-Arribas, A. Lipkin, L. Montelius and S. Shleev (2015). "*Transparent and flexible, nanostructured and mediatorless glucose/oxygen enzymatic fuel cells*." Journal of Power Sources 294: 501-506.

Pankratov, D., R. Sundberg, D. B. Suyatin, J. Sotres, A. Barrantes, T. Ruzgas, I. Maximov, L. Montelius and S. Shleev (2014). "*The influence of nanoparticles on enzymatic bioelectrocatalysis*." RSC Advances 4(72): 38164.

Papra, M., F. N. Büchi and R. Kötz (2010). "I*nvestigating the dynamics of a direct parallel combination of supercapacitors and polymer electrolyte fuel cells*." Fuel Cells 10(5): 873-878.

Pavlidis, I. V., M. Patila, U. T. Bornscheuer, D. Gournis and H. Stamatis (2014). "*Graphene-based nanobiocatalytic systems: recent advances and future prospects."* Trends Biotechnol 32(6): 312-320.

Peyratout, C. S., J. C. Severns, S. R. Holm and D. R. McMillan (1994). "*EPR Studies of Ligand binding to the type 2/Type 3 cluster in tree laccase."* Archives of Biochemistry and Biophysics 314(2): 405-411.

Pia, E. A. D., Q. Chi, D. D. Jones, J. E. Macdonald, J. Ulstrup and M. Elliott (2011). "*Single-molecule mapping of long-range electron transport for a Cytochrome b562 variant*." Nano Letters 11(1): 176-182.

Pifferi, V., M. M. Barsan, M. E. Ghica, L. Falciola and C. M. A. Brett (2013). "*Synthesis, characterization and influence of poly(brilliant green) on the performance of different electrode architectures based on carbon nanotubes and poly(3,4-ethylenedioxythiophene)."* Electrochimica Acta 98: 199-207.

Piontek, K., M. Antorini and T. Choinowski (2002). "*Crystal structure of a laccase from the fungus Trametes versicolor at 1.90-Å resolution containing a full complement of coppers*." Journal of Biological Chemistry 277(40): 37663-37669.

Pita, M., C. Gutierrez-Sanchez, D. Olea, M. Velez, C. Garcia-Diego, S. Shleev, V. M. Fernandez and A. L. De Lacey (2011). "*High redox potential cathode based on laccase covalently attached to gold electrode."* The Journal of Physical Chemistry C 115(27): 13420-13428.

Pita, M., C. Gutierrez-Sanchez, M. D. Toscano, S. Shleev and A. L. De Lacey (2013). *"Oxygen biosensor based on bilirubin oxidase immobilized on a nanostructured gold electrode."* Bioelectrochemistry 94: 69-74.

Pita, M., S. Shleev, T. Ruzgas, V. M. Fernández, A. I. Yaropolov and L. Gorton (2006). *"Direct heterogeneous electron transfer reactions of fungal laccases at bare and thiol-modified gold electrodes*." Electrochemistry Communications 8(5): 747-753.

Pletcher, D., R. Greff, R. Peat, L. M. Peter and J. Robinson (2010). 5 - *The electrical double layer*. Instrumental Methods in Electrochemistry, Woodhead Publishing: 149-177.

Pogacean, F., C. Socaci, S. Pruneanu, A. R. Biris, M. Coros, L. Magerusan, G. Katona, R. Turcu and G. Borodi (2015). "*Graphene based nanomaterials as chemical sensors for hydrogen peroxide – A comparison study of their intrinsic peroxidase catalytic behavior."* Sensors and Actuators B: Chemical 213: 474-483.

Polyakov, K. M., Fedorova, Tatyana V., Stepanova, Elena V., Cherkashin, Evgeny A., Kurzeev, Sergei A., Strokopytov, Boris V., Lamzin, Victor S., Koroleva, Olga V., (2009). "*Structure of native laccase from Trametes hirsuta at 1.8 A resolution."* Acta Crystallographica Section D 65: 611-617.

Prathish, K. P., M. M. Barsan, D. Geng, X. Sun and C. M. A. Brett (2013). "*Chemically modified graphene and nitrogen-doped graphene: electrochemical characterisation and sensing applications."* Electrochimica Acta 114: 533-542.

Pumera, M., A. Ambrosi, A. Bonanni, E. L. K. Chng and H. L. Poh (2010). "*Graphene for electrochemical sensing and biosensing."* TrAC Trends in Analytical Chemistry 29(9): 954-965.

Qiu, H., C. Xu, X. Huang, Y. Ding, Y. Qu and P. Gao (2008). *"Adsorption of laccase on the surface of nanoporous gold and the direct electron transfer between them."* The Journal of Physical Chemistry C 112(38): 14781-14785.

Quintanar, L., C. Stoj, A. B. Taylor, P. J. Hart, D. J. Kosman and E. I. Solomon (2007). *"Shall we dance? How a multicopper oxidase chooses its electron transfer partner."* Accounts of Chemical Research 40(6): 445-452.

Quintanar, L., J. Yoon, C. P. Aznar, A. E. Palmer, K. K. Andersson, R. D. Britt and E. I. Solomon (2005). "S*pectroscopic and electronic structure studies of the trinuclear Cu cluster active site of the multicopper oxidase laccase: Nature of Its Coordination Unsaturation."* Journal of the American Chemical Society 127(40): 13832-13845.

Raistrick, I. D. (1990). "*Impedance studies of porous electrodes*." Electrochimica Acta 35(10): 1579-1586.

Ramasamy, R. P., H. R. Luckarift, D. M. Ivnitski, P. B. Atanassov and G. R. Johnson (2010). "*High electrocatalytic activity of tethered multicopper oxidase-carbon nanotube conjugates*." Chemical Communications 46(33): 6045-6047.

Ramirez, P., N. Mano, R. Andreu, T. Ruzgas, A. Heller, L. Gorton and S. Shleev (2008). "*Direct electron transfer from graphite and functionalized gold electrodes to T1 and T2/T3 copper centers of bilirubin oxidase."* Biochim Biophys Acta 1777(10): 1364-1369.

Ran Liu, S. I. C. a. S. B. L. (2008). "*Poly(3,4-ethylenedioxythiophene) nanotubes as electrode materials for a high-powered supercapacitor."* Nanotechnology 19(21): 215710.

Rao, C. N. R., A. K. Sood, K. S. Subrahmanyam and A. Govindaraj (2009). "*Graphene: the new two-dimensional nanomaterial."* Angewandte Chemie International Edition 48(42): 7752-7777.

Rasmussen, M., S. Abdellaoui and S. D. Minteer (2016). "*Enzymatic biofuel cells: 30 years of critical advancements."* Biosensors and Bioelectronics 76: 91-102.

Rasmussen, M., R. E. Ritzmann, I. Lee, A. J. Pollack and D. Scherson (2012). "*An implantable biofuel cell for a live insect."* Journal of the American Chemical Society 134(3): 1458-1460.

Reculusa, S., M. Heim, F. Gao, N. Mano, S. Ravaine and A. Kuhn (2011). "*Design of catalytically active cylindrical and macroporous gold microelectrodes."* Advanced Functional Materials 21(4): 691-698.

Reinhammar, B. R. M. (1972). "*Oxidation-reduction potentials of the electron acceptors in laccases and stellacyanin."* Biochimica et Biophysica Acta (BBA) - Bioenergetics 275(2): 245-259.

Renault, C., C. P. Andrieux, R. T. Tucker, M. J. Brett, V. Balland and B. Limoges (2012). "*Unraveling the mechanism of catalytic reduction of O_2 by microperoxidase-11 adsorbed within*

a transparent 3D-nanoporous ITO film." Journal of the American Chemical Society 134(15): 6834-6845.

Rivers, T. H., T.W. Schmidt, C.E. and J. Takahashi (2002). "*Synthesis of a novel, biodegradable electrically conducting polymer for biomedical applications."* Advanced Functional Materials 12(1): 1616-3028.

Romero, P. A. and F. H. Arnold (2009). "*Exploring protein fitness landscapes by directed evolution."* Nat Rev Mol Cell Biol 10(12): 866-876.

Rüdiger, O., C. Gutiérrez-Sánchez, D. Olea, I. A. C. Pereira, M. Vélez, V. M. Fernández and A. L. De Lacey (2010). *"Enzymatic anodes for hydrogen fuel cells based on covalent attachment of Ni-Fe hydrogenases and direct electron transfer to SAM-modified gold electrodes."* Electroanalysis 22(7-8): 776-783.

S Bellucci, M. C., A Cucina, GA Carru, and AI Chiaretti (2009). "*Multiwalled carbon nanotube buckypaper: toxicology and biological effects in vitro and in vivo."* Nanomedicine 4: 531-540.

Sakmeche, N., S. Aeiyach, J.-J. Aaron, M. Jouini, J. C. Lacroix and P.-C. Lacaze (1999). "*Improvement of the electrosynthesis and physicochemical properties of Poly(3,4-ethylenedioxythiophene) using a sodium dodecyl sulfate micellar aqueous medium."* Langmuir 15(7): 2566-2574.

Sakurai, T., J. Takahashi and H.-w. Huang (1996). "*FT-IR spectra of the azide-type 3 copper in laccase and ascorbate oxidase."* Chemistry Letters 25(8): 651-652.

Salaj-Kosla, U., S. Pöller, Y. Beyl, M. D. Scanlon, S. Beloshapkin, S. Shleev, W. Schuhmann and E. Magner (2012). "*Direct electron transfer of bilirubin oxidase (Myrothecium verrucaria) at an unmodified nanoporous gold biocathode.*" Electrochemistry Communications 16(1): 92-95.

Salaj-Kosla, U., S. Poller, W. Schuhmann, S. Shleev and E. Magner (2013). "*Direct electron transfer of Trametes hirsuta laccase adsorbed at unmodified nanoporous gold electrodes."* Bioelectrochemistry 91: 15-20.

Schulz, C., R. Kittl, R. Ludwig and L. Gorton (2016). "*Direct electron transfer from the fad cofactor of cellobiose dehydrogenase to electrodes*." ACS Catalysis 6(2): 555-563.

Shao, Y., J. Wang, H. Wu, J. Liu, I. A. Aksay and Y. Lin (2010). "*Graphene based electrochemical sensors and biosensors: a review."* Electroanalysis 22(10): 1027-1036.

Shaolin, M. and K. Jinqing (1995). "*Bioelectrochemical activation and inhibition of polyaniline glucose oxidase electrode by cations.*" Electrochimica Acta 40(2): 241-246.

Sheldon, R. A. (2007). "E*nzyme immobilization: the quest for optimum performance."* Advanced Synthesis & Catalysis 349(8-9): 1289-1307.

Shleev, S. (2017). "*Quo Vadis, implanted fuel cell?"* ChemPlusChem 82(4): 522-539.

Shleev, S., V. Andoralov, M. Falk, C. T. Reimann, T. Ruzgas, M. Srnec, U. Ryde and L. Rulíšek (2012). "*On the possibility of uphill intramolecular electron transfer in multicopper oxidases: electrochemical and quantum chemical study of bilirubin oxidase*." Electroanalysis 24(7): 1524-1540.

Shleev, S., A. Bergel and L. Gorton (2015). "*Biological fuel cells: Divergence of opinion."* Bioelectrochemistry 106, Part A: 1-2.

Shleev, S., J. Tkac, A. Christenson, T. Ruzgas, A. I. Yaropolov, J. W. Whittaker and L. Gorton (2005). "*Direct electron transfer between copper-containing proteins and electrodes.*" Biosens Bioelectron 20(12): 2517-2554.

Shleev, S., J. Tkac, A. Christenson, T. Ruzgas, A. I. Yaropolov, J. W. Whittaker and L. Gorton (2005). "*Direct electron transfer between copper-containing proteins and electrodes.*" Biosensors and Bioelectronics 20(12): 2517-2554.

Shleev, S. V., O. V. Morozova, O. V. Nikitina, E. S. Gorshina, T. V. Rusinova, V. A. Serezhenkov, D. S. Burbaev, I. G. Gazaryan and A. I. Yaropolov (2004). "C*omparison of physico-chemical characteristics of four laccases from different basidiomycetes."* Biochimie 86(9–10): 693-703.

Si, Y. and E. T. Samulski (2008). "*Synthesis of water soluble graphene*." Nano Letters 8(6): 1679-1682.

Siepenkoetter, T., U. Salaj-Kosla, X. Xiao, P. Ó. Conghaile, M. Pita, R. Ludwig and E. Magner (2017). "*Immobilization of redox enzymes on nanoporous gold electrodes: applications in biofuel cells*." ChemPlusChem 82(4): 553-560.

Simon, E. P. T. C. J. S. W. "T*ables of spectral data for structure determination of organic compounds."*

Sinz, A. (2006). "*Chemical cross-linking and mass spectrometry to map three-dimensional protein structures and protein–protein interactions*." Mass Spectrometry Reviews 25(4): 663-682.

Solís-Fernández, P., R. Rozada, J. I. Paredes, S. Villar-Rodil, M. J. Fernández-Merino, L. Guardia, A. Martínez-Alonso and J. M. D. Tascón (2012). "*Chemical and microscopic analysis of graphene prepared by different reduction degrees of graphene oxide."* Journal of Alloys and Compounds 536, Supplement 1: S532-S537.

Solomon, E. I., A. J. Augustine and J. Yoon (2008). "*O_2 reduction to H_2O by the multicopper oxidases."* Dalton Transactions(30): 3921-3932.

Solomon, E. I., R. Sarangi, J. S. Woertink, A. J. Augustine, J. Yoon and S. Ghosh (2007). "*O_2 and N_2O activation by bi-, tri-, and tetranuclear cu clusters in biology."* Accounts of Chemical Research 40(7): 581-591.

Solomon, E. I., U. M. Sundaram and T. E. Machonkin (1996). "*Multicopper oxidases and oxygenases."* Chemical Reviews 96(7): 2563-2606.

Song, S., R. A. Clark, E. F. Bowden and M. J. Tarlov (1993). *"Characterization of cytochrome c/alkanethiolate structures prepared by self-assembly on gold." The Journal of Physical Chemistry 97(24): 6564-6572.*

Sorrell, T. N., C. O'Connor, O. P. Anderson and J. H. Reibenspies (1985). "*Synthesis and characterization of phenolate-bridge copper dimers with a copper-copper separation of >3.5 .ANG.. Models for the active site of oxidized hemocyanin derivatives.*" Journal of the American Chemical Society 107(14): 4199-4206.

Sosna, M., H. Boer and P. N. Bartlett (2013). "*A His-tagged melanocarpus albomyces laccase and its electrochemistry upon immobilisation on NTA-modified electrodes and in conducting polymer films.*" ChemPhysChem 14(10): 2225-2231.

Sosna, M., J.-M. Chretien, J. D. Kilburn and P. N. Bartlett (2010). *"Monolayer anthracene and anthraquinone modified electrodes as platforms for Trametes hirsuta laccase immobilisation."* Physical Chemistry Chemical Physics 12(34): 10018-10026.

Stolarczyk, K., D. Łyp, K. Żelechowska, J. F. Biernat, J. Rogalski and R. Bilewicz (2012). *"Arylated carbon nanotubes for biobatteries and biofuel cells."* Electrochimica Acta 79: 74-81.

Szamocki, R., S. Reculusa, S. Ravaine, P. N. Bartlett, A. Kuhn and R. Hempelmann (2006). "*Tailored mesostructuring and biofunctionalization of gold for increased electroactivity."* Angewandte Chemie International Edition 45(8): 1317-1321.

Szczupak, A., J. Halamek, L. Halamkova, V. Bocharova, L. Alfonta and E. Katz (2012). "*Living battery - biofuel cells operating in vivo in clams."* Energy & Environmental Science 5(10): 8891-8895.

Szot, K., A. Lesniewski, J. Niedziolka, M. Jönsson, C. Rizzi, L. Gaillon, F. Marken, J. Rogalski and M. Opallo (2008). "*Sol–gel processed ionic liquid – hydrophilic carbon nanoparticles multilayer film electrode prepared by layer-by-layer method."* Journal of Electroanalytical Chemistry 623(2): 170-176.

Tam, T. K., M. Ornatska, M. Pita, S. Minko and E. Katz (2008). "*Polymer brush-modified electrode with switchable and tunable redox activity for bioelectronic applications.*" The Journal of Physical Chemistry C 112(22): 8438-8445.

Tan, T.-C., D. Kracher, R. Gandini, C. Sygmund, R. Kittl, D. Haltrich, B. M. Hällberg, R. Ludwig and C. Divne (2015). "*Structural basis for cellobiose dehydrogenase action during oxidative cellulose degradation.*" Nature Communications 6: 7542.

Tasca, F., W. Harreither, R. Ludwig, J. J. Gooding and L. Gorton (2011). "*Cellobiose dehydrogenase aryl diazonium modified single walled carbon nanotubes: enhanced direct electron transfer through a positively charged surface."* Analytical Chemistry 83(8): 3042-3049.

Thorum, M. S., C. A. Anderson, J. J. Hatch, A. S. Campbell, N. M. Marshall, S. C. Zimmerman, Y. Lu and A. A. Gewirth (2010). "*Direct, electrocatalytic oxygen reduction by laccase on anthracene-2-methanethiol modified gold.*" J Phys Chem Lett 1(15): 2251-2254.

Toh, S. Y., K. S. Loh, S. K. Kamarudin and W. R. W. Daud (2014). "*Graphene production via electrochemical reduction of graphene oxide: Synthesis and characterisation."* Chemical Engineering Journal 251: 422-434.

Tominaga, M., N. Noda, T. Hashiguchi, H. Mizuta, D. Kawai and M. Togami (2015). "*Improvement of laccase bioelectrocatalyst at a phosphate templating graphene nanoplatelet plate electrode."* Electrochemistry Communications 59: 32-35.

Trasatti, S. and O. A. Petrii (1991). *Real surface area measurements in electrochemistry.* Pure and Applied Chemistry. 63: 711.

Troughton, E. B., C. D. Bain, G. M. Whitesides, R. G. Nuzzo, D. L. Allara and M. D. Porter (1988). "*Monolayer films prepared by the spontaneous self-assembly of symmetrical and unsymmetrical dialkyl sulfides from solution onto gold substrates: structure, properties, and reactivity of constituent functional groups.*" Langmuir 4(2): 365-385.

Ulyanova, Y., S. Babanova, E. Pinchon, I. Matanovic, S. Singhal and P. Atanassov (2014). "*Effect of enzymatic orientation through the use of syringaldazine molecules on multiple multi-copper oxidase enzymes."* Physical Chemistry Chemical Physics 16(26): 13367-13375.

Vaz-Dominguez, C., S. Campuzano, O. Rüdiger, M. Pita, M. Gorbacheva, S. Shleev, V. M. Fernandez and A. L. De Lacey (2008). *"Laccase electrode for direct electrocatalytic reduction of O_2 to H_2O with high-operational stability and resistance to chloride inhibition."* Biosensors and Bioelectronics 24(4): 531-537.

Vaz-Domínguez, C., M. Pita, A. L. de Lacey, S. Shleev and A. Cuesta (2012). "*Combined ATR-SEIRAS and EC-STM study of the immobilization of laccase on chemically modified au electrodes."* The Journal of Physical Chemistry C 116(31): 16532-16540.

Wagner, N. (2002). *"Characterization of membrane electrode assemblies in polymer electrolyte fuel cells using a.c. impedance spectroscopy."* Journal of Applied Electrochemistry 32(8): 859-863.

Walcarius, A. (2010). *"Template-directed porous electrodes in electroanalysis."* Analytical and Bioanalytical Chemistry 396(1): 261-272.

Wharton, C. W. (1986). "*Infra-red and Raman spectroscopic studies of enzyme structure and function.*" Biochemical Journal 233(1): 25-36.

Windmiller, J. R., A. J. Bandodkar, G. Valdes-Ramirez, S. Parkhomovsky, A. G. Martinez and J. Wang (2012). "*Electrochemical sensing based on printable temporary transfer tattoos.*" Chemical Communications 48(54): 6794-6796.

Wingard, L. B. (1972). *"Enzyme engineering."* Interscience Publisher: New York, NEW YORK, 1972.

Winter, M. and R. J. Brodd (2004). "W*hat are batteries, fuel cells, and supercapacitors?*" Chemical Reviews 104(10): 4245-4270.

Xiao, X., P. Si and E. Magner (2016). "*An overview of dealloyed nanoporous gold in bioelectrochemistry."* Bioelectrochemistry 109: 117-126.

Xiao, Y., F. Patolsky, E. Katz, J. F. Hainfeld and I. Willner (2003). "*"Plugging into enzymes": nanowiring of redox enzymes by a gold nanoparticle."* Science 299(5614): 1877-1881.

Xu, F. (1996). "*Oxidation of phenols, anilines, and benzenethiols by fungal laccases: correlation between activity and redox potentials as well as halide inhibition*." Biochemistry 35(23): 7608-7614.

Xu, F., R. M. Berka, J. A. Wahleithner, B. A. Nelson, J. R. Shuster, S. H. Brown, A. E. Palmer and E. I. Solomon (1998). "*Site-directed mutations in fungal laccase: effect on redox potential, activity and pH profile.*" Biochemical Journal 334(Pt 1): 63-70.

Xu, F., W. Shin, S. H. Brown, J. A. Wahleithner, U. M. Sundaram and E. I. Solomon (1996). *"A study of a series of recombinant fungal laccases and bilirubin oxidase that exhibit significant differences in redox potential, substrate specificity, and stability."* Biochimica et Biophysica Acta (BBA) - Protein Structure and Molecular Enzymology 1292(2): 303-311.

Yang, L. and Y. Li (2005). "*AFM and impedance spectroscopy characterization of the immobilization of antibodies on indium–tin oxide electrode through self-assembled monolayer of epoxysilane and their capture of Escherichia coli O157:H7."* Biosensors and Bioelectronics 20(7): 1407-1416.

Yáñez-Sedeño, P. and J. M. Pingarrón (2005). "*Gold nanoparticle-based electrochemical biosensors."* Analytical and Bioanalytical Chemistry 382(4): 884-886.

Yaropolov, A. I., O. V. Skorobogat'ko, S. S. Vartanov and S. D. Varfolomeyev (1994). *"Laccase."* Applied Biochemistry and Biotechnology 49(3): 257-280.

Yoon, S.-B. and K.-B. Kim (2013). "*Effect of poly(3,4-ethylenedioxythiophene) (PEDOT) on the pseudocapacitive properties of manganese oxide (MnO_2) in the PEDOT/MnO_2/multiwall carbon nanotube (MWNT) composite."* Electrochimica Acta 106: 135-142.

Zaheer, Z. and Rafiuddin (2012). *"Silver nanoparticles to self-assembled films: green synthesis and characterization."* Colloids and Surfaces B: Biointerfaces 90: 48-52.

Zebda, A., S. Cosnier, J. P. Alcaraz, M. Holzinger, A. Le Goff, C. Gondran, F. Boucher, F. Giroud, K. Gorgy, H. Lamraoui and P. Cinquin (2013). "*Single glucose biofuel cells implanted in rats power electronic devices."* Scientific Reports 3: 1516.

Zebda, A., C. Gondran, A. Le Goff, M. Holzinger, P. Cinquin and S. Cosnier (2011). "*Mediatorless high-power glucose biofuel cells based on compressed carbon nanotube-enzyme electrodes."* Nat Commun 2: 370.

Żelechowska, K., K. Stolarczyk, D. Łyp, J. Rogalski, K. P. Roberts, R. Bilewicz and J. F. Biernat (2013). "*Aryl and N-arylamide carbon nanotubes for electrical coupling of laccase to electrodes in biofuel cells and biobatteries."* Biocybernetics and Biomedical Engineering 33(4): 235-245.

Zhao, H. Y., H. M. Zhou, J. X. Zhang, W. Zheng and Y. F. Zheng (2009). "*Carbon nanotube–hydroxyapatite nanocomposite: a novel platform for glucose/O_2 biofuel cell*." Biosensors and Bioelectronics 25(2): 463-468.

Bioelectrochemistry 107 (2016) 30–36

Contents lists available at ScienceDirect

Bioelectrochemistry

journal homepage: www.elsevier.com/locate/bioelechem

Laccase-modified gold nanorods for electrocatalytic reduction of oxygen

Chiara Di Bari [a], Sergey Shleev [b], Antonio L. De Lacey [a], Marcos Pita [a,*]

[a] Instituto de Catálisis y Petroleoquimica, CSIC, c/Marie Curie 2, L10, 28049 Madrid, Spain
[b] Biomedical Sciences Faculty of Health and Society, Malmo University, SE-205 06 Malmo, Sweden

ARTICLE INFO

Article history:
Received 8 July 2015
Received in revised form 24 September 2015
Accepted 4 October 2015
Available online 9 October 2015

Keywords:
Laccase
Graphite
Gold nanorod
Biocathode
Biofuel cell

ABSTRACT

The multicopper oxidase *Trametes hirsuta* laccase (ThLc) served as a bioelectrocatalyst on nanostructured cathodes. Nanostructuring was provided by gold nanorods (AuNRs), which were characterized and covalently attached to electrodes made of low-density graphite. The nanostructured electrode was the scaffold for covalent and oriented attachment of ThLc. The bioelectrocatalytic currents measured for oxygen reduction were as high as 0.5 mA/cm^2 and 0.7 mA/cm^2, which were recorded under direct and mediated electron transfer regimes, respectively. The experimental data were fitted to mathematical models showing that when the O_2 is bioelectroreduced at high rotation speed of the electrode the heterogeneous electron transfer step is the rate-liming stage. The electrochemical measurement hints a wider population of non-optimally wired laccases than previously reported for 5–8 nm size Au nanoparticle-modified electrode, which could be due to a larger size of the AuNRs when compared to the laccases as well as their different crystal facets.

1. Introduction

Laccases, formally known as polyphenol oxidases, are enzymes from the oxidoreductases group known as blue multicopper oxidases, which also comprise bilirubin oxidase, ceruloplasmin and ascorbate oxidase. Laccases have an active site characterized by two different redox centers that contain Cu (II) ions separated in their folded structure. The first of these two centers contains a single Cu cation, named T1 site, and its function is to oxidize a substrate while stripping out four electrons in consecutive steps. The electrons go to the second center, the T2/T3 copper trinuclear cluster, where O_2 is reduced to H_2O [1]. The T1 site redox potential ranges between 400 and 800 mV vs. NHE depending on the laccase natural source [1]. On the other side it is impossible to assess a single redox potential value for the T2/T3 cluster. The catalytic cycle of blue multicopper oxidases contemplates several cluster intermediates [2] that show different redox potentials from each other [3]. Although the values for such redox potentials are experimentally unknown, it is estimated that they are relatively high [4] as some multicopper oxidases' intermediates show a strongly oxidizing and highly reactive behavior [5].

The redox potential of most fungal laccases is high, which allows a very interesting advantage: their ability to biocatalyze the reduction of O_2 to H_2O at very low overpotentials with 100% efficiency and at high turnover rates [1,6]. This characteristic allows such laccases to perform as bioelectrocatalysts in the cathodes of biofuel cells [7,8]. Biofuel cells can be utilized for implantable devices [9] and could take part in future biomedical applications [10]. Including laccase as catalyst in biocathode requires its immobilization on the electrode and the substitution of its natural electron donor substrate by the electrode itself. Redox mediators can facilitate this step, yielding very high biocatalytic O_2 reduction only limited by the O_2 diffusion rate to the enzymatic electrode [11,12]. However, mediated electron transfer (MET) systems involve an additional redox process, therefore diminishing the catalytic redox potential from that of the laccase to the mediator's one. Another possibility is to avoid mediators aiming to maximize the onset potential for O_2 reduction; such approach means developing laccase biocathodes based on direct electron transfer (DET). In this case the goal is obtaining biocatalytic currents as intense as those of MET-based electrodes while minimizing the O_2 reduction overpotential and putting apart the typical problems brought by redox mediators. Achieving such goal requires that the reduction of O_2 performed by the laccase biocathode takes place at the T1 site of the laccase and not at the T2/T3 Cu site [6].

Several strategies to connect laccase and the electrodes by DET have been published either relying on the oriented immobilization of the laccase [13–16] or on its co-immobilization with conductive nanostructures [17–21]. Particularly successful works wired the laccase to graphite electrodes by means of carbon nanotubes, in which the catalytic current was mass-transport limited [22], or by gold nanoparticles that could act as electronic bridges [23]. The latter work showed that small-enough gold nanoparticles (AuNPs) could connect the enzyme active site and the electrode very efficiently; consequently the electron transfer between the laccase and the electrode ceased to limit the whole process and a Nernstian-like process was achieved [23]. Such result opened new interest on wiring laccase to electrodes enhanced by nanoelements.

In the present work we study an alternative disposition of the nanostructured gold, namely nano-rods (AuNRs). The rod-shape offers

* Corresponding author.
E-mail addresses: alopez@icp.csic.es (A.L. De Lacey), marcospita@icp.csic.es (M. Pita).

http://dx.doi.org/10.1016/j.bioelechem.2015.10.003
1567-5394/

Electrochimica Acta 191 (2016) 500–509

Contents lists available at ScienceDirect

Electrochimica Acta

journal homepage: www.elsevier.com/locate/electacta

Fabrication of high surface area graphene electrodes with high performance towards enzymatic oxygen reduction

Chiara Di Bari[a,1], Asier Goñi-Urtiaga[b,1], Marcos Pita[a], Sergey Shleev[c], Miguel D. Toscano[d], Raquel Sainz[b,*], Antonio L. De Lacey[a,*]

[a] Instituto de Catálisis y Petroleoquímica, CSIC, c/Marie Curie 2, L10, 28049 Madrid, Spain
[b] Nanoinnova Technologies SL, c/Faraday 7, 28049 Madrid, Spain
[c] Biomedical Sciences, Faculty of Health and Society, Malmo University, SE-0205 06 Malmo, Sweden
[d] Protein Diversity, Novozymes A/S, Krogshojvej 36, 2880 Bagsvaerd, Denmark

ARTICLE INFO

Article history:
Received 14 December 2015
Received in revised form 13 January 2016
Accepted 14 January 2016
Available online 16 January 2016

Keywords:
Graphene
Laccase
Bilirubin Oxidase
Oxygen Reduction Reaction
Biocathode

ABSTRACT

High surface area graphene electrodes were prepared by simultaneous electrodeposition and electroreduction of graphene oxide. The electrodeposition process was optimized in terms of pH and conductivity of the solution and the obtained graphene electrodes were characterized by X-ray photoelectron spectroscopy, Fourier transform infrared spectroscopy, scanning electron microscopy and electrochemical methods (cyclic voltammetry and impedance spectroscopy). Electrodeposited electrodes were further functionalized to carry out covalent immobilization of two oxygen-reducing multicopper oxidases: laccase and bilirubin oxidase. The enzymatic electrodes were tested as direct electron transfer based biocathodes and catalytic currents as high as 1 mA/cm^2 were obtained. Finally, the mechanism of the enzymatic oxygen reduction reaction was studied for both enzymes calculating the Tafel slopes and transfer coefficients.

1. Introduction

The fabrication of stable and reproducible electrodes is a key issue for the development of electrochemical devices and their implementation in our society. The scientific community has developed electroactive materials and electrode fabrication protocols aiming to tailor them for each electrochemical application. Devices such as fuel cells [1], supercapacitors [2] and batteries [3] need high surface area electrodes, high electrical conductivity and controllable porosity among other properties. High surface area carbonaceous materials, such as carbon nanotubes (CNT) [4,5], carbon nanofibers (CNF) [6,7] or graphene [8,9], have attracted great interest due to their excellent electrical conductivity and mechanical properties. Graphene has been intensively studied in the latter years, focusing on its physicochemical and electrochemical properties to utilize it as a catalytic support on the electrode surface [10,11].

Graphene can be produced following many strategies: mechanical exfoliation of highly oriented pyrolytic graphite (HOPG), thermal decomposition of SiC wafers, chemical vapour deposition (CVD) on metal substrates, substrate-free CVD or reduction of graphene oxide (GO) by chemical, thermal or electrochemical means [12]. Each of these strategies provides graphene with different characteristics. Manufacturing graphene-based electrodes has to overcome the low reproducibility of the current fabrication methods, *i.e.* drop-casting, brushing or spraying [13–15]. Recently, the electrodeposition of graphene oxide and its simultaneous electrochemical reduction on the electrode surface has been proposed as a reproducible method for the fabrication of stable and high surface area electrodes [16–18].

Graphene-based electrodes have been used for several applications, such as biosensing or as support for further immobilization of enzymes [9,10]. Multi-copper oxidases (MCOs) have been widely used in the preparation of biosensors and/or biocathodes due to their capability of catalyzing the oxidation of different organic and inorganic substrates with the concomitant reduction of oxygen to water directly to water without production of highly reactive oxygen species. MCOs typically contain four redox-active Cu ions classified according to their spectroscopic signal as T1 copper and the trinuclear cluster (TNC), which consists on a T2 copper ion and two T3 copper ions [19]. It is generally accepted that the T1 site is the primary electron acceptor from the substrate and then the electrons are transferred to the TNC cluster site which

* Corresponding author.
E-mail addresses: rsainz@nanoinnova.com (R. Sainz), alopez@icp.csic.es (A.L. De Lacey).
[1] These authors contributed equally to the work.

http://dx.doi.org/10.1016/j.electacta.2016.01.101
0013-4686/

Spectroelectrochemical studies of halides inhibition mechanism of multicopper oxidases using azide as an active infrared probe

Chiara Di Bari[1*], Nicolas Mano[2], Sergey Shleev[3], Marcos Pita[1] and Antonio L. De Lacey[1*]

[1]Instituto de Catálisis y Petroleoquímica, CSIC, c/ Marie Curie 2, L10, 28049 Madrid, Spain.

[2]Centre de Recherche Paul Pascal, Université de Bordeaux, UPR 8641, CNRS, Avenue Albert Schweitzer, 33600 Pessac, France.

[3]Biomedical Sciences, Faculty of Health and Society, Malmo University, SE-0205 06 Malmo, Sweden.

* Corresponding authors: cdi.bari@csic.es, alopez@icp.csic.es, +34-915854807

Abstract

An infrared spectroelectrochemical study of *Trametes hirsuta* laccase and *Magnaporthe oryzae* bilirubin oxidase has been performed using azide, an inhibitor of multicopper oxidases, as an active infrared probe incorporated into the T2/T3 copper cluster of the enzymes. The redox potential controlled measurements indicate that N_3^- stretching IR bands of azide ion bound to the T2/T3 cluster are only detected for the oxidized enzymes, confirming that azide only binds to Cu^{2+}. Moreover, the process of binding/dissociation of azide ion is shown to be reversible. The interaction of halide anions, which also inhibit multicopper oxidases, with the active site of the enzymes was studied by measuring the changes in the azide FTIR bands. Enzymes inhibited by azide respond differently upon addition of fluoride or chloride ions to the sample solution inhibited by azide. Fluoride ions compete with azide for binding at one of the T2/T3 Cu ions, whereas competition from chloride ions is almost absent.

Keywords: Multicopper oxidase, infrared, halide inhibition, spectroelectrochemistry

Biosensors and Bioelectronics 97 (2017) 46–52

Contents lists available at ScienceDirect

Biosensors and Bioelectronics

journal homepage: www.elsevier.com/locate/bios

Transparent, mediator- and membrane-free enzymatic fuel cell based on nanostructured chemically modified indium tin oxide electrodes

Elena González-Arribas[a,1], Tim Bobrowski[b,1], Chiara Di Bari[c], Kirill Sliozberg[b], Roland Ludwig[d], Miguel D. Toscano[e], Antonio L. De Lacey[c], Marcos Pita[c], Wolfgang Schuhmann[b,*], Sergey Shleev[a,f,g,**]

[a] Biomedical Science, Health and Society, Malmö University, 20560 Malmö, Sweden
[b] Analytical Chemistry – Center for Electrochemical Sciences (CES), Ruhr-Universität Bochum, D-44780 Bochum, Germany
[c] Instituto de Catálisis y Petroleoquímica, CSIC, C/Marie Curie 2, L10, 28049 Madrid, Spain
[d] Department of Food Science and Technology, BOKU-University of Natural Resources and Life Sciences, Muthgasse 18, 1190 Vienna, Austria
[e] Novozymes A/S, Krogshoejvej 36, 2880 Bagsværd, Denmark
[f] A.N. Bach Institute of Biochemistry, 119071 Moscow, Russia
[g] Kurchatov NBIC Centre, National Research Centre "Kurchatov Institute", 123182 Moscow, Russia

ARTICLE INFO

Keywords:
Indium tin oxide
Nanoparticle
Membrane-free
Mediator-free
Transparent enzymatic fuel cell

ABSTRACT

We detail a mediator- and membrane-free enzymatic glucose/oxygen biofuel cell based on transparent and nanostructured conducting supports. Chemically modified indium tin oxide nanoparticle modified electrodes were used to substantially increase the active surface area without significantly compromising transparency. Two different procedures for surface nanostructuring were employed, *viz.* spray-coating and drop-coating. The spray-coated biodevice showed superior characteristics as compared to the drop-coated enzymatic fuel cell, as a result of the higher nanostructured surface area as confirmed by electrochemical characterisation, as well as scanning electron and atomic force microscopy. Subsequent chemical modification with silanes, followed by the immobilisation of either cellobiose dehydrogenase from *Corynascus thermophiles* or bilirubin oxidase from *Myrothecium verrucaria*, were performed to obtain the bioanodes and biocathodes, respectively. The optimised biodevice exhibited an OCV of 0.67 V and power output of up to 1.4 μW/cm^2 at an operating voltage of 0.35 V. This is considered a significant step forward in the field of glucose/oxygen membrane- and mediator-free, transparent enzymatic fuel cells.

1. Introduction

Biological fuel cells (BFCs) in general, and enzymatic fuel cells (EFCs) in particular, have been envisioned as electrical power sources for self-contained bioelectronics including biomedical devices operating *in vivo* and *ex vivo* (Castorena-Gonzalez et al., 2013; Cosnier et al., 2016, 2014; Falk et al., 2013b, 2014; Halámková et al., 2012; Heller, 2004; Katz, 2014; Leech et al., 2012; Rasmussen et al., 2016; Shleev, 2017).

For certain applications, *e.g.* wearable electronics (Bandodkar and Wang, 2014, 2016; Pankratov et al., 2016) and biosolar cells (Somasundaran et al., 2011), the transparency of the EFC should be taken into account. The use of transparent conductive nanomaterials allows improving the aesthetic and cosmetic issues that are relevant in the case of smart electronic contact lenses (Blum et al., 2014; Parviz, 2009) and body-attachable wearable electronic platforms (Kim et al., 2015; Trung et al., 2016).

The electric power is generated by converting *in situ* available chemical energy from different biofuels present in human tears into electric energy. Several possible biofuels are present in lachrymal liquid, *e.g.* glucose, lactate, ascorbate and pyruvate, as well as neurotransmitters, although they appear in limited supply, while a biooxidant, molecular oxygen (O_2), dissolved in tear fluid is abundantly available (Pankratov et al., 2016). The very first publications detailing BFCs as power sources for electronic contact lenses appeared in 2012–2013: nanostructured glucose/oxygen (Falk et al., 2012) and ascorbate/oxygen (Falk et al., 2013a) BFCs based on direct electron transfer (DET) reactions were fabricated and tested in human lachrymal liquid.

* Corresponding author at: Analytical Chemistry – Center for Electrochemical Sciences (CES), Ruhr-Universität Bochum, D-44780 Bochum, Germany.
** Corresponding author at: Biomedical Science, Health and Society, Malmö University, 20560 Malmö, Sweden.
E-mail addresses: wolfgang.schuhmann@rub.de (W. Schuhmann), sergey.shleev@mah.se (S. Shleev).
[1] These authors contributed equally to this work.

http://dx.doi.org/10.1016/j.bios.2017.05.040
Received 8 April 2017; Received in revised form 18 May 2017; Accepted 22 May 2017
Available online 23 May 2017
0956-5663/

In: Laccase: Applications, Investigations and Insights ISBN: 978-1-53610-556-8
Editor: Amanda Harris

Chapter 4

LACCASE-BASED BIOCATHODES FOR OXYGEN ELECTROREDUCTION IN ENZYMATIC FUEL CELLS

Chiara di Bari, Marcos Pita and Antonio L. De Lacey*
Instituto de Catálisis y Petroleoquímica, CSIC, Madrid, Spain

ABSTRACT

During the last years enzymatic fuel cells (EFCs) have attracted great interest due to their possible applications, especially as electrical power sources for implantable devices in living organisms. In EFCs enzymes are used as biocatalysts for fuel oxidation at the anode and oxidant reduction at the cathode. Depending on the fuel and oxidant available an appropriate choice of enzymes is needed for the biofuel application. The majority of EFCs use oxygen-reducing enzymes at the cathode, as it is a very common oxidant present in most human physiological fluids. Multi-copper oxidases, such as laccase, bilirubin oxidase, ascorbate oxidase, have been studied as possible biocatalysts for the oxygen reduction reaction; their main attractive comes in their skill to reduce oxygen directly to water avoiding H_2O_2 formation. In this review we focus on the use of laccase enzymes as biocatalyst for the fabrication of biocathodes, paying special attention to the different electrode materials and immobilization strategies used to manufacture biodevices based on direct electron transfer (DET) or on mediated electron transfer (MET). Indeed, a larger surface area of the support material allows higher enzyme loading, therefore increasing the current density developed. Nanoparticles, nanofibers, nanotubes, mesoporous and carbonaceous materials have been used for this purpose. A good immobilization strategy enhances the long-term stability of the biodevice while achieving efficient wiring of the enzyme.

Laccases usually exhibit higher activity at acid pH and they are strongly inhibited in the presence of chloride ions. As this could limit their use for possible implantable devices, a strategy has been made for overcoming this problem: native laccases have been engineered by directed evolution for obtaining mutants that show activity under physiological conditions. An alternative strategy followed has been altering the local pH of the biocathode.

Finally, future outlook of laccase-based biocathodes applications are highlighted.

* Corresponding Author: alopez@icp.csic.es.